

Magnetic field directed self-assembly of gold Pickering emulsion for preparing patterned film.

OKPOZO, O.P.

2022

The author of this thesis retains the right to be identified as such on any occasion in which content from this thesis is referenced or re-used. The licence under which this thesis is distributed applies to the text and any original images only – re-use of any third-party content must still be cleared with the original copyright holder.

Magnetic Field Directed Self-Assembly of
Gold Pickering Emulsion for Preparing
Patterned Film

Oghenefego Paul Okpozo

Magnetic Field Directed Self-Assembly of Gold Pickering Emulsion for Preparing Patterned Film

OGHENEFEGO PAUL OKPOZO

Supervisors: Dr. Ketan Pancholi

Dr. Sheikh Islam

A thesis submitted in partial fulfilment of the
requirements of
Robert Gordon University
for the degree of Doctor of Philosophy

December 2022

Declaration

I hereby declare that the research report in this thesis is original and have been completed independently by myself (Oghenefego Paul Okpozo), under the supervision of Dr. Ketan Pancholi and Dr. Sheikh Islam. This PhD thesis has not been submitted for award of any other degree or professional qualification.

Where other sources are quoted full references are given

Oghenefego Paul Okpozo

July 2022

Dedication

I dedicate this thesis to Late Chief F. S. Okpozo who passed on 40 days before I started this journey. I thank you for being an upright man and model who ensured I make positive of every situation in life.

Acknowledgement

This research has been a huge sacrifice from me, but most importantly many individuals who have supported me one way or the other through this journey. I firstly want to thank God almighty for life, strength, endurance, peace, health and His overall support every day of my life. I want to thank my mother, Mrs. Anna Okpozo for her love, kindness, prayers, patience and encouragement. I love you so much mum! I want to thank my siblings, Mrs. Onome Agboola, Mr. Edgar Okpozo, Mrs. Evelyn Esedafe, Mr. Jude Okpozo, and Mrs. Zino Orobor for their prayers, support and tactical scoldings which are needed sometimes, I still love you all much more. I wish to specially thank Bro. Hez Esedafe for stepping in at crucial times during this journey. Truly appreciated!

I want to specially thank my supervisor, Dr. Ketan Pancholi for his kindness, humility, professionalism, insight, support and most especially understanding during difficult moments. I also want to thank second supervisor, Dr. Sheikh Islam for his support, encouragement and professionalism. I wish to thank the graduate school as well for their understanding, support and professionalism during the course of my PhD experience.

I wish to acknowledge special individuals for their kindness and support I will forever be grateful for. I wish to appreciate Mr. Alan McClean, Mrs. Emily Hunter, Mr. David Smith (Rtd), Mr. David Howie, Mr. Patrick Kane, Mr. Slawek Rybczynski, Mrs. Laurie Smith and many others from both School of Engineering and PALS. Even though I was pesty at times, but yet it was all worth it and I thank you all.

I wish to finally appreciate my financial sponsor, Niger Delta Development Commission (NDDC), for supporting me through my PhD program.

Abstract

Patterning plays a vital role in sensor-based devices like Surface enhanced Raman spectroscopy (SERS), surface-enhanced infrared absorption (SEIRA), Radio frequency (RF) antennas and many others. The linear array spacing and width of gold strips has been shown to increase the local intensity through near field coupling with diffracted electromagnetic waves. This rise in local charge boosts vibrational energies of molecules in close surface contact or proximity resulting in increased IR absorption. The strip-like or any other types of patterns are efficiently achieved through top-down nanofabrication processes like atomic-force-deposition, nanoimprinting, UV-Lithography, etc. that involves high capital cost, complex processing and occasionally low throughput. Therefore, this research was undertaken with aim to reduce the process complexities and improve scalability by applying a magnetic and spin coating directed self-assembly (MSCDS) to prepare an optically sensitive dipole-dipole chain-like ordered arrays of the gold nanoparticle pickering ferrofluid in polyvinyl alcohol (PVA) emulsion in form of thin film on glass and silicon substrate. Previously conducted MSCDS processes lacked the control over the dimensions of the prepared patterns. Here, the static magnetic field approach was taken to modify the MSCDS process to overcome the limitation of pattern dimension control providing tuneability for optical applications.

The quantitative image analysis of the patterned thin film allowed for the measurement of pattern geometrical dimension (chain length-CL, chain gap-CG and chain thickness-CT), which was then correlated with processing parameters such as magnetic field configurations (single, compound and concentric), spinning speeds and viscosities of pickering emulsion. Upon optimization, spectroscopical characterisation was performed on prepared patterned thin film to demonstrate the capability of the modified MSDS process in enhancing the molecular detection at low concentrations. The UV-vis spectra of the patterns demonstrated the impact of CT and CG on the degree of gold - iron oxide nanoscale interactions leading to tuneability of absorption bands between 390-700nm. The coupling of the increased optical sensitivity through enhanced charge transfer dynamics with the mid-infra-red range grating order (CT+CG) resulted in an amplification in vibrational band excitation of molecular

bonds. Like in the case of SEIRA measurements of thin film patterns showed a vibrational signal enhancement in asymmetric vibration of -CH₂ (2920cm⁻¹) bonds of PVA by 40%, as CT increased by 178% from 1.2μm at probing 45° grazing angle. Furthermore, the magneto-optical SERS phenomenon involving local polarization of gold nanoparticles through the neighbouring magnetised iron oxide nanoparticle in the presence of external magnetic field was exploited to reveal the varying degree of enhancement in peaks related to Rhodamine 6G (R6G) coated on thin film nanostructure was dependent on magnetized CT/CG morphology and especially C-C-C ring (671 cm⁻¹) Raman peak increased by 12,000% when magnetized by 43mT field.

In summary, the modified MSCDC process is cheap with an expandable throughput rate (>0.1 m²/h) and flexible designs offering both nanoscale and microscale tuneability of pattern dimensions. Even with higher defectivity (~14%) in comparison to the nanoimprinting method, this method can potentially be used to create repetitive array like structure. Furthermore, the use of iron oxide reduces the cost without sacrificing the optical performance and thus contributed to the optical tuneability of the thin film nanostructure thereby making the entire product a potential absorbing antenna and microfluidics thin film for biomolecule detection.

Keywords: Nanofabrication, Magnetic, Iron oxide, Gold, Chain thickness, Chain gap, Ferrofluid, Spin coating, Viscosity, FTIR, UV-Vis, Pickering emulsion, Pixel density, Map, Raman.

List of Publications and Conferences

Published Journal

Pancholi, K., Robertson, P.K., Okpozo, P., Beattie, N.S. and Huo, D., 2018. Observation of stimulated emission from Rhodamine 6G-polymer aggregate adsorbed at foam interfaces. *Journal of Physics: Energy*, 1(1), p.015007.

Okpozo, P. and Pancholi, K., 2023. Study of spatial organisation of magnetic field directed gold-pickering-ferrofluid-nanoemulsion in spin coated film. *Hybrid Advances*, p.100018.

In Journal Publication in progress

Paul Okpozo, Y. Dwivedi, Ketan Pancholi and Sheikh Islam (2023) Magnetically directed self-assembled gold pickering emulsion periodic array for surface enhance infrared spectroscopy, *Advanced Materials*, *submitted

Paul Okpozo, Y. Dwivedi, D.Huo and Ketan Pancholi (2023) Enhancement in SERS Raman signal of Rhodamine 6G in static magnetic field , *journal-of-science-advanced-materials-and-devices*.

List of Conferences

Okpozo, P. O. and Pancholi, K. (2019); Magnetically Tuneable Emulsion Template Nanostructure. Research in Sustainable Environments (RiSE) Conference, Glasgow UK.

Table of Contents

Abstract.....	vi
List of Tables	xiii
List of Figures	xv
Nomenclature	xxi
Abbreviations	xxiii
<i>Chapter 1</i> Introduction.....	1
1.1 Background	1
1.2 Research Motivation	2
1.3 Problem Statements	5
1.4 Aim	7
1.5 Objectives.....	7
1.6 Thesis Summary	7
<i>Chapter 2</i> Literature Review	9
2.1 Chapter in Brief	9
2.2 Nanofabrication and methods of nanofabrication	10
2.3 Methods of fabrication	11
2.3.1 Top-Down Techniques	11
2.3.2 Bottom-Up Approaches	13
2.3.3 Summarised relative quantification of top-down and bottom-up approaches.....	15
2.3.4 Self-Assembly	18
2.4 Control of Nanoparticles or Colloids in Ordered Structural Agglomerates within Nanostructures .	22
2.4.1 Fluidic self-assembly method for creating 2D and 3D colloidal structures	24
2.5 Combination of nanofabrication techniques for building of complex patterned colloidal structures – Spin Coating	30
2.5.1 Spin Coating and Lithographically Patterned Substrate.	30
2.5.2 Spin Coating and Electric Field directed Assembly	31
2.5.3 Spin Coating and Magnetic Field Directed Assembly.....	31
2.6 Research Interest and Fabrication Approach – Spin Coating and Magnetic Field Directed Assembly	32
2.6.1 Magnetism principle and magnetism of colloids.....	34
2.6.2 Spin Coating Mechanism.....	45
2.7 Optical Behaviour of Materials selected for nanofabrication.....	47

2.7.1 Iron oxide-Gold dimer nano-heterostructures	52
2.8 Potential Application of Designed structures	55
2.9 Characterization methods.....	56
2.9.1 Structure Test and Performance.....	56
2.10 Chapter Summary	61
<i>Chapter 3 Preparation of Gold Pickering Ferrofluid Emulsion.....</i>	<i>63</i>
3.1 Chapter Objective	63
3.2 Fabrication components properties tests.....	64
3.3 Materials	66
3.4 Processing Methods.....	66
3.4.1 Ferrofluid Preparation.....	68
3.4.2 Gold Methacrylate Preparation	69
3.4.3 Preparation of PEG-C-M Pickering Ferrofluid Emulsion.....	70
3.4.4 Substrate Preparation	71
3.5 Material Characterisation	72
3.5.1 UV-Vis Measurement	72
3.5.2 DLS Size Measurement, Zeta sizing.....	74
3.5.3 Zeta Potential.....	75
3.5.4 Magnetic Hysteresis.....	77
3.5.5 Transmission electron microscope	79
3.5.6 Fourier Transform Infra-red (FTIR) Spectroscopy	81
3.5.7 Thermal Gravimetric Analysis	85
3.5.8 Determining the viscosity of aqueous Polyvinyl alcohol (PVA).....	86
3.6 Emulsion Size Sorting via Centrifugation	91
3.6.1 System Description	91
3.6.2 Size Distribution Statistics.....	94
3.7 Chapter in Summary	98
<i>Chapter 4 Nanostructure Design</i>	<i>99</i>
4.1 Chapter Objective	99
4.2 Methods.....	100
4.2.1 Optical Microscopy	100
4.2.2 Scanning Electron Microscopy (SEM).....	100
4.2.3 Physical assumptions	100

4.3 Experiment Setup.....	100
4.4 Results and Analysis.....	102
4.4.1 Images of Spin coated samples.....	102
4.4.2 Cluster density distribution analysis.....	108
4.4.3 Pattern Morphology Analysis and Mapping.....	116
4.5 Chapter Summary.....	134
<i>Chapter 5 Thin film Characterisation and Analysis.....</i>	<i>137</i>
5.1 Chapter Objective.....	137
5.2 Equipment and Procedures.....	137
5.2.1 UV-Vis.....	137
5.2.2 FTIR-Transmission mode.....	138
5.2.3 FTIR-Specular reflectance.....	138
5.2.4 SQUID.....	139
5.2.5 Raman.....	139
5.3 UV-Vis spectrophotometry.....	139
5.3.1 Results and Analysis.....	144
5.4 Fourier Transform Infra-Red Spectroscopy.....	161
5.4.1 Transmission mode FTIR data analysis.....	161
5.4.2 FTIR Specular reflectance or grazing angle of incidence (FTIR-SR).....	168
5.5 Magnetization curve.....	180
5.6 Raman Test and Analysis.....	181
5.6.1 Results.....	181
5.7 General Discussion.....	189
5.8 Chapter Summary.....	191
<i>Chapter 6 Conclusion, Recommendation and Future Work.....</i>	<i>193</i>
6.1 About Chapter.....	193
6.2 Conclusion.....	193
6.3 Challenges and recommendations.....	198
6.4 Future Work.....	199
References.....	201
Appendices.....	232
8.1 Estimation of gold methacrylate molecules calculation steps.....	232
8.2 Code for droplet size distribution following centrifugation.....	233

8.3 Centrifugal size sorting fit trend equation	234
8.4 Region of interest measurements for 3.5mPas at 700rpm and 2000rpm	234
8.5 Image density fitting	236
8.6 Sample images of spin coated thin films	237
8.7 Simple Code for Chain thickness and gap Profile scan	238
8.8 Example of scan plot profile for one of the red lines from Figure 4-12(b) with X as pixel divisions (168nm/pixel) and Y as the binary pixel intensity.	239
8.9 Summary of pattern morphology image analysis for PVA 15.2mPas	240
8.10 Energy ratio (QPI) determined from magnetic profile shown in Fig. 4.21 and emulsion property from Table 4.1 and preparation angular speed 3500 rpm	241
8.11 Defectivity determination from Profile scan results from Figure 4-23.....	241
8.12 FTIR Transmission mode absorption data for thin film pattern on optical glass.....	242
8.13 Deconvolved band of UV-Vis Spectra of Samples.....	243
8.14 Deconvolved band of UV-Vis Spectra of Samples.....	245

List of Tables

Table 2-1 List of Top-down approaches; showing techniques, advantages, disadvantages and references.	11
Table 2-1 List of Top-down approaches; showing techniques, advantages, disadvantages and references – contd.	12
Table 2-2 List of conventional bottom-up techniques, showing techniques, advantages, disadvantages and references.	13
Table 2-2 List of conventional bottom-up techniques, showing techniques, advantages, disadvantages and references – contd.	14
Table 2-2 List of conventional bottom-up techniques, showing techniques, advantages, disadvantages and references – contd.	15
Table 2-3 List of directed self-assembly techniques consisting of background information, downsides and references	19
<i>Table 2-3 List of directed self-assembly techniques consisting of background information, downsides and references – contd.</i>	20
<i>Table 2-3 List of directed self-assembly techniques consisting of background information, downsides and references – contd.</i>	21
Table 2-4 Summary of fluidic aided self-assembly methods	25
<i>Table 2-4 Summary of fluidic aided self-assembly methods – contd.</i>	26
Table 3-1: Synthesis products representative format.	68
Table 3-2 Summary of results from magnetic hysteresis to obtain diameter and standard deviation of samples.	79
Table 3-3: Bands and their representation taken from (Merck, 2020)	82
Table 3-4 : presented are obtained values of densities following equation 3.5, viscosities obtained following equation 3.6.	87
Table 3-5 Selected operating conditions for centrifugal size control	92
Table 3-6 Summary of distribution of ultrasonicated sample	92
Table 3-7 Size distribution data of test emulsion following different spin speeds and spin time.	93
Table 4-1 Sample setup and process parameters at room temperature. The density was determined using approach by (Mohsen-Nia & Modarress, 2006).	102
Table 4-2 Region of interest pixel intensity density measurements for sample having viscosity 3.5mPas, spin coated at 700rpm	110
Table 4-4 Example of output from simple program (in Appendix 8.6) that counted number of pixels in each chain block to identify chain thickness and chain gaps within the scanned profile. CntCL and CntGap is number of pixel counts for a chain and gap respectively.	120
Table 4-5 Summary of results obtained from image analysis of sample prepared under 3500 rpm spin speed.	121
Table 4-6 Data of some of the test magnetic setups, Magnet 2 and 3 showing ratios QPI against CL/CT and CT/CG with their respective standard deviation values (SD)	126

Table 4-7 This is a result summary from image analysis of structured sample estimating its area defectivity from gap between consecutive tail and head of chains along an array and short gaps within individual chains (DEFCL).	129
Table 5-1 Summary of band interpretation based on influence of specie ratios	160
Table 5-2 CT and CT/CG from image analysis of 3.3wt% PVA under 3000 rpm spin speed	173
Table 5-3: Identified Raman bands of Rhodamine 6G, the peak intensities at radial locations, $r= 1\text{mm}$, 2mm, 4mm, 6mm for magnetized and $r= 1\text{mm}$ for unmagnetized. The percentage change of magnetized regions from unmagnetized was estimated and placed at the side of respective peak intensities.	187
<i>Table 5-3 Contd.: Identified Raman bands of Rhodamine 6G, the peak intensities at radial locations, $r= 1\text{mm}$, 2mm, 4mm, 6mm for magnetized and $r= 1\text{mm}$ for unmagnetized. The percentage change of magnetized regions from unmagnetized was estimated and placed at the side of respective peak intensities.</i>	188

List of Figures

Figure 1-1: Illustration of research process of combined self-assembly techniques for the short-and-long-range organisation of gold nanoparticles for optical applications 5

Figure 2-1 Illustrative quantification of existing top-down and bottom-up nanofabrication methods; (a) shows the throughput rate (m^2/h) vs resolution (b) shows a three-dimensional quantification consisting of defectivity, complexity and process cost ($£/m^2$). Summary obtained from the following sources; (Radha & Kulkarni, 2014), (Garcia, et al., 2014), (Liddle & Gallatin, 2016), (Biswas, et al., 2012), (Martinez-Chapa, et al., 2020), (Zhang, et al., 2013)16

Figure 2-2 shows the pair of Helmholtz coils, (b) shows the Helmholtz coils installed around the substrate, (c) shows diagrammatic illustration of field lines generated by the Helmholtz coil (HC) across the substrate (S). this figure is courtesy of (Pichumani & Gonzalez-Vinas, 2013). (d) shows the resultant structure of dilute ferromagnetic colloid solution 8mm from centre of substrate under magnetic field $H=0.066T$ and spin speed= $5000rpm$, scale bar= $50\mu m$, courtesy (Pichumani & Gonzalez-Vinas, 2013). (e) resultant structure of ferromagnetic colloid solution 6mm from middle of substrate under magnetic field $H=0.99kA/m$ and spin speed= $2000rpm$, courtesy of (Aslam & Gonzalez-Vinas, 2017). (f) Resultant structure of magnetic colloid at middle of substrate under magnetic field $H=39.7kA/m$ and speed= $2400rpm$, and (g) Resultant structure of magnetic colloid at middle of substrate under magnetic field $H=39.7kA/m$ and speed= $700rpm$. Courtesy of (Aslam & Gonzalez-Vinas, 2019).....32

Figure 2-3 Shows an illustration of the impact of forces and motion on ferromagnetic particles; the fluid flow through spin coating tends to drive the fluid along arrow (1) from a magnetic field line spot (a to b), within the same time scale, the radial directional movement of the substrate tend to carry the particle from field spot 1-a to 2-a, thereby affecting the polarity of the each particle and their relative dipole-dipole interactions.....33

Figure 2-4 Magnetization Hysteresis loop for a ferromagnetic material; showing Remanescence (R) and Coercivity (HC) curves. Courtesy (Barhoum & Garcia-Betancourt, 2018).....36

Figure 2-5 Schematic of coercivity vs particle radius. Courtesy of (Barhoum & Garcia-Betancourt, 2018).....37

Figure 2-6 A truncated image of Hysteresis loop at 0K for non-interacting particle. The slope χ_{ns} is same as χ_{iL} , where it coincides with initial slope from $H=0$. Courtesy (Egli, 2009).....39

Figure 2-7 Microscope images showing; (a) cross-section of single droplet thick chain structure with volume fraction = 0.007, cell thickness = $5\mu m$, $H=31.5mT$, rate at $800mT/min$ from $0mT$. (b) cross-section of column structure at volume fraction of 0.13, cell thickness = $65\mu m$, $H = 38mT$, rate at $0.01mT/min$ from $0mT$. (c) cross-section of Labyrinthine structure with volume fraction 0.12, cell thickness = $50\mu m$, $H = 38mT$, rate at $240mT/min$. Courtesy of (Lawrence, et al., 1994)42

Figure 2-8 (a) Digital images showing the diffraction colour change in a typical CNC dispersion encapsulated in a capillary tube with a width of 1 cm in response to a magnetic field with increasing strength of magnetic field from left to right. (b) Reflectance spectra of the same sample in different magnetic fields. (c) is a schematic illustration of the gap between colloids upon magnetic field strengths. (d) digital photo showing a suspension of CNCs displaying rainbow-like colours due to the variance in the interparticle spacing d and the orientation θ in different regions controlled by the magnetic field. All images were extracted from (He, et al., 2012).43

Figure 2-9 (a) the length of magnetic particle (MP) chain with a diameter of $2\mu m$ is $257.3\mu m$, (b) Effect of mass fraction of MPs on the chain length when the magnetic field strength is $100.77mT$ and the particle diameter d is $1.5\mu m$, (c) Effect of particle diameter on the chain length when the mass fraction is 2% and the magnetic field strength is $100.77mT$, (d) Effect of magnetic field strength on the chain length when the mass fraction is 2% and the diameter of MPs d is $1.5\mu m$. Images are extract from (Zhu, et al., 2021).....44

Figure 2-10 UV-Vis absorption spectra of Iron Oxide, Gold and dimer heterostructure of combined iron oxide and gold. Courtesy (Korobchevskaya, et al., 2011)53

Figure 2-11 UV-visible absorption spectra (in water) for pure gold and iron-gold alloy nanoparticles synthesized from Fe₀ precursor with various molar ratios. The molar ratios of iron and gold are 1:1, 1:2, and 1:3, indicated by circle, cross, and triangle, respectively. Courtesy (Dahal & Chikan, 2008) 53

Figure 3-1: Schematic of manufacturing process of colloids and PEG-C-GM-pi-FF emulsion67

Figure 3-2 (a) is the dried oleic coated magnetite (OCM) after oven drying, (b) is a drop of dispersed OCM in cis-Cyclooctene, (c) is the UV-vis spectra of dilute (0.07g/ml) concentration of OCM in cis-Cyclooctene.....72

Figure 3-3(a) Red colour colloidal solution of gold methacrylate in water, (b) a schematic of gold methacrylate nanoparticle within the solution shown in (a), (c) is a UV-Vis absorption data of gold methacrylate (GM) and PEG coated Gold methacrylate (PEG-C-GM) showing plasmon resonance at peak point 528nm.73

Figure 3-4(a) Image of peach coloured pickering emulsion in a vial, (b) UV-Vis absorption spectra of pickering emulsion with gold nanoparticle (PEG-C-GM) showing broad plasmon between 515-610nm 74

Figure 3-5 (a) An image showing dried lattices of gold methacrylate (Black) and PEG coated gold methacrylate (Purple) on microscopic slides. (b) Size distribution measurement results of GM and PEG-C-GM colloids in a semi log graph.....75

Figure 3-6 Presentation of Zeta potential peak values of varying particle systems77

Figure 3-7 (A) Magnetic hysteresis for magnetite and Oleic coated magnetite (OCM), (b) and (c) presents a magnified range of the hysteresis curve to obtain coercivity (H_c) for both magnetite and OCM materials respectively.78

Figure 3-8 : Transmission electron microscopy of colloids (a) is for Oleic coated magnetite and the histogram beneath shows its mean as 15nm and standard deviation as 2.99nm. (b) is for Gold methacrylate nanoparticles with its histogram plot shown beneath it having a mean of 17nm and standard deviation as 2.57nm. (c) PEG-coated Gold Methacrylate nanoparticles showing its histogram distribution beneath it having a mean of 22nm and standard deviation of 3.8nm.80

Figure 3-9 A TEM image of spin coated dried ferrofluid droplet being Pickered by PEG-C-GM nanoparticles. The evaporation rate and drying from spinning might have led to PEG-C-GM nanoparticles from the interface.81

Figure 3-10 : **(A)** Comparison of components of FF, such as the OA, OCM and cis-Cyclooctene as the continuous phase **(B)** Comparison of infrared spectra between sodium methacrylate, methacrylic acid, Gold methacrylate, PEG 40s and PEG-C-GM **(C)** Comparison of prepared components on the effect of components on PVA, such as PEG-C-GM Pickering Ferrofluid, PVA, PEG-C-GM in PVA, FF in PVA, PEG-C-GM Pickering ferrofluid in PVA.85

Figure 3-11 Is the Thermal gravimetric analysis of (GM) and PEG-C-GM86

Figure 3-12 Setup for contact angle measurement88

Figure 3-13 Contact angle measurements using Contact_angle plugin from Image J® to obtain values for for (a) before glass slide treatment (62.25°), (b) after glass slide treatment (16.85°), the insert was the original image, (c) silicon wafer (49.4°), same before and after treatment. Liquid used was 5 μ L of 0.033% PVA in water.89

Figure 3-14 : Plot of contact angle against respective PVA densities, using treated glass slide; the fitting line for the plot bears the equation contact angle angle $CA = 631.74\rho - 622.33$, with an R squared of 0.9828.89

Figure 3-15 Contact angle of pickering ferrofluid on treated glass slide in water. Image analysed using Low Bond Axisymmetric Drop Shape Analysis (LBADSA) plug-in of Image J®, by (Stalder, et al., 2010)90

Figure 3-16 : Aqueous PVA on substrate with densities with scale bar of 1mm (a) 1.00529 g/ml, (b) 1.0064 g/ml, (c) 1.01068 g/ml, (d) 1.015145 g/ml, and (d) is the representative fitted plot of height vs density of polymer with fit as $39.48\rho - 39.37251$, having an R squared of 0.9721.91

Figure 3-17 Spectra of size distribution of ultrasonicated mixture using DLS Malvern Zeta sizer.92

Figure 3-18: Contour map showing probability density function of size distribution of emulsion droplets for speeds (rpm) and operating time (mins).96

Figure 3-19 Trend line fitting within PDF range (0.005 – 0.09) in a 3D surface plot, generating a power curve with decline rate of 0.6, $R^2=0.85$97

Figure 4-1 (a) Schematic of droplet interaction in magnetized ferrofluid-polymer emulsion. (b) Top-section and (c) Magnetic field distribution across substrate surface. (d) cross-section dimensions of experimental setup. The blue field is the substrate dimension and the red square is the magnet which is 5mm beneath the substrate. 101

Figure 4-2 (a)Image of thin film magnetized patterns on microscopic glass slide with width of 25.4mm. (b) is a magnified image of the dried film magnetic pickering droplet pattern on glass slide. The marked regions Region 1 ($r=0\text{mm}$), Region 2 ($r=4\text{mm}$), Region 3 ($r=7\text{mm}$). 103

Figure 4-3 (a)Darkfield image of sample suing the Olympus BX41 microscope with a 20X 0.4 N.A. M-Plan objective lens. (b) Illustration of 1D pattern morphology showing chain length, chain thickness and chain gap..... 104

Figure 4-4 SEM images of sample where; at centre of substrate (**0 mm**) showing dense cluster of pickering droplets at - (a) 17 pixels/ μm resolution and (b) 1820 pixel/ μm resolution, defined longer chain structures with an average of 4 droplets within its thickness was observed **4mm** from centre of substrate at - (c) 17 pixels/ μm resolution and (d) 1820 pixel/ μm resolution, and at **7mm** from centre of substrate relatively smaller chains were formed with thickness of max. 2 droplets at - (e) 17 pixels/ μm resolution and (f) 1820 pixel/ μm resolution. 106

Figure 4-5 SEM images of cross-section of spin coated samples at 3000rpm showing thickness of film at (a) 0mm, (b) 4mm, (c) 7mm and (d) 12mm. 107

Figure 4-6 The measured points (blue circles) and respective error bars were fitted to generate a trend line with equation ($hr = 574.3 - 43.8r$) with $R^2 = 0.996$, which will amount to an average film thickness of 311nm using Eqn. [4.1], as performed in (Jordan, et al., 2019). 108

Figure 4-7 Spatial plots of integrated pixel density for the region of interest (ROI) areas for representative microscope images. (a & c) both images shows the ROI areas marked by yellow circle for 0.035kg/ms at 700rpm and 2000rpm, respectively; (b & d) the integrated pixel density per area distribution across all ROI areas for 700 and 2000 rpm, respectively. 111

Figure 4-8 Plot of ROI scan data points across (from left to right) of pickering ferrofluid emulsion in PVA (1.7wt.%). The fit $R^2=0.987$ Scale bar in each image is 100 μm 112

Figure 4-9 ROI scan data points across substrate for (a) 43.2mPas @700rpm (b) 43.2mPas @2500rpm. The average $R^2=0.984$. The viscosity of the pickering emulsion in PVA and spin speed affects the pickering droplet density profile. The rest of the fittings are presented in Appendix 8.5. .113

Figure 4-10 Gaussian distribution profile from ROI-integrated density of pickering emulsion cluster density across thin film from spin speeds of 700, 1000, 1500, 2000 and 2500 rpm for; (a) 1.9 mPas, (b) 3.2 mPas, (c) 15.2 mPas and (d) 43.2 mPas. 114

Figure 4-11: The full width half measure (FWHM) of distributions of pickering emulsion in each PVA of viscosities (1.9 mPas, 3.2 mPas, 15.2 mPas and 43.2 mPas) plotted against spin speed (rpm). The

insert shows relative ratio of gradient of the FWHM vs Spin speed plotted against each viscosity of PVA hosting pickering emulsion (where the most viscous liquid, 43.2 mPas is taken as 1).115

Figure 4-12 Average resolution of pitches between chain thickness and gap was determined from region of interest scan profile lines (red lines B, D, F & H) of binary processed plot profile images (a & c). The green lines are manually measured chain lengths. Images (b & d) are generated profile distributions for QPI = 14.2, (a) and QPI = 5.73 (c).120

Figure 4-13 This is a log-log plot representing the ratio between chain thickness and chain gap (CT/CG) is linearly related to QPI (between 1 and 1000), and $QPI \leq 1$ CT/CG is constant. While chain length and chain thickness (CL/CT) unevenly varies with QPI ratio122

Figure 4-14 SEM images of sections of a sample to aid illustration of plot shown in Figure 4-13. (a) Is coherent with section A of Figure 4-13, where it shows a 6mm radius from the centre of the substrate with droplets randomly dispersed and few droplets forming short-singular chain, as shown in the insert image. (b) This is coherent with data points of CT/CG and CL/CT within the blue region and green region of C and B respectively in Figure 4-13. (c) is an illustration for datapoints CT/CG and CL/CT within regions D-F and E-F respectively ($100 \geq QPI \geq 10$) in Figure 4-13. (d) Image of section at the centre of the substrate equivalent to section G of Figure 4-13, where dense columns of droplets dominate structure pattern.124

Figure 4-15 (a) Schematic of plot profile for Magnet setup for magnet 2 (b) and magnet 3 (c).125

Figure 4-16 : Binary processed image profile of (a) Magnet_2 at radius 8.2mm under speed 2000rpm (b) Magnet_3 at radius 4.4mm from centre under speed 3500 rpm. Scalebar is 50um.....126

Figure 4-17 The calculated sets of data shown in **Table 4-6** for magnetic profiles Mag 2 and Mag 3 shown in Figure 4-15 , were fitted into the pattern profile map; the CL/CT ratio for both Magnetic profiles fell within the estimated regions with approximately 30% for Mag_2, 90% for Mag_3 deviation from the profile curve. While for CT/CG, the data points fell within the expected regions with deviations from profile curve approximately 60% for Mag_2 and 50% for Mag_3.127

Figure 4-18 Defectivity trace detection for (a) QPI = 75.4 and (b) QPI = 2.82. The inserts are representative 3D plot profiles of 4 scan region of interest lines across varying chain length within each image. (a) tend to have shorter chains but thicker profile bars, while (b) have longer chains but less thicker bars. The defectivity for (a) is 4.3% with SD = 0.0193 and (b) is 11.6% with SD= 0.0285.128

Figure 4-19 : measured and plotted magnetic field strength profile (B mT) along radial distance r (mm), with a small magnet of 1.5 mm in diameter, the ring is 8mm inner diameter and 12mm in outer diameter.130

Figure 4-20 Nanopatterned thin film on silicon wafer prepared under 3500 rpm spin speed ~ (a) taken with Olympus digital camera, (b) taken with Olympus brightfield microscope under reflection mode with a 5X magnification lens, N.A.= 0.1, and (c) the same microscope but with a 20X magnification lens, N.A.= 0.4.130

Figure 4-21 Thin film nanostructure profile on silicon wafer (a) SEM image 0.1mm close to the centre of the substrate, (b) Binary image 1mm from the centre of the substrate with binarized plot profile of resolution, (c) Binary image 2mm from centre of substrate with binarized plot profile of resolution, (d) Binary image, 4mm from middle of substrate with binarized plot profile of resolution, (e) Binary image, 6mm from middle of substrate with binarized plot profile of resolution, (f) Binary image, 10mm from centre of substrate with SEM image insert and measurements, (g) Binary image, 15mm from centre of substrate with binarized plot profile of resolution.131

Figure 4-22 : Map showing ratio points of nanostructure. The CT/CG trend approximately followed the original CT/CG trend line further establishing the physical phenomenon of the shear and drag effect on column thickness. The CL/CT points between 2mm and 6mm are way higher (almost up to a thousand-fold) than the original CL/CT trend line.132

Figure 4-23 Defectivity profile measurements of random chains with (a) $Q_{pi} = 220.7$ and (b) representative binary plot profiles, (c) $Q_{pi} = 41.5$ and (d) representative binary plot profiles. 133

Figure 4-24 An SEM image of chain interactions upon a silicon wafer. The yellow oval 1 shows evidence of big droplet initiating branching of chains, The yellow straight line 2 is an example of profile line scan for detecting defection which the highlights its deviation due to shifting of chain from straight path in the form of red oval 3 and 4. 134

Figure 5-1 UV-Vis absorption spectra of magnetite at different sizes, the maximum peaks for 10 nm was 372nm, 20nm was 383nm and 30nm was 404nm. Courtesy (Horia, et al., 2020) 140

Figure 5-2 UV-Vis absorption spectra of Iron Oxide, Gold and dimer heterostructure of combined iron oxide and gold. Courtesy (Korobchevskaya, et al., 2011). 141

Figure 5-3 : UV-visible absorption spectra (in water) for pure gold and iron-gold alloy nanoparticles synthesized from Fe0 precursor with various molar ratios. The molar ratios of iron and gold are 1:1, 1:2, and 1:3, indicated by circle, cross, and triangle, respectively. Courtesy (Dahal & Chikan, 2008) 142

Figure 5-4 Illustration of system configuration of (a) gold deposited on substrate overlain by iron oxide, (b) iron oxide deposited on silicon oxide substrate with gold bounded to the iron oxide platelet surface. Courtesy (Thimsen, et al., 2011). 143

Figure 5-5 : Absorbance spectra for the different electrodes. (a1) As-measured absorbance data for the embedded configuration; (a2) comparison of the spectral overlap between Au nanoparticle plasmon resonance and compact Fe2O3 absorbance for the embedded configuration; (b1) as-measured absorbance data for the surface configuration; and (b2) comparison of the spectral overlap between the Au nanoparticle plasmon resonance and Fe2O3 platelet absorbance. Courtesy (Thimsen, et al., 2011)..... 143

Figure 5-6 UV-Vis absorption spectra with internal deconvolved gaussian peaks at various radial locations (a) $r=1\text{mm}$, (b) $r = 2\text{mm}$, (c) $r=4\text{mm}$, (d) $r=6\text{mm}$ and (e) $r=8\text{mm}$. (f) is the plot showing relationship of CT/CG, CT against radial locations r (mm)..... 146

Figure 5-7 Relationship of deconvolved bands (Bnd-A, B, C, D, E & F) data points of their (a) wavelength (b)intensity and (c) FWHM with the radial distance, $r(\text{mm})$, while (d) shows the relation between calculated CT_w values from Eq. (6.2) against radial distance, r (mm). The trend of CT_w was relatively compared with the trends of wavelength, peak intensity and FWHM for all deconvolved bands. 154

Figure 5-8 Schematic illustration of particle-particle interaction and charge transfer (red) within pattern. Added is the expected associated absorption band. Bnd-E has to do with overall density ratio between gold nanoparticles and iron oxide nanoparticles 156

Figure 5-9 The SEM image of thin film sintered at 600°C sample showing iron oxide (dark oblate spheroid) and gold nanoparticles (bright spheres) for exemplary illustration on particle system configuration. 159

Figure 5-10 Spectra of thin film nanostructure (45.2mPas PVA- PEG-C-GM-pi-FF at spin speed of 1000 rpm) on glass substrate with different radial position r (mm)..... 162

Figure 5-11 FTIR absorption spectra acquired at various radial points on the thin films prepared by spinning the PEG-C-GM-FF nanoemulsion dispersed in PVA solution having 1.9mPas viscosity (a) at 700 rpm (b) at 2500 rpm. The variation in values of the intensity of 2927 cm^{-1} peaks in relation to various radial locations extracted from the (c) spectra in (a) and (d) spectra in the (b). The fitted curve to the peak intensity data in (c) and (d) follow the half -normal distribution. Rest of the data and plots are in the supplementary information. 163

Figure 5-12 Spatial half-normal IR absorption intensity distribution obtained from the various radial location on the surface of the film prepared at different viscosities and coating speed. 165

Figure 5-13 Linear fit of the FWHM-FTIR-Trans absorption at 2927 cm^{-1} versus FWHM of ROI-Image.	168
Figure 5-14 Full (4000 cm^{-1} to 650 cm^{-1}) reflectance spectra of thin film on optical glass substrate scanned at angle of incidence (a) 20°, (b) 45° and (c) 82°.....	169
<i>Figure 5-15 : Specular Reflectance spectra showing the vibration signal intensities of; PVA CH asymmetric (2905 cm^{-1}) and symmetric (2846 cm^{-1}) bonds (a) 20°, (b) 45° and (c) 82°, and PVA C=O (1729 cm^{-1}) and CA C=O (1707 cm^{-1}) for (d) 20°, (e) 45° and (f) 82°. The relationship plot between measured vibrational signal intensities for bands 1729 cm^{-1}, 2905 cm^{-1}, 2846 cm^{-1} and 1707 cm^{-1}, against CT/CG, for (g) 20°, (h) 45° and (i) 82°.....</i>	172
Figure 5-16: Shift of O-H band of PVA versus the change on CT/CG ratio	175
Figure 5-17: (a) Specular reflectance IR spectra at varying CT/CG ratios of gold- Fe_3O_4 heterostructures highlighting a change in vibrational intensities of longitudinal optical (LO) and Transverse optical (TO) bands of SiO_2 . (b) Relative transmittance spectra of nano-antennas of different gold nanowire lengths prepared on silicon wafer with a natural SiO_2 Layer (thickness 3nm). Courtesy (Neubrech, et al., 2010).	176
Figure 5-18: FTIR-SR of thin film patterned structure at (a) 20°, 3 layers (b) 45°, 3 Layers (c) 82°, 3 Layers (d) 20°, 6 layers (e) 45°, 6 Layers (f) 82°, 6 Layers (g) 20°, 9 layers (h) 45°, 9 Layers (i) 82°, 9 Layers.	178
Figure 5-19: A 6 layered coating of (PVA 15.2mPas and spin speed of 2500) thin film nanostructure on glass slide, showing interference colour effect when tilted at oblique angles ($\sim 35^\circ$ from normal). ...	180
Figure 5-20 Magnetic Hysteresis curve of 5mm cut of coated sample on silicon wafer. Insert is the close look of magnetization curve close to the origin to identify the coercivity and magnetic susceptibility.	181
Figure 5-21: A schematic showing the setup to coat the pickerin gdroplet thin film structure deposited on silicon wafer with Rhodamine 6G. The wafer elevated 2mm from the supporting frame and in between two sets of 130 mT square magnets with opposite poles facing each other 15 mm apart. The measured average magnetic field above the substrate was 43mT. The Raman microscope beam was perpendicularly focused on the thin film at radial locations, $r = 1\text{mm}, 2\text{mm}, 4\text{mm}$ and 6mm	182
Figure 5-22: Raman Spectra of R6G on test sample (showing three separated Raman shift ranges) subjected to zero magnetic field (at $r=1\text{mm}$) and with magnetic field (at $r= 1\text{mm}, 2\text{mm}, 4\text{mm}$ and 6mm).	186
Figure 6-1 (a) sample of cross-coating pattern, (b) sample of iron oxide-resin pellets for generating secondary magnetic fields	197
Figure 6-2 The ranking placement of magneto-spin coating nanofabrication technique based on criteria of resolution, throughput, defectivity, complexity and cost with reference from (Figure 2-1).	198

Nomenclature

M_p Magnetization of particle (A/m)

M_s Saturation of magnetization (A/m)

M_d Domain magnetization of bulk magnetic particle (A/m)

ϕ is the volume fraction of magnetic solid to carrier liquid and surfactant

V volume (m^3)

m magnetic dipole moment ($A.m^2$)

D_m Diameter of magnetic particle (m)

B is the magnetic field strength (Tesla)

Ω_{MT} Thermal Stability number

K_B Boltzmann constant (1.380649×10^{-23} N.m/K)

T Temperature (K)

E_d Energy of dipole interaction (N/m)

χ_i Magnetic Susceptibility

H_T Total applied magnetic field (A/m)

H_e External magnetic field (A/m)

H_i magnetic field after deduction of demagnetization effect from external field (A/m)

H_o Coercivity (A/m)

μ_o vacuum magnetic permeability ($4\pi \times 10^{-7}$ N/A²)

h film thickness (m)

h_i is the characteristic film height (m)

ω angular velocity (rad/sec)

ρ density of fluid (Kg/m^3)

η is the viscosity (Kg/ms)

v_f is the fluid velocity (m/s)

Re Reynold's number

W_{rev} is the rotation speed in (rev/min)

h_0 Initial film thickness (m)

r_0 initial radial location (m)

t time (sec)

σ_g log normal of the standard deviation

μ_g mean

μ_x expected mean value

σ_x standard deviation

x_u random variable for statistics

G_{res} Mass of gold residue

G_{vol} Volume of gold residue

$G_{NP(vol)}$ Volume of gold nanoparticle with capping molecules (m^3)

$G_{NP(i)}$ Number of gold nanoparticles in residue

MC_m mass of Methacrylate molecules burnt off from gold nanoparticle (kg)

MC_n Number of moles in Methacrylate

MC_i Number of molecules of burnt Methacrylic acid

MI_N Magneto-Inertia number

Q_{pi} ratio between magnetic packing energy and fluid inertia

x spatial distance (m)
 r radial location on substrate (m)
 m_{DD} is droplets dipole moment of interaction (A.m²)
 P_{SC} pressure on droplet by fluid inertia (N/m²)
 ρ_{pol} density of polymer (Kg/m³)
 CE_{FF} Energy generated on droplets from spinning (N)
 d_{FF} is the droplet diameter (m)
 ω_{acc} average angular speed during acceleration (rad/s)
 t_{acc} acceleration time (s)
 $SD(Log)$ Log to the base of 10 of standard deviation
 PD_{DP} is the pixel density of data points
 PD_m is pixel density from trend (mean) line fit
 N_{DP} is number of data points within each trend
 V_{FF} is the volume of spherical ferrofluid droplet (m³)
 u_p is the velocity of polymer over from centrifugal action (m/s)
 E_{CL} thin film parameter
 DEF_{CL} short gaps within individual chains (m)
 DEF_A Area Defectivity (m²)

M_{DR} magnetization of the droplet (A/m)
 F_D magnetic force on a droplet (N)
 V_{FD} is the volume of droplet (m³)
 N_d number of droplets
 d_{pol} Diameter of polymer coated droplet (m)
 V_{sub} Volume of droplet (m³)
 L_{ss} Gap between droplets edge to edge (m)
 $\chi_{i(DR)}$ Susceptibility of droplet
 $H_{T(DR)}$ Total magnetic field experienced by droplet (A/m)
 F_{d-d} Dipole-Dipole force between droplet (N)
 F_p Packing force (N)
 E_d Magnetic dipole potential energy (A.m²)
 ζ_{CC} Dipole Coupling Constant
 P_{NT} Packing stability number
 v_p is particle velocity (m/s)
 $FTIR_{abspt}$ Fourier Transform absorbance value
 T_{GR} Exponential gradient of individual trends for Pixel density/FTIR absorption vs MI_N/Re
 CT_w Dimensionless group of clusters captured within spectrometry scan area

Abbreviations

SR-FTIR Specular Reflectance Fourier Transform Infra-red
LSPR localized surface plasmon resonance
SERS Surface enhanced Raman spectroscopy
FTIR-Trans Fourier Transform Infra-red Transmission mode
SEM Scanning Electron Microscope
TEM Transmission Electron Microscope
PEG-C-GM-pi-FF Polyethylene glycol coated gold methacrylate Pickering ferrofluid
PEG-C-GM PEG-Methacrylate capped gold
PVA Polyvinyl alcohol
OCM Oleic coated magnetite
PEG 40S Polyethylene glycol 40 stearate
DLS Dynamic Light Scattering
SQUID Superconducting quantum interference device
GM Gold methacrylate
SM sodium Methacrylate
MA Methacrylic acid
FF Ferrofluid
CCD Charge couple device
LBADSA Low Bond Axisymmetric Drop Shape Analysis
PDF Probability density Function
rPDF relative Probability Density Function
MMPDF Multimodal Probability Density Function
CT Chain Thickness
CG Chain gap
CL Chain Length
EMD Packing energy
EFI fluid inertia energy
CM gap between consecutive tail and head of chains along an array
CA-CO C=O of carboxylic acid
FA-CO C=O of Fatty acid
MA-CH Methyl group of Methacrylic acid
PVA-CH Methyl group of Polyvinyl Alcohol
Bnd Deconvolved absorption Band
BB Band broadening
BN Band Narrowing
RS Red shift
BS Blue shift
BSL-C Baseline correction

Chapter 1 Introduction

1.1 Background

Nanomaterials are essential in our modern-day world because they exhibit physicochemical properties like electrical, optical, magnetic, thermal, and chemical compared to their bulk counterparts. Two key reasons responsible are; (a) Quantum effect dominates the behaviour of materials at the lower end of the nanoscale where the optical, magnetic and electric behaviours are affected (Khan, et al., 2019). (b) the large surface area per volume ratio of material encourages the high activity of electrons which enable the transfer of energy across interfaces, thereby making them more chemically reactive and in some cases superior mechanical properties (Zhang, et al., 2013) (Shi, et al., 2017).

Several physicochemical properties of nanomaterials are exploited to improve application performances. Such could be electrical, magnetic, electromagnetic waves, chemical, or mechanical. One of the most researched is the electromagnetic waveform of interaction, in a particular context, light-matter interactions (Fazio, et al., 2019). This is where electromagnetic waves are harnessed and converted into other desired forms of energy; which are already seen in photocatalysis (Beydoun, et al., 1999), optical diagnostic sensors (Majhi, et al., 2018), photovoltaics (Surek, 2005) (Saunders & Turner, 2008) and telecommunications. There are materials with exceptional characteristics on their interaction with electromagnetic waves that are used widely across the nanotechnology industry, such as gold and silver. These materials exhibit an oscillation of exciting cloud of electrons at their surface by an incident wave of light, often termed surface plasmons, (Barnes, 2003) (Nasseri, et al., 2016) (Barrow, et al., 2011). It becomes surface plasmon resonance (SPR) when the wavelength of incident light matches the resonant frequency of collective electrons (Amendola, et al., 2017) (Liu, et al., 2018). These plasmons lead to strong absorption/scattering of incident light as they locally enhance the optical intensity by many orders of magnitude as much as $10^4 - 10^6$, depending on their size, morphology and dielectric environment (Xu, et al., 2000) (Kasani, et al., 2019). It has been investigated that the aggregate of plasmonic colloidal particles in 1D, 2D and 3D arrays enhances their local electromagnetic field by more than a trillion-fold in

magnitude (Blatchford, et al., 1982); however, depending on their interfacial gaps (Harris, et al., 2009) (Chen, et al., 2013) (Wei, et al., 2004).

The 1D chain assemblies of the optical materials have found many applications including sensing, as their large aspect ratio or repeating geometrical structure can enhance the optical scattering, absorption or photonic transport (Li & Cullum, 2005) (Xiao & Yeung, 2014) (Kasani, et al., 2019). The 2D chains show the enhanced plasmonic excitation of the gold nanorods or arrayed chains of gold nanoparticle aggregates junctions compared to zero dimensional nanoparticles in many applications, where anisotropy leads to increased physical properties (Kravetz, et al., 2018). The control of concentration per unit area and array gaps offer tunability of field intensity, where such systems benefit from its waveguide structure (Valenti, et al., 2016). The waveguide structure performs by diffracting incident electromagnetic waves towards their proximity interfaces, thereby increasing the pathlength of photons (Huang & El-Sayed, 2010) (Linic, et al., 2011). Such scattered fields from diffracted light can act in countering the damping oscillations associated with a single particle response (Deng, et al., 2020). Therefore, the appropriate tuning of periodic arrays (i.e., particle/cluster size and gaps in between them) significantly determines the overall material output quality (Brongersma, et al., 2011). This, therefore, projects the essence of fabrication by patterning and layering of colloids on templates to ensure this phenomenon is efficiently utilised within manufactured devices.

There are several fabrication techniques for preparing 1D and 2D chain assemblies; such as photo-lithography, electron beam lithography nanoimprint lithography, template guided assembly of nanoparticles, soft-lithography, electro-spun nanofibres, nanoskiving, etc. Although, these methods are costly, slow in throughput, inability to offer tuneability of the resulting structures, as well as physical properties and scalability (Wiley, et al., 2010) (Watt, et al., 2005) (Biswas, et al., 2012).

1.2 Research Motivation

The challenges highlighted in the previous paragraph inspired the research interest in the fabrication of complex material from nanoscale resolution to large scale clustering patterns using a cost-effective, high throughput and less toxic approach in the form of magnetic-field directed self-assembly of the colloids (Ge, et al., 2011).

The subject material to be organised (gold nanoparticles) is poorly magnetic responsive. Thus, one cost-effective and smart way of establishing a short-range organisation of gold nanoparticles is by using liquid-liquid interface of sub-micron emulsions (Binks & Lumsdon, 1999) (Larson-Smith & Pozzo, 2012). On the basis that the fabrication system is a magnetic-stimulated assembly, ferrofluid (consists of Fe₃O₄ nanoparticles in oil phase) emulsion is considered for piggy backing gold nanoparticles as it has been performed by Sachdev and co. in making 7.7µm gold-pickering-ferrofluid droplets (Sachdev, et al., 2017). Ferrofluid also possesses unique properties like combined Neel rotation, Brownian motion and excellent translation (Mou, et al., 1994) (Lawrence, et al., 1994) (Hartmann & Mende, 1984) (Landers, et al., 2016). The interface of ferrofluid and aqueous liquid (water) can serve as a medium for ordering gold nanoparticles (Guttula, 2007), and such complexity and flexibility of material coupling and patterning was anticipated to bring unique optical characteristics. Conventionally, the use of magnetic dipole interactions between nanoparticles to prepare the colloidal structures is widespread for its quick means of building high ordered structures (i.e., because of its quick field reversibility or fast switching of magnetic field polarity) that makes it easily tuneable. However, the control over its aspects ratio, chain length and gaps are difficult (Grzelczak, et al., 2010) (Harraq, et al., 2022). Many times, the small chain gap leads to establishment of connections between them to form thick columns or labyrinth structures (Mou, et al., 1994). To prepare the discrete chains with nanometre/micrometre gaps on surface of the substrate, it is essential to introduce separating effect between chains. A way of achieving it is by fluid inertia under spin coating mechanism which can provide an opportunity to stretch the chain radially while aligning the particles using magnetic field. The balance between inertial fluid force and magnetic field allows control over the colloid assembly morphology. The combination of magnetism with spin coating in forming thin layered-high-ordered structures have seldomly been reported.

The combination of both methods have been investigated in the past, (Pichumani & Gonzalez-Vinas, 2011) (Pichumani & Gonzalez-Vinas, 2013) (Aslam & Gonzalez-Vinas, 2017) (Mourkas, et al., 2021). In these works, Helmholtz current coil as a magnetic field source was used while the substrate hosting the colloidal liquid was spun. The resulting film with complex structures that was formed were devoid of

repeating pattern of defined geometrical features such as chain representing the colloidal dipole-dipole interaction. In these techniques, a force-vector problem arose when nanoparticles in the fluid simultaneously experienced; (i) shear force of radially driving fluid inertia propagating from middle of the substrate to the edges, (ii) magnetic flux acting in a direction perpendicular to the substrate plane and (iii) the angular direction from spinning substrate. Magnetically responsive particles align along a single or group of flux lines (Li, et al., 2017) (Tracy & Crawford, 2013) (Singamaneni, et al., 2011) (Bozorth, 1951) and the rapid movement from spinning and stationary flux line would lead the particles experiencing “magnetic flux-line switching”. Such switching distorts polarity of particles and as well as their dipole interaction in forming a chain or group of chains.

In this research, this limitation was addressed by making the substrate laden with pickering ferrofluid emulsion subjected to only two competing forces: magnetic and radially-driven fluid inertia. It was ensured by placing a stationary permanent magnet underneath the host substrate to eliminate the flux switching problem.

In brief, this research is a combination of three fabrication techniques, namely; pickering emulsion of gold on ferrofluid (short range organisation), magnetic stimulated assembly (long range organisation) and spin coating (for thin film 2D patterning). Figure 1-1 provides diagrammatic illustration of this research.

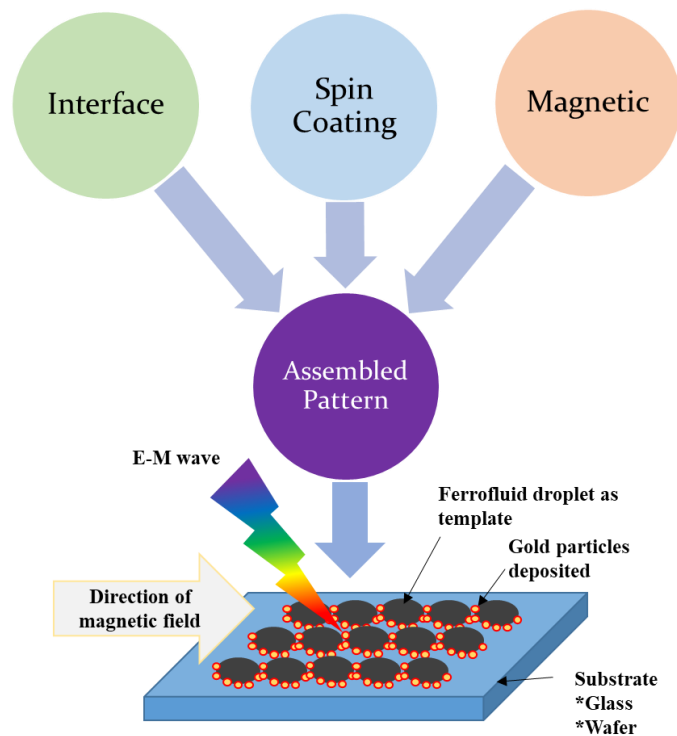


Figure 1-1: Illustration of research process of combined self-assembly techniques for the short-and-long-range organisation of gold nanoparticles for optical applications

1.3 Problem Statements

To develop a high-throughput method that prepares a patterned film on substrate is indispensable to many applications. A pattern having repeating 1D chains is very useful in modifying the optical behaviour of materials. Since magnetic directed assembly is the preferred method in preparing 1D chains of gold nanoparticles, the fact that gold is not a magnetic responsive material brings up a different challenge. One way of overcoming this problem was by applying gold nanoparticle as a pickering phase around a ferrofluid nano-emulsion (now will be referred as “ferrofluid pickering emulsion”) that was then subsequently dispersed in aqueous polyvinyl alcohol.

The ferrofluid droplets can easily orient along a magnetic field direction and relax quickly whenever the field is removed (Landers, et al., 2016) (Fannin, et al., 1993). The interface between two immiscible fluids (ferrofluid and water) possesses electric charge within the electric double layer (Lewis, 1937) that attract and control the density of adsorbed gold nanoparticles (Booth & Dryfe, 2015) (Claire, et al., 2019) (Ghosh & Boker, 2019). Thus, the preparation of pickering emulsion system requires

optimising the hydrophilic-lipophilic coating of the gold nanoparticles to allow adsorption at the interface of oil and aqueous phases. This can be achieved by either using a linker molecule or polymeric grafting (Durand-Gasselín, et al., 2010) (Qi, et al., 2014) (Megiel, 2017) (Kimmins & Cameron, 2011). This concept saves materials used as well as retains the magnetic properties of the particles within the pickering system when subjected to weak magnetic fields (Ivanov & Zubarev, 2020). Applying coating alters the magnetic moment ratio of the material in response to applied magnetic field and therefore, the optimisation of the coating materials, thickness was required for successful preparation of the film.

The effective control of chain length, thickness and gap between the pickering ferrofluid chains using magnetic field depends on the size of droplets, as well as the magnetic field strength and anisotropy (Tracy & Crawford, 2013) (Li, et al., 2017) (Ivanov, et al., 2007). Upon considering how chain lengths can be controlled, the type of magnetic source required is vital. Neodymium permanent magnet is small, fairly in light weight, cheap and flexible to setup. However, it has a short-range field that is inhomogeneous, thus causes particles as well as ferrofluid pickering emulsion to form heterogenous lattices when in close proximity (Tracy & Crawford, 2013). This heterogenous lattices form 3 dimensional structures which in some cases lack array patterns. Since the patterning to be created is from an emulsion system, the application of spin coating to create thin film and effectively minimize dense lattice formations is ideally a quick, cheap and easily manipulative technique for coating the emulsions over a substrate (Bornside, et al., 1987).

A combination of spin coating and radially-directed magnetic field parallel to the surface of the spinning substrate setup generates an opportunity to investigate the effect of competing forces; magnetic and inertial drag on droplets caused by the continuous phase subjected to spinning action. The permanent magnets are known for generating inhomogeneous field and complex lattices, the counteracting force from fluid inertia would likely minimize that effect, therefore the control of ferrofluid pickering emulsion size, carrier fluid viscosity, magnetic field strength and average spin speed will potentially determine the degree of patterns, chain length, chain thickness and gap between the chains (Dowling, et al., 2004).

The morphology of the chain thickness and chain gaps consisting of gold and iron oxide interactions would influence the optical dynamics of electromagnetic wave within its structure. There have been studies on iron-oxide gold optical enhancement in surface enhanced Raman Spectroscopy (SERS) where depending on concentration of gold to iron influences the degree of near field scattering and plasmonic behaviour of gold. It would be interesting to observe the optical behaviour of the formed agglomerated pickering emulsion, as well as a first-time trial in surface enhanced Infrared spectroscopy (SEIRS). Magneto-Raman test carried on the prepared thin film nanostructure to observe its enhancement effect on analytes (Rhodamine 6G).

1.4 Aim

The aim of this research is to use a self-assembly method to create an optically active patterned nanomaterial.

1.5 Objectives

- 1) To conduct a study and establish synthesis of ferrofluid and polyethylene glycol grafted gold methacrylate nanoparticles preparations.
- 2) To setup a controlled manufacturing process that can attain sub-micron (<500nm) gold-pickering ferrofluid emulsion with a low degree of polydispersity.
- 3) To conduct a study on the effect of alternating of parameters in the form of magnetic configurations, aqueous PVA fluid viscosities and spin coating speeds on pattern distribution and resolution dimensions.
- 4) To conduct optical study of developed structures, to observe its optical enhancement using Fourier transform spectroscopy, UV-Vis absorption spectroscopy and Magneto-Raman spectroscopy.

1.6 Thesis Summary

In chapter 2 literature review is presented firstly on nanofabrication, types of nanofabrication, areas of applications of nanostructures. In the second part, the history, underlying science and applications of magnetism for the development of nanostructured materials.

In chapter 3, materials, method of synthesis and characterisation of processed materials was presented. This covers the preparation of ferrofluid, gold methacrylate and polyvinyl alcohol used for the first part of the investigation. Along with it are its characterisation, such as size, zeta potential, Fourier transform Infra-red spectroscopy analysis of synthesised materials, Transmission electron Microscopy, UV-vis absorption spectroscopy, SQUID, contact angle, and Thermal gravimetric analysis.

Chapter 4, presents the experiment setup, magnetic field distribution, controlling parameters for the creation of patterns which involve density of polymer carrier and spin coating speeds. The patterns created were image analysed using grayscale pixel density from the region of interest sections of scaled images. Images were obtained from darkfield microscopy and Scanning electron microscopy. The measure dimensions of patterns were matched with the combined input energy of magnetic and fluid inertia to create dimensionless maps.

Chapter 5, presents the optical study of patterns using FTIR-transmission, specular reflectance-FTIR, UV-Vis spectroscopy and Magneto-Raman spectroscopy. Each spectra were analysed with relation to the pattern dimensionality and concentration ratio between iron oxide and gold dimer species.

Chapter 6, presents overall discussion, recommendations, conclusion and future work of this study.

Chapter 2 Literature Review

2.1 Chapter in Brief

This chapter conversation began with the three major approaches of nanofabrication methods (top-down, bottom-up and self-assembly). self-assembly approach was more of the focus because of its ability to effectively combine both high-resolution short-range organisation of colloids and extending it into a long-range span. Thus, discussions on the physical phenomenon contributing to the formation and organisation of colloids into lattice structures, as well as techniques like fluidic, interfacial, thermal, electrical, magnetic, optical and acoustic methods for organising colloids. Various types of fluidic methods were briefly discussed, as spin coating method was the preferred technique in this research because of its quick and cheaper means of organizing colloids. Given the reasons stated above, various types of self-assembly coupling methods based on spin coating were discussed, such as; (a) spin-coating and lithographic template, (b) spin coating and electrical method, and (c) spin coating and magnetic methods, from which Spin-coating and magnetic coupling self-assembly method was overall the main nanofabrication interest in this project. This combination was previously tested by Gonzalez-Vinaz and co., as their approach were presented and discussed, showing the technical difference between theirs and this project. Going forward with the main objective, fundamental topics based on – (a) Magnetism and magnetic materials, and (b) the basics of Spin coating, were all presented. Optical study is a common path used in analysing the behaviour of a structure designed from any type of nanofabrication technique through the behaviour of an incorporated photo-responsive a probe material - gold (a plasmonic noble metal). Discussed are series of multiple journals on the crucial and effective periodic organisation of gold nanoparticles that would phenomenally lead to enhancement of electromagnetic field energy within the complex material. Rendering it applicable as a surface plasmon sensors and more. Including heterodimer structures of gold and iron oxide, explaining the optical phenomenon as a result of their combination. This chapter was finally capped off with brief highlights on tests necessary for the characterization of constituents and overall structures in this project.

2.2 Nanofabrication and methods of nanofabrication

In nanofabrication, the area of application determines the level of technicality required in the designing and manufacturing process of nanostructured materials. There are five factors that control this process, and they are; levels of precision, scalability, repeatability, cost and recently toxicity (Sudha, et al., 2018), (Dolez, 2015). In terms of precision, applications such as optics require accurate dimensioning to take advantage of a certain band(s) of the electromagnetic wave, like sensor gratings. In terms of scalability, depending on application requirement, could be challenging especially with the resolution of fabrication and precision. For higher resolutions (1-50 nm for example) and final dimension of device (100 μm^2 for example) is challenging because of the required machine needed to create this resolution, and its size to process the required dimension. In terms of repeatability, the design ought to be systematic to allow easy fabrication process and ability to produce exactly the same product smartly. In terms of cost, the design requirement (such as resolution and application), and the type of fabricated material determines the setup of the manufacturing facility. Cost is one of the major drawbacks towards industrial scale production of nanofabricated device and the reason nanofabrication is not practiced in most countries. In terms of toxicity, nanoparticles unique size and surface area activity could stand as a potential threat to human health if it penetrates cell membranes, as well as environmental impact (Singh & Nalwa, 2007). This is specially the case where nanoparticles are free and not fixed to the material. Apart from nanoparticles being limitedly exposed within established industrial workplaces (or labs) and some safe cosmetic products, it is necessary for manufacturers to assess the potential risk and life cycle of a material, so as to inform relevant regulatory agencies (Dowling, et al., 2004).

Nanostructures can be fabricated using variety of techniques, ranging from Lithography and etching of materials on substrate, Micromachining of substrate for assisted alignment of nanoparticles, molecular configuration where polymeric molecules assist in patterning attached nanoparticles, external field (magnetic, electric, optical) control of responsive nanoparticle of interest over substrate. Nanofabrication techniques are split into three main categories; (i) Top-Down, (ii)

Bottom-Up, and (iii) Self-Assembly. The next few sections provide the current methods and further details of each fabrication category.

2.3 Methods of fabrication

2.3.1 Top-Down Techniques

Top-down techniques majorly involve the process of machining materials to a specific size and shape, where they operate by three standard procedures; Masking, coating/deposition of materials, and etching. Essentially, the concept of creating patterns within a substrate to meet device functionality requirement, fundamentally relies on lithographic mapping. Therefore, without lithography, specific functionality of a material would be difficult to achieve, especially where precision is required for optical and electronic applications. The table below (**Table 2-1**) comprises a list of lithography techniques.

Table 2-1 List of Top-down approaches; showing techniques, advantages, disadvantages and references.

Top-down method	Technique	Advantages	Disadvantages	References
Optical Lithography	This uses powerful light beam within a particular wavelength that is converged with lenses to focus within small resolutions.	<ul style="list-style-type: none"> • It is an established and long existing technique of micro/nano fabrication for production of chips. • The smallest achieved is a 5nm resolution with an Extreme Ultraviolet light source. 	<ul style="list-style-type: none"> • Resist type is selective. • Diffraction limit of light and reflection losses through optical elements. • The machine design is complicated and expensive. • Requires state of the art expensive clean room 	(Perez-Murano, et al., 2020), (Okazaki, 2015), (Watt, et al., 2005), (Biswas, et al., 2012)
E-beam, Ion-beam, X-ray lithography	This uses an electron beam of reduced dimensions to write on the top surface of a resist coated material, making it essentially a 2D scanning system. It is a mask-less form of lithography, making it suitable for producing photomask for photolithography.	It has short wavelength and high energy density of electrons which allows fabrication of ultra-fine features and sizes with high contrast on substrate.	<ul style="list-style-type: none"> • It has a low throughput process and low productivity because of its serial process and partly manually operated. • It is expensive and requires clean room. 	(Watt, et al., 2005), (Okazaki, 2015),

Table 2-2 List of Top-down approaches; showing techniques, advantages, disadvantages and references – contd.

Top-down method	Technique	Advantages	Disadvantages	References
Soft Lithography	The application process is similar with nanoimprint lithography. It differs in the form of creating a more flexible polymeric mould (like PDMS) that is used to stamp other wet polymers and create patterns on substrate.	<ul style="list-style-type: none"> • The stamps are flexible. • They can be used to create large scale patterns. • Resolutions can go as low as less than 70 nm. • In combination with It is low in cost compared to other conventional methods and has a high throughput. 	<ul style="list-style-type: none"> • Relies on other Lithographic machines to generate template. They are restricted in the types of materials that can be used as resists. • It is challenging applying this technique on curved surfaces. Initially, they require high capital. 	(Qin, et al., 2010), (Zhao, et al., 1997), (Rogers & Nuzzo, 2005)
Scanning probe lithography	This technique uses high resolution probe for depositing molecules (or nano-particles) onto substrate in patterns. Such are; Scanning tunnelling microscopy, Scanning Probe microscopy, Atomic force microscope, Near field scanning probe lithography	<ul style="list-style-type: none"> • Very good at selective deposition of nanoparticles or molecules on substrate. • It currently provides a line width of 15nm and a resolution of 5nm. • Multiple probes can be used to generate high throughput at a large scale. • Can be used to chemically modify surfaces, and remove previously deposited structures 	<ul style="list-style-type: none"> • For SPM, a low scanning speed is experienced because of the hysteresis effect of the piezoelectric ceramic. • The equipment is costly. • Tip degradation due to friction and contamination 	(Xu & Chen, 2020), (Okazaki, 2015), (Tseng, et al., 2005), (Fan & Luo, 2018), (Howell, et al., 2020)
Nanoimprint Lithography	This is a process where a designed template is pressed into a deformable material to create a pattern.	<ul style="list-style-type: none"> • Its imprint can generate 3D structures with one step, making it high in production throughput and low cost processing. • It is cheap and does not require clean room. 	<ul style="list-style-type: none"> • Mainly suitable for wet/polymeric materials. • Large scale production is challenging for densely packed nanostructures. • Relies on other lithographic technique to generate template. • The moulds have to be replaced after series of consecutive imprints, especially after undergoing high pressures, and heating and cooling cycles; thus causing stress and wear of the mould. 	(Tiginyanu, et al., 2011), (Biswas, et al., 2012), (Acikgoz, et al., 2011)

General Challenge with Top-down approaches

The setback involved in most of the techniques had to do with the substrates being pre-treated and post treated during patterning process, especially when adding a resist layer and then removing it with chemical etchant. The Initial process is time consuming and its throughput is low (in the sense of patterning a small area on substrate mm² per unit time). However, repeated process is less time consuming as some situations just require stamping in patterns (like in nanoimprint methods). Also, in most top-down procedures, achieving pristine patterns at low resolutions (<10nm) is challenging, which then pushes for machine advancement by incorporating more quality parts, which therefore increases the overall cost of equipment. Another challenge is the limit of printing small and possibly planar patterns.

2.3.2 Bottom-Up Approaches

In this approach, materials are built from the molecular scale into very high resolution (<5nm) fine patterned (and or layered) structures. It is a case where chemistry of materials plays a huge role in the pattern/structures being developed. Making this approach hugely dependent on chemical synthesis of materials which then gives birth to expansive research and discoveries on variety of material/chemical combinations that exhibits unique characteristics.

Table 2-3 List of conventional bottom-up techniques, showing techniques, advantages, disadvantages and references.

Type	Technique	Advantages	Disadvantages	References
Atomic layer epitaxy	A process of uniform thin film deposition where surface of substrate is exposed to two alternating chemical vapor reactants.	<ul style="list-style-type: none">• Ability to control thickness of deposited film.• Capability to prepare multi-layered structures in a continuous process.• Can be used for designing hollow complex structures	<ul style="list-style-type: none">• Majority of process relies on high temperature, therefore can be energy consuming.• Challenge in ALE design apparatus in delivering gas reactants over large substrate areas without plasma damage to the surface and long cycle times due to inefficient gas flow paths.• Process cannot be used for all surfaces	(Ritala & Leskela, 1999), (Maula & Oy, 2010), (Rius, et al., 2017), (Biswas, et al., 2012), (Kim, et al., 2009)

Table 2-4 List of conventional bottom-up techniques, showing techniques, advantages, disadvantages and references – contd.

Type	Technique	Advantages	Disadvantages	References
Vapor phase deposition Chemical Vapor deposition (CVD), Physical Vapor deposition (PVD)	Is a process where precursors react under high temperatures and low pressures (or atmospheric pressure) to form desired film on a substrate and bind to its surface. In some cases, reacts with the substrate to form thin film	<ul style="list-style-type: none"> • It covers wide range of coating materials in metals, semiconductor, polymers, alloys, ceramics and high purity nanofilms. • Can cover a large area in production, making it an economical batch process. • Possibility of depositing porous nanofilms. 	<ul style="list-style-type: none"> • Requires high temperatures for the process (>600°C), which is energy demanding. • Process could be toxic and corrosive because of the gases used. 	(Rius, et al., 2017), (Biswas, et al., 2012),
Sol-Gel	It is a wet chemical process where inorganic precursors in the form of functional colloids or alloys dispersed within a sol are allowed to hydrolyse and take on patterns formed by the polymeric network behaviour of the sol deposited over a substrate.	<ul style="list-style-type: none"> • It is a cost effective process. • It is flexible in the sense of controlling the growth of metal colloids within the solution. • Produces compositions not possible through solid-state fusion. • It flexibility allows coating on a lot of variety of substrate surfaces 	<ul style="list-style-type: none"> • The cost of chemicals may be high for some processes. • There is often high-volume shrinkage which might alter the patterns. 	(Carter & Norton, 2007), (Danks, et al., 2016), (Biswas, et al., 2012)
Molecular (or Colloidal) Self-Assembly - MSA	This is a process where molecules of a compound of interest complementary binds itself under entropic (energy minimization) to form repeatable patterned structures. It is a strategy considered to imitate nature/biological systems.	<ul style="list-style-type: none"> • The system relies on weak forces (Van der Waals) to obtain reversible solution processing of MSAs. • It is flexible and can be synthesised to form electrostatic bonding with inorganic particles to form, for example metal-ligand binding. • If system efficiently applied would allow mass production of various nanostructured materials/systems on a large scale at a low cost. • Due to its flexibility, it can be used to develop multi-functional systems 	<ul style="list-style-type: none"> • MSA is still at the experimental stage and not completely understood. Owing to the fact that most of molecular assemblies present a high degree of complexity and are difficult to isolate individually. • It is research intensive and too chemistry dependent. 	(Biswas, et al., 2012), (Rius, et al., 2017), (Kazmaier & Chopra, 2000),

Table 2-5 List of conventional bottom-up techniques, showing techniques, advantages, disadvantages and references – contd.

Type	Technique	Advantages	Disadvantages	References
DNA Scaffolding	The structure and size of the DNA is used to organise other molecules or nanoparticles into its molecularly programmed pattern/configuration.	<ul style="list-style-type: none"> • The 2nm diameter and 3,4nm helical repeat miniature DNA possesses remarkable programmable molecular recognition. • It has a large variety of sequences to form arbitrary shape • It possesses the capacity to form extremely low-resolution nanostructures. • It is flexible as it can be used in combination with inorganic materials. 	<ul style="list-style-type: none"> • Still not practicable in an industrial scale. • It is a process not suited for high temperatures. 	(Li, et al., 2009), (Zhang, et al., 2013), (Surwade, et al., 2011)

General challenge with bottom-up approaches

Some major technological challenges still remain to be solved, which include the surface preparation and conditioning for the controlled deposition of the atoms, control of impurities and site uniformity, quality of the reactants, etc. Another is the challenge in achieving little or no long-range pattern order, making it dependent on patterned templates.

2.3.3 Summarised relative quantification of top-down and bottom-up approaches

The type of nanofabrication technique to be used depends on the application requirement, material selectivity and resolution. For top-down approaches, resolution is very accurate with minimum defects, although, the throughput rate is low (less than 10^{-2} m²/h). The technique with the highest throughput so far under this category of nanofabrication is the Nano-imprint. Bottom-up approaches which rely on atomic/molecular interactions under “natural forces” to build structures generates low resolution value structures with the highest in Sol-gel (~10nm) and the lowest in atomic layer deposition (~2nm). This system has high throughput, especially when done in batches (>1 m²/h). Figure 2-1(a) provides a quantification summary to categorize top-down and bottom-up approaches in the format of throughput (m²/h)

vs resolution (nm), with the average values for each mentioned process obtained from (Radha & Kulkarni, 2014), (Garcia, et al., 2014), (Biswas, et al., 2012), (Martinez-Chapa, et al., 2020), (Zhang, et al., 2013).

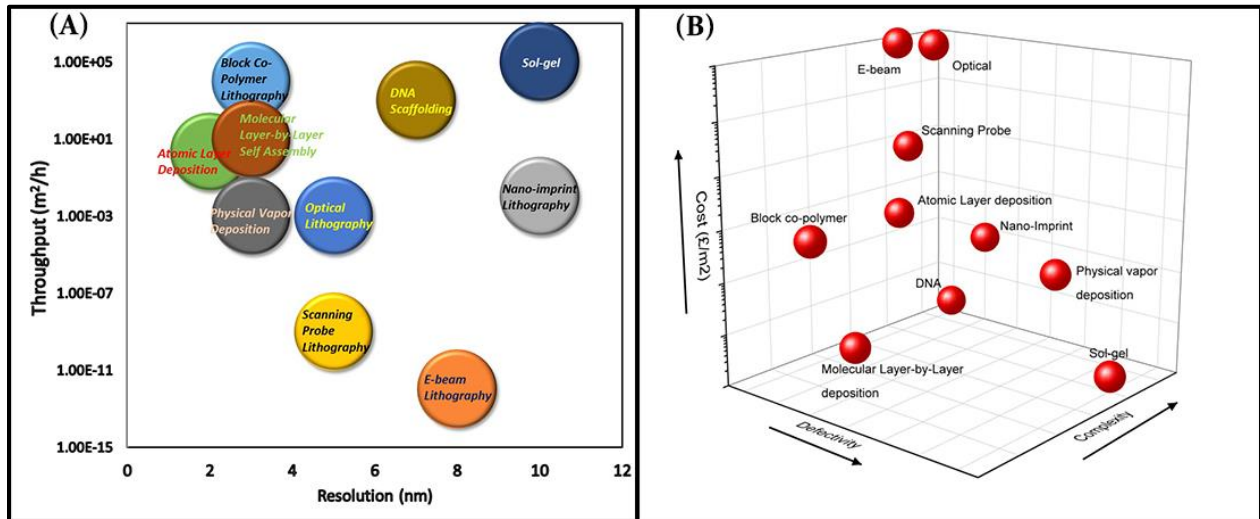


Figure 2-1 Illustrative quantification of existing top-down and bottom-up nanofabrication methods; (a) shows the throughput rate (m²/h) vs resolution (b) shows a three-dimensional quantification consisting of defectivity, complexity and process cost (£/m²). Summary obtained from the following sources; (Radha & Kulkarni, 2014), (Garcia, et al., 2014), (Liddle & Gallatin, 2016), (Biswas, et al., 2012), (Martinez-Chapa, et al., 2020), (Zhang, et al., 2013)

Top-down approach of nanofabrication generally tend to be costly, although depending on the application and resolution requirement. One such instance are systems requiring chip design for electronics; the use of optical and E-beam lithography would likely yield a throughput production cost close to the proximity of £100/m² (Liddle & Gallatin, 2016). For example, lithographic machines such as the ASML Extreme Ultraviolet (EUV) that can mark close to 5nm resolution cost about £108 million (Clark, 2021). Also, in most cases clean room is desired which are rated based on ISO, size, air filtration and air changes per hour (Yang, 2003). According to some commercial reports, cost of acquiring one can be as high as £10,000s per square meter depending on the application purpose (Bullimore, 2020). Other set of costs are that of machine maintenance, clean room maintenance, energy consumption costs, etc. (Lawes, 2007). It is often said that bottom-up approaches are cheap to produce, although no real value has been estimated (Liddle & Gallatin, 2016). A summary of this parameter is presented in Figure 2-1(b).

Complexity of a product designed by either of the nanofabrication processes is defined by the degree of functionality, information content, precision and perfection it required (Liddle & Gallatin, 2016). Just as E-beam and photo lithographic methods require masking and etching process, material components and the required precision surely puts it in high ends of the spectrum of complexity. Scanning probe is flexible enough to deposit variety of materials across complicated geometrical patterns thus placing it medium-high (Garcia, et al., 2014). Nano-imprint is used to pattern complex geometries in variety of polymeric materials, which can be used to build complex hierarchical structures; therefore, making it fairly high in complexity (Biswas, et al., 2012). Most bottom-up techniques like block copolymer, molecular layer-by-layer and atomic layer deposition work with one type of material and their geometric patterns are naturally non-modifiable; thus, making it a straight forward less complex process (Yuan & Dornfeld, 2010). However, others like sol-gel and DNA give opportunity for structure editing that offers the final product high degree of multifunctionality, therefore, increasing the degree of complexity process (Biswas, et al., 2012), (Zhang, et al., 2013). A general summary of this parameter is presented in Figure 2-1 (b).

Clearly, for structures requiring only modest short-range order, the presence of pattern defects is not an issue. Defects generated in top-down fabrication processes may be difficult to get rid of, but are essentially deterministic and can be eliminated by, for example, rigorous approaches to cleanliness. By contrast, bottom-up approaches rely on the combination of thermodynamics and kinetics to generate the structures of interest (Biswas, et al., 2012). This means that, for interactions with finite energies operating over finite times, there will, almost always, be a significant number of defects present. This happens either as a result of thermal fluctuations (for low energy of formation defects) or kinetic trapping (Liddle & Gallatin, 2016). A summary of this parameter is presented in Figure 2-1 (b).

It can be seen that the top-down approaches provide fairly high resolution, low defectivity and high complexity, however their throughput rate and cost remains a challenge, while bottom-up procedures are fairly cheap, medium to high complexity, low resolution but with medium to high defectivity. Due to its high potential as a

means of manufacturing low resolution structures involving molecules/atoms/compounds, its deficiency for long range manufacturing can be improved through combination with top-down approach. Such combinations are termed as self-assembly (or guided-self-assembly) approaches.

2.3.4 Self-Assembly

Self-assembly involves the combination (“Bridging”) of top-down and build-up approaches. This happens in such a way patterns are established within the substrate of interest using either the Lithography or force field technique to create long-range arbitrary patterns where particles, molecules, or thin films are deposited and grown within the structures. Self-assembly can be categorised under “Externally-Directed” and “Template-Directed” self-assemblies (Whitesides, et al., 2005). Externally-Directed or Stimulated self-assemblies are methods where an external force field/energy is used to stimulate the organisation of units (or blocks) particles/molecules into orders in the direction of the force. Examples of such methods are magnetic, electrical, optical, thermal, pH and hydrodynamics (fluid flow field) methods (Grzelczak, et al., 2010), (Grzelczak, et al., 2019). Based on the circumstances of self-assemblies formation, each procedure is considered to be specially defined in terms of; (i) Host set-up (Template), (ii) Stimulation (External or Internal), and (iii) Directed (or not directed). Template-Directed self-assembly methods has to do with the conventional top-down lithography designed templates created for the long-range organisation of bottom-up particles/molecular complexes.

2.3.4.1 Techniques and current developments in self-assembly approach in building nanostructures

There have been several sets of techniques designed and applied in the creation of nanostructures. **Table 2-6** provides examples and references of Template-directed-self-assembly methods, and Stimulated-directed-self-assembly methods.

Table 2-6 List of directed self-assembly techniques consisting of background information, downsides and references

Directed self-assembly Technique	Background	Downside	References
Surface functionalised Lithographic template and nanoparticles (<i>Template-Directed-Self-Assembly</i>)	A chemical category. The template acts as a structural guide where locations on the substrate are chemically modified and act as attractive spots for nanoparticles where they align accordingly to the pattern of the template. A self-assembly non-dissipative system where particles form structures while attaining their energetic minimum	Hard templates have poor control over periodicity, especially if there's lack of spatial distribution of reactive sites to agglomerate target particles	(Rycenga, et al., 2009), (Mayer, et al., 2016), (Xia, et al., 2003), (Yin, et al., 2001), (Li, et al., 2013)
Liquid interfaces (<i>Stimulated-Directed-self-assembly</i>)	A self-assembly non-dissipative system where particles form structures while attaining their energetic minimum. In such system, the reduction in interfacial energy is the driving force leading to the assembly of nanoparticles at the interface. This results from surface tension, evaporation of solvent, capillary forces and possibly the combination of both. The particles are coated with specific ligands and concentration to make it a Janus-type particle which easily sits at the interface between immiscible phases. Depending on the liquids involved, the parking order and density of particles can differ based on its ligands average charge, inorganic or organic electrolytes within the liquid medium. Examples: Pickering emulsions, Nano-plasmonic liquid-like mirrors	The process could be irreversible or un-adjustable once attained. It applies to relatively large (>~20um) particles. Lacks efficient long-range order.	(Andala, et al., 2012), (Chen, et al., 2011), (Booth & Dryfe, 2015), (Flatté, et al., 2008)
pH (<i>Stimulated-directed-self-assembly</i>)	A self-assembly non-dissipative system where particles form structures while attaining their energetic minimum. Concentration of ions or protons in solution can influence functionalised nanoparticles by altering hydrogen bond interactions or repulsive electrostatic interactions causing the particles to agglomerate in certain configurations.	The introduction of chemical stimuli (acid or bases) to change the pH leads to the accumulation of by-products (such as water and salts) which affects the number of assembly-disassembly cycles.	(Liu, et al., 2021), (Pan, et al., 2014),

Table 2-7 List of directed self-assembly techniques consisting of background information, downsides and references – contd.

Directed self-assembly Technique	Background	Downside	References
Thermal (<i>Externally-stimulated self-assembly</i>)	A self-assembly non-dissipative system where particles form structures while attaining their energetic minimum. Thermally responsive materials are designed by functionalizing nanoparticles with molecules that change in properties (conformity and/or intermolecular interactions) upon varying temperatures.	Temperature induced phase transition of nanoparticle-grafted thermo-responsive polymer typically leads to uncontrolled nanoparticle precipitation. To remediate this, different other thermo-responsive polymers are added which then leads to more species involved in the system	(Costanzo & Beyer, 2007), (Li, et al., 2020),
Hydrodynamics (Fluid-flow) (<i>Externally-Directed-self-assembly</i>)	This involves the use of macroscopic viscous flow to direct the assembly of disordered particles into ordered structure. Controlling factors are the shear rate, shear strain, particle volume fraction, particle interaction potential and polydispersity. Examples are microfluidic channels, Spin Coating, Doctor blade, etc.	For the ordering to happen, high flow strength is required and if the volume fraction is less than the equilibrium fluid-crystal phase boundary, the structure will be disordered.	(Chen, et al., 1992), (Jia, et al., 2020), (McConnell, et al., 1995), (Ni, et al., 2012), (Panine, et al., 2002)
Optical (<i>Externally-Stimulated-Directed-Self-Assembly</i>)	External Field effective system. This is a system where nanoparticles are made photo-responsive via functionalisation with ligand monolayers terminated with light switchable moieties. Upon photo-excitation, the polymer polymerizes, changing the polarity state of the nanoparticle-polymer compound to spontaneously assemble into aggregates.	Requires photo-sensitive molecules within the system. In some cases where molecules are not, the attached particle needs to be photo-responsive by converting the photons plasmon energy to heat which then polymerizes thermal responsive molecules locally. Other, than both methods, this technique is rather limited.	(Bapna, et al., 2013), (Kim, et al., 2019), (Kuzyk, et al., 2016), (Čižmár, et al., 2010), (Aubret, et al., 2018)
Electrical (<i>Externally-Stimulated-Directed-Self-Assembly</i>)	This is a dissipative form of self-assembly where structures are not in their energetic minimum, rather adopt a new static non-equilibrium state. Electric field affect the collection of dispersed particles with respect to the properties of both the particles and carrier medium. Depending on the electric field geometry, strength, and frequency (for Alternating Current), particles polarisation in contrast to the surrounding medium, mobile and immobile charges distribution; determines the direction, dipolar strength and degree of agglomeration of electrophoretic particles.	The chemical configuration have to be carefully selected in order to avoid electric breakdown which then affects free charges in the system, thus leading to degradation.	(Demirors & Alison, 2018), (Fraden, et al., 1989), (Hasley & Toor, 1990), (Mittal, et al., 2008), (Dommersnes & Fossum, 2016),

Table 2-8 List of directed self-assembly techniques consisting of background information, downsides and references – contd.

Directed self-assembly Technique	Background	Downside	References
<p>Magnetic <i>(Externally-Stimulated-Directed-Self-Assembly)</i></p>	<p>This is another dissipative form of self-assembly where structures are not in their energetic minimum, rather adopt a new static non-equilibrium state. The application of external magnetic field influences the magnetic responsive particle to form dipole-dipole aggregate due to magnetic susceptibility contrast between the particle and carrier medium. Depending on the particle shape and distribution of field, structures created can be in either 2D or 3D form. This technique can deliver instantaneously through boundaries or medium impermeable to chemical or optical stimuli. It is flexible in such a way it can be applied throughout an entire sample or locally precisely.</p>	<ul style="list-style-type: none"> • This method relies more on magnetic responsive particles (Fe, Ni, Co). Not all materials are magnetically responsive. However, some do exhibit at nanoscale but it is weak. Even upon that, they are not sufficient for nano-structuring. • The smaller the particle, potentially the more field strength required to get it magnetized and mobilized. • Precise control and timing is required as nanoparticles structure formats can switch from dipolar chains into complex lattices. 	<p>(Ge, et al., 2011), (Demirors, et al., 2013), (Erb, et al., 2009), (Promislow & Gast, 1996), (Saini, et al., 2021), (Urbach, et al., 2003)</p>
<p>Acoustic Field <i>(Externally-Stimulated-Directed-Self-Assembly)</i></p>	<p>This is a process where an acoustic source-Piezo electric transducer, generates acoustic radiation that drives particles towards positions within the medium dictated by its field pressure gradient. Within the pressure gradient acoustic nodes are generated from the interference between incident and reflected waves, forming a superposition where the local pressure at that node is zero (A standing wave). Therefore, within the medium, there are nodes and antinodes (High local pressure zones). In acoustic pressure node, particles more dense or less compressible than the medium migrate here, while at the antinode, particles less dense or more compressible than the medium migrate here. Acoustic node gap is dependent on frequency</p>	<ul style="list-style-type: none"> • This process must be done within a fluidic medium. • In most cases ordered particles are immediately captured using a UV curable fluid or rapidly dried to capture them within wave node regions 	<p>(Akella & Juarez, 2018), (Shabaniverki, et al., 2018), (Shabaniverki & Juarez, 2021)</p>

Self-assembly approach is a desired process because of its cost effective, robust, flexible and advancing techniques in nanofabrication and most investigators are capitalising on this parallel technique to create highly functional complex materials. The use of colloids is an essential piece in bottom-up assembly of materials, where its unique size and shape profiles help in establishing energy responsive and interactive materials. Thus, the efficient periodical organisation of particles/colloids as building blocks for materials to form crystalline structures that can be used as an intermediary for larger and more complex structures is essential in self-assembly approach of material fabrication.

Colloidal materials can be metallic or non-metallic, and it determines the method of preparation which could either be by suspension, emulsion, dispersion, or precipitation. To achieve a particular size range, shape and morphology of colloidal particles, several techniques on synthesis have been developed over time involving pH value of solution, concentration of catalyst, composition of reagents, types of solvent, and reaction temperature. Several reviews offer a complete overview of colloidal particles synthesis and characterization (Patra & Baek, 2014) (Landfester, 2006) (Mingos, 2014).

In order to keep colloidal particles well dispersed and to avoid agglomeration while in suspension, the surface of the particle is functionalised with chemical moieties (e.g. -OH, -COOH). In some cases shelled by metallic or oxide compounds.

2.4 Control of Nanoparticles or Colloids in Ordered Structural Agglomerates within Nanostructures

Nanoparticles of materials exhibit unusual properties, and its agglomerates can positively or negatively impact the overall material functionality. Depending on the area of application, agglomerates/aggregates are useful in optics where for example, (a) localized surface plasmon resonance which facilitates high electron transfer across noble metal nanoparticles surfaces (Khan, et al., 2019), (b) Random lasing from dye-surfactant micelle agglomerate (Pancholi, et al., 2018) and dye-noble metal nanoparticle composite (Wan, et al., 2017), (c) Diffusion of incoming radiation and increased rate of energy conversion for catalysis (Pellegrino, et al., 2017), (Lakshminarasinha, et al., 2008). Meanwhile in building polymer nanocomposites

for example, agglomerates/aggregates negatively hinder the mechanical performances of the material (Zare, 2016) (Zare, 2016). Thus, it is vital to control agglomerates of nanoparticles in terms of location, density, order of arrangement and overall dispersity within a host medium. Therefore, mechanically and chemically preparing the host medium to attract and capture the right quantity of nanoparticles in ordered configuration per area/volume is essential.

Creating topographically complex surfaces with nano or submicron periodicity helps in the formation of 2-dimensional or 3-Dimensional colloidal crystals which are essential for developing optical and electronic devices, biological active substrates, photonic band gap, data storage, photonic crystals and sensors. The control of gaps, spacing, layering formation and overall interparticle interaction is dependent on the balance of forces between them, such as;

- a) Van der Waals – This interaction is prominent between individual particles of sub-micron to nano-size range within a very short distance (approx. $\leq 10\text{nm}$) from each other. Particles can exploit this energy for self-assembly.
- b) Electrostatic Interaction – Such interaction can either be repulsive or attractive depending on the particle surface charge. Within a liquid an electric double exists which creates an electric field here the Debye screening length is determined by the solutions pH, electrolyte concentration and particle concentration. This system affects the movement of charged particles, thus influences colloidal crystal formation.
- c) Capillary forces - When a liquid ridge exists between particles, two phenomenon occurs: the first is an attractive force between the particles due to the wettability, surface tension and meniscus at the surfaces of the particles. The second is a repulsive force due to viscosity of the liquid which creates Laplace pressures keeping the particles apart.
- d) Steric Effect - Steric interactions are commonly used to stabilize particles when long term stability is required by grafting some polymer on the particle surface. However, the amount of polymer to be added has to be accurately chosen, otherwise unwanted destabilization effects (instead of stabilization) such as depletion induced flocculation or bridging flocculation can arise.

- e) Magnetic attraction – Is a phenomenon that occurs with magnetic responsive nanoparticles where an introduction of magnetic field polarises the electrons of the particle which therefore initiates periodic attraction between them thereby forming either 2D or 3D structures depending on the strength of the introduced field. This force of attraction system is quick and offers tuneability better than the others.

2.4.1 Fluidic self-assembly method for creating 2D and 3D colloidal structures

The use of fluids for the organisation of colloids is an established area of colloidal science where the role of intermolecular and fluidic forces help in achieving highly organised structures. **Table 2-9** provides summary of the established and yet progressive methods of fluidic assisted colloidal structures.

Table 2-9 Summary of fluidic aided self-assembly methods

Methods	Description	References
Sedimentation	This technique relies on gravitational sedimentation of colloid particles to self-assemble within a medium of lesser density than the colloids. The ordering pattern is controlled by the free energy minimization or entropy maximization. This technique can be used to build hierarchical structures that can be used to create opals and inverted opals bandgap photonic crystals for optical applications.	(Zhou, et al., 2005), (Gonzalez, 2016), (Lee, et al., 2004).
Confined-convective self-assembly	In this technique, certain shape is etched on the substrate to create confinement to trap colloids as the carrier fluid evaporates. The confinement helps to improve capillary attraction of colloids to form 2 D or 3D assembly of particles.	(Kim, et al., 2005), (Wu, et al., 2008), (Zhang, et al., 2014), (Xing, et al., 2020)
Dip coating	This method involves immersion of a substrate into a solution containing particles and then continuously extracted at a controlled speed thereby allowing the fluid meniscus with the substrate to allow closed packed monolayer of particles. This process is valid for particles greater than 1 μm .	(Manstrangeli, et al., 2009), (Zhang, et al., 2013), (Binker, 2013).
Drop casting and evaporative drying	This method is based on drying of droplet of suspended particles. The radial evaporative flow (which is dependent on the flux and density of the fluid), recirculating 'Marangoni' flow (controlled by surface tension gradient) and flow caused by DLVO adhesion force. Known for its simplicity and speed, the downside to this method is the efficient control of flow within the droplet caused by the rapid evaporation which would finally result to non-uniform patterned colloids on substrate.	(Cai, et al., 2020), (Rabani, et al., 2003), (Han & Lin, 2012), (Lin, 2012), (Binker, et al., 1999), (Grosso, et al., 2004)
Deposition during retraction of liquid meniscus within a microfluidic chamber	In this technique the meniscus of the solvent forms at the edge of the capillary tube due to surface tension and it causes weaker solvent-solvent interactions that results to faster endothermic solvent evaporation. The surface tension gradient existing between the bulk solvent and meniscus helps driving the colloids toward the contact line (Marangoni flow) between the fluid and the capillary substrate. The localized increase in colloids at the edge of meniscus causes a pi-pi stacking forming 3-Dimensional patterns.	(Jose, 2015), (Shin, et al., 2019), (Kong, et al., 2015).
Electrophoretic deposition	When an imposed electric field through electrodes in a colloidal solution, the electric field moves excess charge in the diffuse layer surrounding the particle, thereby creating a slip at the interface between particle and surrounding liquid. For a uniform Direct current (DC) field, a fluid flow is induced on the particle that translates its motion in the direction of the applied field, opposite the overall slip velocity. This leads to monolayer arrays which are reversible upon removal of electric field and are not in adhesive contact with the electrode surface. In Alternative electric (AC) field, the particles self-organise normal to the plane of the electrode forming a close or non-close 2-dimensional hexagonal structure.	(Brisson & Tilton, 2002), (Dickerson & Boccaccini, 2012), (Oberdick & Majetich, 2013), (Bailey, et al., 2000). (Bazin & Faure, 2012)

Table 2-10 Summary of fluidic aided self-assembly methods – contd.

Methods	Description	References
Self-assembly at gas-liquid interface	In this technique a 1-dimensional monolayer is allowed to form at air liquid interface within a constraint. As the bulk liquid is discharged at a slow rate through a lower exit channel of the tank, leading to gradual lowering in liquid level, the constrained monolayer gradually settles and adheres to a substrate just beneath the liquid level.	(Lotito & Zambelli, 2016), (Poirier & D., 1996), (Zhang, et al., 2014), (Liu, et al., 2019), (Roger, et al., 2018)
Langmuir-Blodgett technique	This technique utilizes both surface tension and evaporation from the liquid air interface to form nanopatterns of amphiphilic molecular functionalized nanoparticles at the interface of a volatile and a non-volatile sets liquid. Water is used in most cases as the non-volatile liquid and the particles are closed packed by surface pressure from the external barrier placed in the water. Then after the substrate is slowly pulled upward normal to the film where it gets transferred unto its surface.	(Ulman, 1991), (Chen, et al., 2007), (Martin-Garcia & Velazquez, 2014), (Kohoutek, et al., 2020)
Inkjet printing	This technique involves the use of a molecular scale, self-assembling surfactant as an ink component, where it helps forming macroscopically patterned nanostructures with the attaching colloids during ink-jet printing. The nearly uniform sized ink droplets undergo self-assembly of particles on evaporation, producing hemispherical colloidal aggregates with ordered structure. The size, shape and structure of colloidal aggregates is determined by the interfacial properties between the ink and colloid. Although the ink printing pattern resolution is low, where the grating gap is large.	(Ko, et al., 2004), (Delekta, et al., 2020), (Sowade, et al., 2016), (Fisslthaler, et al., 2008), (Cui, et al., 2009)
Spray coating	This technique is employed for colloidal solutions, where the solvent has high boiling point, poor colloidal stability for larger droplets. The spraying techniques allows for small droplets to be deposited on substrate, thus giving room for rapid evaporation of solvent and overall stability of colloidal assembly	(Tsurko, et al., 2017), (Celik, et al., 2020)
Spin coating	This process is traditionally used to create uniform layers of photoresist onto wafers for lithographic patterning in semiconductor industry. It operates by rapid acceleration yielding a centrifugal force that will cause some liquid mass to be ejected and topographical film thinning. The final film thickness is dependent on balance between adhesive and shear forces. The thickness of film can range from hundreds of microns to tens of nanometres depending on liquid properties like vapor pressures, viscosity and density. It has also been explored for the formation of 2D and 3D colloidal crystal structure, where the rapid or gradual evaporation of the solvents forms meniscus between colloidal particles, therefore establishing capillary pressures that pull the particles closer together.	(Han, et al., 2019), (Xia, et al., 2004) , (van Dommelen, et al., 2018), (Chen, et al., 2013)

The bulk techniques have a common challenge with the thermodynamic effect on particles while solvent evaporates, especially in patterning colloidal suspensions which encompasses different hydrodynamic and interfacial forces that influences how particles interact at interfaces and solid surfaces (Celio, et al., 2006), (Kralchevsky & Nagayama, 2001). This therefore affects the capability of producing high quality 2D crystals. In order to surpass this challenge, most techniques would rely on machined or etched templates for patterning to minimize the instability over long range coating and notably establishing means to take advantage of light by diffraction. However lithographic equipment required to create such sub-micron patterns are pricy to possess and maintain.

Interestingly, a way of surpassing the thermodynamic challenges associated with long range ordering and circumventing the need for precision lithographic equipment, is the use of liquid-liquid interface for the agglomeration of colloids by Pickering emulsion; which is seen to be an easier, quicker and cheaper way of achieving such objectives (Guttula, 2007). It also offers thermodynamic stability with colloids being irreversibly indissociable from the interface (Binks, 2002). This is so because the energy of adsorption is higher than the thermal energy ($K_B T$) at room temperature (293 K), (Binks & Hozorov, 2006). It also maximizes use of colloidal material with little or no waste (Nie, et al., 2008).

The use of immiscible liquids interface for the organisation of colloids can be achieved when particles are driven by charges towards interface where they can attain equilibrium. Several techniques like the solution pH adjustments, salt ions, ion exchange, and polymeric grafting of colloids are used to achieve colloidal migration from bulk solution to its orientation and stability at the 2-phase interface. (Binks & Lumsdon, 1999)

Salts, also called promoters, dissociate in water by yielding ions near the interface of opposite charge to that of the particles (Aveyard & Binks, 2003). Any particles arriving from water to the interface partially submerge in the oil phase, and the Coulombic repulsion between interfacial particles is screened. This reduction in repulsion combined with the ever-present van der Waals attraction allows the particles to pack closely at the interface and remain. An example involves the

assembly of gold nanoparticles (AuNPs) at the liquid–liquid interface, where the coulombic repulsive and van der Waals attractive forces exert influence on the adsorbed AuNPs. Thus, the surface charge density (σ) of adsorbed AuNPs critically influences their tendency to adsorb and their equilibrium interfacial surface coverage. (Scanlon, et al., 2018), (Wang, et al., 2005).

For particles containing ionizable surface groups such as $-\text{SiOH}$, $-\text{COOH}$, or $-\text{NH}_2$, changing the pH of the aqueous phase has also been used to effect particle activation (Binks & Lumsdon, 1999), (Binks, et al., 2006). At pH values around the isoelectric point (IEP) of the solid, particles are of low charge and are rendered more hydrophobic compared to pH values far from the IEP where they are charged and fully wettable by water. Particles of low charge stabilize oil-in-water (o/w) emulsions, however, when pH increases the particles can also trigger emulsion phase inversion from o/w to w/o.

Alternatively, short-chain alcohols such as methanol and ethanol when added to water (up to 50 vol %) result in the spontaneous assembly of charged metal particles to the o/w interface to produce reflective films (Younan, et al., 2010). Alcohol molecules were deemed to reduce the charge density on particle surfaces by competitive adsorption in which charge stabilizing ions, e.g., citrate, are displaced from particle surfaces. Reincke and coworkers (Reincke, et al., 2004) demonstrated that the addition of ethanol renders hydrophilic citrate-stabilized gold nanoparticles at the water/n-heptane interface, eventually leading to the formation of a closely packed monolayer.

Studies on the phase transfer of gold hydrosol have shown that by employing straight-chain longer alkylamines, it is possible to transfer carboxylic acid derivatized gold nanoparticles at the water–toluene interface (Chen & Kimura, 2001), as well as by introducing ligands or thiolates (Park & Park, 2008), (Wang, et al., 2005). When nanoparticles are functionalized with desired ligands, the surface-binding properties of the nanostructure is further tailored to improve its interaction with the surrounding and attain stability. With this stability hierarchical self-assembly of particles can be transformed into robust architectures. (Ghosh & Boker, 2019)

The use of particle migration and interface colloidal stabilisation techniques like pH, salt ions and short chain alcohols are not quite attractive in some aspects of nanofabrication. Especially when a carrying forward manufacturing process by adding other materials that could be sensitive to conditions within the dispersing phase (i.e., pH, salt ion concentration, alcohols, etc.). If the conditions of the colloidal solution were to be altered in order to accommodate secondary materials, the zeta potential would change, and then affect particle three phase contact angle, thereby affecting the stability of Pickering emulsions (Binks & Clint, 2002), (Tang, et al., 2014). Therefore, functionalization and surface coating deem to be preferable option, especially for this research, because the bulk solution condition can be adjusted to accommodate other secondary materials without influencing the zeta potential of particles being situated at the interface of an emulsion droplet. Examples of such are; (i) the Polyethylene glycol (PEG) based molecule for coating gold citrate nanoparticle modifying it to be both oil and water wettable (Kelly, et al., 2003), (Wang, et al., 2020), (ii) the use of thiol-terminated PEG and alkane thiol to surface modify gold citrate nanoparticle which was used for creating Pickering emulsion, (Larson-Smith & Pozzo, 2012), (Larson-smith & Pozzo, 2011). Both capping around gold nanoparticle through hydrogen bonding and gold-ligand bonding are effective methods of stabilizing gold nanoparticles for pickering emulsions. However, the cost of acquiring ligands is high compared to coating gold citrate with PEG. For example, as at the time of writing this thesis, the cost of thiol terminated PEG from Sigma Aldrich was approximately £260/gram, (Aldrich, 2022).

Interestingly there are variety of ways for the organisation of such hybrid colloids as already presented in **Table 2-9**. Most of those techniques are; inherently slow, require large volume of colloidal solution, and are difficult to scale up. Spin coating however, is widely used for coating polymer thin films over large areas, making it well suited for creating 2D colloidal crystals, with major advantages in; rapid formation, high-throughput, extremely low amount of colloidal solution requirement, high degree of reproducibility, and scalability for colloidal assembly (Kralchevsky & Nagayama, 2001). This technique was applied for the 2D lattice organisation of uncapped 4 nm gold colloids reaching lengths exceeding 1 μm (Das, et al., 2008).

Despite the easy formation of 2D and 3D closed packed colloidal structures via these methods, the formation of complex patterns is often desired, thus most systems would require coalition with patterned templates or external field forces to achieve complex structures.

2.5 Combination of nanofabrication techniques for building of complex patterned colloidal structures – Spin Coating

There are lots of directed self-assembly combinations for enhanced control of colloids/nanoparticles to form well-ordered complex structures. Examples of such include; Template and magnetic field guided self-assembly (He, et al., 2013), (Xue & Furlani, 2014), Template and electric field self-assembly (Crassous & Demirors, 2017), (Winkleman, et al., 2005), Template and Fluid capillary force (Sharma & Dhawan, 2019), (Celio, et al., 2006), Acoustic field and Fluid flow (Akella & Juarez, 2018), Fluid Interface/Capillary and Electric field (Aubry, et al., 2008), (Janjua, et al., 2009), Capillary force and Magnetic field (Bharti, et al., 2015). Several other combinations can be read through in reviews by (Grzelczak, et al., 2010), (Liljestrom, et al., 2019), and (Grzelczak, et al., 2019).

Spin coating being one of the fastest fluidic and capillary interfacial self-assembly technique, makes it of interest to this research. Interestingly, it has been applied in direct integration with standard microfabrication approaches, such as lithographically machined templates, chemically modified and patterned substrate, electric field, and magnetic field (Banik & Mukherjee, 2018) (Bartlett, et al., 2012) (Pichumani & Gonzalez-Vinas, 2011).

2.5.1 Spin Coating and Lithographically Patterned Substrate.

Often times, 2-dimesnional colloid lattice created by spin coating have some long-range order defects as a result of the process being radially symmetrical about the centre of rotation (Arcos, et al., 2008). Thus, the introduction of lithographically patterned substrate aid in improving local colloid clustering, long-range ordering on the substrate, as well as non-conventional hexagonal close packing arrays. Ozin and Yang were one of the pioneers that applied this technique, with a motivation to overcome the challenge posed by using capillary-pressure driven influx of colloids into patterned substate; which involved poor filling of channels by colloids due to

channel blocking. Therefore, by introducing spin coating the uniform spreading of colloids by centrifugal force in combination with gravity-driven sedimentation and evaporation induced capillary forces, led to rapid settlement and crystallization in etched pits (Ozin & Yang, 2001). Banik and Mukherjee investigated the impact of particle diameter, colloid concentration in solvent, height of pattern features, and rotational speed on ordering of colloids on patterned substrate. Higher colloidal concentration and spin speed yield perfect ordering. Also, when the etched grooves are 20% less than particle diameter, the pattern failed at confining particles (Banik & Mukherjee, 2018). Other related works are (Xia, et al., 2004; Xia, et al., 2004), (Xia & Brueck, 2004). The challenge with these approaches is that they encounter the problem of pattern flexibility and periodicity, where to fabricate a different pattern would be costly since top-down machining process is relatively expensive.

2.5.2 Spin Coating and Electric Field directed Assembly

Pioneers of this approach, Bartlett and Co developed a setup that consisted of an electrode placed beneath the substrate to establish an electric field with its direction being made stationary in the rotating frame (Bartlett, et al., 2012). The electrode design and setup was made to break the conventional axial symmetry orientation of colloids by just spin coating alone. Also, the field strength regulation controlled local orientation of formed colloidal lattices. The challenge with electric current driven assembly is the risk of the electric current potentially jeopardizing the integrity of some material component and interfere with the distribution of free charge carriers, (Liljestrom, et al., 2019), (Crassous, et al., 2014).

2.5.3 Spin Coating and Magnetic Field Directed Assembly

Some group of investigators (Pichumani & Gonzalez-Vinas, 2011), (Pichumani & Gonzalez-Vinas, 2013) (Aslam, et al., 2016) and (Aslam & Gonzalez-Vinas, 2017) developed a stimulated-directional self-assembly approach in the form of spin coating and magnetism. A Helmholtz coil system was designed around the spin coater to generate an alternating magnetic field while spinning a ferromagnetic colloidal solution. Figure 2-2(a), (b), and (c) shows setup, (d), (e), (f) and (g) shows resultant structure types under varying magnetic field strength and spin speed. It can be observed that, the higher the spin speed and lesser field strength leads to lesser

colloidal interaction for building ordered structures. While lesser spin speeds and higher field strengths led to a 3-dimensional hierarchical lattice structure. Although, the 3-dimensional structure might not be suitable for thin film nanostructure on template.

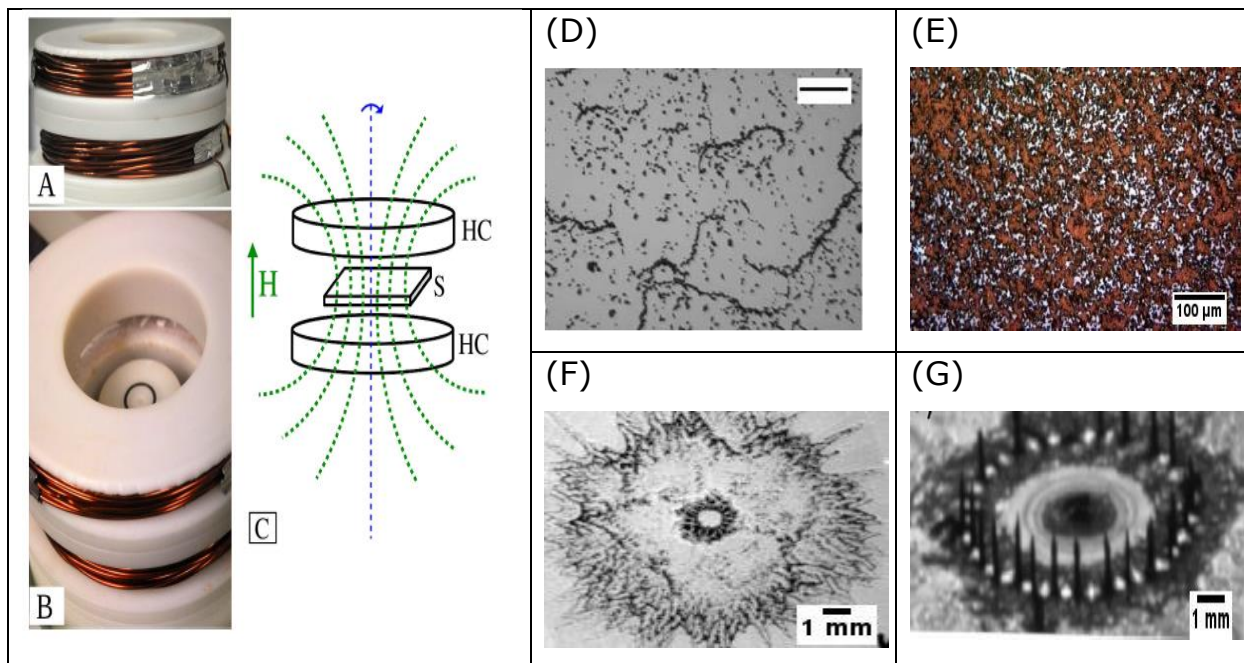


Figure 2-2 shows the pair of Helmholtz coils, (b) shows the Helmholtz coils installed around the substrate, (c) shows diagrammatic illustration of field lines generated by the Helmholtz coil (HC) across the substrate (S). this figure is courtesy of (Pichumani & Gonzalez-Vinas, 2013). (d) shows the resultant structure of dilute ferromagnetic colloid solution 8mm from centre of substrate under magnetic field $H=0.066T$ and spin speed=5000rpm, scale bar=50µm, courtesy (Pichumani & Gonzalez-Vinas, 2013). (e) resultant structure of ferromagnetic colloid solution 6mm from middle of substrate under magnetic field $H=0.99kA/m$ and spin speed=2000rpm, courtesy of (Aslam & Gonzalez-Vinas, 2017). (f) Resultant structure of magnetic colloid at middle of substrate under magnetic field $H=39.7kA/m$ and speed=2400rpm, and (g) Resultant structure of magnetic colloid at middle of substrate under magnetic field $H=39.7kA/m$ and speed=700rpm. Courtesy of (Aslam & Gonzalez-Vinas, 2019)

2.6 Research Interest and Fabrication Approach – Spin Coating and Magnetic Field Directed Assembly

Magnetism on its own is a non-intrusive technique that only acts on a magnetically responsive material, where it polarises such materials along the direction of the field vector. In a colloid solution, particles tend to interact in a dipole-dipole chain-like manner that spans over a long distance (over a million fold) in comparison to the particles individual sizes. With the understanding of spin coating (fluidic) approach on the rapid and uniform distribution of colloids across the substrate, the introduction of magnetic particles and magnetic field is believed to orient these particles along the

established vector field lines by creating dipole-dipole interaction of colloids to build structures along the magnetic field lines. The challenge realised from their setup (Pichumani & Gonzalez-Vinas, 2011), (Pichumani & Gonzalez-Vinas, 2013), (Aslam, et al., 2016), (Aslam & Gonzalez-Vinas, 2017) and (Aslam & Gonzalez-Vinas, 2019) was the direction of the field lines relative to the spinning direction of the substrate and direction of the fluid inertia. These multi-directional forces created an irregular colloidal structure (illustratively described in Figure 2-3); where the spinning substrate supporting the solution carries a particle of interest (yellow-cross) across several flux lines (green star) within a particular radial circumference (red-arrow), while the radial-directional motion of the fluid (brown and blue arrows) tends to drive the particle across several flux lines along the radial direction. An additional influential force that could have contributed to the resultant structure is the capillary pressure developed by the evaporating solvent on the particles trying to establish closed packed colloidal lattices. These multi-directional forces and capillary pressures created a complex structure that requires more intricate study.

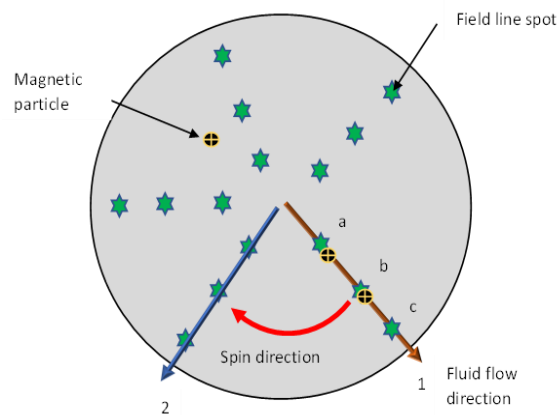


Figure 2-3 Shows an illustration of the impact of forces and motion on ferromagnetic particles; the fluid flow through spin coating tends to drive the fluid along arrow (1) from a magnetic field line spot (a to b), within the same time scale, the radial directional movement of the substrate tend to carry the particle from field spot 1-a to 2-a, thereby affecting the polarity of the each particle and their relative dipole-dipole interactions.

In this research however, permanent magnets of less than or equal to 0.5 tesla of different configurations were placed below the substrate to create a stationary radial field (just as (Bartlett, et al., 2012) did using an electrode and electric field), that would minimize the force contention to two parallel but opposing forces. This operates

by magnetic pull of particles toward the centre, while it faces radially outward directed fluid inertia, see Figure 4-1 for setup. The control of spin speed and magnetic field strength would offer tunability of structure resolution, thereby making the system flexible in generating multiple designs without tedious modification or reprocessing like that of Lithographic templates or a simple fluidic assembly.

Before any further ado, it is necessary to present and discuss the principle of magnetism and the role of magnetically controlled colloidal assembly.

2.6.1 Magnetism principle and magnetism of colloids

Magnetism and magnetic materials have been an integral tool for controlling and manipulating structures and fabricated devices in a non-intrusive manner. In our world today, there are majorly four (4) categories of magnetic responsive materials, and they are Paramagnetic, Ferromagnetic, Ferrimagnetic and Diamagnetic (Ohring, 1995) (Gupta, et al., 2017).

Paramagnetic materials are types of materials that are weakly attracted to a magnetic field. Under such exposure, they form internally induced magnetic fields in the direction of the applied magnetic field. In chemistry of elements, most atoms with incompletely filled atomic orbitals, having unpaired electrons yield magnetic dipole moments due to their spin which align along with applied external magnetic field line direction (Gupta, et al., 2017). They do not retain magnetization when magnetic field is removed because thermal effect randomizes their spin orientation. Examples are Aluminium, Magnesium, Sodium, Lithium, Fe_3O_4 , Fe_2O_3 etc.

Ferromagnetic materials are type of materials that are strongly attracted to a magnetic field because their spins are aligned to the direction of the field, and can even retain some of the magnetism after the field has been removed. This is possible for the materials in bulk form because within them are tiny regions called magnetic domains (Ohring, 1995). These domains contain individual spins pointing in different direction under zero magnetic field within the material, making it zero net magnetic moment. Since the domain are not fixed in place within the material, the introduction of strong external magnetic field causes the spin of electrons in atoms close to the domain wall to shift the border as it orients in the same direction as other electron

spins in other domains along the field direction. Therefore, when magnetic field is removed, domains will remain aligned and possibly unable to return to its minimum energy configuration (Bowler, 2019). Ways of demagnetizing such materials are either by Annealing (heating and Cooling), Vibration by hammering, or by magnetic field oscillation from a degaussing coil magnet. Example of such materials are Iron, Nickel and Cobalt, as well as their alloys.

Ferrimagnetic materials are such where a certain percentage of electron spins having magnetic moments in opposite direction to the majority magnetic moments in orientation along the magnetic field direction within the material. Based on the fact overall moments are unequal, the majority of spin direction drives the magnetic nature of the material. In ferrimagnetic materials, there are two different types of atoms within a unit cell, where one has a smaller magnetic moment and in opposite direction compared to the other, thus making the unit lattice material to behave like a small magnet with north and south poles (Globus & Duplex, 1969). Example of such materials are Magnetite.

Antiferromagnetic materials are similar in behaviour to ferrimagnetic, but differ by the fact that the opposite directional magnetic moment from the spin of atomic electrons exists in a different sub lattice or unit cell to the rest magnetically oriented and directed magnetic moments of other unit cells (Fiebig, et al., 2008). Examples of such materials are hematite, chromium, iron-manganese alloy, nickel oxide, etc.

Diamagnetic Materials are materials that respond by repulsion upon introduction of magnetic field. The magnetic moments align in opposite direction to magnetic field direction (Kao, 2004). Such materials are copper, silver, lead, bismuth, mercury, etc.

The ability of material to respond and retain certain quantity of magnetic field (magnetization-M) from a magnetic source of strength (H) is realised via testing its susceptibility from M-H hysteresis loop using Gouy method (Sawadh & Kulkarni, 2000) or superconducting quantum interference device (SQUID) (Reich, et al., 2006). The Hysteresis loop provides two essential parameters that characterize the material tested and they are Remanence (R) and Coercivity (H_c) (Barhoum & Garcia-Betancourt, 2018), see Figure 2-4. Remanence is the magnetization left in a material after the external field has been removed. Coercivity is a measure of the ability of

the material to withstand magnetic field without becoming demagnetized. The magnetism of a material varies with temperature; therefore, tests are carried out under varying degrees of temperatures. At some temperatures, termed the Curie temperature of a magnetic material, the magnetic property changes; like iron, magnetite becomes paramagnetic. Thus, with increased temperature, the material weakens in its magnetic susceptibility.

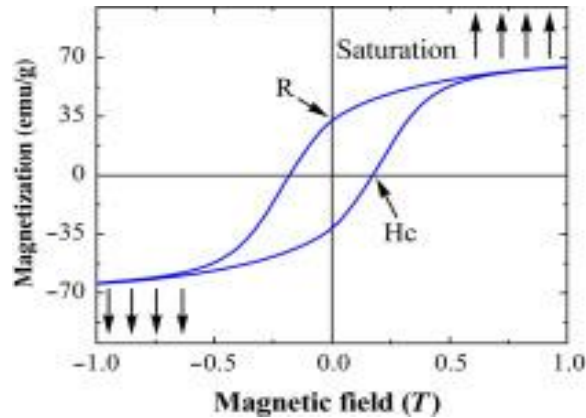


Figure 2-4 Magnetization Hysteresis loop for a ferromagnetic material; showing Remanence (R) and Coercivity (HC) curves. Courtesy (Barhoum & Garcia-Betancourt, 2018)

Despite variety of naturally existing materials exhibiting unique forms of magnetism, as well as some processed alloys, it was discovered that magnetism of materials tend to behave differently at nanoscale (Gupta, et al., 2017). This is expected, because as the size of materials get smaller, the quanta properties begin to dominate. At nanoscale, depending on nanoparticle size, they behave either paramagnetic, ferromagnetic, ferrimagnetic or diamagnetic. The coercivity is a size and shape dependent parameter that generally affects the thickness of the hysteresis loop. In ferromagnetic materials that possess multi-domains with unequal magnetization in the bulk form for example, a critical size of particle possessing a single domain yields a maximum coercivity value (where magnetization is uniformly attained within the domain at lowest free energy) (Barhoum & Garcia-Betancourt, 2018). Beyond that size, particle has more than a single domain and coercivity reduces due to energy consumed for domain wall formation; thus would require more field strength to get magnetized up to saturation levels. while further below that size, coercivity reduces down to zero value, where it becomes superparamagnetic. This is the point where

material loses its magnetism to thermal effects. Figure 2-5 provides an illustration of this.

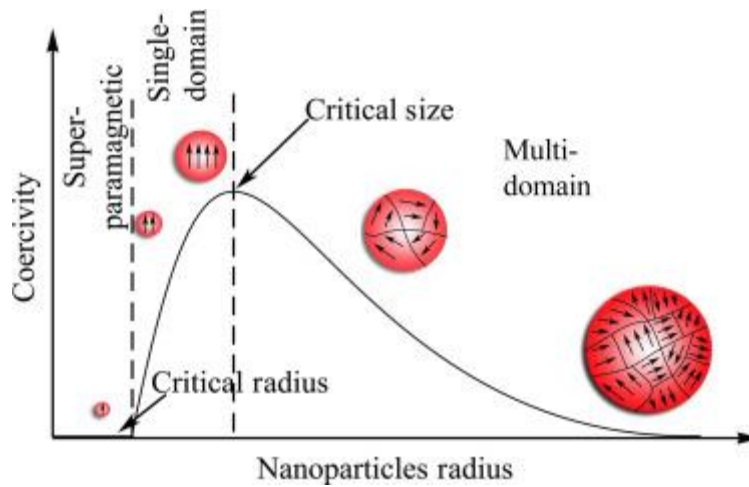


Figure 2-5 Schematic of coercivity vs particle radius. Courtesy of (Barhoum & Garcia-Betancourt, 2018).

2.6.1.1 Magnetization theory

Assume the particles to be spherical and adopting the Langevin theoretical form for paramagnetic behaviour (Bozorth, 1951), the magnetization, M_p is given as;

$$M_p = M_s \mathcal{L}(\mathcal{U}) = \phi M_d \mathcal{L}(\mathcal{U}) \quad [2-1]$$

$$\mathcal{L}(\mathcal{U}) = \text{Coth}(\mathcal{U}) - 1/\mathcal{U} \quad [2-2]$$

$$\mathcal{U} = \frac{\pi D_m^3 M_d B}{6} \quad [2-3]$$

Where, ϕ is the volume fraction of magnetic solid to carrier liquid and surfactant, B is the magnetic field strength (Tesla), M_s is the saturation magnetization of all domains which corresponds to all dipoles being aligned with the field, M_d is the domain magnetization of the bulk magnetic particle.

$$M_d = \frac{m}{V} \quad [2-4]$$

with volume V and magnetic dipole moment m .

$$V = 1/6 \pi D_m^3 \quad [2-5]$$

D_m is the diameter of magnetic particle, assumed to be spherical.

The saturation magnetization $\mu_0 M_s$ is the maximum measured magnetization at the highest applied magnetic field. For a single paramagnetic particle to successfully be activated and perhaps trap or mobilize by magnetic field is dependent on factor termed the Thermal Stability Number, Ω_{MT} . It is the dimensionless ratio between Magnetic energy and thermal energy (Nguyen, 2012). It tells if the magnetized particles orient with the magnetic field lines or randomly displaced by thermal fluctuation. It is expressed as;

$$\Omega_{MT} = \frac{U}{k_B T} \quad [2-6]$$

Since fabrication nanostructured devices with the use of nanoparticles to create patterns on substrate with nanoscale resolutions, the paramagnetic characteristic of materials is often utilized because of its flexibility and ease of control and it can be reordered; unlike most self-assembly methods where colloids become irreversibly organised within their place of target. When subjected to external magnetic field, they orient forming either dipole to dipole 1-dimensional chain like, 2-dimensional sheet like or 3-dimensional crystalline structure (Wang, et al., 2013). Several nanostructured devices have been manufactured with magnetic materials and magnetism for photonics, drug delivery, storage devices, microfluidic pumps, etc.

The translational dipole-dipole interaction of particles enables it to form high resolution patterns that is desired for creating closed packed and ordered colloidal assembly. There are theoretical models developed to account for the dipole-dipole interaction of colloids under the influence of external magnetic field. The energy of magnetic interaction between two uniformly magnetized spherical particles having magnetic moments m_1 and m_2 is;

$$E_d = -\frac{\mu_0}{4\pi} \left(\frac{3(m_1 r_w)(m_2 r_w) - r_w^2(m_1 m_2)}{r_w^5} \right) \quad [2-7]$$

μ_0 is the vacuum magnetic permeability, r_w is the distance between particles from their centres. The magnetic moment for an individual particle is;

$$m_{1or2} = \mu_0 \frac{4}{3} \pi D_m^3 \chi_i H_T \quad [2-8]$$

Where, H_T is the total applied field given as the sum of the external applied field H_e and the field from the induced magnetic moments in all the neighbouring particles in the chain. This can easily be calculated, assuming point dipoles between every particle, giving; (Leal-Calderon, et al., 1994) (Franklin, 2003);

$$H_T = H_e + H_i \quad [2-9]$$

Where H_i is obtained from deduction of the effect of demagnetization factor from external field (Franklin, 2003);

$$H_i = H_e - M_P D_{dm} \quad [2-10]$$

H_e is the actual magnetic field, given as $H_e = B/\mu_0$

The intrinsic susceptibility χ of the magnetic particle within a media from an experiment data, represents the initial slope of a magnetization curve, see Figure 2-6. It describes the magnitude of magnetic response shown by a magnetic material at low field strengths. A large value of χ corresponds to strongly magnetic material, while a small value corresponds to a weakly magnetic material. It is represented by the equation below (Franklin, 2003);

$$\chi_{iL} = \frac{M_S \mathcal{L}(0) \mu_0}{B} = \frac{M_P \mu_0}{B} \quad [2-11]$$

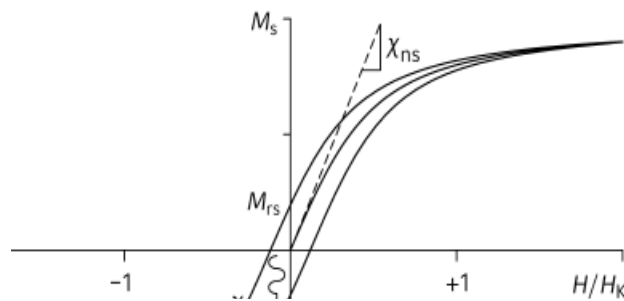


Figure 2-6 A truncated image of Hysteresis loop at 0K for non-interacting particle. The slope χ_{ns} is same as χ_{iL} , where it coincides with initial slope from $H=0$. Courtesy (Egli, 2009)

χ_i is the susceptibility of spherical particle (Maria, 2017);

$$\chi_i = \frac{\chi_{iL}}{1 + \frac{1}{3}\chi_{iL}} \quad [2-12]$$

Ferromagnetic materials are often used for magnetic self-assembled systems and iron-based materials are common and fairly cheap compared to the rest. It can be functionalised and attached to other materials to create for example polymeric spheres, silica core shell, metallic core shell, magnetic alloys, ferrofluids, wires, etc.

Ferrofluids are a unique heterogenous material that behaves like normal fluid at zero magnetic field, to appearing solid-like under magnetic field. Invented in 1963 by Steve Papell of NASA for the purpose of serving as a fuel carrier or pump under magnetic drive at zero gravity in space (Kole & Khandekar, 2021). The main purpose for its invention however was not utilized by NASA, yet found other uses, such as dynamic loud speakers, lubricant in bearings, etc (Kole & Khandekar, 2021). It is mostly made from ferromagnetic or ferrimagnetic particles being coated by surfactant bilayer where it is dispersed in carrier fluid (depending on surfactant, it can be either a hydrophobic or hydrophilic solution). The most commonly utilized form of ferrofluid for pattern control/manipulation on substrate are the hydrophobic type. Ferrofluids have been used for colloidal patterning on substrate for the transport and deposition of colloids on topographical slots of a template (He, et al., 2012). Interestingly, it has been used as an emulsion droplet for determining stearic hindering force of repulsion of surfactant between two droplets (Poulin, et al., 1997), (Leal-Calderon, et al., 1994).

In this research however, ferrofluid emulsion droplets was utilized in building chain-like or columnar clusters upon substrate to form patterned structures under the influence of magnetic field for the organisation of secondary probe (gold) nanoparticles. Compared to ferromagnetic-polymeric hard spheres that are also fairly easy to manufacture, ferrofluid stands out by;

- Ferrofluid emulsion droplet is easier to manufacture, even just by homogenization or ultrasonication, and already acts as hard sphere at zero magnetic field.

- The ferromagnetic particle within the hydrocarbon phase is paramagnetic because of its size and can easily rotate and orient due to thermal fluctuations at zero magnetic field, as well as form dipole interactions with neighbouring particles along the direction of applied magnetic field.
- The interface between droplet and continuous phase can serve as trap and carrier medium for Janus particles, to build interfacial assembly of secondary particles, thereby achieving nanoscale and macroscale resolution self-assembly structures.
- Depending on the vapor pressure of the hydrocarbon carrier, the ferrofluid can easily evaporate by tuning its environment thermodynamically to leave particles within the substrate. In most cases require lesser heat compared to hard spheres.

Based on the response and ease of control of ferrofluid droplets under magnetic field excitation, group of authors, (Mou, et al., 1994), (Lawrence, et al., 1994) carried out a study on the structure of ferrofluid emulsion under the influence of varying magnetic field strength. Using Sodium Dodecyl Sulphate (SDS) as the surfactant coating for an averagely sized 500nm ferrofluid droplets dispersed in D₂O and water. The entire solution was confined within a thin cell of varying thickness as structure formations were observed using a microscope. From their investigations, it was realised that;

- Chain droplet formation develops within a fraction of a second under a homogeneous magnetic field. Especially for cases where dipole-dipole energy is greater than thermal fluctuation energy within the system; and the ratio between both energy forms respectively is known as the coupling ratio.
- Cell thickness and volume fraction of droplets controlled the chain lengths and interaction between chains (gap between chains, chain or cluster width). Where, thicker cells and small volume fraction of droplets give single chains with droplet diameter thickness at equal repulsion distance from one another. Thinner cells and large volume fraction produce small

repulsion gap and larger column chain diameters from aggregates of existing single chains. Figure 2-7(a) and (b).

- Gradual introduction of magnetic field and finally low magnetic strength yields well distinguished columnar structures with even gaps between them. On the other hand, rapid introduction of magnetic field up to a high strength value would organise the emulsion into worm-like or Labyrinthine structures. Figure 2-7(b) and (c).

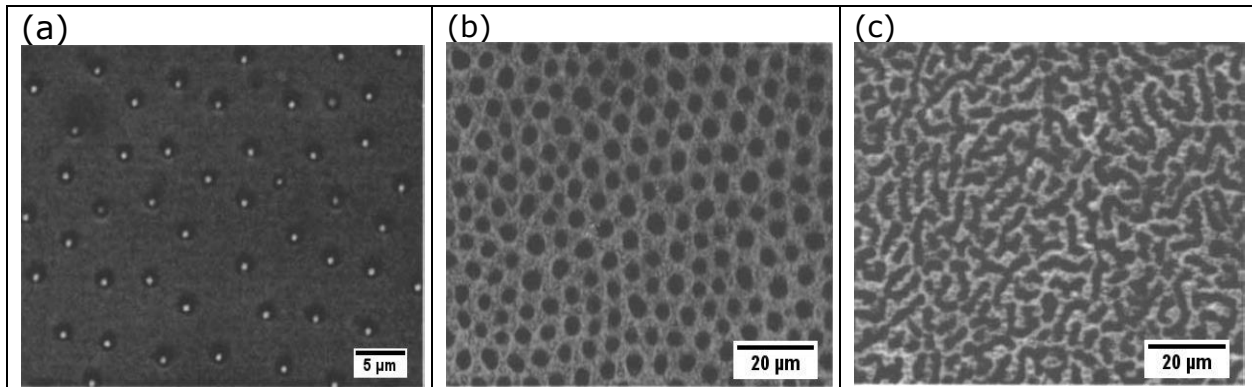


Figure 2-7 Microscope images showing; (a) cross-section of single droplet thick chain structure with volume fraction = 0.007, cell thickness = $5\mu\text{m}$, $H=31.5\text{mT}$, rate at $800\text{mT}/\text{min}$ from 0mT . (b) cross-section of column structure at volume fraction of 0.13, cell thickness = $65\mu\text{m}$, $H = 38\text{mT}$, rate at $0.01\text{mT}/\text{min}$ from 0mT . (c) cross-section of Labyrinthine structure with volume fraction 0.12, cell thickness = $50\mu\text{m}$, $H = 38\text{mT}$, rate at $240\text{mT}/\text{min}$. Courtesy of (Lawrence, et al., 1994)

As earlier highlighted, spin coating interestingly creates a thermodynamic condition that causes solvent phases to evaporate and the entire solution to dry. This is known because of the low pressures created at the surface of the substrate dependent on spin speed that pushes the pressure-temperature condition to points about the gas phase region of the compound's (solvent's) P-T curve.

2.6.1.2 Magnetic structure and electromagnetic wave diffraction detection (Light trapping)

There have been several studies on the use of magnetism and magnetic colloids for creating long range diffraction patterns (Dreyfus, et al., 2009), (He, et al., 2012), (Libaers, et al., 2009). The linear gratings formed from magnetic guided assembly are flexible and easily tuneable to achieve grating resolutions that can match variety of wave bands of the electromagnetic spectrum. An example of such approach was

carried out by He et al. (He, et al., 2012), where a monodispersed superparamagnetic Fe_3O_4 colloids was placed in a rectangular capillary cell and then subjected to magnetic field parallel to the thin section of the cell. The formation of the colloidal nanocrystal clusters (CNCs) generated colours matching sub-bands of the visible electromagnetic spectrum upon incident light at slightly deviated angles from normal; with colours ranging from blue to dark red, see Figure 2-8. The type of colour captured depends on the gap between particles which matches the wavelength of light. These gaps are controlled by the intensity of magnetic field at that region of the cell.

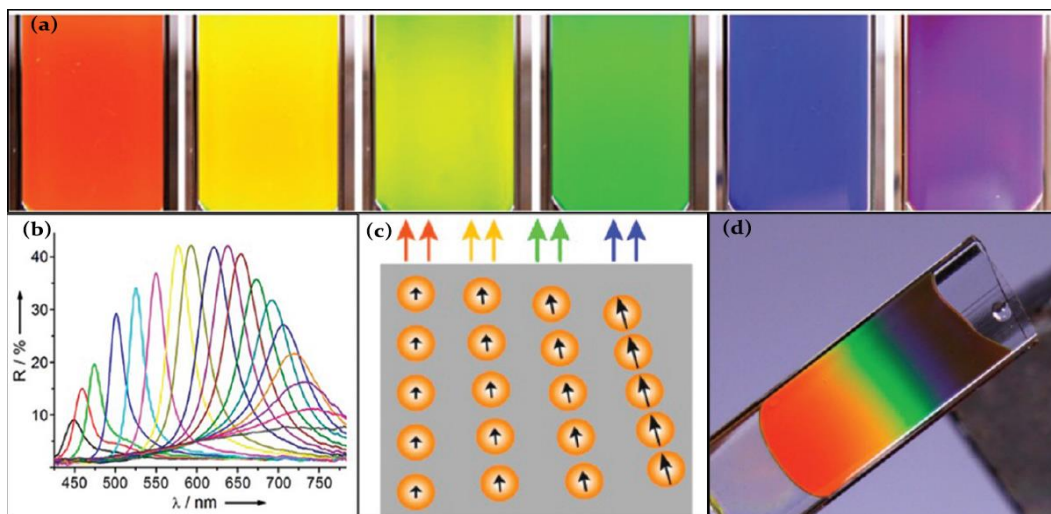


Figure 2-8 (a) Digital images showing the diffraction colour change in a typical CNC dispersion encapsulated in a capillary tube with a width of 1 cm in response to a magnetic field with increasing strength of magnetic field from left to right. (b) Reflectance spectra of the same sample in different magnetic fields. (c) is a schematic illustration of the gap between colloids upon magnetic field strengths. (d) digital photo showing a suspension of CNCs displaying rainbow-like colours due to the variance in the interparticle spacing d and the orientation θ in different regions controlled by the magnetic field. All images were extracted from (He, et al., 2012).

Studies have been undertaken to quantify the impact of magnetic field on formed chain gaps, thickness and length of magnetised colloids that influences the size and resolution of diffraction gratings through image analysis, (Zhu, et al., 2021), (Soni & Desai, 2022). Zhu and co. (Zhu, et al., 2021) carried out image analysis on series of captured magnetised colloidal formations whereby depending on the concentration and size of colloids in solution subjected to a selected magnetic field strength, the chain length varies. From their report, chain length tends to be longer when the colloids are bigger in diameter, while as it grows to be longer with increase in

magnetic field strength, at some point it begins to reduce and the chain thickness increases. The reason is because individual colloids become more responsive to magnetic force more than the dipole-force of interaction, thereby creating zip-like colloidal interactions. An example of such outcome is shown as Figure 2-9.

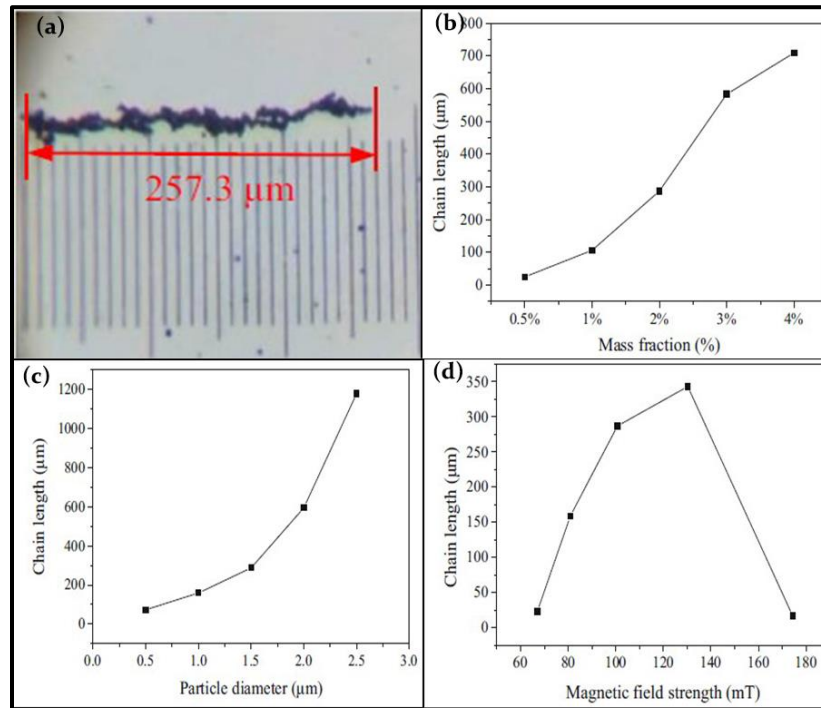


Figure 2-9 (a) the length of magnetic particle (MP) chain with a diameter of $2 \mu\text{m}$ is $257.3 \mu\text{m}$, (b) Effect of mass fraction of MPs on the chain length when the magnetic field strength is 100.77mT and the particle diameter d is $1.5 \mu\text{m}$, (c) Effect of particle diameter on the chain length when the mass fraction is 2% and the magnetic field strength is 100.77 mT , (d) Effect of magnetic field strength on the chain length when the mass fraction is 2% and the diameter of MPs d is $1.5 \mu\text{m}$. Images are extract from (Zhu, et al., 2021).

The image analysis carried out by Soni and Desai worked on the concept of pixel identification based on the dimensions of structures. Images of sample structures were taken with a brightfield inverted microscope and were processed by setting pixel intensity threshold to map out regions of the magnetized colloidal structures. The obtained pixel data of mapped region were then converted to readable dimensions following the set global scale. From their investigation, they realised large chains contribute to structure formation, while short chains under high magnetic field strength hindered light transmission.

Based on the formation of linear patterns formed by magnetised colloids, the role of potentially formed gratings diffract light in a way similar to that of polarizers. The incident light waves come in longitudinal and transverse forms of propagation; if the alignment of colloidal particles along the magnetic field lines where they are in perpendicular direction to the propagation of incident light, the outcome is a transverse field optical transmittance wave. While, if the magnetic field directed particles align parallel to the incident light would yield a longitudinal optical transmittance wave of propagation (Li, et al., 2008) (Helseth, 2009) (Pu, et al., 2009). It is therefore clear to say that the dominant wave of propagation through a magnetically aligned colloidal system is dependent on the direction of alignment, direction of incident light and magnetic field strength. The setups used by the above-mentioned investigators were based on transmission of propagated waves with polarizers placed before the and after the samples respectively and the intensities difference between input and output light were used as indicators.

2.6.2 Spin Coating Mechanism

It is a method that spreads and make thin films in the order of micrometres and nanometres through centrifugal force. Emslie and Co. (Emslie, et al., 1958) were the first to analyse and model the spreading of a Newtonian fluid on a planar substrate rotating with constant angular velocity. The centrifugal force drives the fluid radially outwards, as the viscous force and surface tension between the substrate and liquid causes a thin residual film to be left over the substrate. (Lawrence & Zhou, 1991). Emslie and Co. assumed a Newtonian behaviour of fluids, which applied a linear relationship between shear stress and shear rate. However other influential conditions such as gravitational gradients, viscosity, temporal variations in concentrations, vertical diffusivity were all neglected in the model. Several improved models have been devised incorporating the neglected conditions. However, the selection is dependent on the components used for the process.

$$h = k\omega^\vartheta \quad [2-13]$$

where h is the film thickness, ω is angular velocity in radians/sec, k and ϑ are empirical constants. The constants are dependent on various parameters, especially with the physical properties of the polymer, polymer substrate interaction and

rheological properties. From experiments, several authors (Bornside, et al., 1987), (Daughton & Givens, 1982), (Lai, 1979), (Meyerhofer, 1978) have observed the exponent, ν , to be approximately 0.5. Evaporation of solvents also occur due to the low pressures at the surface of the spinning material would lead to further decrease in film thickness (Lawrence, 1988).

Ignoring evaporation term, the basic physics were first worked by Emslie et al (Emslie, et al., 1958). Equating the viscous and centrifugal forces per unit volume gives

$$-\eta \frac{\partial^2 v_f}{\partial z^2} = \rho \omega^2 r \quad [2-14]$$

Where, η is the viscosity, r is radial velocity at any point (r, θ, z), v_f is the fluid velocity

$$\omega = \frac{\pi}{30} W_{rev} \quad [2-15]$$

W_{rev} is the rotation speed in rev/min

Integrating with boundary conditions that $v = 0$ at the substrate surface of $z = 0$, and that $dv/dz = 0$ at the free surface where there cannot be a shearing force given;

$$v_f = \frac{\rho}{\eta} \left(-\frac{1}{2} \omega^2 r z^2 + \omega^2 r h z \right) \quad [2-16]$$

h is the film thickness. r and h can be determined after time, t , of spinning from initial condition of liquid placement; h_0, r_0 .

$$h = \frac{h_0}{(1+4Kh_0^2t)^{0.5}} \quad [2-17]$$

$$r = \sqrt{\frac{r_0^2 h_0}{h}} = r_0(1 + 4Kh_0^2t)^{0.25} \quad [2-18]$$

$$K = \rho\omega^2/\eta \quad [2-19]$$

2.7 Optical Behaviour of Materials selected for nanofabrication

In this research the materials selected were Fe₃O₄ in ferrofluid and gold nanoparticles to study the impact of heterostructure on plasmonic behaviour on analytes. The interface between ferrofluid and aqueous liquid were used for orientating gold nanoparticles in the form of pickering emulsion, as already described in section 2.4.1. Therefore, the magnetic ordering of the pickering droplets would offer a new dynamism to the optical response of the structure. The next few paragraphs in this section provides insight into electromagnetic interaction with particles and their behaviour within a structure.

The efficient utilization of incident electromagnetic waves (particularly light) on a material structure is a crucial aspect for photo-conversion processes. Natural materials that respond to incident electromagnetic radiations by its electrons moving from ground state to a higher energy state; generating holes and electrons in the case for semiconductors and high energy (hot) electrons for plasmonic metals (Haug & Schmitt-Rink, 1984) (Berger, et al., 2005) (Tisdale, et al., 2010) (Liu, et al., 2018). Several materials have energy band levels that have to be attained before being excited, and this has to be surpassed by the energy of the incident electromagnetic wave (i.e., its frequency) (Lehman & Ziesche, 1990) (Lässer, et al., 1981) (Fritzsche, 1971) (Moss, 1967). This is one reason why different photo responsive materials get excited at different optical wavelengths. For example, TiO₂ (rutile) absorption band peak at 329nm with its band gap at 3.75 eV, NiO absorption peak is at 334nm, and band gap at 3.75 eV, just to mention a few (Strehlow & Cook, 1973). The rate of electron excitement and mobilization within a material is dependent on density of photon interaction with the material molecules. Although generated electrons can get hindered or limited through collisions with holes (for semiconductors/metal oxides) or other electrons (for plasmonic materials) (Zhu, 1994) (Powell, 1976) (Dubi &

Sivan, 2019). This situation affects the efficiency of the photo-excitation within a material. There are several routes on controlling such behaviour, particularly for semiconductors and metal oxides, but the three main ones are; (i) nano-scaling of material (Tsendzughul & Ogwu, 2020) (Nair, et al., 2018) (Kamat, 1993), (ii) coupling with a more efficient photo-responsive material (Imtiaz, et al., 2019) (Fu, et al., 2019) (Zong & Wang, 2014), and (iii) host medium structure (Pylarinou, et al., 2021) (Guo, et al., 2017) (Zhang & John, 2021).

Nano scaling of materials, according to the British Standard Institution (BSI), is the manipulation and control of matter (or materials) on the nanoscale dimension by using scientific knowledge of various industrial and biomedical applications which generally lies in the range of 1-100 nanometres (Kearns, 2010) (Whitesides, et al., 2005). Materials within this scale are for short, termed Nanomaterials, and they exhibit enhanced properties such as electrical, optical, magnetic and chemical in comparison to their bulk counterparts (Tronc, 1996) (Wang, et al., 2003). Two key reasons responsible are; (a) the large surface area per volume ratio of material which makes them more chemically reactive through high activity of electrons which interact and transfer energy across surfaces easily because of lesser collisions (Zhang, et al., 2013) (Li & Wang, 2020) (Wang, et al., 2003). (b) the quantum effect dominates the behaviour of materials at the lower end of the nanoscale where the optical, magnetic and electric behaviours are affected (Khan, et al., 2019) (Beger, 2016) (Kumar & Kumbhat, 2016). For example, the control of conductance on charge transport through two-terminal molecular junctions of a conducting material (Guédon, et al., 2012).

Coupling with a more photo-responsive material is a technique that has hugely being practised for years to step up efficiency factor of primary material. This stimulation can occur in several ways; (i) excitation of primary element from the radiation of the secondary element: which means to say that upon excitation of the secondary material by the incident photons, their radiative decay release photons in either a higher frequency (up-conversion) or lower frequency (down-conversion) that matches the excitation frequency of the primary material it is coupled with, followed with local increase in photon density per contact area (Liu, et al., 2022) (Kumar, et

al., 2022) (Yu, et al., 2022) (Richards, et al., 2012). (ii) filling the conduction band of the primary material with the migrated electrons of a photo-excited secondary material (Humayun, et al., 2018). This mechanism occurs for metal-semiconductor pair in the form of hot electrons diffusing through an established Schottky barrier at the interface into the conduction band of the semiconductor (Hwang, et al., 2007). It also occurs for semiconductor-semiconductor pair, where the electrons of a photoexcited secondary semiconductor diffuses from its conduction band into the conduction band of the primary semiconductor, with generated holes taking the opposite route (Humayun, et al., 2018). This process stimulates the photo-absorption of the primary material, even in response to low photon densities.

Host medium structure contributes by manipulating propagation of photons about the material of interest. Structure types like opals, inverse opals lattice, and linear gratings do take advantage of optical phenomena like Whispering gallery mode, coherent and incoherent scattering of light leading to random walk of photons across the structure (Pham, et al., 2020) (Zhang & John, 2020) (Grandidier, et al., 2011) (Wang & Qi, 2019). The scientific explanation to this involves the trapping and time elongation of photons of a particular wavelength within a structure so as to increase overall density of photons per material surface area (Wang & Qi, 2019). This happens to counter the fast quenching of electrons from collisions or fast recombination of holes and electrons in a way that it increases rate of photon interaction and thus photo-excitation beyond its quenching or recombination rate (Fallah, et al., 2019) (Dotan, et al., 2013).

In recent times, researchers have been combining these three routes to elevate the efficiency of final product (Valenti, et al., 2016). However, such combinations would depend on the application requirement, availability and cost of materials, type of fabrication technique and its associated cost. In this research, consideration is given to iron oxide-gold dimer nanostructures, so as to study the impact of host medium structure on optical response of the dimer heterostructure.

Iron oxide nanoparticles growingly plays a vital in the field of optics because of its unique ability to become electrically active when illuminated with light. UV-Vis spectroscopy studies on this material shows it has an absorption peak at

approximately 380nm with a long gradual declining tail down to 1100 nm (Horia, et al., 2020). It has fairly low band gap of (3.01 eV for magnetite, 2.2eV for Hematite) for generating electron and holes upon photo excitation, its abundance in nature, and ease in processing makes it an attractive material for applications such as water splitting, catalysis, etc (Radoń, et al., 2017) (Gilbert, et al., 2009) (Gurudayal, et al., 2018) (Vallabani & Singh, 2018). However, the quantum efficiency of iron oxide for photo-conversion tends to be low due to rapid recombination of the few quantities of photo-generated holes and electrons, and low mobility of holes (Korobchevskaya, et al., 2011). The timescale for this decay according to timescale absorption studies falls within 200 femtoseconds (Uemura, et al., 2022). This makes iron oxide a poor conductive material with poor photocurrent efficiencies (Anderman & Kennedy, 1988) (Alexandrov & Mott, 1996) (Iordanova, et al., 2005). Based on this challenge, iron oxide is often paired with a more photo-excited material to enhance its charge generation. For example, with dyes, other metal oxides and plasmonic metals (Gurudayal, et al., 2018) (Gilbert, et al., 2013).

Gold nanoparticles on the other hand, is a resonant dielectric material known for its optical sensitivity and electromagnetic response under the visible light spectrum (Pluchery, 2012), (Amendola, et al., 2017), (Scarabelli, 2018). Its electrons from the conduction band are excited by photons of a particular range of visible light spectrum where they tend to oscillate at the material's surface. This excited cloud of electrons is termed surface plasmon polaritons (SPP) (Pluchery, 2012), (Liu, et al., 2018). The plasmon oscillation generates an electric field with range of around 300nm from the interface between metal and a dielectric medium, that exponentially decays in intensity with distance from the particle's surface (Homola, et al., 1999). When considering gold nanoparticle size that is way smaller than its excitation wavelength of light, the plasmon resonance phenomenon still holds. Based on this, the material is known for breaking the diffraction limit of light, as it is able to locally enhance the optical intensity within that size scale by several orders of magnitude ($10^4 - 10^6$), such phenomenon is termed - Localised surface plasmon resonance (LSPR). (Russier-Antoine, et al., 2014), (Cheng, et al., 2016), (Bryche, et al., 2016). A limitation with gold nanoparticles involves the fast deactivation and limited electron mean free path as a result of electron scattering (Ye, et al., 2018) (Kreibig & Frangstein, 1969).

However, the high density of hot electrons enables it to remain an highly efficient conducting material.

The unique property of plasmonic nanoparticles described in the previous paragraph is an essential building block for the development of optical metamaterials (Choi, et al., 2011), (Lee, 2015), (Chen, et al., 2020). An essential contribution of metamaterials is to increase the refractive index of the system to an unnaturally high level over a large frequency range that results in broadband slow light (light trapping) (Lu, et al., 2015). The structural organisation and high-resolution patterning of gold colloids is beneficial in enhancing the property of the material through collective energy contribution from individual colloids (Koenderink, 2009), (Schulz, et al., 2020). For example, gold nanoparticle aggregates that are set in either 1D, 2D or 3D arrays, yield an enhanced local electromagnetic field that is beyond trillions of fold in magnitude (Alaeian & Dionne, 2012), (Kravetz, et al., 2018). The magnitude is directly dependent on size and shape of nanoparticles, and gap between them; as these would control both polarization and magnetization at the optical domain (Lee, 2015). Also, the long-range organisation of plasmonic nanoparticles in ordered arrays enables far-field coupling of both local plasmon and scattered light from the diffraction modes of arrays. Therefore, this new type of system is defined as Lattice Plasmon Resonance (LPR) or surface lattice resonance (SLR) - (Scarabelli, et al., 2021). Such system offers flexibility as it can be fine-tuned to improve on both its near field and far-field effects. Structurally, near-field has to do with the control of size, shape and cluster density of particles per unit section within the array, while the far field contribution relies on the array size, gap and length across substrate holding clusters of nanoparticles (Huang, et al., 2007). The array resolution acts as a form of grating with periods comparable to the wavelength of the incident electromagnetic waves, where under appropriate conditions the scattered fields correspond to diffraction of the incident electromagnetic waves in the plane of the array (Wang, et al., 2011) (Kasani, et al., 2019). The array formation of metamaterial assembly can act as wave guide which generally increases the pathlength of photons (Huang & El-Sayed, 2010), (Chen, et al., 2018), (Linic, et al., 2011). This is possible because the scattered fields can act to counter the damping of the single particle response (Deng, et al., 2020). Thus, by appropriate tuning of the array period one can significantly

increase the quality factor of the resonance; which is theoretically defined as the ratio between the resonance wavelength, and the width of the resonance (Molet, et al., 2021), (Kravetz, et al., 2018), (Koenderink, 2009).

2.7.1 Iron oxide-Gold dimer nano-heterostructures

2.7.1.1 Plasmonic effect

The pairing of gold and iron oxide to form heterodimer structures is a technique that have been researched in areas like catalysis (Lee, et al., 2010) (Lin & Doong, 2011) (Wu, et al., 2009), Multimodal contrast imaging (Zhu, et al., 2014) (Cai, et al., 2012), hyperthermia treatment (Hedayatnasab, et al., 2020), drug delivery (Estelrich, et al., 2015), etc. The interfacial interaction between this pair is unique, whereby excited electrons from gold nanoparticle tend to diffuse from its Fermi level to the conduction band of the iron oxide causing charge accumulation at the defect states of the interface (George, et al., 2011) (Comin, et al., 2012). As earlier highlighted, such physical process causes iron oxide to be more photo-receptive, which lead to an increase in its electron-hole generation, even surpassing its recombination (Comin, et al., 2012) (Korobchevskaya, et al., 2011). Thus, making the iron oxide material behave as an electron reservoir.

There have been several ways of synthetically designing this dimer heterostructures, which can be chemically and/or thermally prepared into alloys, core shell, dumbbell, or randomly mixed nanoparticles cluster structures. Such synthesis are well detailed in these review papers; (Tarkistani, et al., 2021) (Liu, et al., 2018) (Nguyen, et al., 2018). When UV-Vis absorption test is conducted on this heterodimer structure, the concentration ratio and particle configuration determine the profile of its absorption spectra. The iron oxide-core-gold-shell nanostructures for example show a redshifted, reduced peak and broadened gold plasmon resonance absorption band from a conventional gold resonance of $\sim 520\text{nm}$ (see Figure 2-10). The degree of shift depends on the thickness of the gold shell; where a thinner shell leads to farther red-shift in plasmon resonance than a thicker shell. The reason for the shift is as a result of electron deficiency at the gold nanoparticle surface because of its migration toward the dimer structure interface. This led to an overall increase in absorption across the spectra. Two sets of investigators realised something quite different from absorption

spectra of dimer heterostructures. The first group (Dahal & Chikan, 2008) prepared the structures in a bimetallic alloy form through thermal process, where it gave a bimodal absorption peak at 395nm and 670nm (see Figure 2-11). The other group (Thimsen, et al., 2011) prepared a cluster mixture of gold nanoparticles overlain with iron-oxide nanoparticles (they termed “Embedded” configuration) yielded a bimodal peak spectrum at 400nm and 690nm. This is a massive red-shift of plasmon resonance of gold (i.e., approximately 130nm shift) and a distinct absorption peak of iron-oxide at ~400nm.

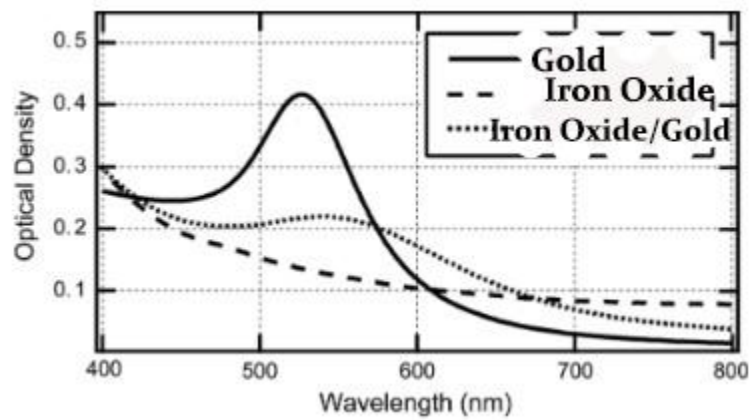


Figure 2-10 UV-Vis absorption spectra of Iron Oxide, Gold and dimer heterostructure of combined iron oxide and gold. Courtesy (Korobchevskaya, et al., 2011)

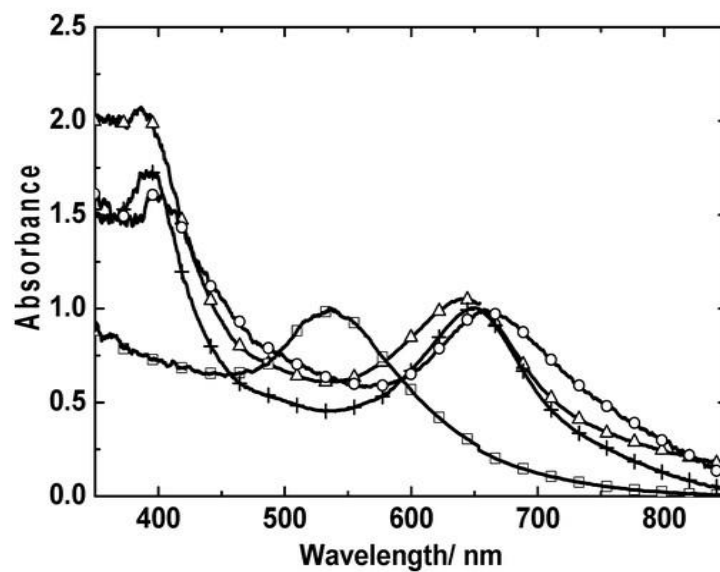


Figure 2-11 UV-visible absorption spectra (in water) for pure gold and iron-gold alloy nanoparticles synthesized from FeO precursor with various molar ratios. The molar ratios of iron and gold are 1:1, 1:2, and 1:3, indicated by circle, cross, and triangle, respectively. Courtesy (Dahal & Chikan, 2008)

As earlier highlighted regarding the cause for the redshift of gold plasmon resonance, this shows a highly electron deficient gold with its electrons diffusing towards multiple interfacial contact with iron oxide. For short, more iron oxide nanoparticles/atoms contacting the surface of a single gold nanoparticle led to realisation of such bimodal spectra. This deemed to be consistent with an investigation carried out by (George, et al., 2011) comparing a spherical and rod-like iron oxide dimer structures with gold nanoparticles. They realised not only just a faster dynamics of charge mobilization but also a fast trapping of hot electrons from gold at the numerous defect states at the interface. Another addition to this, is with increase in gold concentration per unit concentration of iron oxide, leads to blue-shifted plasmon resonance absorption band from the 690nm, followed by a decrease in absorption intensity for iron-oxide at 400nm.

After careful observation from these journals, it was realised that; (i) on achieving mid-visible absorption with a broad significant plasmon resonance of gold, the concentration of gold needs to be higher than iron oxide with minimal contact and majority of its surface exposed to radiation. (ii) on achieving low frequency UV (395nm) and near infra-red (690nm) bimodal bands, the gold concentrations need to be less than iron oxide, followed by multiple and dense interfacial contact, as both materials surfaces are exposed to photo-radiation. noble metals. (iii) A Q-factor on the order of 10 is typical of Au and Ag nanostructures in the visible–near-infrared spectral range³⁷, while the Q-factor of ferromagnetic nano-antennas in the same spectral range is on the order of 3–4, depending on the material, shape, and size of the nanoantenna^{6,7}. Higher Q-factor values, approaching that of noble metals, can be obtained using multi-layered ferromagnetic/noble metal nano-antennas. In summary, the design of heterostructures, concentration ratio and configuration allow for the tunability of local field energy and intensity.

2.7.1.2 Magneto-Plasmonic effect

The iron-oxide is known to possess magneto-optical (MO) activity, arising from spin-orbit coupling of the electrons, which results in a weak magnetic-field-induced intensity and polarization modulation of reflected (Kerr-effect) and transmitted

(Faraday-effect) light (Višňovský, et al., 2001) (Argyres, 1955). Conventionally, optical electric field enhancement is achieved on iron oxide via induced localized plasmon excitations as a result of pairing with plasmonic materials. A different dynamics take hold upon introduction of magnetic field; where in the first part, the application of an external magnetic field H induces a net magnetization M in the iron-oxide that turns on the MO activity in the material. In the other part, the Localized plasmon resonance (LPR) drives a second, MO-induced Localized Plasmon Resonance in a direction orthogonal to both M and the LPR. The radiation re-emitted by this second MO-induced LPR (MO-LPR) becomes polarized in a direction perpendicular to that of the incident radiation and determines the magnetic-induced polarization change, known as the Kerr effect (López-Ortega, et al., 2020). This phenomenon behaviour is often tested using either the Kerr effect or Faraday effect spectroscopies (Chen, et al., 1997) (Qiu & Bader, 1995). Recent experiments and theoretical investigations of the MO Kerr effect in variety of systems made of heterodimer or MO nanostructures, have shown how the excitation of a LPR can act upon the phase of the reflected light which can be used to tune the light polarization through the manufacturing of the nanostructures dimension and shape as seen in 2D flat-optics nanodevices, such as rotators, modulators, and isolators and very small refractive index changes in label-free biosensing applications (Maccaferri, et al., 2014) (Liu, et al., 2009).

On considering practical applications, the organisation of the dimer nanostructures into arrays or lattice structures would contribute to its long-range effect, just as described for gold colloids. The combination of near field and far-field effects, is also deemed to increase the overall performance of the system. This goal makes long-range ordering through nanofabrication highly essential.

2.8 Potential Application of Designed structures

It is expected that the resolution of the thin film thickness will likely be less than 500 nm with a much larger surface plane coverage. Due to this design, consideration was given to potential areas of application;

- I. The involvement of plasmonic nanostructures have been extensively used for two types of sensors (Li & Cullum, 2005): Surface plasmon sensors (SPS) and

Surface Enhanced Raman Spectroscopy (SERS) sensors. In SPS, the plasmon resonance is sensitive to changes in environmental refractive index induced by adsorption or binding of foreign molecules on the plasmonic material surface. This results in a change in the plasmon resonance frequency, which can be used to generate calibration curves for sensing applications. SERS sensors on the other hand, operate by plasmonic amplification of Raman signals. Raman scattering is the result of inelastic light scattering and is used to detect vibrational and rotational properties of a molecule. (Hazle, et al., 1990), (Kasani, et al., 2019).

- II. The role of particles as light nano-sources for optical imaging is also a non-invasive diagnostic method (Xiao & Yeung, 2014) (Peng, et al., 2015) (Zhang, et al., 2011). It is said to emit enough transparent light to be able to cross body tissues, with wavelengths ranging in the body spectral window, typically in the NIR region. Plasmonic NPs, like gold NPs, exhibit strong unique and tuneable optical properties within the visible to NIR spectral region, and can play the role of nano-sources (Choi, et al., 2011). Besides, gold is characterized by a high atomic number, and thus, a high electronic density, making these NPs also suitable to be used in dark field microscopy (DFM), optical coherence tomography (OCT), computed tomography (CT) and photoacoustic (PA) imaging (Nguyen, et al., 2018).

2.9 Characterization methods

2.9.1 Structure Test and Performance

This stage involves tests carried out to study the impact of preparation variability on final structure of a design and the responsive behaviour of its patterned nanostructure.

2.9.1.1 Microscope-assisted UV-Vis Spectrophotometry

This is a non-intrusive optical method in determining the optical behaviour in terms of absorption or reflection of a material's long-range lattice structure. This is used to understand the effect of pattern/cluster on photo-absorption of material (Liu, et al., 2014). A reflection mode setup allows the incident light to interact with particles from the surface with charges diffusing through the structure formations. Studies have

been conducted on both a 10 nm size single gold nanoparticle and aggregated 2D film structure with degree of gap separation (Minati, et al., 2015). It was realised from their investigation that with smaller gaps in between, the higher the plasmon coupling between particles which resulted in a broad plasmon band with maximum absorption at ~700 nm; in comparison to 520 nm plasmon resonance band for single gold particle. Another technique used was different sizes of gold nanodot arrays prepared by direct contact printing method deposited on an indium Tin oxide substrate (Kim, et al., 2014). The UV-vis absorption spectra revealed redshift in plasmon band peaks and broadening of band width as the nanodot sizes increased. These examples are indications of expectancy of changes in absorption band in response to structure colloid concentration and dimensional gap between colloids.

2.9.1.2 Specular reflectance Fourier transform infra-red (SR-FTIR) for Surface enhanced infra-red spectroscopy (SIRS)

Just like conventional Fourier Transform spectroscopy, the beam is incident on a material at certain angles to provide vibrational analysis of the top few nanometres of the surface of the material (Pepper, 1995). Group of investigators (Maß, et al., 2019) used a test sample (mercaptohexadecanoic acid-MHDA) coated over gold grating strips having different widths and grating periods. They realised that with changing strip width sizes at constant grating periods, the ratio between two CH₂ (asymmetric and symmetric) vibrational bands of MHDA changed in absorption intensity. A similar investigation was carried out on PMMA molecules where its excitation was enhanced in the presence of gold grating period (Wang, et al., 2013). They realized that grating period that matched the vibrational frequency of the analyte gave the highest absorption in overall reflectance intensity and signal enhancement factor. What was observed from both studies was that apart from the local enhancement created by gold strips, the pattern dimensions influenced a particular group of vibrational bands close to the grating diffraction size. This is a concept that would be adopted for the long-range structure SR-FTIR analysis.

2.9.1.3 Surface Enhanced Raman spectroscopy (SERS)

Fundamentally, Raman spectroscopy is based on the interaction between incident electromagnetic field and probe material that results in inelastic scattering of light. This scattered light come in 3 parts (Akanny, et al., 2021) (Majee & Mishra, 2021);

- a) Rayleigh scattering. The oscillation frequency of this scattered light is the same as that of the incident radiation. They do not contain any information on the probed material.
- b) The second is termed Stokes scattering. This frequency of this scattered light oscillates at a lesser frequency than that of incident radiation. This scattered light provides information on the probed material.
- c) The final part is the anti-Stokes scattering. This scattered radiation oscillates at a higher frequency than the probing light frequency. This contains information on the population of thermally excited vibrational states.

Surface enhanced Raman spectroscopy (SERS) involves the use of a metallic or semiconducting surface to enhance incident light interaction with analyte materials so as to amplify signal. The electromagnetic enhancements are made possible through the excitation of localized surface plasmon resonance (LSPR) modes in metal substrates (Brown, et al., 2007), as well as charge transfer from a semiconducting surface to molecules (Campion & Kambhampati, 1998).

This equipment setup is used to observe spectral response of nanostructured materials in the form of inelastic scattering of photons from the material so as to identify Raman spectral shift of material components of interest. The amplification of signal resulting from a metallic or semiconducting surface on enhancing energy interaction with analyte materials within a structure leads to the system definition of Surface enhanced Raman spectroscopy (SERS). The electromagnetic enhancement is made possible through the excitation of localized surface plasmon resonance (LSPR) modes in metal substrates (Brown, et al., 2007), as well as charge transfer from a semiconducting surface to molecules (Campion & Kambhampati, 1998). The use of Fe₃O₄-Au dimer system as probe nanoparticles for SERS applications have been growing interest because of its tunability and reusability. The use of just gold nanoparticles can offer enhancement factors as high as 10⁷. Fe₃O₄-Au on the other

hand can offer twice as much (Wheeler, et al., 2012). Another contribution is the gap control between probing particles. Referring to the work by (Wheeler, et al., 2012), a magnetic field was used to increase the degree of agglomeration of Fe₃O₄-Au core-shell dimer structure which helped by narrowing the gap between particles. This led to a red shift of surface plasmon of gold and subsequently to an overall broadband absorption spectrum which enhanced the signal by 14 times the factor of 10⁶. Aside the technique mentioned previously, the micro-arrays setup for SERS application have been gaining attention of several researchers (Chen, et al., 2008) (Duan, et al., 2020). The arrays of Fe₃O₄-Au nanoparticles for example, help in providing reproducible signals in SERS measurements (Ye, et al., 2015). In general, the Fe₃O₄-Au nanoparticle improves the spectrum range of the material as well as its plasmonic enhancement which improves SERS signals when compared to just gold nanoparticles. The aggregate of nanoparticles enhances the SERS signal further, while the array arrangement of the clusters provides consistency and reproducibility of signals.

2.9.1.4 Magneto – Surface Enhanced Raman Spectroscopy (SERS)

The application of a magnetic field in SERS is an effective way to manipulate the plasmon electrons through Lorentz force in the intermediate state of the Raman process; which results in the manipulation of the Raman molecular vibration intensity (Silenko, et al., 2017) (Grillo, et al., 2017). There have been several studies conducted that show the Raman intensity of materials using this method. Like in the case of MoS₂ monolayer, bilayer and bulk mode subjected to magnetic field perpendicular to its surface (Ji, et al., 2016) leading to fine-tuning of intensity by the magnetic field. This magneto-optical effect stems from a magnetic-field-induced symmetry breaking for the electron motion in the inelastic Raman scattering process (Chuntonov & Haran, 2013).

2.9.1.5 Optical and Electron Microscopies

Microscopes are used to observe tiny particles under high resolution. Optical microscopes utilize visible light and sets of magnification lenses to observe objects down to approx. 400nm which is the threshold of visible light lowest wavelength. The images can be captured using a CCD or CMOS camera. Optical microscopy offers a

range of observation methods, such as; Dark-field, Phase contrast, Confocal (Liu, et al., 2014). The darkfield microscopy was utilized in this research and it creates an enhanced contrast by superposition of shining specimen on dark background (Liu, et al., 2014).

The use of electrons instead of light substantially improves the resolution of nano-patterns, especially when other factors such as the diameter of the light spot and the contrast of the sample, reduce the optical resolution. Thus, structures of a few nm can be distinguished using this method, known as scanning electron microscopy (SEM). Which has a factor ~ 100 better compared to ordinary light microscopy. In electron microscopies, a beam of electrons are directed from a tungsten filament source through magnetic coils onto or through a specimen, which is then picked by the detector/monitor by reflection from specimen (Scanning electron microscope) or behind the specimen (Transmission electron microscope). Surface pattern of structure can be observed at resolutions as high as 10nm using the SEM, while for resolutions as low as 1nm, TEM can be used to study the morphology, configuration of atoms within a certain metallic particle.

Overall images from these sets of microscopies can be further analysed using image analysis software like image J® to process the data from being just qualitative to quantitative report. The scaled image would assist in obtaining dimensionality of structures that can be used for qualitative comparison with other data, like absorption spectroscopy. This data would help in confirming relationships and impact of structure patterning resolution on optical behaviour of particles within a defined long-range structure. Image analysis of magnetically ordered iron oxide structure have been carried out by several investigators who derived their algorithm for image processing and structure size quantification (Soni & Desai, 2022) (Domínguez-García, et al., 2018). A common processing step carried out by both sets of investigators was to convert images to a binary format (8 bit), giving you a black and white distinct contrast for easy profiling and generating 2-point pixel values. This makes it easy for the software to automatically measure those boundary points and to finally provide measured values with respect to the set scale dimension. However, more technical steps were taken in their respective software algorithm. Dimensions achieved by Soni

and Desai (Soni & Desai, 2022) were chain length and chain width. Thus, in this research, chain length, width and gap between chains would be estimated. In addition, darkfield images give a fairly contrast image (black and white), especially when the source of illumination is an led white light. This would likely make image processing easier.

2.10 Chapter Summary

This chapter began with nanofabrication methods, covering its essence, classes, and categories (top-down, bottom-up and self-assembly approaches). The conversation was then stepped down into self-assembly approach focusing on physical phenomenon contributing to the formation and organisation of colloids into lattice structures, as well as techniques like fluidic, interfacial, thermal, electrical, magnetic, optical and acoustic methods for organising colloids. Attention was then directed at fluidic methods and the various types which were briefly discussed. Amongst the discussed, spin coating method was the preferred technique because it was classified as one of the quickest and cheapest means of organizing colloids. Given the reasons stated above, spin coating was adopted in this project, which further made it a necessity to briefly highlight series of self-assembly coupling methods, such as; (a) spin-coating and lithographic template, (b) spin coating and electrical method, and (c) spin coating and magnetic methods. Spin-coating and magnetic coupling self-assembly method is overall the main nanofabrication interest in this project because both techniques combined are cheap, non-intrusive, quick, and flexible. This combination was previously tested by Gonzalez-Vinaz and co., as their approach were presented and discussed, showing the technical difference between theirs and this project. Beyond this major objective, it was essential to discuss on the two main key mechanisms of this process – (a) Magnetism and magnetic materials, and (b) the basics of Spin coating, which were all presented. It was essential to justify this fabrication approach and pattern through the basics on the behaviour of photo-responsive nanostructured materials by incorporating a probe material - gold (a plasmonic noble metal). It has been investigated and published across multiple journals, the crucial and effective periodic organisation of gold nanoparticles that would phenomenally lead to enhancement of electromagnetic field energy within the material. Rendering it applicable as a surface plasmon sensors. Heterodimer structure

of gold and iron oxide was also presented, explaining the optical phenomenon as a result of their combination. This chapter was finally capped off with brief highlights on tests necessary for the characterization of constituents and overall structures in this project.

Chapter 3 Preparation of Gold Pickering Ferrofluid Emulsion

3.1 Chapter Objective

In this chapter, list of basic materials, synthesis and processing steps are designed and executed for the manufacturing of gold pickering-ferrofluid emulsion for thin film nano and sub-micron structures production. Synthesis and production of Fe_3O_4 nanoparticles from iron powder, the surface modification, stabilization and dispersion of Fe_3O_4 in cis-Cyclooctene to form ferrofluid. Next, the preparation of Gold-methacrylate nanoparticles by chemical reduction and seeding from gold III chloride as conventionally carried out using Turkevich approach. In order to render the produced gold nanoparticle to be both oil and water wettable, its surface requires partial capping with Polyethylene glycol 40 stearate an interfacial stabilizer. The fastest way to create a sub-micron sized emulsion is via ultrasonication. This is the first time this technique will be used to create sub-micron gold pickering ferrofluid emulsion, as different from the microfluidic technique used by Sachdev and co (Sachdev, et al., 2017). It is known, ultrasonicated emulsions are usually random in size distribution with a large degree of polydispersity. A way of mitigating this is (for the first time also) by centrifugal segregation which is employed to segregate bigger droplets from smaller ones because the density of ferrofluid is more than the dispersing phase (water). The analysis on required spin speeds and time frame required to attaining a particular size range being the dominant extracted for further processing is vital. The last dispersing phase (aqueous polyvinyl alcohol) provides emulsion stability and useful during the magnetic-spin coating process because it creates Laplace pressures which further safeguards pickering droplets from coalescing. Series of characterization tests such as pH, zeta potential, zeta sizing, contact angle, UV-Vis spectroscopy, Transmission electron microscopy, magnetic hysteresis, Thermal Gravimetric analysis and Fourier transform infra-red spectroscopy will be carried out to characterize the products after each synthesis step.

3.2 Fabrication components properties tests

Conventionally, self-assembly approach in building nanostructured materials require series of synthesis across stages of manufacturing, thus making testing of material components at each stage crucial to achieving target structure and overall material quality.

pH – This test is useful in identifying excess ionic charge within the solution during synthesis in order to maintain colloidal stability of the system. It also helps to determine if most or all of excess charged ions are removed after rinsing.

Zeta potential – This test is essential in determining surface charge of a particle or nanostructure after series of synthesis as it helps to identify if complex systems are stable or unstable (Mourdikoudis, et al., 2018). The zeta potential have been used to identify the degree of ligand interaction or surface coating of nanoparticles by adsorbed surfactants, which alter the nanoparticle surface charge density, and its hydrophilic-lipophilic balance (or three phase contact angle) through covalent surface modification, (Pilapil, et al., 2016), (Boakye-Ansah, et al., 2020), (Wong, et al., 2021). For example, the reduction in surface charge of a citrate-based gold nanoparticle using electrically neutral PEG capping agent which consist of polymeric layers supports nanoparticle assembling at the liquid-liquid interface, (Wang, et al., 2020), (Kelly, et al., 2003) .

Zeta sizing (Dynamic light Scattering- DLS) – This test helps in determining size of synthesised nanoparticle or complex structure within a carrier like water or solvents with known refractive index, viscosity and dielectric constant. It is useful in identifying effective synthetic method in controlling size distribution. It works in measuring the light scattering as a function of time combined with Stokes-Einstein assumption which is used to determine the hydrodynamic diameter of the nanoparticle that is under Brownian motion within the solvent (Kato, 2012).

Contact angle measurements – It is used to determine degree of wettability between a substrate and coating solution. This helps in knowing the degree of surface modification required to either increase wettability or reduce it. Contact angle is

measured in degrees with angles greater than 90° shows wet favourable and angles less are of course less wettable.

Fourier transform infra-red (FTIR) spectroscopy – a technique where electromagnetic wave within the infra-red region excites IR responsive molecules within a material causing it to vibrate, stretch or rotate in order to determine the molecular configuration in terms of bonds, types of molecules and compounds. It is helpful during the synthesis process to determine the degree of material modification and to ensure bonds between materials are established (Blanco-Andujar, 2014).

UV-vis absorption spectroscopy – This is an optical test carried out to determine the wavelength of light the particle absorbs, and also qualitatively estimate size, shape, concentration and degree of agglomerate/aggregates within optically responsive particles (Haiss, et al., 2007).

Transmission electron microscopy – This is a system where uniform current density of electron beam is used to observe the morphology and atomic configuration of nanoparticles within a thin sample, where resolutions approach 1 nm (Reimer & Kohl, 2009). This can be used to estimate the actual size of nanoparticles with dense coating that might have been overestimated by DLS. Since DLS depends on Brownian motion (speed) of particle within the liquid (Mourdikoudis, et al., 2018).

Thermal Gravimetric Analysis – This is a test that involves determining the percentage mass of coating material around a particle; especially when the material is organic in nature and the particle metallic. The reason for this is because the equipment operates by heating the sample to burn off the coating material while simultaneously measuring the mass (Green, 2014).

Magnetic Hysteresis measurement – This is a measurement carried out to determine the magnetic nature and capacity of a material or structure using either the Gouy device or SQUID (Blanco-Andujar, 2014).

3.3 Materials

All chemical purchases were made from Sigma Aldrich.

Iron powder (fine), Cis-Cyclooctene ($[\text{CH}_2]_6[\text{CH}]_2$, Mw 110.2 g/mol), Hydrochloric acid (HCl, 37%), Nitric acid (HNO_3 , 65%), Ammonium Hydroxide (NH_4OH , 30% Ammonia in water), Poly Vinyl Alcohol – PVA – 88% hydrolyzed (Mw 88000 g/mol), Oleic acid ($\text{C}_{18}\text{H}_{34}\text{O}_2$, Mw 282.46 g/mol), Gold (III) chloride (AuCl_3 , 30 wt. % in dilute HCl – Mw 339.79 g/mol), Sodium methacrylate ($\text{C}_4\text{H}_5\text{NaO}_2$, Mw 108.07 g/mol), Isopropanol ($\text{C}_3\text{H}_8\text{O}$, 70%), Polyethylene Glycol 40 Stearate (PEG 40S, Mw 328.53 g/mol), Deionized water (H_2O , 18.2 M Ω -cm resistivity)

3.4 Processing Methods

This sub-section describes manufacturing process for magnetite nanoparticles and ferrofluid, gold nanoparticles, pickering emulsion and aqueous Polyvinyl-alcohol. Prior to any process, glass wares were treated with piranha solution containing 30 ml of Sulfuric acid and 10ml hydrogen peroxide to remove unwanted impurities. It was then rinsed several times with deionized water and oven dried using a Gallenkamp hotbox oven at 50 °C. The Figure below (Fig 3.1) provides schematics of the manufacturing process to aid visualization. Table below (**Table 3-1**) presents acronyms of stage products during synthesis process for easy referral.

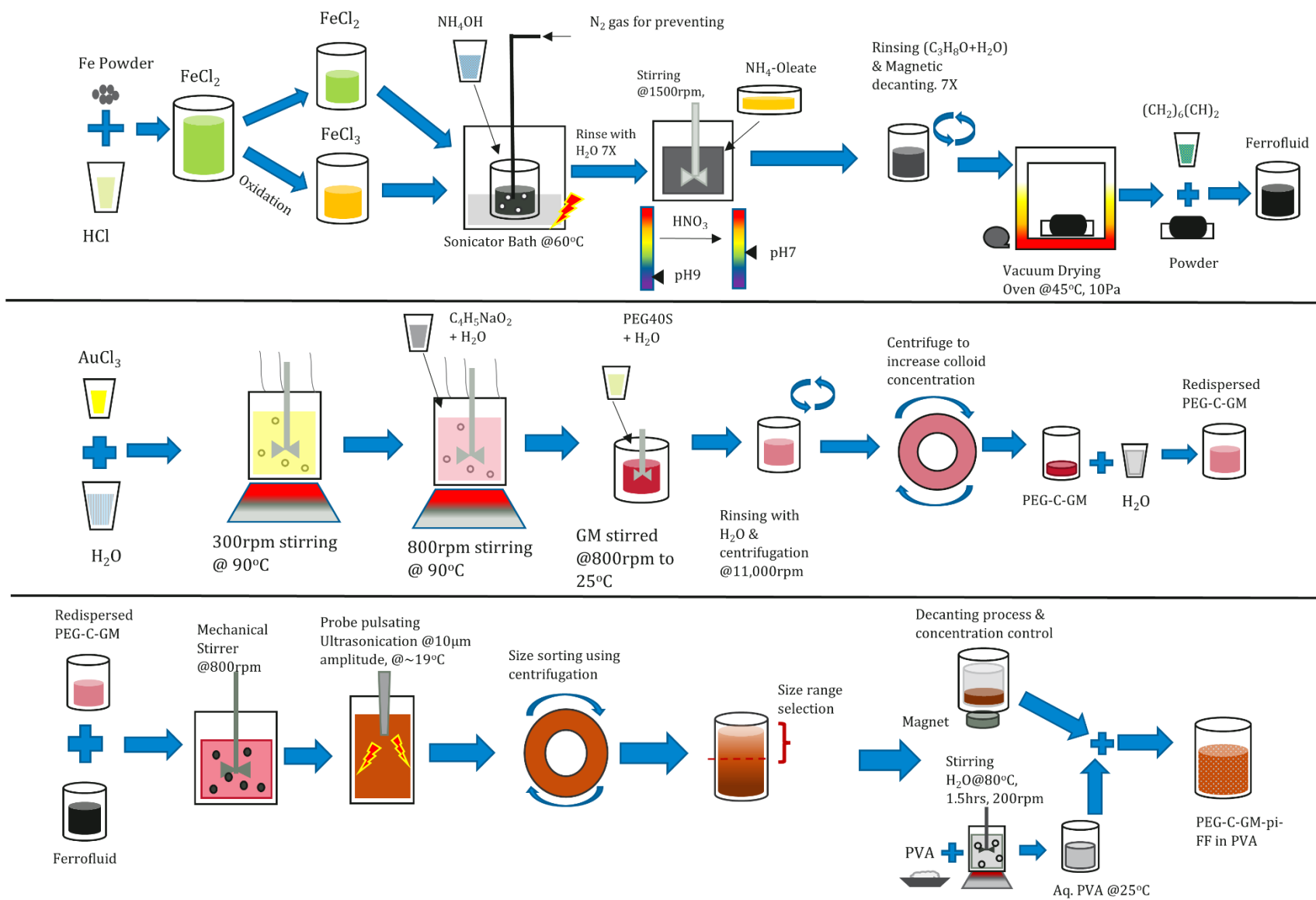


Figure 3-1: Schematic of manufacturing process of colloids and PEG-C-GM-pi-FF emulsion

Table 3-1: Synthesis products representative format.

Full name	Acronym	Full name	Acronym
Magnetite	Fe ₃ O ₄	PEG40S capped Gold Methacrylate	PEG-C-GM
Oleic coated magnetite	OCM	Gold Methacrylate Pickering Ferrofluid	GM-pi-FF
Gold Methacrylate	GM		
Ferrofluid	FF		

3.4.1 Ferrofluid Preparation

20g of iron powder was dissolved in a solution of 100ml deionized water 18.2 MΩ-cm resistivity and 100ml of Hydrochloric acid that formed iron (II) chloride (FeCl₂). The solution was split into two and one of them was oxidized to iron (III) chloride (FeCl₃) after exposure to air/oxygen for 48 hours. Both solutions were sieved through using glass fibre filter to remove undissolved solids. On observing guidelines from other processes described elsewhere (Lai, et al., 2017), (Rosensweig, 1985) and (Patricia, et al., 1999), 2ml of Iron (II) chloride and 2.5ml iron (III) chloride were added into a 100ml of deionized water in a beaker being agitated in an ultrasonicator bath operating at 40kHz frequency at 60°C. The solution was purged with nitrogen gas to prevent oxidation of iron (II) chloride by air. About 60ml of Ammonium Hydroxide (NH₄OH) was then added drop-wise into the solution for about 20 mins that resulted in a change of the solution pH from ~2 to ~9. This subsequently led a colour change of the solution from orange to brown, and then finally black indicating complete formation of magnetite (Fe₃O₄) nanoparticles. The first prepared batch of Fe₃O₄ nanoparticles was separated by magnetic sedimentation (using permanent magnets) as liquid was removed. This method of separation was repeated several times (7 times) while washing with deionized water to remove excess ammonium salts, and afterwards separated nanoparticles were dried and stored for characterization.



In the other series of batches while the pH of solution was at 9, ammonium-Oleate (NH_4 -Oleate) soap was made by mixing 10 ml of Ammonium Hydroxide and 15g of Oleic acid in 20ml of deionized water (Roe, et al., 1949). 8g of the paste was then added into the magnetite suspension, and stirred using a rotor stator for 25 mins at 1500rpm. 8ml of excess ammonia was added within 1 min during the stirring process. 10ml of Nitric acid was then added dropwise to form salts with excess ammonium ions and reduce the pH to 7. During this process, ionic exchange took place where NH_4^+ reacted with the NO_3^- to form ammonium nitrate salt, while the oleic ions interact with the Fe_3O_4 nanoparticles to establish layers of coating for stability. The prepared coated Fe_3O_4 nanoparticles were then precipitated and rinsed several times with isopropanol ($\text{C}_3\text{H}_8\text{O}$) and deionized water to remove excess ammonia and ammonium salts, and then allowed to dry in vacuum oven at 45°C , 10 Pa for 24 hrs. Since the process was repeated in batches, 1g of oleic acid coated iron oxide (Fe_3O_4) was separated for characterisation and 5g was dispersed in 7ml of Cis-Cyclooctene [$(\text{CH}_2)_6(\text{CH})_2$] to create the oil-based ferrofluid.

3.4.2 Gold Methacrylate Preparation

Gold methacrylate was prepared following the process; 0.0196g of Gold (III) Chloride was diluted in 5ml of deionized water. 0.407g of Sodium methacrylate dissolved in 20ml of water was prepared. The diluted Gold (III) Chloride was poured into a 100ml of deionized water boiling at 90°C while being stirred using a magnetic stirrer (Hussain, et al., 2003). 12 ml of dissolved sodium methacrylate was added at once into the boiling solution. The mole ratio between gold ions and methacrylate ions is 1:39. The process was then observed for 15 mins as the solution turned from transparent to a red-wine colour (see Figure 3-3 b) of dispersed colloids. This meant that the free excess acrylic ions established hydrophobic interactions/network with the acrylic ions attached to the gold, to create a double layer/charge that promoted repulsion and stability of the colloids within the solution (Hussain, et al., 2003). After cooling to room temperature (21°C), $20\mu\text{g/ml}$ of PEG 40S solution was added to the gold colloid and allowed to mix in a 200ml beaker sealed with aluminium foil while using a magnetic stirrer at 500rpm for 6 hours. This was to establish a layer of coating by hydrophobic interaction, thereby making the particle dispersible in water even

after modifying the pH (Deng, et al., 2012) (Escudero, et al., 2017). The PEG-capped gold Methacrylate (PEG-C-GM) nanoparticles were then separated from solution using a Eppendorf® centrifuge 5418 at 11000rpm and were rinsed with deionized water. This was repeated four times to remove sodium salts and excess PEG molecules. The final treated particles were left in 15ml of deionized water until further use. The concentration of the particles in water at this stage was 4.2 ± 0.2 mg/L, the zeta potential and particle sizes for both PEG capped and uncapped are shown in Figure 3-6 and Figure 3-5 respectively. The TEM image of PEG-Methacrylate capped gold (PEG-C-GM) nanoparticle is shown in Figure 3-8 (b & c).

3.4.3 Preparation of PEG-C-M Pickering Ferrofluid Emulsion

4mL of gold methacrylate colloid solution was dispersed in 20 mL of deionized water and sonicated using sonicator bath for 5 mins. 70 μ L of ferrofluid was dispersed in the solution by stirring at 800 rpm using a rotor stator for 8 minutes to create micron sized droplets ($\sim 400\mu$ m diameter). Then the pickering emulsion was formed using a probe type MSE® Soniprep 150 ultrasonicator, operated at 10 μ m probe amplitude displacement, with a frequency of 20 kHz for 10 minutes, and a pulsation of 10 seconds on, 3 seconds off. The system was kept cool ($\sim 19^\circ\text{C} \pm 2^\circ\text{C}$) by inserting it into a temperature regulating jacket. The pickering emulsion size was tested using Malvern zeta sizer, and the average droplet size was 450 ± 300 nm, see Figure 3-17. 2 mL solution was extracted and weighed initially, giving about 3.8 mg. It was left in a chamber for water molecules to evaporate and was then weighed afterwards, where it weighed 2.9 mg. This helped in determining the concentration to be dispersed in the polymer.

Six more batches were prepared following the same procedure. 15ml of emulsion solution was poured into 20ml each of the 6 centrifugal tubes and was centrifuged using an unbranded device at a predetermined speed of 1000 rpm for 10 mins to reduce degree of polydispersity. Prior to the selection of the speed and time process for size control, series of speed and time tests were conducted and size distribution map plotted as shown in the results and analysis (Section 3.6). The concentration of droplets was increased by placing a 2 Tesla magnet beneath the beaker containing the centrifuged emulsion solution, while the partially clear water was carefully

decanted. The new mixture was termed Polyethylene glycol coated gold methacrylate Pickering ferrofluid (PEG-C-GM-pi-FF). A 4mL portion of the concentrated sample was exposed at ambient conditions for water to evaporate leaving an approximate dried mass of 6.4g

At the same time 5wt.%, 3.3 wt.%, 1.7 wt.%, and 1.3 wt.% of aqueous Polyvinyl alcohol (PVA) was prepared by adding PVA powder into DI water and stirred at 200 rpm for 10 minutes using a magnetic stirrer (Bunn, 1948), (Byron & Dalby, 1987), (Lo, et al., 2017) (Kozlov, 2004). The solution was then heated up to 80°C for 1.5 hours to finally obtain a clear viscous liquid. The liquid was allowed to cool down and then stored in a capped 500ml bottle.

5 mL of concentrated Pickering emulsion was then added into 10 mL of aqueous solution of PVA and stirred at 400 rpm for 1 hour using a rotor mixer.

3.4.4 Substrate Preparation

A plane microscopic glass slides (1237-3118) from Fisher, is 0.8-1.0mm thick, a refractive index of 1.5171, density of 2.479, strain point at 513°C and softening point at 720°C. These were conventional (standard) properties of microscopic slides, following documentations for light microscope accessories by Agar Scientific (AgarScientific, 2010).

Silicon wafer was purchased from Pi-Kem, and it possesses properties such as; *crystal growth*-float zone, *grade* - prime or optical, *diameter* - 4", *type* - p-type, *dopant* - boron, *orientation* - 110, *resistivity* - 10,000 ohm-cm, *thickness* - 525 μm , *surface* - double side polished, *roughness* - <2 Angstroms, *Flatness (TTV)* - <1 μm . These were according to Pi-kem web documentations (Pi-Kem, 2019).

These substrates were firstl cleaned to remove particle debris on the surface with 20 weight percent of Isopropanol in water, and then dried in an oven at 60°C for one hour, especially for the glass slide. The effect of this treatment was tested using contact angle measurement.

3.5 Material Characterisation

3.5.1 UV-Vis Measurement

This is a non-intrusive method in determining the optical response of a processed material. Using the Perkin Elmer Lambda 850 spectrophotometer, OCM, GM, PEG-C-GM and PEG-C-GM-pi-FF were scanned at a rate of 1nm per second with a spectral bandwidth of 0.1nm. Before each sample run, a blank scan (from 350nm – 900nm) of the pure carrier fluid (water in the case of GM, PEG-C-GM, PEG-C-GM-pi-FF, and cis-Cyclooctene for the OCM) were carried out. This is so that the carrier fluid spectra would not contribute to the actual analyte spectra.

3.5.1.1 Oleic coated magnetite

The vacuum-oven dried OCM, Figure 3-2(a) was broken down and dispersed in Cis-Cyclooctene, to form ferrofluid, shown in Figure 3-2(b). The UV-Vis spectrum of a 5uL ferrofluid redispersed in 20 ml of Cis-Cyclooctene was obtained. The resulting spectrum in Figure 3-2(c) matches the spectrum obtained from other findings (Liu, et al., 2010).

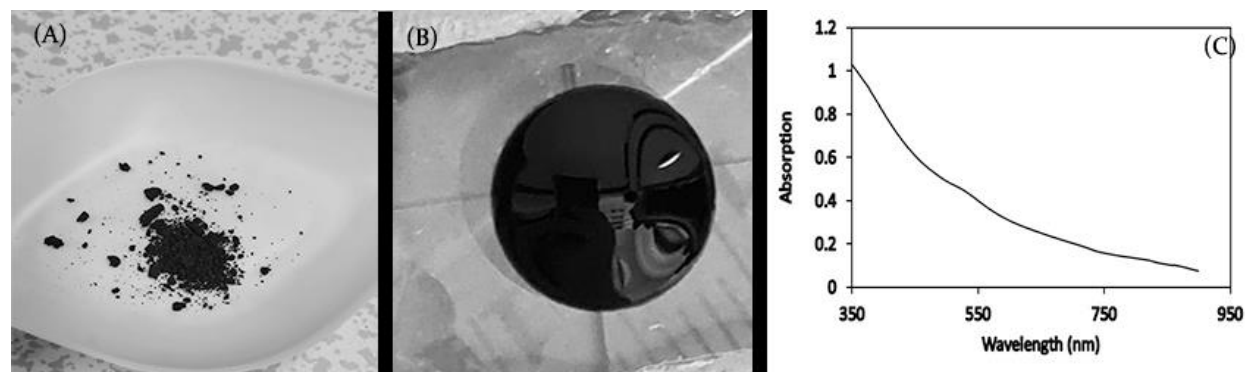


Figure 3-2 (a) is the dried oleic coated magnetite (OCM) after oven drying, (b) is a drop of dispersed OCM in cis-Cyclooctene, (c) is the UV-vis spectra of dilute (0.07g/ml) concentration of OCM in cis-Cyclooctene.

3.5.1.2 Gold Nanoparticle

UV-Vis spectrum was acquired for both freshly prepared GM and PEG-C-GM. As shown in Figure 3-3(c), surface plasmon for both sets of colloids was evident at peak 528nm, which matches with previous observation (Hussain, et al., 2003). Hussain et al. observed the peak at 524nm for the gold acrylate colloid containing similar

components. As seen in the Figure 3-3 (a), the prepared GM colloids showed a typical red colour of gold as observed in other works (Hussain, et al., 2003) (Frens, 1973). The methacrylate ion adsorbed on the gold nanoparticles maintain the charge around the particles through hydrophobic-tail interaction as shown in schematic in Figure 3-3(b) and prevent the flocculation.

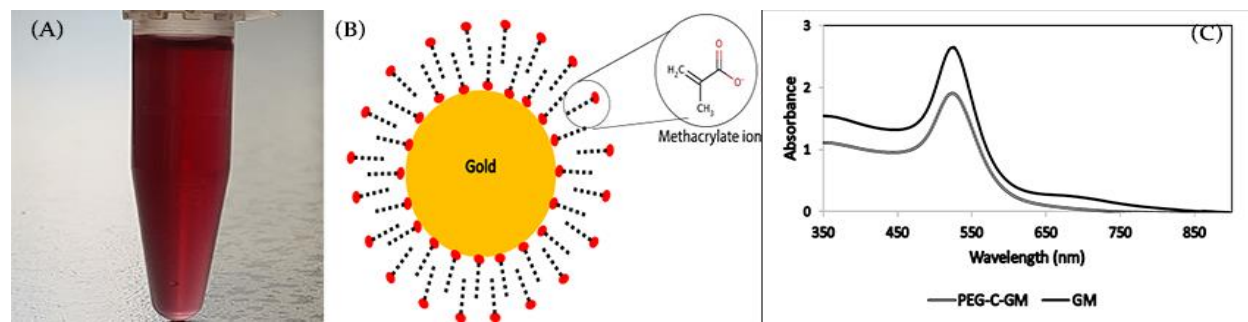


Figure 3-3(a) Red colour colloidal solution of gold methacrylate in water, (b) a schematic of gold methacrylate nanoparticle within the solution shown in (a), (c) is a UV-Vis absorption data of gold methacrylate (GM) and PEG coated Gold methacrylate (PEG-C-GM) showing plasmon resonance at peak point 528nm.

3.5.1.3 Pickering Emulsion

PEG-C-GM-pi-FF emulsion was left to settle in a vial for several minutes after ultrasonication, with Figure 3-4(a) showing the prepared the solution which appeared peach in colour. UV-vis test was carried out to observe the absorption spectra of PEG-C-GM-pi-FF emulsion, where Figure 3-4(b) shows the UV-Vis spectra. The spectra indicate a broad absorption spectrum between 515nm to 610nm. It is similar in terms of attaching gold nanoparticles to an iron oxide particle core as presented in a previous work (Reguera, et al., 2016), (Nguyen, et al., 2018). It could be possible that the FF droplet surface in PEG-C-GM was not fully covered by gold nanoparticles, as a signature wavelength peak for iron oxide was observed.

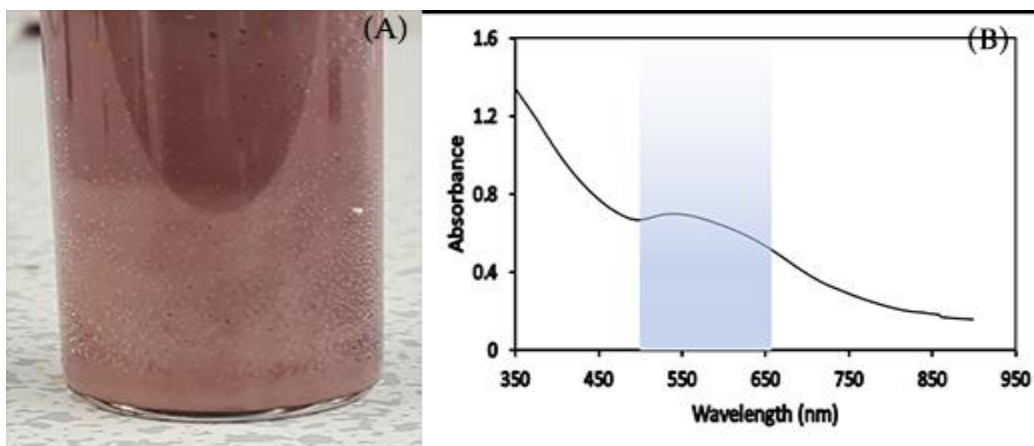


Figure 3-4(a) Image of peach coloured pickering emulsion in a vial, (b) UV-Vis absorption spectra of pickering emulsion with gold nanoparticle (PEG-C-GM) showing broad plasmon between 515-650nm

3.5.2 DLS Size Measurement, Zeta sizing.

This Dynamic light scattering system (DLS) operates by measuring the light scattering as a function of time combined with Stokes-Einstein assumption which is used to determine the hydrodynamic diameter of the nanoparticle that is under Brownian motion within the solvent (Kato, 2012). Although this technique was not perfect in determining the size of coated particles, therefore requiring other methods for cross-validation. DLS measurements were conducted with a Zetasizer Nano ZS instrument from Malvern at a fixed angle of 173° (backscattering detection) with a He-Ne laser ($\lambda = 633 \text{ nm}$; 4 mW) and digital autocorrelator. The mean particle size was determined by a number plot

A 5 μL of prepared GM (prior to addition of PEG 40S) was dispersed in 10ml of deionized water. Out of 10 ml, the 3ml of solution was poured into a PMMA cuvette and placed into the Malvern zeta sizer Nano zs using DLS mode for scanning at 20°C operating temperature. The scanner was set to 14 runs per scan and reported value by taking cumulative average of the three scans, as it was repeated for the PEG-C-GM suspension. 2ml of GM and PEG-C-GM colloids were laid side by side to dry, and Figure 3-5(a) shows a comparison of dried nanoparticles. The dark lattice film represented the GM agglomerated nanoparticles, while the purple lattice showed for PEG-C-GM nanoparticles. The GM appeared blackish due to high hydrophobic interaction amongst acrylic molecules of particles leading to agglomeration as in the

case experienced in gold acrylate investigation by Hussain and co. (Hussain, et al., 2003). The PEG created a coating layer for GM nanoparticles, keeping them preserved from agglomeration and from irreversible dispersion. This have been witnessed in gold colloid system under colorimetric studies (Li & Rothberg, 2004) where colloid colour changed from red to purple and cetyltrimethylammonium bromide gold surface coating (Li, et al., 2020) colour change from red to dark blue. Size distribution of GM and OEG-C-GM measured with zeta sizer is shown in Figure 3-5(b). The average hydrodynamic size of particles for gold methacrylate was 18.63nm with standard deviation of 3.91, while PEG-C-GM gave a mean diameter of 28.8nm with standard deviation of 7.4. This meant that the PEG 40S created a coating layer of approximately 5nm. The dynamic light scattering (DLS) results were cross-checked with results from TEM analysis of particles in section 3.5.5.

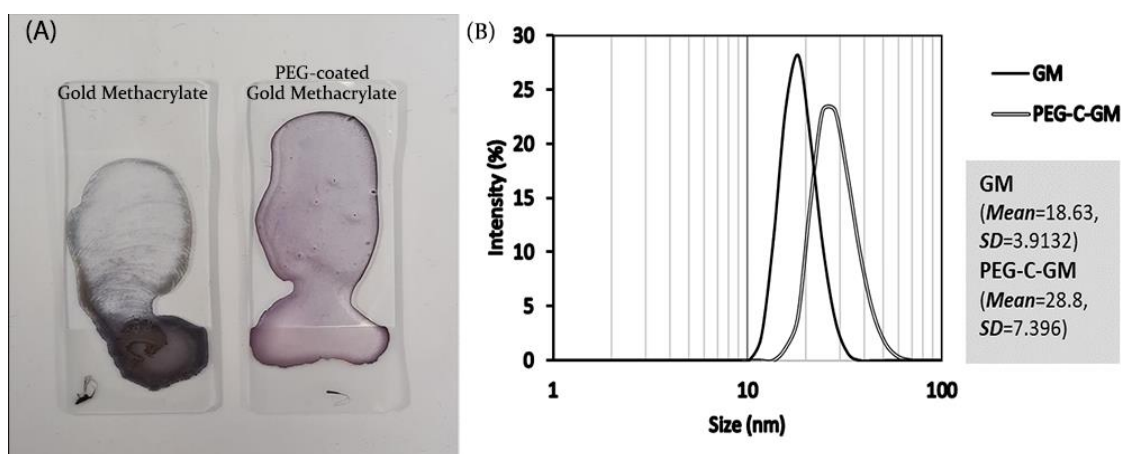


Figure 3-5 (a) An image showing dried lattices of gold methacrylate (Black) and PEG coated gold methacrylate (Purple) on microscopic slides. (b) Size distribution measurement results of GM and PEG-C-GM colloids in a semi log graph.

3.5.3 Zeta Potential

This test helped in determining the charge on particle surface, and how well each stage of synthesis affected the integrity of the nanoparticles. It also helped in identifying if complex systems were stable or unstable (Mourdikoudis, et al., 2018). Measurements were conducted with a Zetasizer Nano ZS instrument from Malvern. Zeta potential is the electrokinetic potential in colloidal suspension. It is the electric

potential at the slipping plane located at interface of surrounding bulk (mobile) fluid and stationary fluid adsorbed to the surface of the particle.

Zeta potential measurement were conducted for PEG-C-GM-pi-FF in DI water that was injected into Malvern ® DTS1070 disposable cuvettes. 12 Zeta runs at 21°C operating temperature was the setting and the concentration of samples tested are as follows;

- $1.12 \pm 0.1 \mu\text{g/L}$ of GM in DI water
- $1.5 \pm 0.2 \mu\text{g/L}$ of PEG-C-GM in DI water
- 5 μL of PEG-C-GM-pi-FF was diluted in 10ml of water
- Aqueous PVA was further diluted to 0.01wt.% in water
- 0.2mg of Ferrofluid ultrasonicated in 20ml of 1.7wt.% aqueous PVA. 10 μL of emulsion diluted in 25ml of water.
- DI water used as base test liquid.

The Zeta potential results are shown in Figure 3-6. The overlaying of the free attached carboxylic acid led to an increased electronegative charge about each gold nanoparticle set at a high value of -29.8mV, with pH at 5.6 (Hussain, et al., 2003). However, the PEG 40s coating reduced the charge due to its zwitterionic nature. The gold pickering ferrofluid emulsion showed a lower electronegativity, which could be as a result of decrease of surface exposure gold nanoparticles sitting at the liquid interface or insufficient amount of PEG-C-GM around the droplet. Aqueous PVA showed low electronegativity making it suitable to work with the pickering emulsion, as two electronegative charges repel, thereby eliminating the possibility of chemical bonds/linkages formed that might distort formation of droplets dipole-dipole chains upon introduction of external magnetic field.

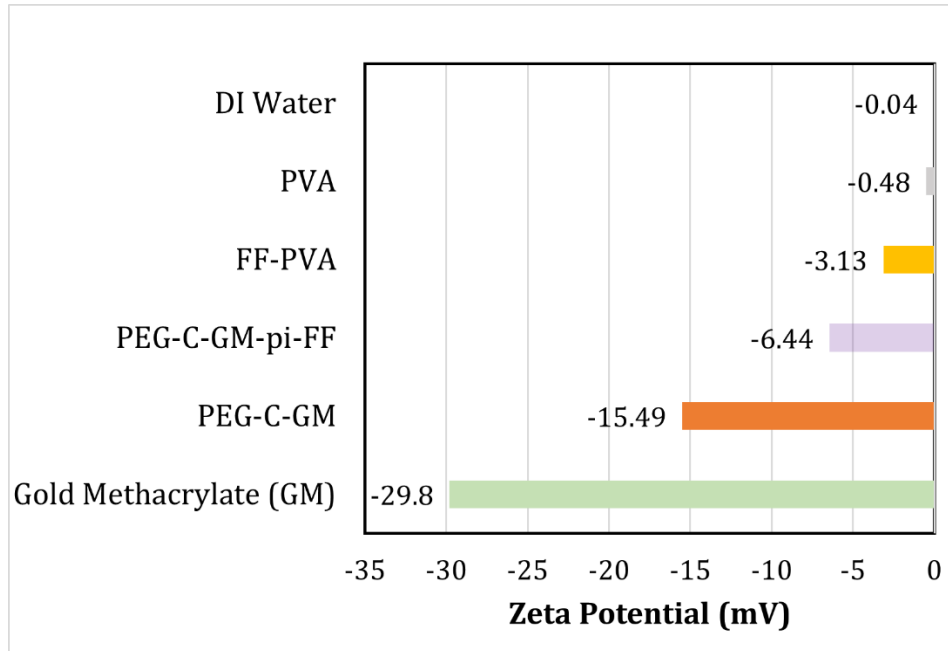


Figure 3-6 Presentation of Zeta potential peak values of varying particle systems

3.5.4 Magnetic Hysteresis

This was a measurement carried out to determine the magnetic nature and capacity of a material or structure using a Superconducting quantum interference device (SQUID) (Blanco-Andujar, 2014). A magnetometer device that measures extremely subtle magnetic fields as low as 5×10^{-14} Tesla. 1g each of the samples were tested at 300K. The test generated M-H (magnetic moment vs magnetic field) curves shown in Figure 3-7(a) for both Fe_3O_4 particles and OCM.

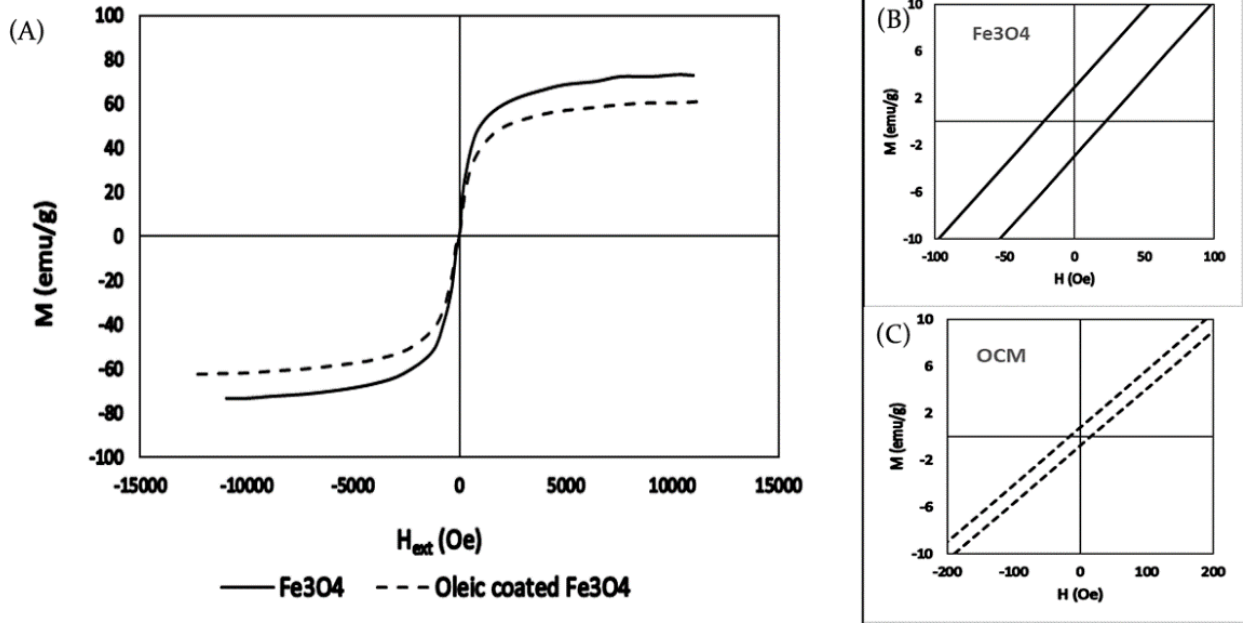


Figure 3-7 (A) Magnetic hysteresis for magnetite and Oleic coated magnetite (OCM), (b) and (c) presents a magnified range of the hysteresis curve to obtain coercivity (H_o) for both magnetite and OCM materials respectively.

The M_d for Fe_3O_4 nanoparticle is 446 kA/m. the saturation of magnetisation M_s for Fe_3O_4 and OCM are 374.755 kA/m and 219.906 kA/m respectively The magnetic susceptibility χ_{iL} , which is the initial slope of the curve coinciding at $H=0$ for Fe_3O_4 and OCM are 8.567 and 1.54 respectively. The coercivity of Fe_3O_4 nanoparticles and OCM from Figure 3-7(b & c) are 1.753 kA/m and 1.275 kA/m respectively. The obtained experiment data were used to determine effective diameter and standard deviation of tested materials using model generated by Chantrell and co. (Chantrell, et al., 1978) (O'grady, et al., 1993) (see equations [3-2]&[3-3])

$$D_m = \left\{ \left[\frac{18KT}{\pi M_d \mu_o} \right] \times \sqrt{\left[\frac{\chi_{iL}}{3M_s H_o} \right]} \right\}^{1/3} \quad [3-2]$$

$$\sigma_m = \sqrt{\ln(3\chi_i H_o)} \quad [3-3]$$

$$\chi_i = \frac{\chi_{iL}}{1 + \frac{1}{3}\chi_{iL}} \quad [3-4]$$

Where,

M_d is the saturation of magnetization of bulk material, χ_{iL} is the initial susceptibility from magnetization of test sample, χ_i is the reduced initial susceptibility, M_s is saturation magnetization of test sample, H_o is the coercivity of the test material, μ_o is the free space magnetic permeability, given as $4\pi \times 10^{-7} \text{ N/A}^2$.

Table 3-2 Summary of results from magnetic hysteresis to obtain diameter and standard deviation of samples.

Material	Density (Kg/m ³)	X _{IL}	X _I	Ms (kA/m)	Ho (kA/m)	M _d (kA/m)	D _m (nm)	σ _m
Fe ₃ O ₄	5150	8.57	2.2	374.8	1.75	446	14.1	3.1
OCM	3640	3.16	1.5	220	1.28	446	13.7	2.9

$1 \text{ Oe} = 79.5575 \text{ A/m}$, $K_B = 1.381 \times 10^{-23} \text{ N.m/K}$, $1 \text{ emu/g} = 1 \text{ Am}^2/\text{kg}$

The obtained sizes of samples were compared with TEM image size distribution averaging in section (3.5.5). Upon test of OCM dissolved in Cis-Cyclooctene, the saturation of magnetization obtained was 29.5 kA/m.

3.5.5 Transmission electron microscope

This test involves gaining a high-resolution view on synthesised materials between 100nm and 1nm (Reimer & Kohl, 2009). It can also be used to determine nanoparticle morphology, size, and entire atomic arrangement (for specialised alloys). It works by electron beams guided through a thin section of material on a TEM-grid.

The TEM was carried out to observe iron and gold nanoparticles morphologies, as well as visualize how they all aligned within pickering droplet setup. 5 μL of magnetite colloid solution and PEG-C-GM solution was deposited on TEM grids and allowed to dry under vacuum (8 Pa) at 20°C. As for the pickering droplet in water solution, a microscopic slide was mechanically etched using a hand drill to contain and hold the TEM carbon film copper made grid. The solution was spin-coated over the grid and glass slide. The grid was removed and no further action was taken prior to the electron microscope scan. The equipment used was the JEOL® 1200TEM – 80kV accelerating voltage for the image capturing.

Figure 3-8 (a, b, and c) reveals the TEM images of Oleic coated magnetite, gold methacrylate and PEG coated Gold Methacrylate, respectively. The nanoparticles diameter were measured manually using line tool drawn across each particle sample in Image J® and histogram distribution of sample sizes were plotted using Origin®

software. The statistical mean and standard deviations were also determined. The histogram distribution plots for each colloid type were placed beneath the respective colloid images Figure 3-9 shows an image of a dried ferrofluid droplet Pickering with gold nanoparticles.

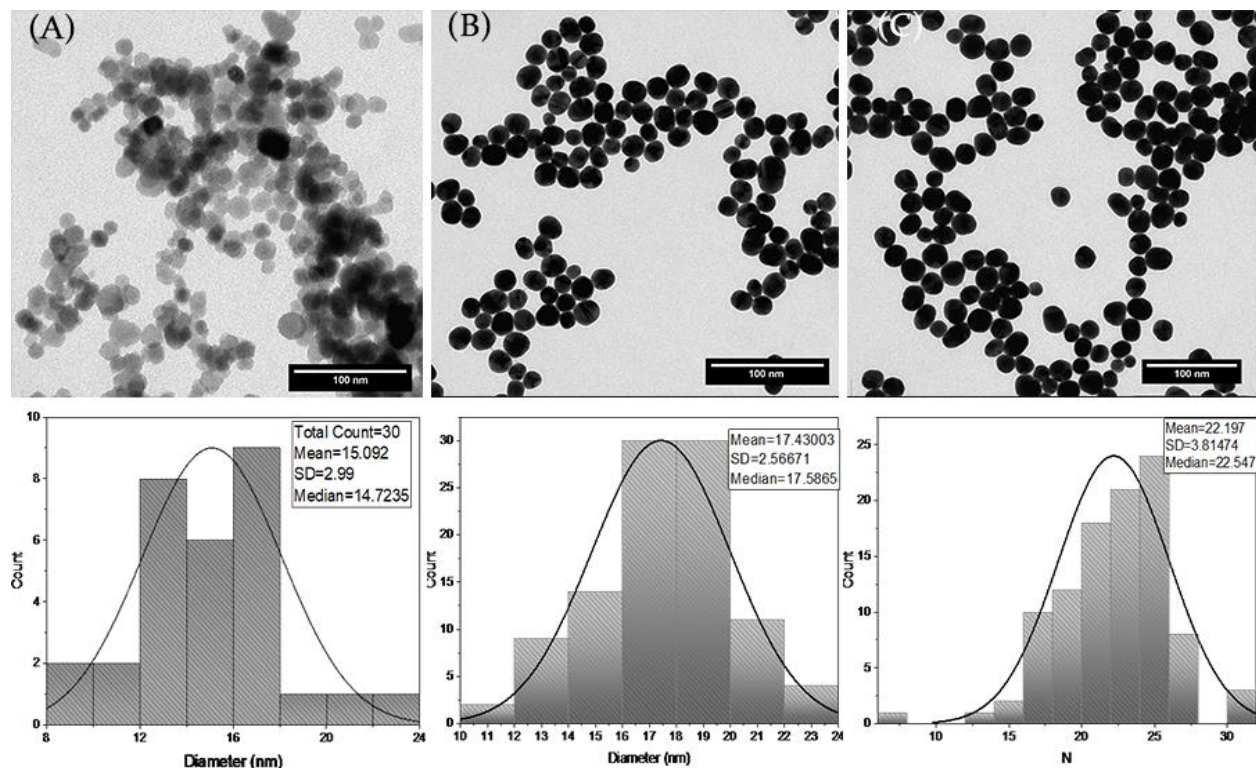


Figure 3-8 : Transmission electron microscopy of colloids (a) is for Oleic coated magnetite and the histogram beneath shows its mean as 15nm and standard deviation as 2.99nm. (b) is for Gold methacrylate nanoparticles with its histogram plot shown beneath it having a mean of 17nm and standard deviation as 2.57nm. (c) PEG-coated Gold Methacrylate nanoparticles showing its histogram distribution beneath it having a mean of 22nm and standard deviation of 3.8nm.

Recalling the magnetic hysteresis data from which the diameter and standard deviation of Fe_3O_4 and OCM nanoparticles were determined through in section 3.5.4; the diameter difference between Hysteresis data and TEM for Fe_3O_4 was $\sim 1\text{nm}$ irrespective of standard deviation. Meanwhile the thickness of oleic molecule layering around magnetite nanoparticles are;

$$(15.1 - 13.7)/2 = 0.7 \text{ nm}$$

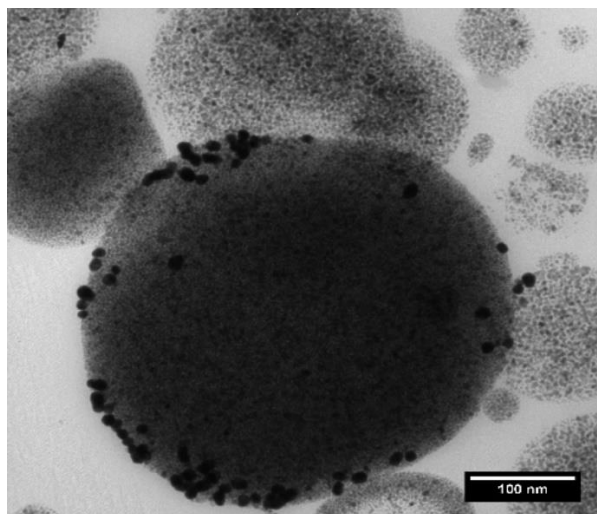


Figure 3-9 A TEM image of spin coated dried ferrofluid droplet being Pickered by PEG-C-GM nanoparticles. The evaporation rate and drying from spinning might have led to PEG-C-GM nanoparticles from the interface.

3.5.6 Fourier Transform Infra-red (FTIR) Spectroscopy

Is a non-intrusive technique where electromagnetic waves within the mid infra-red region excites IR responsive molecules within a material causing it to vibrate, stretch or rotate in order to determine the molecular configuration in terms of bonds, types of molecules and compounds (Blanco-Andujar, 2014). This form of test helps to identify molecular bonds that have been interchanged or established between species during synthesis process.

The Thermo Scientific™ Nicolet™ iS™ 10 infra-red spectroscope was set to acquire a spectrum in range between 400 cm^{-1} to 4000 cm^{-1} . A background correction was set by scanning a clean microscopic slide in air. The equipment automatically calibrated against CO_2 anomaly. The number of scans was set to 16. Prior to scanning each samples, individual components of the sample, i.e., the Polyvinyl Alcohol (PVA), Gold methacrylate (GM), sodium Methacrylate (SM), Methacrylic acid (MA), Polyethylene 40 stearate (PEG40S), PEG-capped gold methacrylate (PEG-C-GM), Oleic acid (OA), oleic coated magnetite (OCM), Ferrofluid (FF), PEG-C-GM pickering Ferrofluid (PEG-C-GM-pi-FF), and PEG-C-GM-pi-FF dispersed in PVA were all scanned to identify the key band changes as a result of molecular interaction.

Table 3-3: Bands and their representation taken from (Merck, 2020)

Band (cm ⁻¹)	Representation	Band (cm ⁻¹)	Representation
3100 - 3000	C=H stretching	567	Fe-O
2845	C-H stretching	2928	CH ₂ asymmetric
1760	C=O stretching	2850	CH ₂ symmetric
1465	C-H bending	1708	C=O carbonyl
750	C-H bending	1285	C-O stretch
1463	O-H in plane	935	O-H out of plane
1595	-COO- asymmetric stretch	2918	C-H symmetric stretch
1541	-COO- symmetric stretch	1428	O-H band carboxylic acid

3.5.6.1 Oleic coated magnetite (OCM) and ferrofluid (FF) - Figure 3-10 (A)

This section summarises the spectra of components Oleic acid-(OA) (Figure 3-10(A) – 1), oleic coated Fe₃O₄-(OCM) (Figure 3-10(A) – 2), cis-Cyclooctene (Figure 3-10(A) – 3), and ferrofluid-(FF) (Figure 3-10(A) – 4).

Upon coating with Fe₃O₄, a decrease in absorption for the CH₂ symmetric and asymmetric stretch vibrations (2849 cm⁻¹ and 2918 cm⁻¹) was observed, which corresponded to oleic acid being successfully bounded to the surface of Fe₃O₄ nanoparticle (Figure 3-10(A) – 2) (Jaime, et al., 2015). The carbonyl band at 1708 cm⁻¹ was absent in the OCM due to the complexation via carbonyl bond (Figure 3-10(A) – 2). Two new bands that appeared at 1595 cm⁻¹ and 1541 cm⁻¹ are attributed to the asymmetric and symmetric stretch of -COO- group, respectively. The presence of these bands is a consequence of complexation between iron atoms and the carboxylate groups. The loss in 1730 cm⁻¹ band of C=O stretching signifies carboxylic acid loss. The two bands, 1428 cm⁻¹ and 1403 cm⁻¹ signifies O-H bending of carboxylic acid, (Ling, et al., 2006), , (P., et al., 2013).

The infrared spectrum of ferrofluid (Figure 3-10(A) – 4) was dominated by cis-Cyclooctane vibrations which buried the other vibrations. The bands in the range of 2975-2845 cm^{-1} are assigned due to the (CH), while -CH deformation peaks appear in the range of 1470 cm^{-1} -1370 cm^{-1} . The C-C skeleton vibrations peaks appear at 1175 cm^{-1} -1140 cm^{-1} , with The Fe-O bending vibration band at 567 cm^{-1} still existing (Figure 3-10(A) – vi) (Ahangaran, et al., 2013).

3.5.6.2 Gold Methacrylate (GM) - Figure 3-10 (B)

This section discusses on absorption bands of basic components for the preparation of PEG-C-GM, such as; sodium methacrylate-(SM) (Figure 3-10(B)-1), methacrylic acid-(MA) (Figure 3-10(B)-2), Gold methacrylate-(GM) (Figure 3-10(B)-3) PEG40S (Figure 3-10(B)-4) and PEG-40S capped gold methacrylate-(PEG-C-GM) (Figure 3-10(B)-5).

In detail, the preparation of gold-methacrylate colloids, the solution is left with free methacrylate molecules. These extra methacrylate molecules graft around the gold methacrylate surface layer due to covalent forces, where it is evident from the CH_2 trans related to band at 1360 cm^{-1} (Figure 3-10(b)-iv). This is revealed from the carboxylic end pointing outward causing the particles to repel under the effect of electrostatic charges on the layer surface (Filopoulou, et al., 2021). The FTIR spectrum of GM is similar to that of silver capped poly(methyl methacrylate) (Noorsaiyyidah Darman, et al., 2012) with the broad band of O-H stretching appearing at 3327 cm^{-1} (Figure 3-10(B)-ii). The bands in the range of 1700 – 1711 cm^{-1} assigned to C=O (Figure 3-10(b)-iii) stretching conjugated acid signifies freely attached methacrylic acid, as reported by Abyaneh et al. on the interaction of gold particles with methacrylate via carbonyl bond (Abyaneh, et al., 2006). Upon adding the PEG40S, the O-H bending vibration of the capped GM particles appears at 1411 cm^{-1} , while band in the range of 1240 – 1107 cm^{-1} (Figure 3-10(b)-v) assigned to C-O stretching alkyl aryl ether. C-O stretching vibration assigned to secondary alcohol of the PEG40S and vinyl ether at 1101 and 1205 cm^{-1} , respectively, disappears for the PEG40S capped GM particles. 836 cm^{-1} (Figure 3-10(b)-vi) bending alkene of the methacrylate molecule (Mehdihasan I., et al., 2018). The gold methacrylate spectrum

was similar to the reported elsewhere (Duan, et al., 2008); (Chang, et al., 2009). Although, the intensity of PEG-C-GM spectrum was suppressed significantly.

3.5.6.3 Polyvinyl Alcohol (PVA) and its collective mixtures - Figure 3-10 (c)

This section discusses on PVA and corresponding mixtures in PVA such as; PEG-C-GM-pi-FF (Figure 3-10(C)-1), PVA (Figure 3-10(C)-2), PEG-C-GM-PVA(Figure 3-10(C)-3), FF in PVA(Figure 3-10(C)-4), PEG-C-GM-pi-FF-PVA(Figure 3-10(C)-5).

It was noticed that the PEG-C-GM pickering led to reduction in molecular vibrations of ferrofluid (Figure 3-10(C)-1), revealing the droplet was potentially densely covered. The comparison of PVA spectra (see Figure 3-10 (C)-2) with FF, GM, PEG-C-GM-pi-FF in PVA revealed the PVA vibration dominating infrared spectra. In case of FF in PVA spectra an amalgam of vibrations due to cyclooctane and PVA appeared, which altered the transmittance. This was not noticed with PEG-C-GM-pi-FF, which exhibited very similar transmittance spectra to that of PEG-C-GM-PVA, yet confirming the interfacial coverage by PEG-C-GM on FF.

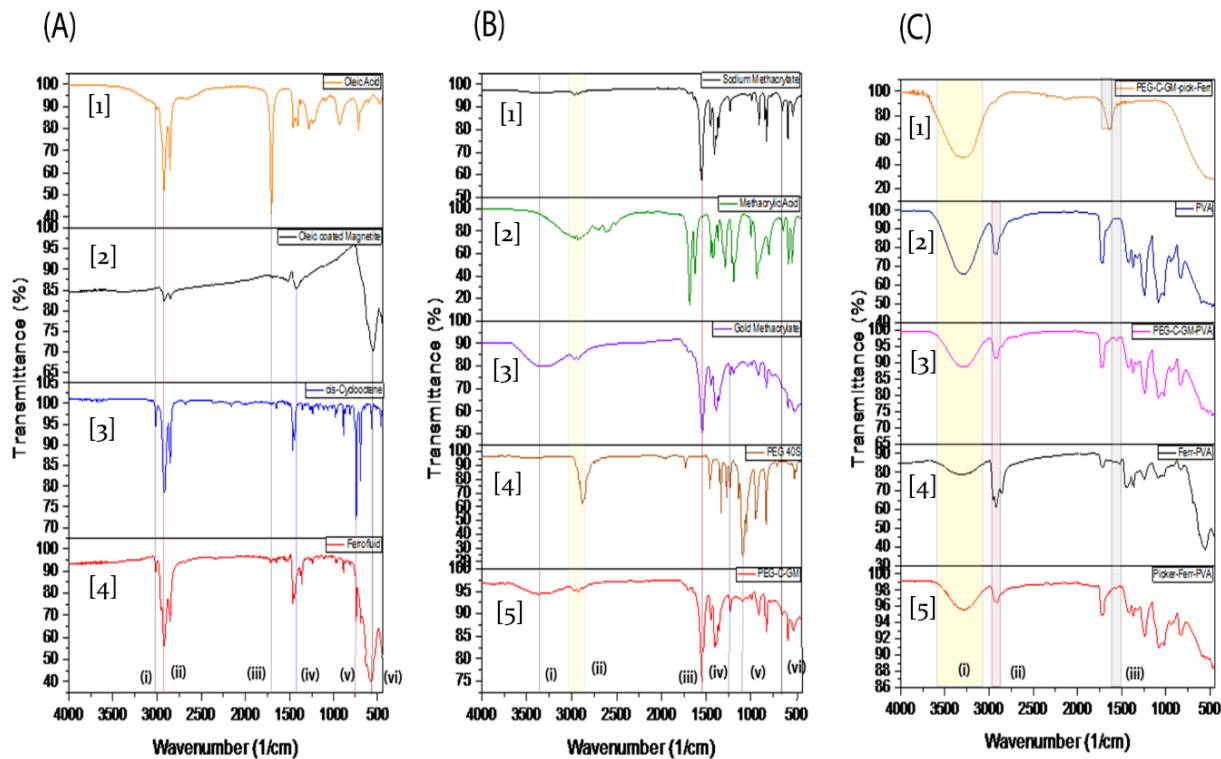


Figure 3-10 : **(A)** Comparison of components of FF, such as the OA, OCM and cis-Cyclooctene as the continuous phase **(B)** Comparison of infrared spectra between sodium methacrylate, methacrylic acid, Gold methacrylate, PEG 40s and PEG-C-GM **(C)** Comparison of prepared components on the effect of components on PVA, such as PEG-C-GM Pickering Ferrofluid, PVA, PEG-C-GM in PVA, FF in PVA, PEG-C-GM Pickering ferrofluid in PVA.

3.5.7 Thermal Gravimetric Analysis

This test helps in determining the density of degree of polymeric coating on nanoparticles. It works by raising the temperature of the samples to burn and evaporate the coating while measuring the mass, until only metallic residue is left. The information obtained from this test can be used to estimate the amount of coating molecules per nanoparticle (Green, 2014).

The system setup for this process required a platinum pan, a nitrogen purge flow at 10ml/min, maximum temperatures set at 600°C from 22°C with a ramp rate of 10°C/min with the process to run for 60 mins. The initial mass of GM was 17.5mg and the PEG-C-GM was 13.5mg. Figure 3-11 shows the mass distribution with temperature change of the samples; where for GM decomposition initiated from approximately 270°C up to 420°C before a constant mass was attained (depicted as

the residue), PEG-C-GM showed an initial gentle decline between 30°C and 260°C before a steep decline up to 420°C, afterwards a stable residual mass was reached. GM showed a loss of 6.5% and PEG-C-GM was 12.8%.

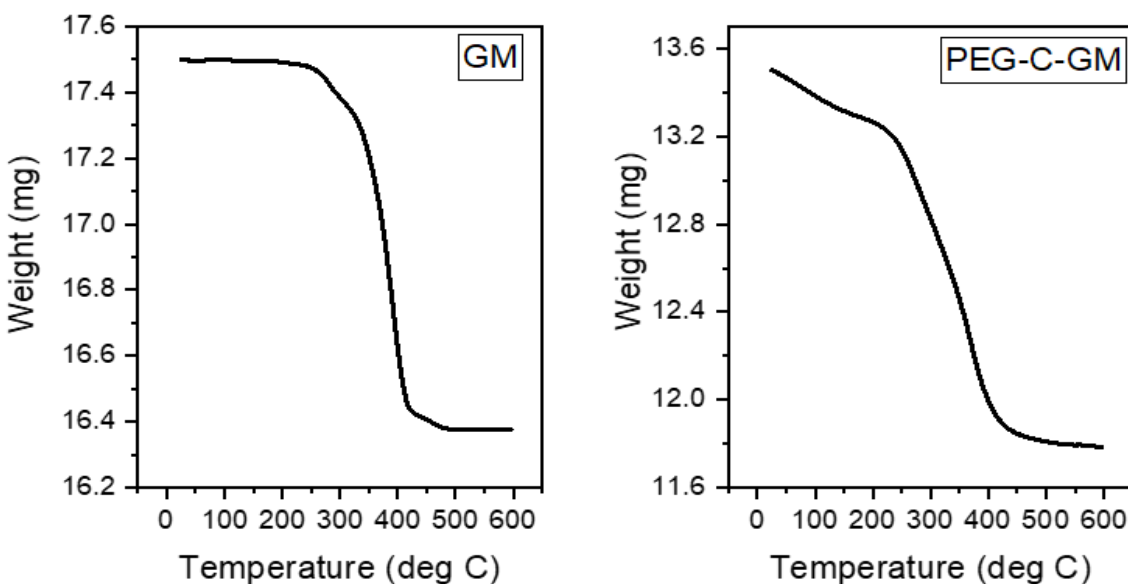


Figure 3-11 Is the Thermal gravimetric analysis of (GM) and PEG-C-GM

3.5.7.1 Estimation of coated methacrylate molecules on gold nanoparticle surface

To determine the number of methacrylate molecules coated about gold nanoparticle surface, a calculation stepwise process was adopted from previous work (Bajaj, et al., 2020). The calculation steps led to number of gold particles in the residue to be 3.06×10^{14} and number of methacrylic molecules around a 17.4 nm gold particle is estimated to be 25665 molecules/particle. Appendix 8.1 shows the calculation step.

3.5.8 Determining the viscosity of aqueous Polyvinyl alcohol (PVA)

Four types of concentrations of PVA were prepared in terms of weight fraction (5wt.%, 3.3 wt.%, 1.7 wt.%, and 1.3 wt.%) in water and their properties such as density, viscosity, wettability on substrate (contact angle) and liquid height on substrate were measured.

The density of PVA can easily be determined using Eqn. [3-5] from works done by Mohsen-Nia and co who carried out test for 88,000 Molecular Weight (88% hydrolyzed) PVA.

$$\rho(g/ml) = a + bw \tag{3-5}$$

Where;

w is weight fraction in water, a and b are constants in the equation dependent on temperature.

For the case of operating at 20°C the values for a and b according to (Mohsen-Nia & Modarress, 2006) are 1.002 g/ml and 0.2629 g/ml respectively. The densities were calculated and presented in **Table 3-4**.

The viscosity (η mPas) was determined using a model (Eqn. [3-6]) for PVA with Molecular weight between 86.5-89%. In the model, T is the absolute temperature (Kelvin) and c_m is the PVA concentration in solution. This model has an average absolute deviation of 1.6%.

$$\ln(\eta/T^{0.5}) = \alpha_m(1/T) + \beta_m \tag{3-6}$$

$$\alpha_m = 1700.52 - 6685.71 c_m + 11034.01 c_m^2 \tag{3-7}$$

$$\beta_m = -8.73 + 27.80 c_m - 42.86 c_m^2 \tag{3-8}$$

The obtained values are presented in **Table 3-4**.

Table 3-4 : presented are obtained values of densities following equation 3.5, viscosities obtained following equation 3.6.

Weight Fraction	Density of PVA (g/ml)	Viscosity of Polymer (mPas)
0.0125	1.005286	1.94
0.0167	1.00639	3.2
0.033	1.010676	15.2
0.05	1.015145	43.2

3.5.8.1 Contact Angle

The setup for measuring contact angle is shown below (Figure 3-12). 8 μL of aqueous PVA was placed close to the edge of the substrate, while the substrate was placed on an x, y and z adjustable stage. The images with resolution (640X480) were captured using a 2-megapixel infinity CMOS colour camera to give 0.107 pixels/ μm , whilst connected to and operated by installed software in a computer. Images were saved in TIFF format and then transferred for further processing. The CMOS camera was connected to a 0.7 – 5X optical variable magnifying lens to increase object profile per pixel. Prior to capturing the droplets, the intensity and distribution of light from the halogen bulb (light source) was reduced and uniformly dispersed using an opaque translucent plastic sheet as filter to avoid sections of light on the CMOS sensor uneven, except for the highly contrast droplet.

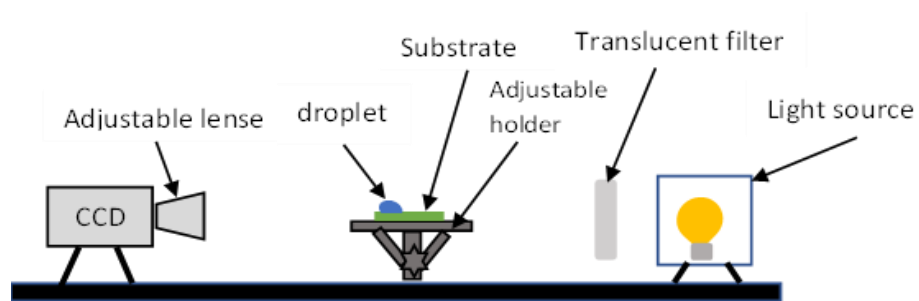


Figure 3-12 Setup for contact angle measurement

The software used in analysing images for contact angle values was Image J®, specifically with a contact angle plugin designed by Marco Brugnara (Brugnara, 2006). The plugin detects the edge of the drop and fits its profile to a circle or an ellipse, from which the tangent to the triple line contact is calculated and drawn. On having a θ_{left} and θ_{right} values generated at the edge contact point, where the values were subtracted from 180 to obtain the contact angle values (Lamour, et al., 2010). The image profile in Figure 3-13 shows the use of contact angle plugin to determine contact angle of 0.033% weight of PVA in water on glass slide; before treatment (a) giving an average contact angle of 62.25°, and after treatment (b) with contact angle of 16.85°, the insert is the same image without the drawn lines, while Figure 3-13 (c) was for the solution on silicon wafer. The contact angle barely

changed even after treatment, maintained at 49.4°. In general, aqueous PVA solution was very much wettable on the surface of both materials. A trend of contact angle was determined using the same technique for various percent weight of PVA (or density), and then plotted against each other as shown in Figure 3-14.

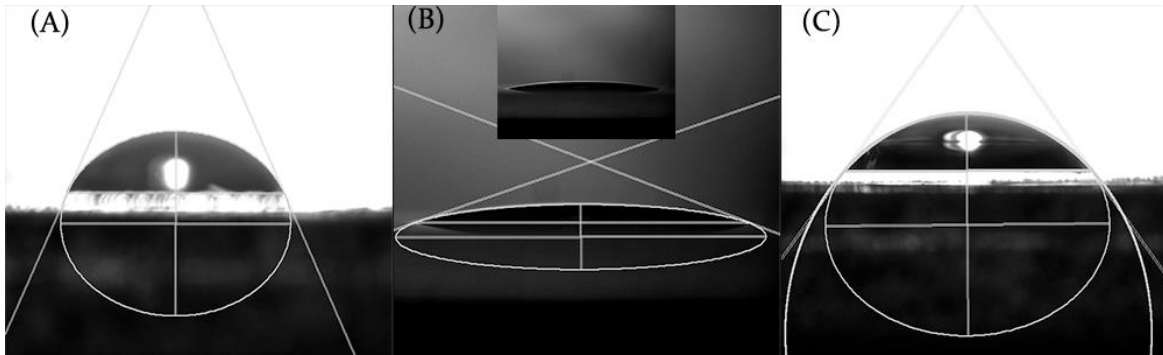


Figure 3-13 Contact angle measurements using Contact_angle plugin from Image J® to obtain values for for (a) before glass slide treatment (62.25°), (b) after glass slide treatment (16.85°), the insert was the original image, (c) silicon wafer (49.4°), same before and after treatment. Liquid used was 5 μ L of 0.033% PVA in water.

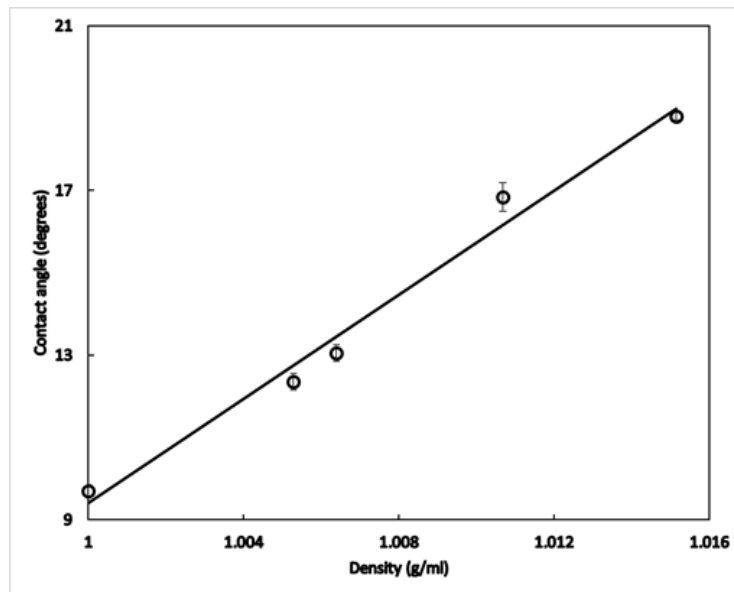


Figure 3-14 : Plot of contact angle against respective PVA densities, using treated glass slide; the fitting line for the plot bears the equation contact angle angle (CA) = 631.74 ρ – 622.33, with an R squared of 0.9828.

The general purpose for the wettability test that resulted in lower contact angles associated with substrates is to ensure even spreading of solution into thin film during spin coating without having problems like comet streaks or uneven film coverage. Next step in this section was to determine the contact angle of pickering ferrofluid in

water over the glass slide substrate. The ferrofluid conventionally wets the glass substrate and silicon wafer effectively with both air and water as surrounding medium. However, with the pickering system involved, it is hypothesised that the pickering gold particles would make the droplets poorly wettable on both types of substrates. The observatory setup used in this case was similar to that described in the first paragraph of this sub-section, but with an addition of a rectangular glass vessel. This vessel hosted half of the treated glass slide with deionized water deposited to occupy the whole vessel. A macro-sized gold pickering ferrofluid obtained from rotor stator shearing process was deposited on the glass substrate in the vessel. The droplets appeared as beads and images were taken and analysed using another contact angle measurement technique based on Low Bond Axisymmetric Drop Shape Analysis (LBADSA) plug-in of Image J®, by (Stalder, et al., 2010). Figure 3-15 shows t?

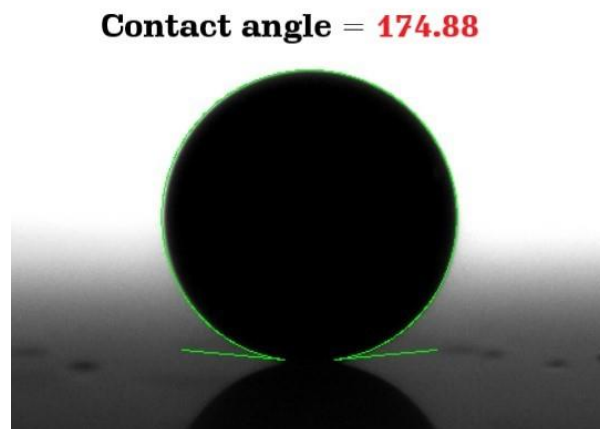


Figure 3-15 Contact angle of pickering ferrofluid on treated glass slide in water. Image analysed using Low Bond Axisymmetric Drop Shape Analysis (LBADSA) plug-in of Image J®, by (Stalder, et al., 2010)

The benefit of the substrate treatment was to improve wettability of aqueous PVA on its surface, as it would encourage thin film formation and reduce the possibility of forming comet streaks, as well as pin hole defects (Krishnan, 1978), (Mouhamad, et al., 2014), (Lawrence, 1988).

3.5.8.2 Height of polymer on glass substrate

1ml of aqueous PVA was deposited on glass substrate and allowed to spread under its own weight before taking contrast images via transmission mode to observe the

liquid height from the surface of the flat substrate. The reason for this investigation was to estimate the length of dipole chains to be formed within the liquid thickness. Figure 3-16 presents images and final fitted plot for all concentrations (or density) of tested PVA solutions.

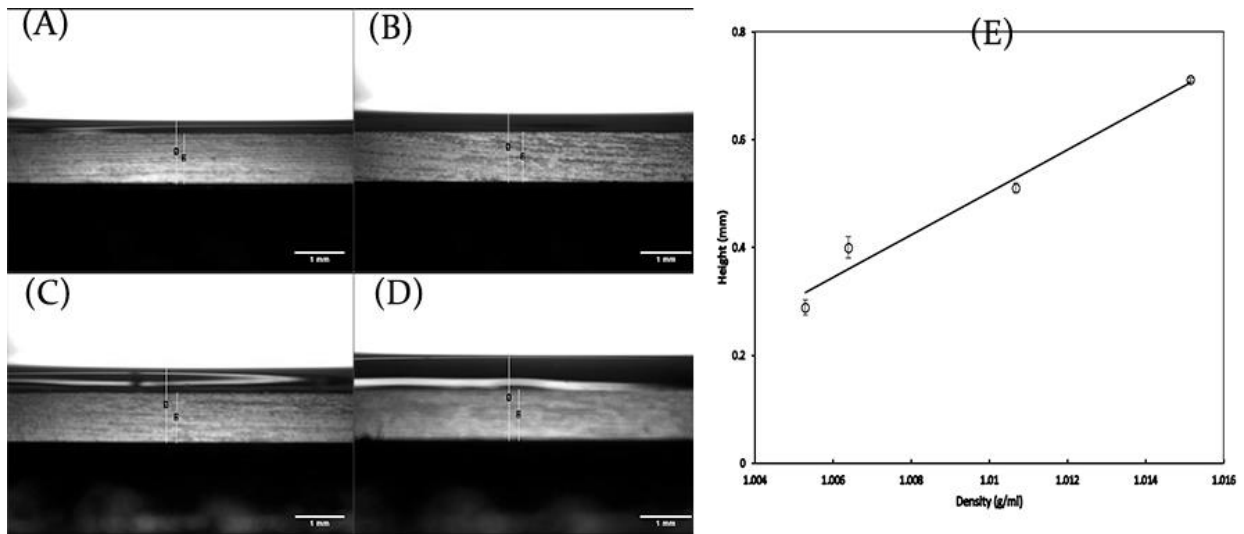


Figure 3-16 : Aqueous PVA on substrate with densities with scale bar of 1mm (a) 1.00529 g/ml, (b) 1.0064 g/ml, (c) 1.01068 g/ml, (d) 1.015145 g/ml, and (e) is the representative fitted plot of height vs density of polymer with fit as $39.48\rho - 39.37251$, having an R squared of 0.9721.

3.6 Emulsion Size Sorting via Centrifugation

3.6.1 System Description

According to several studies on centrifugal process of particle suspensions, particles migrate to the bottom as a result of difference in densities between the particles themselves and carrier fluid. Larger particles tend to accelerate faster towards the bottom of the tube because of the overall mass they possess considering multiplying density by volume (Minelli, et al., 2018). In the case of ferrofluid which is an heterogeneous material of particle in fluid medium, the particle increases the density of the entire phase (attaining $\sim 1.6\text{g/ml}$), more than water. Thus, in this investigation, PEG-C-GM-pi-FF droplets were subjected to centrifugal action to segregate bigger droplets from smaller droplets within a specific time frame in order to narrow the entire size distribution. Malvern Zeta Sizer equipment was used to check size distribution after each run. The Type of centrifuge used has the following specifications; 200V-240V, Maximum Speed: 7500 r/min, Timer Range: 0-60 min.

The 10 cm height tube was filled with the ferrofluid emulsion up to 1 cm from the tip. The tubes were placed into the rotor slots positioned at 44.4° and the selected operating parameters were used (**Table 3-5**).

Table 3-5 Selected operating conditions for centrifugal size control

Speed (rpm)	Time for each spin speed (mins)
3100	5, 10, 15, 20
3700	5, 10, 15, 20
4100	5, 10, 15, 20
4500	5, 10, 15, 20
4800	5, 10, 15, 20
5100	5, 10, 15, 20

The size distribution after ultrasonication and measurement using DLS/ seta sizer is shown below, Figure 3-17 and summary in **Table 3-6**. The emulsion system was prepared in batches of 20ml with all amounting to 300ml of mixture.

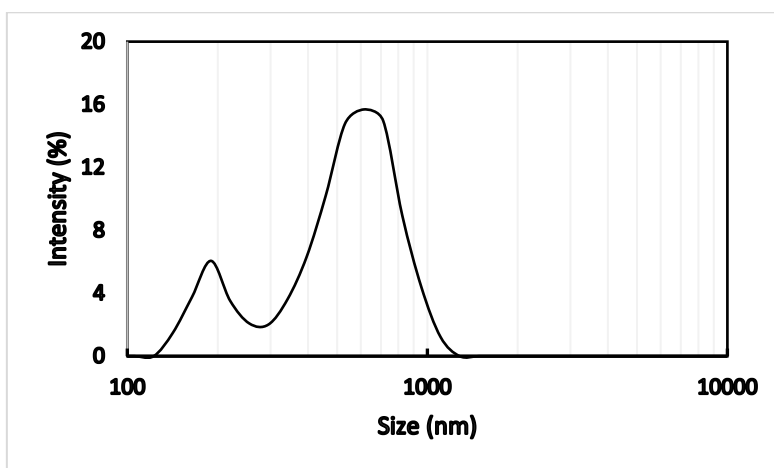


Figure 3-17 Spectra of size distribution of ultrasonicated mixture using DLS Malvern Zeta sizer.

Table 3-6 Summary of distribution of ultrasonicated sample

Mean 1 (nm)	Mean 2 (nm)	Fraction 1	Fraction 2	Standard Deviation 1 (nm)	Standard Deviation 2 (nm)
609.7	170.4	0.804	0.196	240	15.5

The outcome of centrifugation following the selected operating parameters as shown in **Table 3-7** were obtained using zeta sizer.

Table 3-7 Size distribution data of test emulsion following different spin speeds and spin time.

Speed (RPM)	Time (min)	mean1	mean2	fraction1	fraction2	StD1	StD2
3100	0	609.7	170.4	0.804	0.196	240	15.5
	5	578.9	175.9	0.815	0.185	212	18.04
	10	421.6	112.5	0.551	0.449	115.1	42.58
	15	340.9		1		38	
	20	342		1		34.2	
3700	0	609.7	170.4	0.804	0.196	240	15.5
	5	598.4	179.9	0.26	0.74	191	25.83
	10	581.8	233	0.167	0.833	100.2	57.5
	15	216.3		1		36.87	
	20	213.6		1		32.15	
4100	0	609.7	170.4	0.804	0.196	240	15.5
	5	587.3	174.6	0.375	0.625	185.7	29.59
	10	578.9	220	0.131	0.869	86.3	60.5
	15	210		1		34.69	
	20	208.4		1		30.11	
4500	0	609.7	170.4	0.804	0.196	240	15.5
	5	562.5	218.7	0.079	0.921	150.6	36.18
	10	220		1		75.7	
	15	208.1		1		50.27	
	20	207		1		28.62	
4800	0	609.7	170.4	0.804	0.196	240	15.5
	5	260.7		1		58.5	
	10	214.3		1		32.74	
	15	205.2		1		27.25	
	20	200.6		1		26.97	
5000	0	609.7	170.4	0.804	0.196	240	15.5
	5	220.7		1		28.75	
	10	209.8		1		26.58	
	15	202.1		1		26.72	
	20	198.9		1		26.69	

StD signifies standard deviation

3.6.2 Size Distribution Statistics

The size distribution obtained from Zeta sizing application comes in the form of a semi log plot. To observe the distribution density of specific range of droplet sizes (e.g., $400 \pm 150 \text{nm}$), a probability density function (PDF) for modal and bi-modal distribution was used for the sets of data obtained from the zeta sizer measurements. During centrifugal process, the migration of droplet causes a change in observed sample size. Taking the density of all sample sizes accumulating to 1, each range of sizes change in concentration within the sample. Thus, the likelihood of a range of droplet size to be within a certain fraction of the sample is what PDF determines.

The probabilistic model for PDF used for lognormal of particle size distribution that emerged from the centrifugal size control process is described from (Eqn. [3-9]). The simple reason is because, the particle size distribution is represented in a log format, and the shape profile in the form of gaussian possesses properties that can easily be used in the model to estimate change in particle size distribution. Such as, the mean, median, standard deviation, etc.

A lognormal distribution of random variable x_u is a model relates the expected mean value μ_x and standard deviation σ_x , whose density function is expressed by equation [3-9] (Crow & Shimizu, 1987), (Chang, 2015).

$$PDF(x_u, \mu_x, \sigma_x) = \frac{1}{\sigma_g \sqrt{2\pi}} e^{-0.5 \left[\frac{\ln(x_u) - \mu_g}{\sigma_g} \right]^2} \quad [3-9]$$

Where;

$$\sigma_g = \sqrt{\ln \left(\left(\frac{\sigma_x}{\mu_x} \right)^2 + 1 \right)}$$

$$\mu_g = \ln(\mu_x) - \frac{1}{2} \sigma_g^2$$

σ_g, μ_g are the log normal of the standard deviation and mean respectively.

The expression of PDF presented above is suited for single modal distributions. However, for actual physical cases like the distribution from pickering emulsions, a multimodal approach is utilized having weighing factors for each mode, of which all

sums to unity. Multimodal lognormal distribution is presented as Eqn [3-10] (Ferrari, et al., 2016).

$$MMPDF(x_w, \mu_x^i, \sigma_x^i, w^i) = \sum_{i=1}^m \frac{w^i}{x \sigma_g^i \sqrt{2\pi}} e^{-0.5 \left[\frac{\ln(x) - \mu_g^i}{\sigma_g^i} \right]^2} \quad [3-10]$$

Where;

$$\sigma_g^i = \sqrt{\ln \left(\left(\frac{\sigma_x^i}{\mu_x^i} \right)^2 + 1 \right)}$$

$$\mu_g^i = \ln(\mu_x^i) - \frac{1}{2} (\sigma_g^i)^2$$

$i, m, \mu_x^i, \mu_g^i, \sigma_x^i, \sigma_g^i$ and w^i are the modal number, number of multimodal, mean of a selected mode distribution, log normal of the selected mode distribution, standard deviation of a selected modal distribution, log normal of the selected modal distribution and fractional weight of the selected mode (amongst others where their sum equals unity), respectively.

The Probability density function for the data provided was programmed for size distribution range from 80 nm to 1600nm using Visual Basic Macro environment in Microsoft excel application. The syntax is shown in *Appendix 8.2*. The sum of the initial outcome was less than unity. The reason was because of the interval selected between selected size (meaning, the smaller the intervals, the higher the value close to unity). Using smaller interval could lead to some form of challenge when plotting the data, hence an interval of mainly 100 nm was utilized in this program. Also, the tolerance limit was set as: $PDF_x = 0, \text{ if } PDF_x < 0.001$. As the total of the data was less than unity, the total for each time run was used to divide individual PDFs for each size, so as to obtain relative Probability Density Function (rPDF) values. The resulting data was plotted as a contour surface distribution consisting of a Relative PDF, Size (nm) and Time for spin (min) for all six speed selections, Figure 3-18.

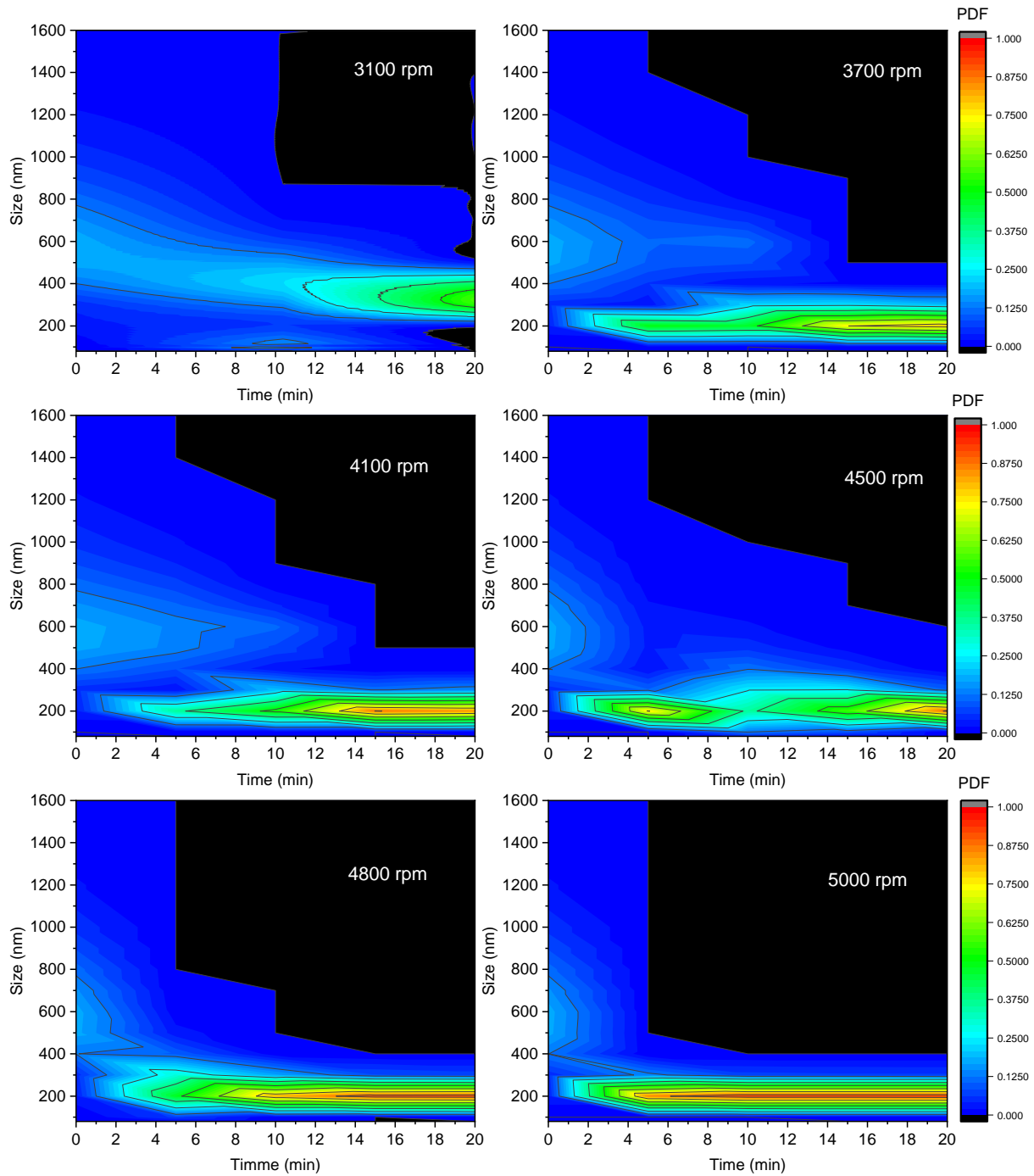


Figure 3-18: Contour map showing probability density function of size distribution of emulsion droplets for speeds (rpm) and operating time (mins).

The representation was further summarized by multiplying the spin speed (rpm) with time (mins) to obtain number of revolutions affecting the probability density fraction of a particular size or size range of droplets. This was plotted into a 3-dimensional contour map using Origin software, Figure 3-19.

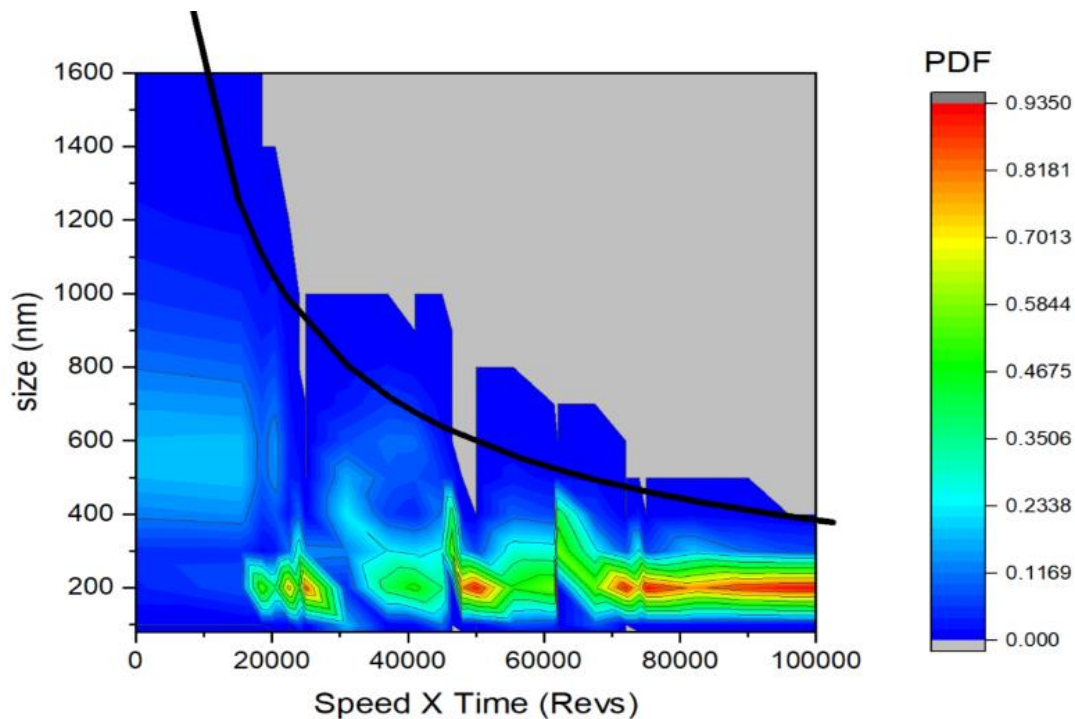


Figure 3-19 Trend line fitting within PDF range (0.005 – 0.09) in a 3D surface plot, generating a power curve with decline rate of 0.6, $R^2=0.85$.

Taking from the revised 3-dimensional plot, lesser revolutions (< 20,000rpm) produced a broader distribution with the maximum PDF between 600nm – 800nm with values about 0.19. With increasing revolutions, the distributions decay to a constant distribution range between 100nm and 200nm. The maximum PDF about 0.93 relates to approximately 200nm diameter. Observing this decay and finding out the trend it takes, a 3D surface plot was generated (Figure 3-19). A range of PDF between 0.005 and 0.09 for larger range of droplets per each revolution was curve fitted (black line in **Error! Reference source not found.**), and this generated Eqn. [0-1] in *Appendix8.3*.

The exponential decline rate 0.64 is associated with the degree of droplet size range reduction within the retrieved solution. The rate could be associated with density differential between dispersed and continuous phases, and possibly viscosity of the continuous phase. More study on this process can be carried out in the future. The PDF for 200nm droplet increased from ~ 0.1004 to ~ 0.912 , which alternatively means 89% increase. Its range (200 ± 30 nm) accounting for 20% of narrow distribution range between 100nm and ~ 400 nm.

3.7 Chapter in Summary

This chapter presented a list of materials and synthesis steps used in the manufacturing of the gold pickering-ferrofluid emulsion for thin film nano and sub-micron structures. It started with the procedure of chemically processing iron powder into oleic coated Fe_3O_4 (size $\sim 14\text{nm}$) which was dispersed in cis-Cyclooctene to form ferrofluid. Next, the Gold-methacrylate nanoparticles (size $\sim 21\text{nm}$) was prepared by chemical reduction and seeding from gold III chloride. The gold nanoparticles were then partially capped with Polyethylene glycol 40 stearate as an interfacial stabilizer. Both sets of materials were ultrasonicated to form bimodal distributed PEG-coated-gold methacrylate pickering ferrofluid (PEG-C-GM-pi-FF) droplets in water, aka. Pickering ferrofluid emulsion (size, $440\text{nm} \pm 300$). The degree of emulsion size polydispersity was minimized using centrifugal segregation control that attained an average size of $230\text{nm} \pm 50$. The controlled size distribution was then dispersed into aqueous Poly-vinyl alcohol to provide viscosity and stability for dispersed pickering droplets. Series of characterization tests such as zeta potential was used to identify the surface charge change of PEG-C-GM, zeta sizing was used measuring size of pickering droplets after each centrifugal segregation step, contact angle was used to estimate the wettability of the substrate, UV-Vis spectroscopy was used to measure the change in optical absorption between GM and PEG-C-GM-pi-FF, Transmission electron microscopy for pictural observation of PEG-C-GM on ferrofluid droplet, magnetic hysteresis for estimating saturation of magnetization of Fe_3O_4 and size of particle, Thermal Gravimetric analysis was implemented for measuring the degree of coating of methacrylate and PEG40S on gold nanoparticles, and Fourier transform infra-red spectroscopy were carried out on samples to monitor changes in bond interactions after each synthesis step.

Chapter 4 Nanostructure Design

4.1 Chapter Objective

This chapter presents an experimental study on a stimulated-directed self-assembly technique involving the design of magnetically tuned thin film nanostructure. A PEG-C-GM-pi-FF in aqueous PVA emulsion will be subjected to magnetic field and spin coating action. This will lead toward investigating the effect of magnetic and inertia forces (by centrifugation) on the degree of magnetic chain cluster distribution and alignment of pickering droplets. Pickering droplets will be dispersed in four separate concentrations of aqueous PVA viscosities and subjected to spin speeds from 700rpm to 3500rpm, within a set operating spin time. This combination would hypothetically create relationships amongst essential parameters such as magnetic strength, magnetic fluid susceptibility, continuous phase viscosity and spin coating speed. The series of test is believed to yield flexibility and tunability of manufacturing process toward obtaining desired chain cluster distribution, as well as realising possible limitations. Optical microscopy, and scanning electron microscopy (SEM) will be used to capture images of structure and further analysed using image processing software like image J®, for estimating pickering droplet density distribution and formed patterns resolutions.

4.2 Methods

4.2.1 Optical Microscopy

Images of samples were captured using an Olympus® BX41 Darkfield microscope with M-plan Achromat MPLN-BD 50X, NA 0.5. All 1920 X 1080 images were obtained with resolution 0.17 $\mu\text{m}/\text{pixel}$. The position of the slides was shifted along one axis as the other axis was kept constant, so as to take capture the structure as it changes in resolution along a radial direction. The positional readings for each snap shots were recorded from the Vernier scale on the microscope stage. Darkfield microscopy offered a close to grayscale imagery with the droplets bright and background dark; this makes it easier to distinguish structure from background. The images were analysed using Image J® tool.

4.2.2 Scanning Electron Microscopy (SEM)

Dried spin coated samples were tested using a Quanta 650 FEG SEM. A low-pressure vacuum of 0.825 Torr, accelerating voltage for electrons (HV) is 20kV and working distance of $10\pm 1\mu\text{m}$ was used for all point scans depending on the magnification. The purpose of SEM was to have a higher magnification observation of areas with high resolution of the structure.

4.2.3 Physical assumptions

There are other forces which might contribute to its re-dispersion, such as, thermal effect and electrostatic repulsion by the picker colloids. However, the rate of dispersion is limited by the hydrodynamics of the base fluid's viscosity. The static magnetisation field will provide sufficient time for the magnetized droplet to drift towards a droplet clusters in vicinity, forming longer and well separated chains. The magnetic field needs to be strong enough to induce droplet interaction otherwise, the droplet cluster form 2D patterns.

4.3 Experiment Setup

The magnetized PEG-C-GM-pi-FF in a PVA solution was expected to migrate toward areas of stronger magnetic field, forming dipole-dipole dense clusters and chains as shown in Figure 4-1 (a). This behaviour was accomplished with the setup in Figure

4-1 (a) showing the cross-section view of the design; where the magnet was approximately 5 mm beneath the surface of the substrate, (b) showing the top section and dimensions of the substrate. A Neodymium 2.5mm dimensional square magnet was purchased from First4magnets®, and its surface reads a high as 202mT using a VTSYIQI® probe type gaussmeter. The probe type gaussmeter detects within the ranges, 0~200mT~2000mT (1mT=10Gs), at resolutions of 0.1mT (Accuracy 1%), and operating temperatures between -10°C~40°C.

The plot profile in Figure 4-1(c) shows the measured magnetic field distribution across the substrate (mT) of the setup in Figure 4-1 (b).

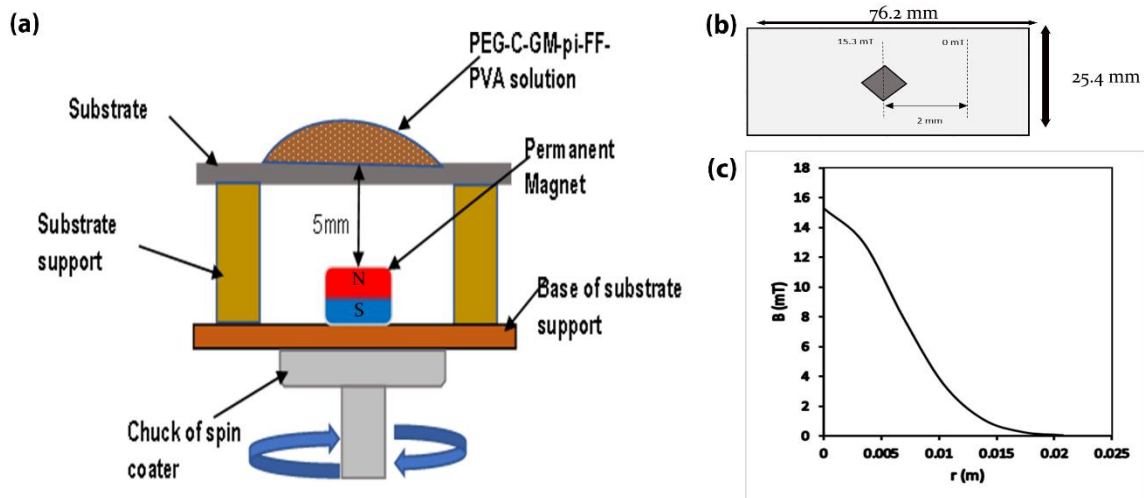


Figure 4-1 (a) Schematic of droplet interaction in magnetized ferrofluid-polymer emulsion, showing cross-section dimensions of experimental setup with magnet 5mm beneath the substrate (b) Top-section and dimension of magnet and substrate (c) Magnetic field distribution across substrate surface.

The setup was spun using a SCS™ 6800 spin coating series equipment under variable speed programmed to operate within specified time frame. The time for the process was divided into three sections; the first, an acceleration from 0 rpm to top speed for 1 second; secondly, a constant top speed for 54 seconds; and the third, a deceleration for 5 seconds. **Table 4-1** summarises the experimental procedure for this process. The slide fitted with the magnet was placed on the chuck of the spin coater, and the substrate support is a layered 1mm thick removable double sided acrylic tape. The same tape was used to stick the glass substrate subjected to coating.

The PEG-C-GM-pi-FF in different concentrations of Aqueous PVA (1.7% ,5%, 3.3%, and 1.3w/w%) was made following the procedure described in Section 3.5.8. The parameters such as aqueous PVA viscosity and spin speed were varied (**Table 4-1**) for the observation of change in geometric morphology in the thin film pattern. A maximum speed was attained following the operation time of 1 sec acceleration, constant speed for 54 secs and 5 secs deceleration. All these are summarised in **Table 4-1**.

Table 4-1 Sample setup and process parameters at room temperature. The density was determined using approach by (Mohsen-Nia & Modarress, 2006).

Weight percent PVA	Density (kg/m ³)	Viscosity mPa.s, (kg/ms)	Surface Tension (mN/m)	Centrifugal speed (rev/min)	Time (sec)
5%	1015	43 (0.043)	50.83	700, 1000, 1500, 2000, 2500.	60
3.3%	1011	15 (0.015)	51.72	700, 1000, 1500, 2000, 2500.	60
1.7%	1006	3.2 (0.0032)	52.84	700, 1000, 1500, 2000, 2500.	60
1.3%	1005	1.9 (0.0019)	53.3	700, 1000, 1500, 2000, 2500.	60

Prior to the spinning process, 0.5ml of PEG-C-GM-pi-FF in PVA solution was allowed to settle on the substrate for 60 seconds. This gave enough time for the droplets to interact with the magnetic field and build chain clusters. After 60 seconds of spinning process it was noticed the thin film coating had dried, except for thin film emulsions operated at 700rpm which dried 2 minutes afterwards. This partly wet sample allowed clusters of pickering droplets to disassemble once removed from the setup. Therefore, drying of the pickering emulsion film under high speed (in this case, >700rpm) is necessary for the structure to remain fixed after completing spin coating process.

4.4 Results and Analysis

4.4.1 Images of Spin coated samples

4.4.1.1 Thin Film Imaging

A representative image of prepared thin film patterned structure, using a PVA viscosity of 15.2mPas and a spin speed of 2500rpm (Figure 4-2). The centre of the thin film appeared denser due to the brown-like colour of aggregated PEG-C-GM-pi-FF droplets. On moving radially outward from the centre, the colour appearance gradually fade due to lesser aggregated PEG-C-GM-pi-FF droplets. The thin film

nanostructures also possessed 2-fold symmetries projection, which is an indication of long-range ordering of PEG-C-GM-pi-FF droplets (Giuliani, et al., 2010).

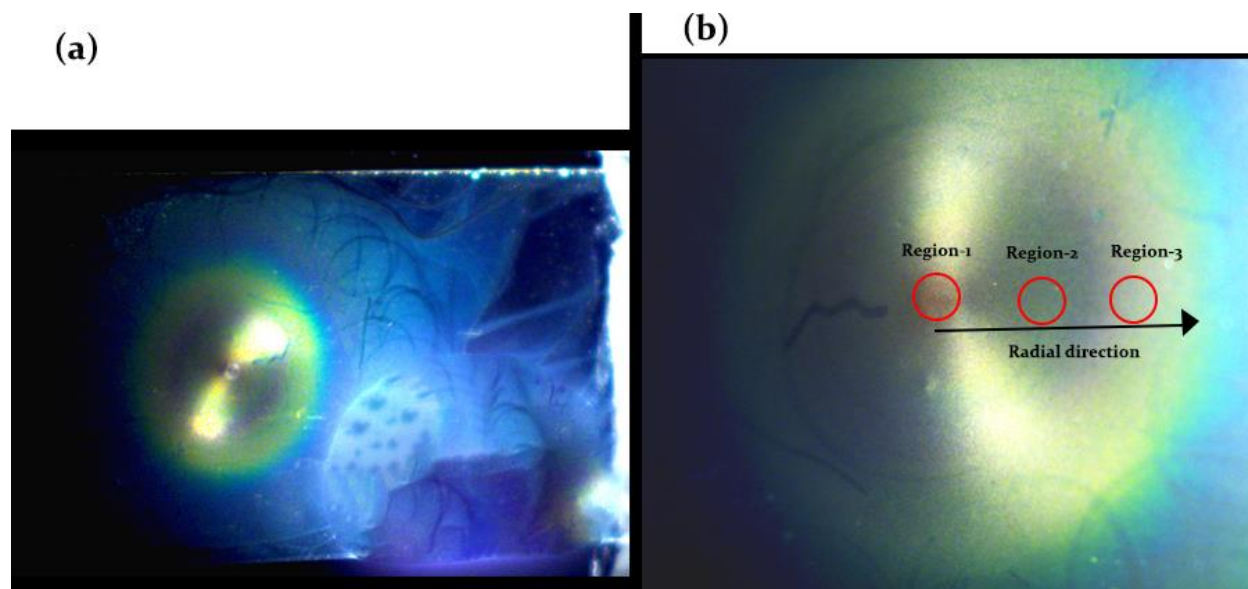


Figure 4-2 (a) Image of thin film magnetized patterns on microscopic glass slide with width of 25.4mm. The thin circular thread markings are located at the backside of the substrate. (b) is a magnified image of the dried film magnetic pickering droplet pattern on glass slide. The marked regions Region 1 ($r=0\text{mm}$), Region 2 ($r=4\text{mm}$), Region 3 ($r=7\text{mm}$).

4.4.1.2 Darkfield Microscopic Image

The Figure 4-3(a) represents a 2.4 pixel/ μm resolution darkfield microscopic image of Region-2 (Figure 4-2 (b)) of prepared patterned thin film (PVA 15.2mPas, 2500rpm) structure. The ordered chains of PEG-C-GM-pi-FF droplets are visibly white and the gaps between is the dark background. A proper illustration of the 1D pattern morphology showing chain gap, chain thickness and chain length is shown in Figure 4-3(b).

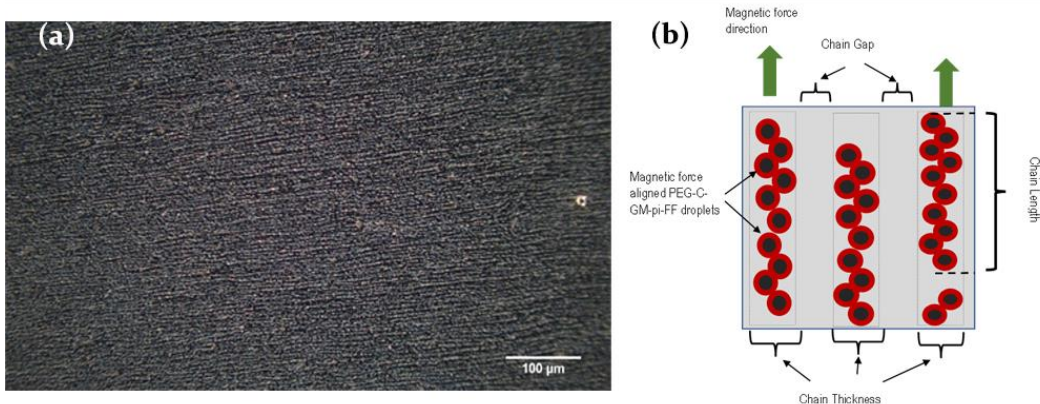


Figure 4-3 (a) Darkfield image of sample using the Olympus BX41 microscope with a 20X 0.4 N.A. M-Plan objective lens. (b) Illustration of 1D pattern morphology showing chain length, chain thickness and chain gap.

4.4.1.3 Scanning Electron Microscopy (SEM)

Due to the resolution limit of the optical microscopes, SEM images were used to observe the patterned structure at higher resolutions (Figure 4-4) (17 pixels/ μm for images at the left and 1820 pixels/ μm for images at the right) at three separate locations (0 mm, 4 mm, and 7 mm). These images also provided the opportunity to observe the degree of PEG-C-GM-pi-FF droplets interaction. The density of pickering droplet cluster was more at the centre than other parts of the film by relative comparison; thus, the middle (Region-1) of the circular assembled structure profile of film (Figure 4-2 (b)) was taken as the radial origin (0 mm). At 0 mm, Figure 4-4(a) shows dense and stacked packing of the pickering droplets forming columns/labyrinth structures at the centre of the substrate; implying that the high magnetic field strength at that region attracted high spatial density of pickering droplets which may have led to formation of layers of pickering droplet. This behaviour of overlay packing of pickering droplets was as a response to the magnetic field flux direction, where fields close to the centre of the substrate are directed perpendicular to the surface of the substrate. This field direction causes droplets to align and pile upon one another due to dipole-dipole interaction. This was further clarified with image (Figure 4-4(b)), which showed irregular oriented pickering droplets, confirming the hypothesis of formed layers of droplets. At 4 mm from the centre (region 2) of the thin film (Figure 4-2 b), a relatively more defined pattern was observed with lesser cluster density as

a result of lesser packing order than region 1, as well as longer chains and increased gaps between them (Figure 4-4 (c) and (d)). This type of ordered formation of pickering droplets could be as a result of the effect of increased shear force on magnetized pickering droplets by the increased velocity of aqueous PVA fluid at that radial point. The velocity of a fluid on a spinning disc under constant angular speed increases with increase in radius (Emslie, et al., 1958). Region-3 (7 mm from the centre of thin film) shows formation of shorter chains relative to those in Region-2 (Figure 4-4 (e)). The structure formation in this region has more gaps in between chain cluster as they get thinner in thickness (Figure 4-4 (f)). At this point the magnetic field strength was relatively lower (i.e., taking from the magnetic field profile, Figure 4-1 (c)) compared to the increased fluid inertia that led to destabilization and disorientation of pickering droplet from the magnetic vector field.

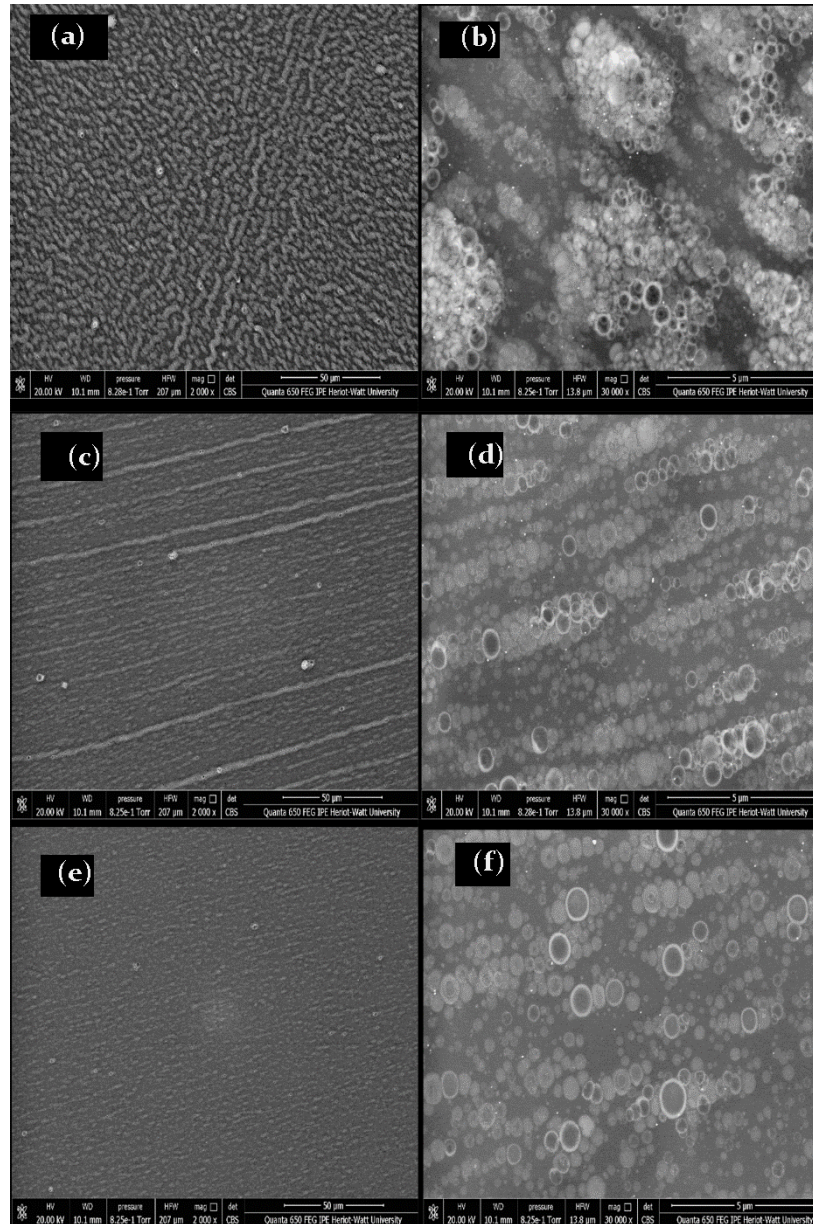


Figure 4-4 SEM images of sample where; at centre of substrate (**0 mm**) showing dense cluster of pickering droplets at - (a) 17 pixels/ μm resolution and (b) 1820 pixel/ μm resolution, defined longer chain structures with an average of 4 droplets within its thickness was observed **4mm** from centre of substrate at - (c) 17 pixels/ μm resolution and (d) 1820 pixel/ μm resolution, and at **7mm** from centre of substrate relatively smaller chains were formed with thickness of max. 2 droplets at - (e) 17 pixels/ μm resolution and (f) 1820 pixel/ μm resolution.

Additionally, for the estimation of thin film thickness, cross-section images of the thin were taken, measured and analysed (images shown in Figure 4-5). A prepared 3000-rpm spin coated sample with 1.5wt% aqueous PVA on silicon wafer substrate was split through the centre into four sections and the film thickness was measured by using the SEM measuring toolkit at three regions, 0mm (a), 4mm (b) 7mm (c) and

12mm (d). Their respective heights were then plotted (Figure 4-6). The middle of the substrate is presumably the area with the highest film thickness because that is the location of the least centrifugal force and least fluid inertia and energy. Therefore, measurements is taken from the middle point to other radial locations

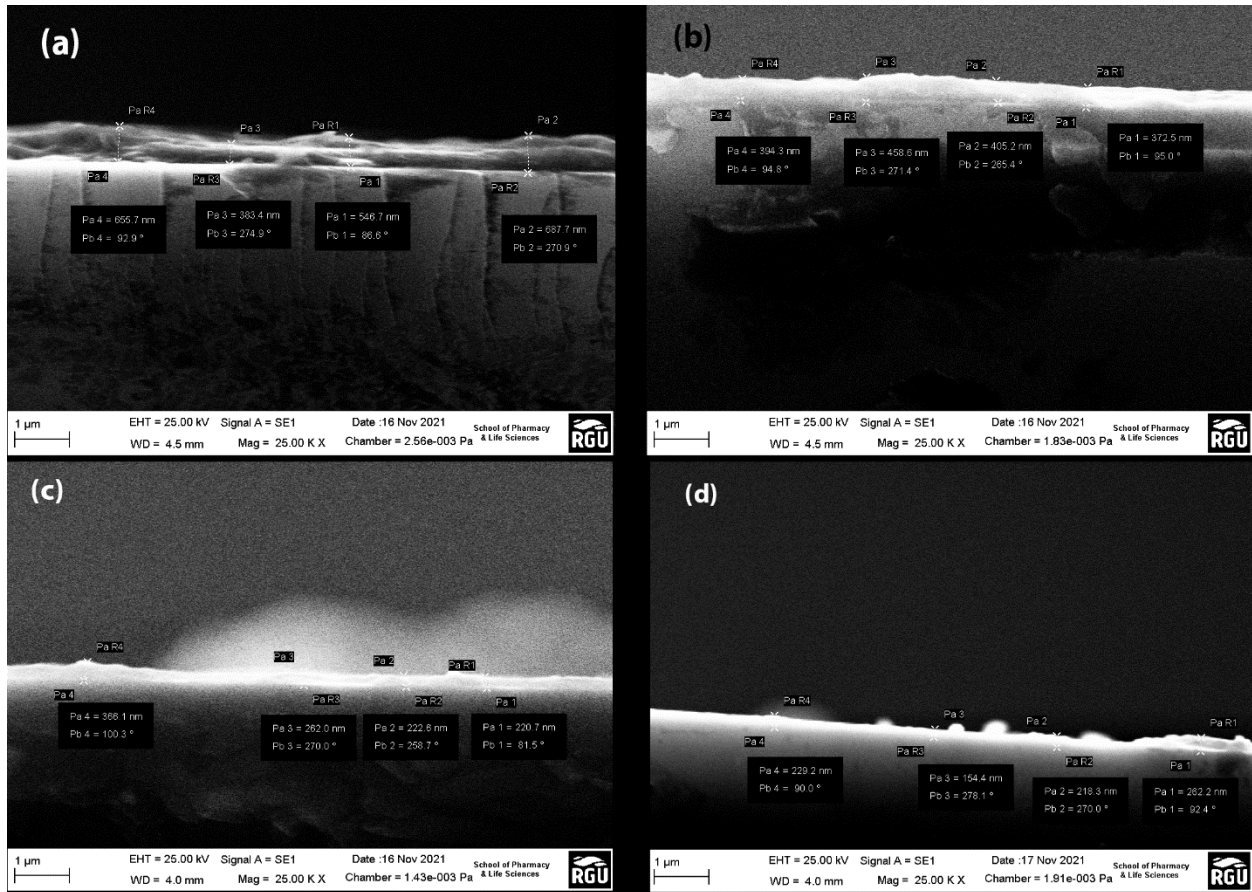


Figure 4-5 SEM images of cross-section of spin coated samples at 3000rpm showing thickness of film at (a) 0mm, (b) 4mm, (c) 7mm and (d) 12mm.

To have the average film thickness between 0mm and 6mm regions, an integration-averaging technique (Jordan, et al., 2019) was applied (see Eqn. [4-1]) on the linear fit trend ($h(r) = 574.3 - 43.8r$) with an $R^2 = 0.996$, thus yielding an average film thickness of 311 nm.

$$h_{avg} = \frac{1}{r_n - r_0} \int_{r_0}^{r_n} h(r) \quad [4-1]$$

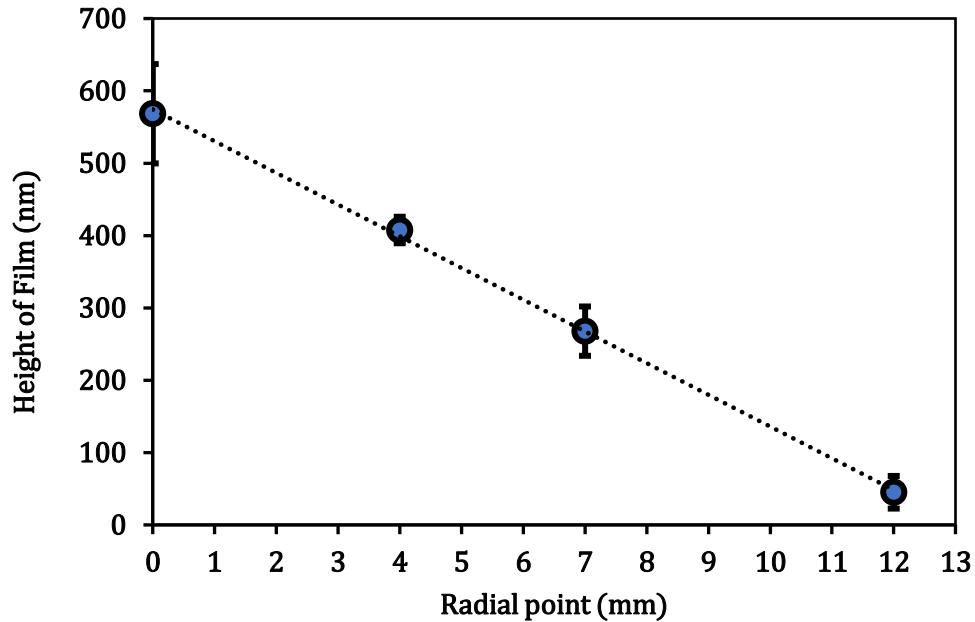


Figure 4-6 The measured points (blue circles) and respective error bars were fitted to generate a trend line with equation ($h(r) = 574.3 - 43.8r$) with $R^2 = 0.996$, which will amount to an average film thickness of 311nm using Eqn. [4.1], as performed in (Jordan, et al., 2019).

The profile of the film height potentially results from the magnetic pull of droplets towards the substrate surface, shear thinning by fluid inertia and shrinkage of drying polymer.

So far from these observations, it is obvious that the magnetic field is stronger at the centre, which then grows weaker moving away radially from the centre. While reverse is the case for the fluid inertia; which is less at the centre but increasing radially. The contouring effect of both forces at different regions in thin films would determine the types and degree of cluster formations within the structure. The next section provides quantitative analysis of pickering droplet cluster formations within thin film.

4.4.2 Cluster density distribution analysis

In this section, darkfield microscopy images of sections of the thin film were converted to binary format; causing the pickering droplets to appear as white and the background black. The contrast between the two showed the grayscale for droplet being higher compared to background. This allowed for the use of image analysis to identify the droplet density, which was related to number white pixels per unit area of region of interest. This was so as to create particle density distribution profile

across coated substrates prepared under different PEG-C-GM-pi-FF in PVA solution viscosities and spin coating speeds.

4.4.2.1 Region of Interest - Integrated Pixel Density image analysis

The integrated pixel density image analysis was carried out by creating a shape profile (circle or square) that act as a boundary marker, encircling a specific sample portion of the image - Region of Interest (ROI). In this procedure, images of spin coated samples were captured using Olympus Darkfield microscopy with a 20X, 0.4 N.A. M-Plan objective lens. The position of the slides was shifted along one axis while the other axis was kept constant. To obtain images at specific regions of the thin film on substrate, the vernier scale on the microscope stage was used to record the positions of observation with reference from the centre of the film. The images were analysed using Region of Interest (ROI) grayscale quantification process in Image J®. The pixel brightness density of the grayscale images were measured and accounted for; ranging from the darkest pixels to the brightest ones. Regarding the region of interest, a macro was created to measure the pixel densities and their spatial distribution within a defined marked area/region (yellow circles) in Figure 4-7. As for the measurement, parameters such; as

Area of region, Mean, Standard deviation, Mode, Min, Max and Integrated density were pre-selected in image J® for determining the pixel density per scan area.

In the first stage of analysis, the rate of change of cluster density within several microns (in this case within $\sim 20 \pm 5$ micrometre range), series of concentric rings of different radial sizes were selected and measurements taken. The centres of two sets of PEG-C-GM-pi-FF in PVA (3.2mPas) films that were prepared at 700rpm and 2000rpm spin speeds (Figure 4-7 a & c respectively) were first analysed. The pixel density covered by each concentric ring was divided by their respective scan area to obtain the integrated density per unit area (μm^2). The integrated pixel density per area in thin film of 700rpm is presented in **Table 4-2**, while that of 2000rpm is located in *Appendix 8.4*. The integrated density/area of thin film structure under 2000 rpm spin speed was approximately constant (~ 4080) from ROI_1 up to ROI_3, before declining as area increased down to ROI_6. A graphical illustration of this estimated values was plotted by placing the diameter of each circle in the x-axis (i.e., one radius

in negative ordinate and the other in positive ordinate) and the integrated density/area in the y-axis (Figure 4-7 (d)). This profile represents the cluster density distribution shown in Figure 4-7 (c). This was the same for structures prepared under 700rpm spin speeds (Figure 4-7 a & b). On comparing both Figure 4-7 (b) and (d), the following observations were made;

considering the peak point at 0mm, the increase in spin speed from 700rpm to 2000rpm created a stronger fluid inertia in the region that depreciated the column of cluster layers by ~160%.

the difference between the peak of the cluster and lowest point is 5% for 700rpm, while for 2000 rpm it is 35%. This means due to increased spin speed, the fluid inertia force rose high enough by effectively overcoming the magnetic force resulting in reduced cluster density close to the centre of the film. Thus, forming a steep slope profile.

Table 4-2 Region of interest pixel intensity density measurements for sample having viscosity 3.5mPas, spin coated at 700rpm

Label	Area	Integrated Density	StdDev	Int. Den./Area
ROI_1	8.48E+02	3.46E+06	3.30E+01	4.08E+03
ROI_2	5.15E+03	2.10E+07	1.40E+01	4.08E+03
ROI_3	1.58E+04	6.45E+07	1.43E+01	4.08E+03
ROI_4	3.84E+04	1.55E+08	1.44E+01	4.04E+03
ROI_5	7.03E+04	2.80E+08	1.45E+01	3.99E+03
ROI_6	1.38E+05	5.37E+08	1.46E+01	3.89E+03

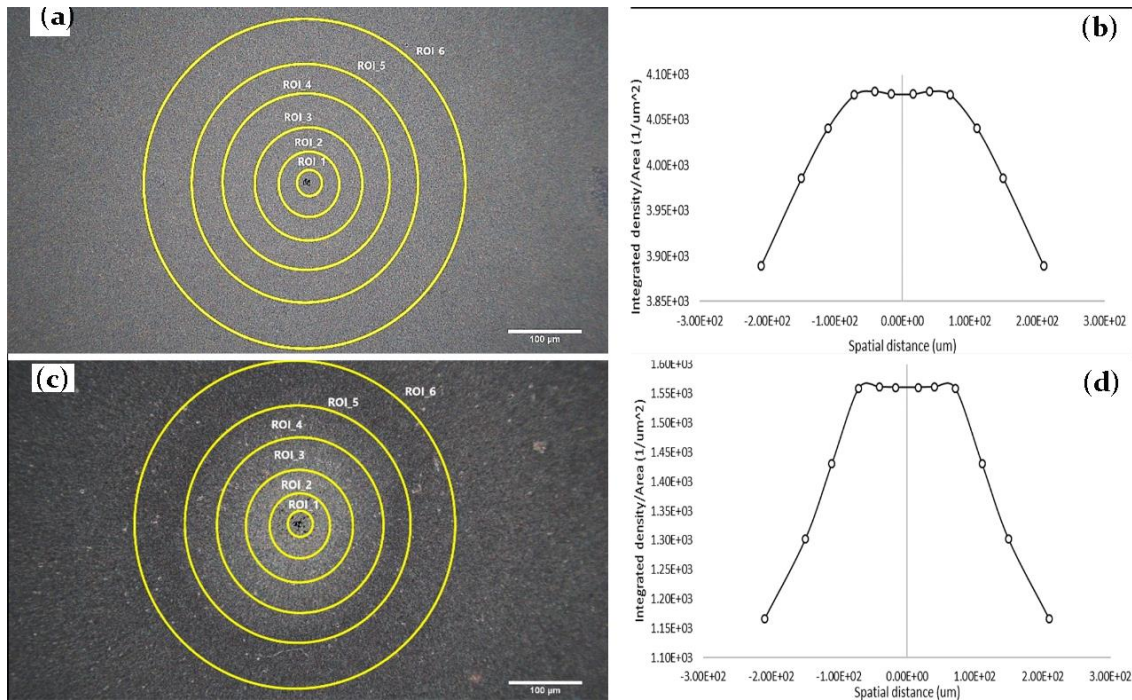


Figure 4-7 Spatial plots of integrated pixel density for the region of interest (ROI) areas for representative microscope images. (a & c) both images shows the ROI areas marked by yellow circle for 0.035kg/ms at 700rpm and 2000rpm, respectively; (b & d) the integrated pixel density per area distribution across all ROI areas for 700 and 2000 rpm, respectively.

From the final outcome, we saw that ROI sizes for 1,2 and 3 were approximately the same, hence for the rest of the image analysis experiment, ROI_3 ($1.58 \times 10^4 \text{ um}^2$) was utilized.

4.4.2.2 Density distribution analysis

In the next phase, a long-range radial distribution of pickering droplets profile was constructed by averagely fitting integrated densities of each scanned radial point using the ROI_3 ($1.58 \times 10^4 \text{ um}^2$). The integrated density was not divided by the region of interest area because it was the same size used for all scanned radial points. An example of how the integrated density parameter value was plotted against radial distance (from left to right) for a given sample with aqueous PVA viscosity of 45.2mPas, spun at 2500 rpm is shown in Figure 4-8. The trend followed a half-normal distribution with a higher pixel density at the centre of the film ($r=0\text{mm}$).

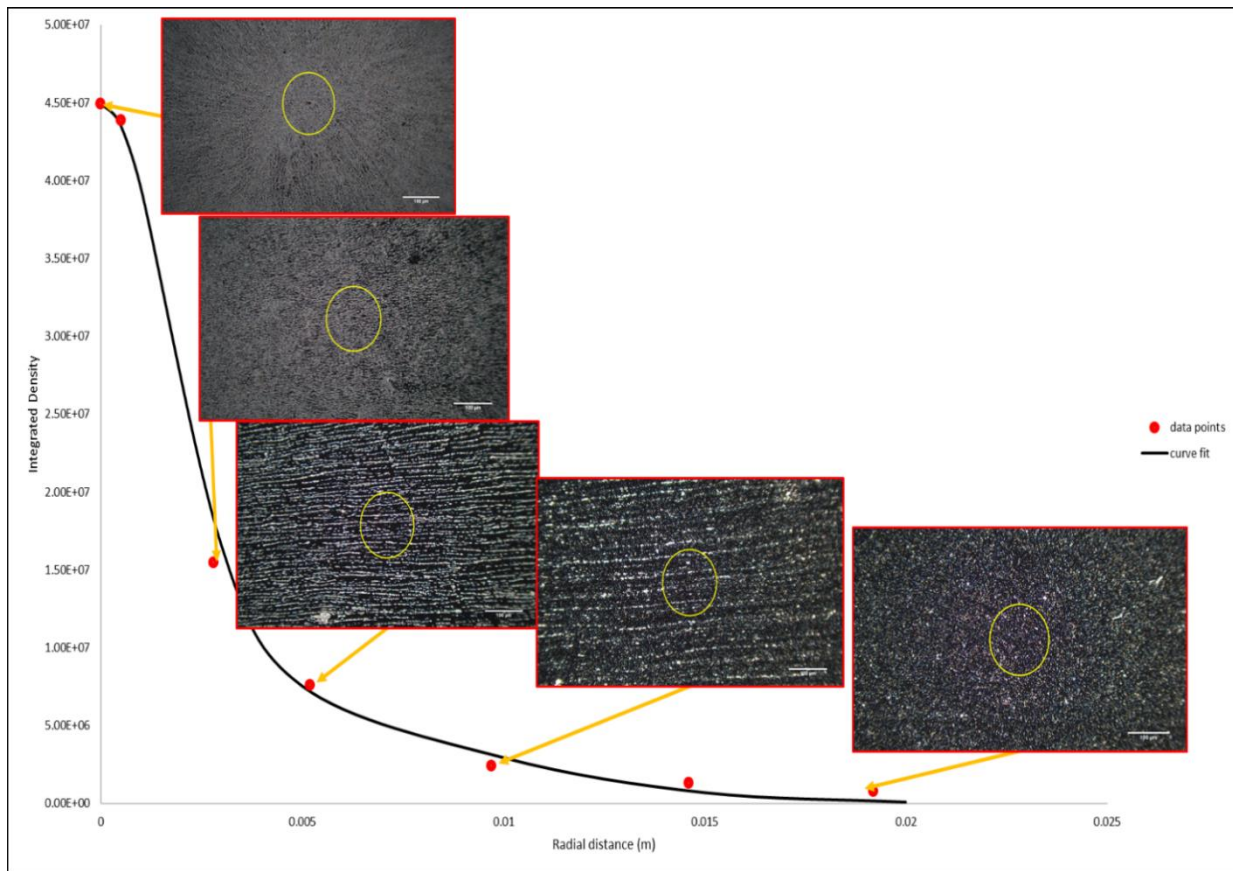


Figure 4-8 Plot of ROI scan data points across (from left to right) of pickering ferrofluid emulsion in PVA (1.7wt.%). The fit $R^2=0.987$ Scale bar in each image is 100 μm

4.4.2.3 Interpretation of thin film preparation following process presented in Table 4-1.

This section presents the estimation and distribution of cluster density across the coating over the substrate subjected to varying conditions presented in **Table 4-1**. The process of interpretation followed the analysis used for plotting Figure 4-8. An example for pickering emulsion in 5wt.% PVA and spin speeds at 700rpm and 2500rpm is shown in Figure 4-9 a & b respectively. The peak at 0mm for 700rpm shows higher value than that of 2500rpm, which is due to lesser inertia and thicker film based on fundamental spin coating theory explained by Emslie and co. (Emslie, et al., 1958). The rest Pickering emulsion and spin speeds (**Table 4-1**) were analysed the same way. The data were presented as half normal distribution, shown in Figure 4-10. The rest of the distributions representing preselected viscosities and spin

speeds fitting related to both Figure 4-9 and Figure 4-10 are provided in *Appendix 8.3*. The change in profile under constant magnetic field is influenced by the viscosities of the pickering emulsion in PVA and selected spin speeds.

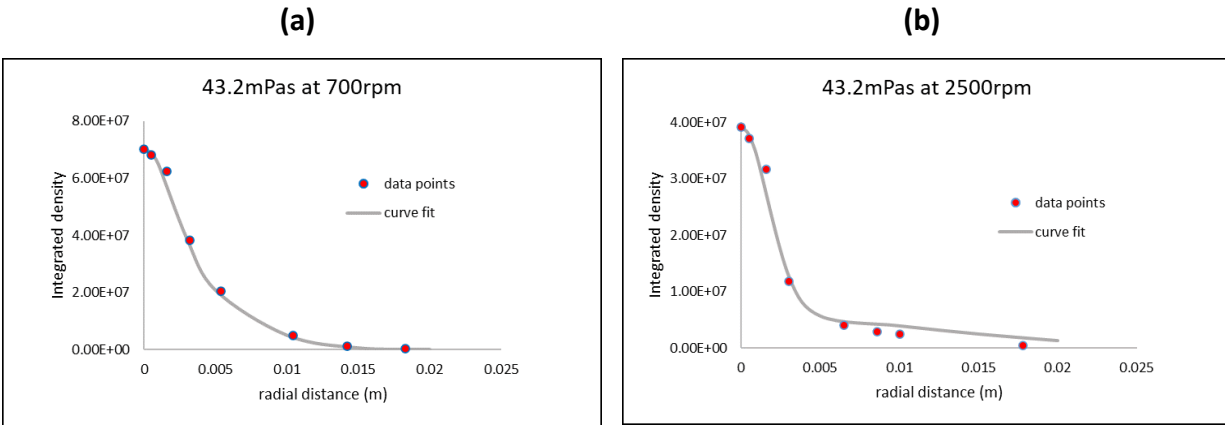


Figure 4-9 ROI scan data points across substrate for (a) 43.2mPas @700rpm (b) 43.2mPas @2500rpm. The average $R^2=0.984$. The viscosity of the pickering emulsion in PVA and spin speed affects the pickering droplet density profile. The rest of the fittings are presented in Appendix 8.5.

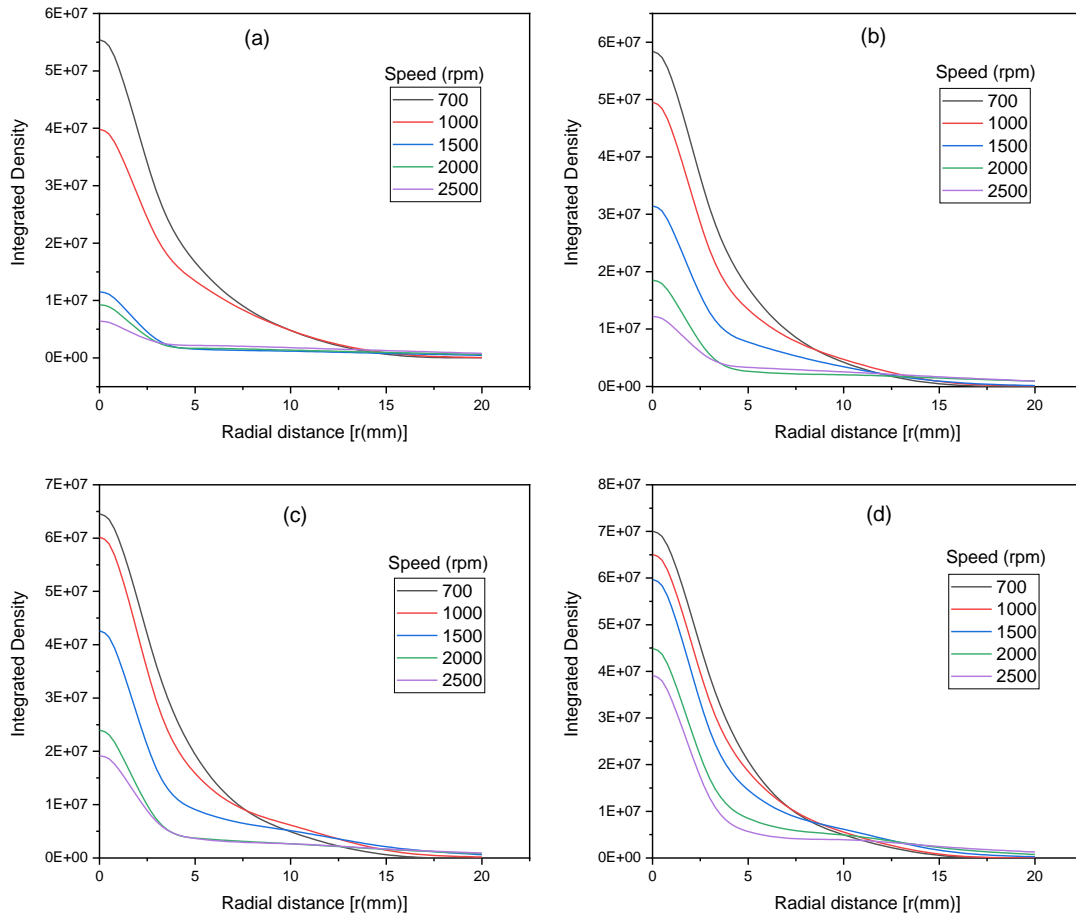


Figure 4-10 Gaussian distribution profile from ROI-integrated density of pickering emulsion cluster density across thin film from spin speeds of 700, 1000, 1500, 2000 and 2500 rpm for; (a) 1.9 mPas, (b) 3.2 mPas, (c) 15.2 mPas and (d) 43.2 mPas.

The profiles from Figure 4-10 overall shows the impact of viscosity on the distribution of clusters when they are relatively compared per spin speed. The initial height of each aqueous PVA (Figure 3-16) hosting emulsion may have played a role in column cluster thickness (droplet layers). Thus the highest viscosity has the highest integrated density at the centre of the film. The rate of change of profile for each viscous solution across different spin speeds was better compared by using their full width half measures (FWHM). The FWHM identifies with the degree of spread of the pickering droplet cluster density across the thin film. This was estimated using Gaussian fitting tool in Origin® software. The model formula used for fitting data points is shown in equation (4-2).

[4-2]

$$y = y_o + \frac{Ae^{-\frac{4 \ln(2)(x-x_c)^2}{(FWHM)^2}}}{(FWHM)\sqrt{\frac{\pi}{4 \ln(2)}}}$$

Where, y_o is the lowest data point, x_c is the middle of substrate ($r=0\text{mm}$), A is the area covered by the curve.

The plot of FWHM vs spin speed (rpm) for each aqueous PVA viscosity is shown in

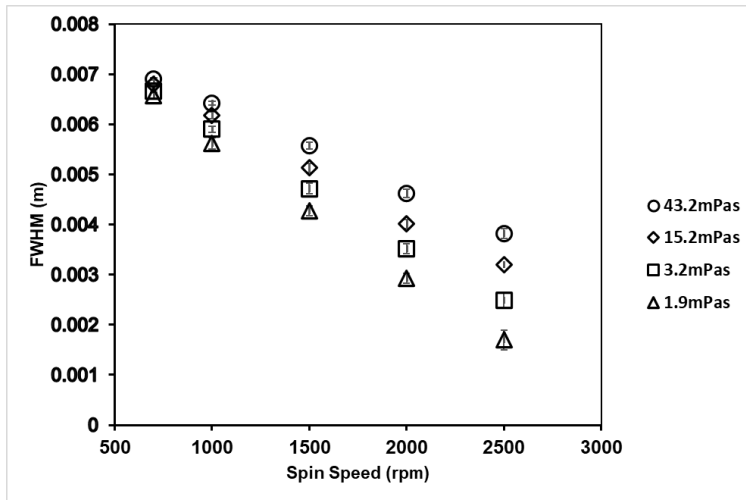


Figure 4-11.

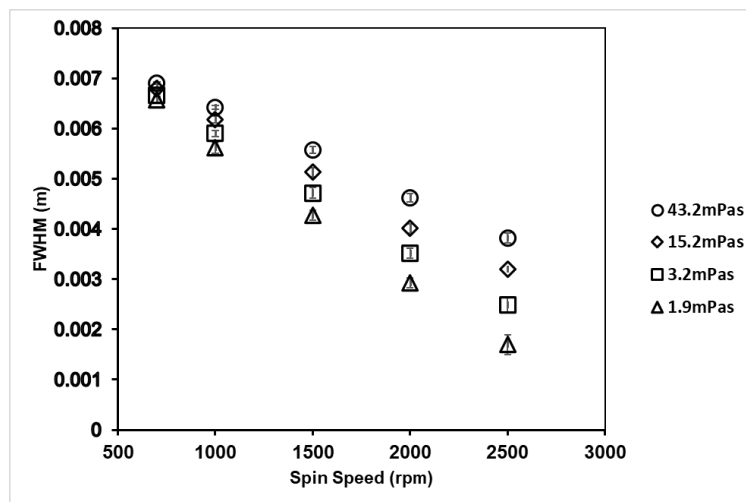


Figure 4-11: The full width half measure (FWHM) of distributions of pickering emulsion in each PVA of viscosities (1.9 mPas, 3.2 mPas, 15.2 mPas and 43.2 mPas) plotted against spin speed (rpm).

The rate of change of FWHM of pickering droplet cluster distribution as speed decreases differ for all types of PVA viscosities. The decrease in viscosity leads to lesser degree of PEG-C-GM-pi-FF cluster spread due to lesser density that is unable to enhance the inertia force required to displace magnetised PEG-C-GM-pi-FF. It can

also be observed that from the radial position of $0.013\text{m} \pm 0.004$ and above, the integrated density of droplets were lesser at higher spin speeds than lower spin speeds. This likely resulted from gradual displacement of droplets from the concentrated central region ($>0.01\text{m}$) to farther regions of the substrate.

The statistical distribution profile only tells the relative quantity of pickering droplets at specific regions of the substrate. However, the pickering droplet dipole-dipole interaction by magnetic field in structuring linear diffracting orders of linear chains and gaps also potentially changes across the thin film. Thus, the measured changes would qualitatively relate to the applied magnetic and fluid inertia forms of energies to further capture the tunability of the patterning resolution.

After observation via images of samples prepared under varying viscosities and spin speeds (see *Appendix 8.5*), the preferred configuration selected going forward for thin film nanostructure coating on glass slide was 15.2mPas PVA viscosity and speed 2500rpm . The reason was because it gave a better grating profile/pattern consistently (see *Appendix 8.6*).

4.4.3 Pattern Morphology Analysis and Mapping

The generated pattern from the magnetic and spin coating process provides unique trends, where the region close to the centre of the substrate experiences stronger magnetic field force compared to the force of inertia through centrifugal action. On moving further away from the centre, the centrifugal (inertia) forces become more dominant than magnetic force observed by analysis from the previous section. In order to understand how these forces impact on 2-dimensional linear arrangement of particles within the thin film and overall resolution of structure, a map for structure resolution was generated that depended on dimensionless quantities and ratios. Parameters such as the chain length (CL), chain thickness (CT), array gap or chain gap (CG) were set in ratios, such as; CL/CT and CT/CG . CL/CT explains how the chain length changes with respect to the chain thickness, where higher magnetic field strength develops thicker columns or labyrinth that are irregular and closed packed therefore breaking the consistency of having a long dipole-dipole chain order. CT/CG identifies the change in chain thickness with respect to array gap. Under strong magnetic field energy, the droplets are close packed or tightly aggregated with very

tiny gap in between. However, under weaker magnetic field strength, the gaps are more obvious. Therefore, each of these ratios were then related to the ratio between magnetic energy and energy of a fluid on a spinning disc.

The magnetic field impacts on the pickering droplets of an heterogenous mixture. The pickering droplets aggregate under the influence of magnetic field to form thin or thick chains or columns depending on the location at substrate surface and magnetic field strength. This packing of pickering droplets to form aggregates is determined from the packing energy formula (Mingsheng, et al., 2013);

$$EMD = m_{DD} \cdot B \quad [4-3]$$

Where;

B is magnetic field strength in $\text{Kg}/(\text{A}\cdot\text{s}^2)$ at a particular radial point (R) on the substrate surface, m_{DD} is droplets dipole moment of interaction ($\text{A}\cdot\text{m}^2$), and it is given as (Kang, et al., 2004);

$$m_{DD} = \left(\frac{\pi d_f^3}{6}\right) \left(\frac{M_{DR}\mu_o}{B}\right) \left(2\frac{B}{\mu_o} - M_{DR}D_{dm}\right) \quad [4-4]$$

d_f is the diameter of the droplet, M_{DR} is the magnetization (A/m) of the pickering droplets, μ_o is free space magnetic permeability, given as $4\pi \times 10^{-7}$ Henry/m and D_{dm} is the demagnetization factor, it is assumed to be $1/3$ due to their spherical shape (Maria, 2017). $M_{DR} = 0.06 \times M(H)$ is the equivalent magnetization of pickering droplet that comprises of magnetized magnetite nanoparticles from the $M(H)$ curve is shown in Figure 4-1 (c).

When this pack of pickering droplets is subjected to spin coating (centrifugal action), this energy tries to distort the aggregates and disperse the pickering droplets.

Since it is already defined the magnetic packing energy, EMD (referring to Equation [4-3]), the fluid inertia energy EFI is defined as;

$$EFI = \frac{1}{2} \rho_{pol} V_{FF} u_p^2 \quad [4-5]$$

Where; V_{FF} is the volume of spherical ferrofluid droplet, u_p is the velocity of polymer over from centrifugal action.

By definition, the velocity of thin liquid over a spinning disc is given as Eq. [4-5];

$$u_p = \frac{\rho_{pol}\omega^2 R h_0^2}{\mu} \quad [4-6]$$

$$V_{FF} = \frac{\pi d_{FF}^3}{6} \quad [4-7]$$

$$EFI = \frac{\rho_{pol}^3 \omega^4 h_0^4 R^2 \pi d_{FF}^3}{\mu^2 \cdot 2 \cdot 6} \quad [4-8]$$

Therefore, the energy ratio EMD/EFI was used to identify and correlate impact of both energies on resolution of pattern in thin film. The purpose for this was based on the force contention between the driving fluid and magnetic dipole-dipole force which occurred locally as the shear stress of the fluid between the magnetized droplets (i.e., assuming they are hard spheres) potentially led to breakup of chain length, trimming of chain width and increase in gaps. Thus, the study on displacement of particles was carried out using the x, y coordinate system, where the characteristic chain length was taken radially from the centre and liquid inertia taken to be dependent on the characteristic height of liquid from the surface of the substrate.

The characteristic height used for this study was; h_i , the new film height after t (sec) of spinning to top spin speed, ω from initial rest $\omega = 0$, and initial height h_0 . The average speed ω_{acc} was determined by taking the average of integrated area across the acceleration time t_{acc} of 1 sec. 'R' is the radial position of substrate under investigation. Thus, the solution provided as shown in Eqn. ([4-9]).

$$\omega_{acc} = \frac{1}{t_{acc}} \left[\frac{1}{2} t_{acc} \omega \right] \quad [4-9]$$

On applying the spin coating expression derived by Emslie and co, (Emslie, et al., 1958), the height of film after spin time t (sec), can be determined using Equation ([4-10]).

$$h_i = h_0 / \sqrt{1 + \frac{4\rho_{pol}\omega^2 h_0^2 t}{3\mu}} \quad [4-10]$$

The ratio, $E_{CL} = h_i/R$, is defined as the thin film parameter (Lawrence & Zhou, 1991), (Weidner, 2018). When used to divide the ratio EMD/EFI gives a dimensionless

parameter Q_{PI} . This parameter plotted against CL/CT and CT/CG ratios to develop the pattern resolution map.

4.4.3.1 Mapping

The sets of samples used for this study were made from the Pickering emulsion dispersed in aqueous 3.3wt.% PVA. The images of coated samples were taken using darkfield microscopy, and were processed into a binary construct with the use of image J®. This was done by converting the images into 8 bit, sharpening the profile and edges, then enhancing the contrast by 10%, and lastly making a binary of them which counted pixel intensity as 0 for black and 255 for white by using the plot profile tool. This process helped in establishing an efficient distinction on the droplet assembly profile across the film from the background. Figure 4-12 shows an example of such profile analysis of images taken from magnetic profile (shown in Figure 4-1(c)), with spin speeds of 3500 rpm and radial points at 1mm, 2.5mm and 4.2mm from centre of substrate. The combination of the above mentioned three parameters established ratios $Q_{PI} = 14.2$ and 5.7 for Figure 4-12 (a & c) respectively. The images in Figure 4-12 (a & c) are binary processed images. While Figure 4-12 (b & d) are the 3D plot of the scans for the 4 locations (red lines in Figure 4-12 a & c) separated approximately $50 \mu\text{m}$ apart. The binary plot distributions appeared more clustered for Figure 4-12 (b) while least thick for (d). The entire lines are challenging to distinguish, therefore the number of bar divisions greater than zero were counted as droplet, while values at zero taken as gap. The division utilized in this analysis was $167\text{nm}/\text{pixel}$. A brief example of data is shown in *Appendix 8.8*, where it shows the binary values (>0 and 0) for each 167 nm divisions. This do not actually represent the thickness of chains and chain gaps. Therefore, a simple code was written (presented in *Appendix 8.6*) to group consistent divisions of white pixel (>0) and black pixel (0) into number of pixels in chain thickness (CntCT) and number of pixels for chain gaps (CntGap) respectively, with an example shown in **Table 4-3**. The estimated numbers were multiplied by $0.167 \mu\text{m}$ to obtain the dimensional thickness and gaps of chains. The average and standard deviation of the profiles are shown in **Table 4-4**. The average values (Av) of the combined for scanned profile were

reprocessed to obtain the ratio between thickness of chain and gap between them by $Av/(1-Av)$.

The same procedure was executed for chain length (green profile lines in Figure 4-12 a & c), which was drawn and measured manually. However, the breakage of dipole-dipole chain that led to variations in estimated chain lengths following measurements using the condition of chain breakage when break gap is $>2 \mu\text{m}$.

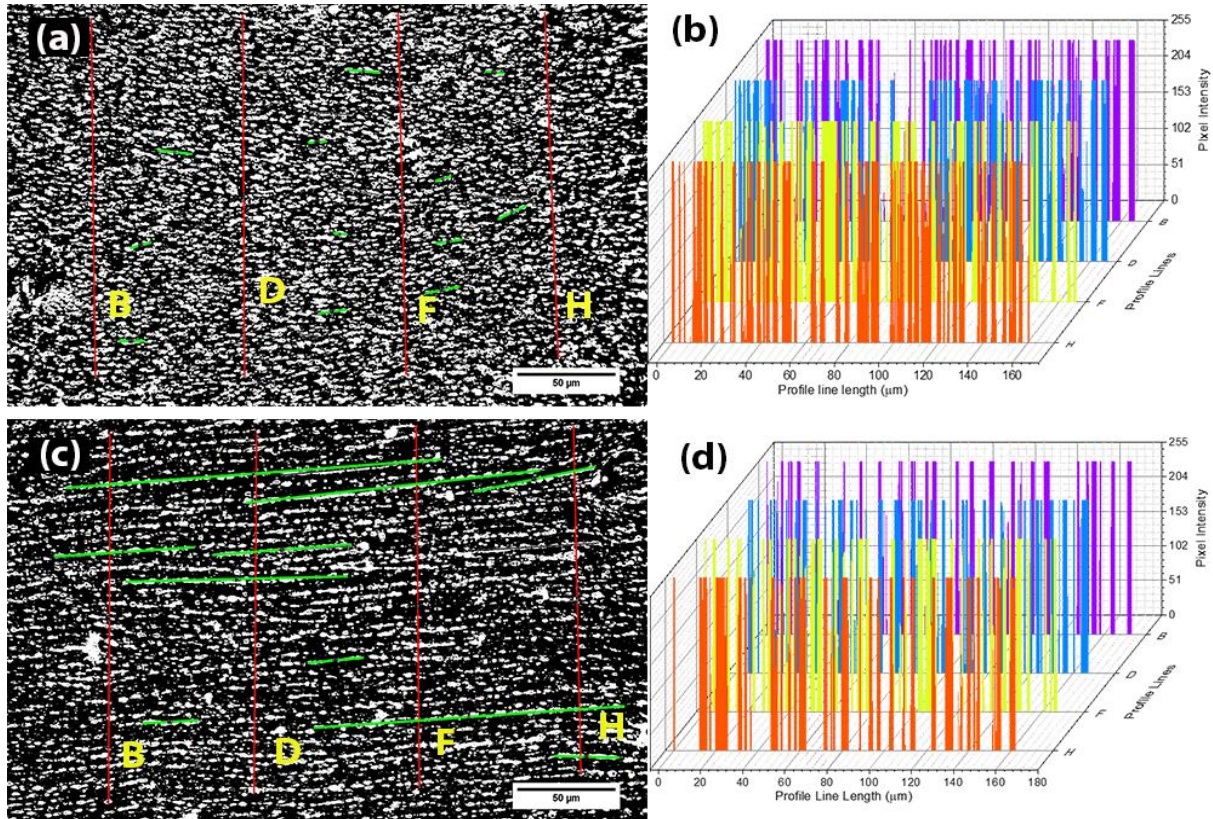


Figure 4-12 Average resolution of pitches between chain thickness and gap was determined from region of interest scan profile lines (red lines B, D, F & H) of binary processed plot profile images (a & c). The green lines are manually measured chain lengths. Images (b & d) are generated profile distributions for $QPI = 14.2$, (a) and $QPI = 5.73$ (c).

Table 4-3 Example of output from simple program (in Appendix 8.6) that counted number of pixels in each chain block to identify chain thickness and chain gaps within the scanned profile. CntCL and CntGap is number of pixel counts for a chain and gap respectively.

Scan profile 1		Scan Profile 2		Scan Profile 3		Scan Profile 4	
Total No. Rows							
805		857		931		885	
CntCL	CntGap	CntCL	CntGap	CntCL	CntGap	CntCL	CntGap

4	3	3	2	6	5	2	1
5	2	4	14	1	5	9	1
4	11	3	2	2	5	2	3
8	6						

Table 4-4 Summary of results obtained from image analysis of sample prepared under 3500 rpm spin speed.

3500 RPM									
r (m)	CG (μm)	CT (μm)	CL (μm)	SD-CG	SD-CT	SD-CL	CL/CT	CT/CG	Q_{PI}
0.001	2.32	2.66	42.7	0.14	0.23	5.32	2320	1.15	13
0.0025	2.65	2.46	93	0.22	0.2	1.72	1060	0.93	5
0.0042	2.82	2.15	209	0.5	0.07	19.	672	0.73	2
0.0049	3.05	1.94	98	0.58	0.14	13.5	622	0.64	1.5
0.0057	5.03	1.215	1.21	0.32	0.076	0.34	883	0.24	1

SD represents Standard deviation

The averaging of chain thickness, chain gap and chain length across different regions for each spin speeds (2000rpm, 2500 rpm, 3000 rpm and 3500 rpm) can be found in *Appendix 8.9*. The series of ratio values (CT/CG and CL/CT) were calculated to establish non-dimensional values and relationships. Ratio CT/CG was calculated because it provided the estimation of the grating size, as well as observation on how the effective change of thickness and gap relied on the variations in values of Q_{PI} . Ratio between CL and CT (CL/CT) was calculated in order to relatively quantify the effective change between cross-section and length of dipole chains. In a situation where multiple stacking of pickering droplets that formed clusters, the chain thickness increased gradually forming vertical columns with growing numbers of breakage between chains. Also, when fluid velocity was high enough, it sheared and pulled oriented pickering droplets from their positions to create chain length breakages.

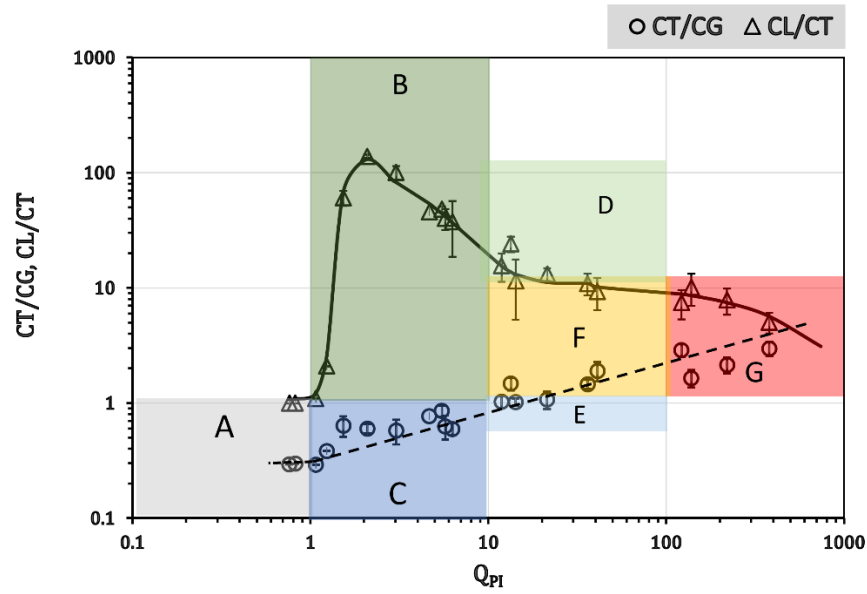


Figure 4-13 This is a log-log plot representing the ratio between chain thickness and chain gap (CT/CG) is linearly related to Q_{PI} (between 1 and 1000), and $Q_{PI} \leq 1$ CT/CG is constant. While chain length and chain thickness (CL/CT) unevenly varies with Q_{PI} ratio

Taking cue from the works done by (Mou, et al., 1994), (Lawrence, et al., 1994), it was explained how increasing strength of magnetic field would drive droplets to form thicker columns, and further more into Labyrinth-type structures. Q_{PI} was calculated to realise sections of the substrate and deposited solution facing varying degrees of energy dominance between magnetic and centrifugal forces. Two relationships of log plots (Figure 4-13) was created involving CL/CT vs Q_{PI} and CT/CG vs Q_{PI} with radial points as a common factor between each dimensionless ratio.

At $Q_{PI} < 1$, the sets of points for CT/CG and CL/CT are constant; because in this domain (region A), the fluid inertia energy is higher than the magnetic, leading to pickering droplets being randomly dispersed by centrifugal forces which is in consonance with other magnetic dimensionless numbers like the Magnet Bond number, Hartman number, Magnetic Laplace number, Thermal stability number, etc.; where at ratio values below unity, the contending energy component dominates over the magnetic (Ganguly & Puri, 2010), (de Gennes & Pincus, 1970), (Williams, et al., 2010). This is significant at points farther from the centre of the film with relatively lesser concentration of droplets compared to the centre, therefore having more gaps

between each droplet. This is also the reason why CG is greater than the diameter of the droplets (i.e. CT), as identified in Figure 4-14(a). For CL/CT in region A, the values are unity because it identifies with the diameter of the droplets.

Regarding energy ratio range **$(1 = < Q_{PI} \leq 10)$** , region B for CL/CT and region C for CT/CG were analysed. In region B, the magnetic energy becomes growingly greater than the fluid inertia, where a rapid change of chain length in comparison to chain thickness was observed. The sharp rise from CL/CT=1 to CL/CT~100 within the short range of energy ratio ($1 = < Q_{PI} < \sim 2$) identifies with a growing number of droplet-droplet interaction toward chain formation (see Figure 4-14 (a)-insert). This increase was coupled with the gentle increase in chain thickness from clustering of droplets as CT/CG increased from 0.1 to 0.5 with gaps still larger between each formed group chains in region C. At $Q_{PI} = 2$, where the inertia energy was within the range of at least half of the magnetic energy to the maximum chain length (from CL/CT~100) was attained where CT/CG = 0.5 (see Figure 4-14 (b)). The increasing values of Q_{PI} towards 10 led to a gentle exponential decline in CL/CT; which insinuates the growth of thicker chains from the increase in magnetic field and lesser inertia velocity about that region of the substrate. Meanwhile at that energy ratio point, the CT/CG=1, signifying high grating divisions of the same chain thickness and gap, thus lesser wobbling or thickness variation due to excessive multiple droplet clustering within each chain, as can be seen in Figure 4-14 (b)-insert.

On **$10 < Q_{PI} \leq 100$** , The decline of CL/CT continues well into region D, where noticeable levelling begins to emerge from $Q_{PI} \sim 20$ till ~ 100 (at CL/CT ~ 10), as can be seen in Figure 4-14 (c). A transition was observed as the chain thickness increases in contrast with the gap between each chain, and this tends to be within ranges ($0.9 \leq CT/CG < \sim 2$) between regions E and F, while ($9 \leq CL/CT < \sim 20$) between regions D and F showing a nearly perfect straight-line distinction with chain length approximately 10 times more than chain thickness (Figure 4-14 (c)). In this region, the chain thickness is relatively the same as that of the chain thickness found within the range ($6 = < Q_{PI} < \sim 10$). Therefore, the reason for the shortening of the chain lengths was because of the growing columns from the overlaying of pickering droplets. The overlay packing of pickering droplets from dipole-dipole interaction

close to the centre of the substrate is as a response to the near perpendicular magnetic field flux direction (to the substrate surface); thereby causing growing column-wise repulsion in the θ -direction, which initiates the out of focus alignment, irregularities and identified chain breaks in this region.

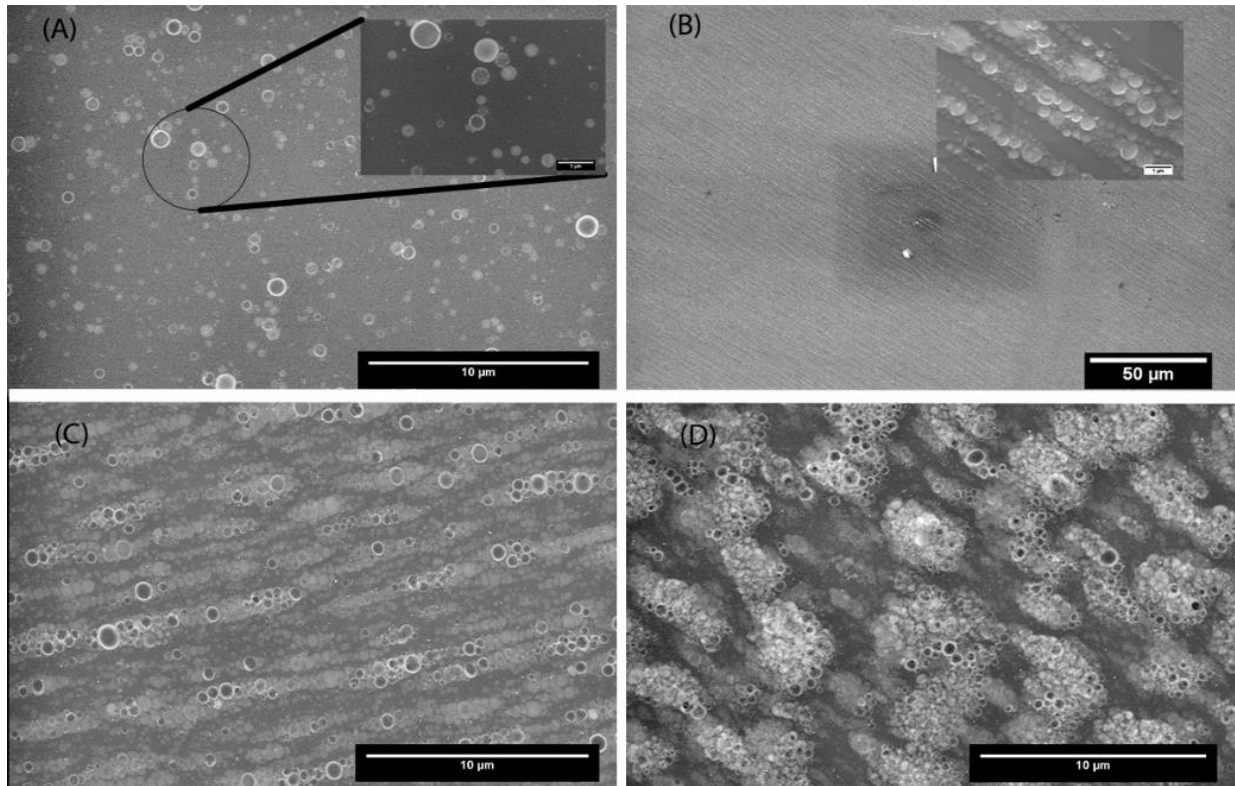


Figure 4-14 SEM images of sections of a sample to aid illustration of plot shown in Figure 4-13. (a) Is coherent with section A of Figure 4-13, where it shows a 6mm radius from the centre of the substrate with droplets randomly dispersed and few droplets forming short-singular chain, as shown in the insert image. (b) This is coherent with data points of CT/CG and CL/CT within the blue region and green region of C and B respectively in Figure 4-13. (c) is an illustration for datapoints CT/CG and CL/CT within regions D-F and E-F respectively ($100 \geq Q_{PI} \geq 10$) in Figure 4-13. (d) Image of section at the centre of the substrate equivalent to section G of Figure 4-13, where dense columns of droplets dominate structure pattern.

For range of $Q_{PI} > 100$, CL/CT is seen to rapidly decrease, showing an increase in chain width and shortening of chain length with more frequent breaks; pointing out that droplets are highly responsive to external magnetic field as multiple directional domains are established amongst interacting droplets; thus, making dipole-dipole interaction dominant in z-direction and side repulsions in θ direction. This is solely due to the heterogenous field distribution nature of permanent magnets and its position underneath the substrate. This thick columns with small gaps in between them can be noticed with an exponential rise in CT/CG towards a value of 5 as energy

of magnetization and viscous effect becomes 10^2 fold greater than energy by inertia. Figure 4-14 (d) shows an image depicting the trend seen in region G indicates the dominant nature of the magnetic field energy, as more thicker columns with worm-like or labyrinth-like formats are established. They have little gaps in-between with little or no significant chains to see. This is true because the CT/CG data points begin to rise higher, while CL/CT decreases as they become the same value at $CT/CG = CL/CT = 4$ (where; $Q_{PI} \sim 5 \times 10^2$).

It is vital to state that the trend line fitted for data points in Figure 4-13 does not necessarily and potentially represents data from processes with other magnetic field configurations. However, the mapped regions essentially identify and encompasses data from any preparation process.

4.4.3.2 Other Magnetic Configurations

This section involves the testing of the map created in section 4.4.3.1 with two different magnetic setup and field profiles, using similar spin speeds as applied in the previous profile. Figure 4-15 shows schematics and plot profiles for the two types of magnetic setups. It is magnetic profiles measured from the centre to outer radial range at x, y, and diagonal directions were averaged to obtain the profile of each setup revealed in Figure 4-15 (a).

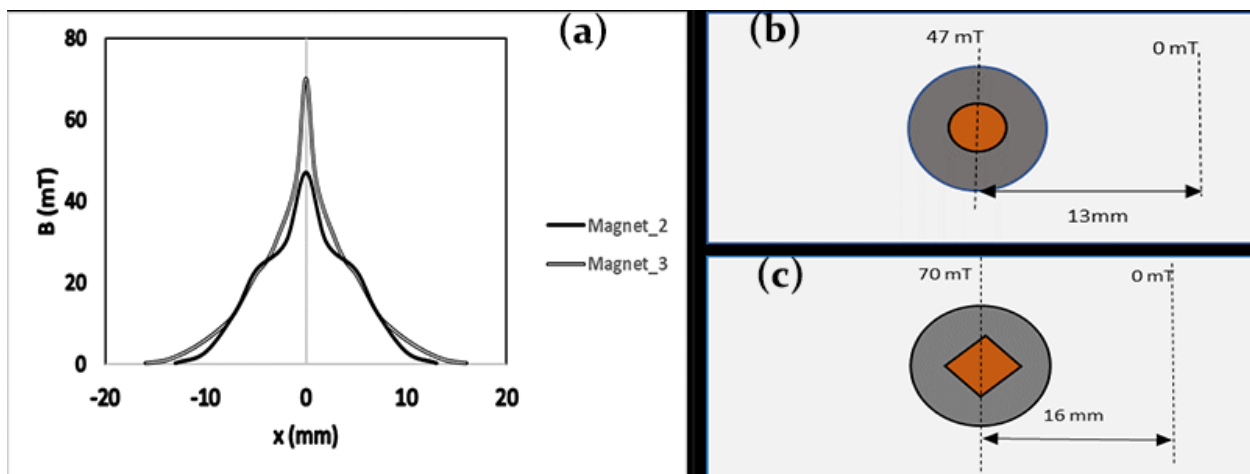


Figure 4-15 (a) Schematic of plot profile for Magnet setup for magnet 2 (b) and magnet 3 (c).

The preparation procedure used was the 15.2mPas PVA under varying spin speeds. The scan locations and respective energy ratio was matched with the ratios of

CT/CG and CL/CT, along with their respective standard deviations from their variations determined from an example of high-resolution pattern image processing shown in Figure 4-16, along with the full data presented in **Table 4-5**.

Table 4-5 Data of some of the test magnetic setups, Magnet 2 and 3 showing ratios QPI against CL/CT and CT/CG with their respective standard deviation values (SD)

Magnet Profile	r (mm)	Speed (rpm)	Q _{PI}	CL/CT	SD	CT/CG	SD
Mag_2	8.1	2000	4.02	69.76	19.55862	0.391602	0.056022
	7.7	2500	3.40	95	12.93556	0.397527	0.013383
	7.4	3000	2.82	61.10	19.86875	0.394434	0.055393
	6.6	3500	4.41	132.92	24.70177	0.491759	0.044645
Mag_3	7	2000	18.1	30.8	9.824	0.512057	0.048482
	7.2	2500	6.95	84.8	22.00	0.454376	0.044517
	5.3	3000	48.1	21.9	9.98	0.672242	0.017388
	6.5	3500	6.75	121	12.22	0.45088	0.052774

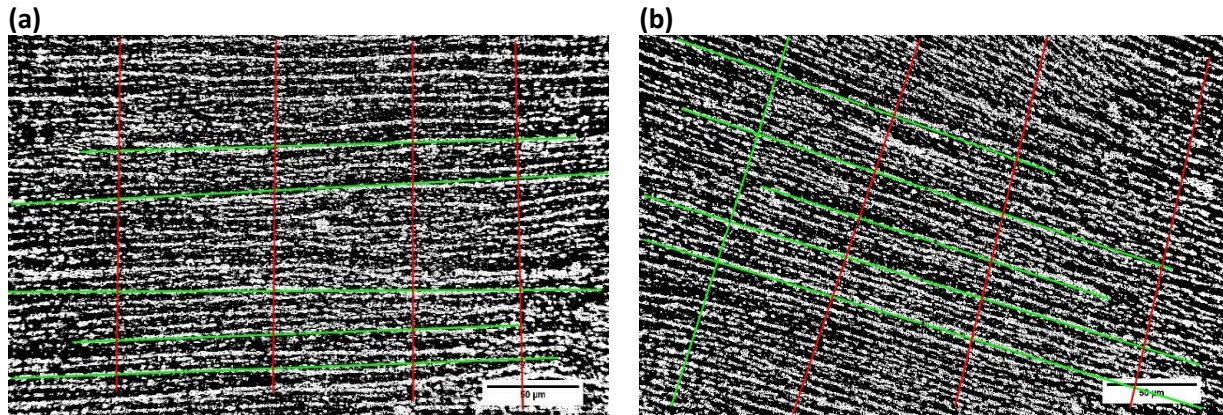


Figure 4-16 : Binary processed image profile of (a) Magnet_2 at radius 8.2mm under speed 2000rpm (b) Magnet_3 at radius 4.4mm from centre under speed 3500 rpm. Scalebar is 50µm.

When data points from **Table 4-5** were placed on the designed map from Figure 4-13, they tend to lie deviated from the pre-constructed lines of CT/CG and CL/CT (see Figure 4-17). The deviation points from these lines were calculated and it was realised that for Mag_2, CT/CG deviated by ~50% and CL/CT deviated by 30%. As for Mag_3, CT/CG deviated by ~50% and CL/CT deviated by ~90%

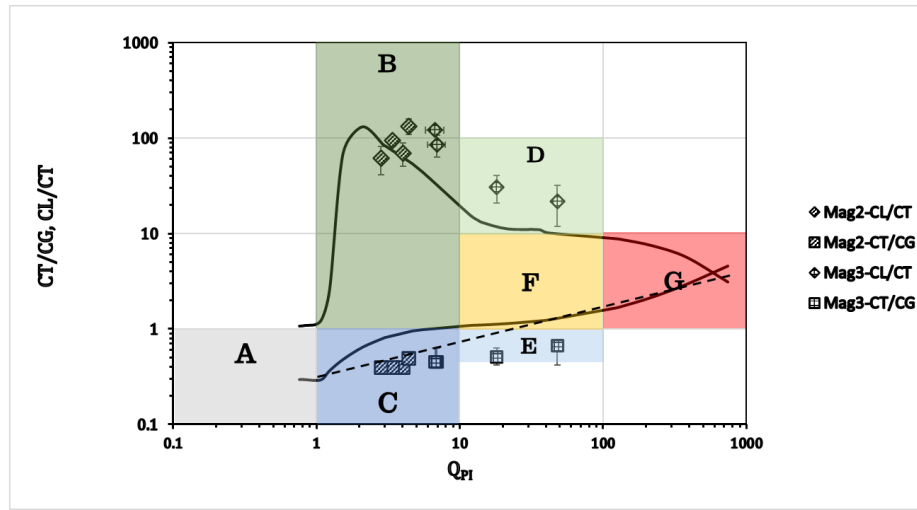


Figure 4-17 The calculated sets of data shown in **Table 4-5** for magnetic profiles Mag 2 and Mag 3 shown in Figure 4-15 , were fitted into the pattern profile map; the CL/CT ratio for both Magnetic profiles fell within the estimated regions with approximately 30% for Mag_2, 90% for Mag_3 deviation from the profile curve. While for CT/CG, the data points fell within the expected regions with deviations from profile curve approximately 60% for Mag_2 and 50% for Mag_3.

Understanding the deviations of pattern data points from both magnetic setups, it is perhaps clear that stronger magnetic fields would lead to longer chains and higher chain thickness to chain gap resolutions.

It can be observed that the datapoints of the tested magnetic profiles lie within the expected regions of the map; where thin longer chains as long as 500 μm with distinctive and fairly consistent gaps at 10 μm , (as shown in Figure 4-17) are more prevalent in regions where the energy ratio is within the range $1 \leq Q_{PI} \leq 10$. From these profiles tested, it can be seen that strong magnetic fields as high as 20mT and centrifugal speeds as high as 1.5 m/s are necessary to create long chain arrays within the Q_{PI} range mentioned previously.

4.4.3.3 Defectivity

Extending the limits of nanofabrication toward sub-micron to nanometre scale using self-assembly approach has its impact on pattern consistency. This has been one of the biggest challenges towards industrial adaptation; especially with the challenge of an efficient means of estimating degree of defectivity within a prepared structure using a particular preparation process. Image analysis has been a useful technique in identifying such defects and estimating the degree of defection. Such that the images are taken from less defined formations showing defects of less optimum areas

compared to optimum ones. Defect density is estimated as the number or size of defect per unit section of region of interest.

Therefore, in this section, lines were drawn along chain lengths of binary processed images of sections within the substrate. As already know, the profile scan data provides a histogram resolution of droplets (white) and gaps (black) of the scanned area; with the white having values greater than zero while black values are equal to zero. Figure 4-18(a&b) presents binary processed images of Q_{PI} of 75.4 for (a) and 2.28 for (b). Their respective inserts are 3-dimensional plot showing the specific scan line, scan line length (um) and binary pixel intensity. The resolution of this binary points was 167nm. From the plot profile the number of binary points at zero were automatically counted and multiplied by the resolution to obtain the total length covered by the gap. This total length was then divided by the scan length of the profile, thus providing an average value of the defect. Since the scan lines in this case are four in number, an average was further estimated alongside its standard deviation. The degree of defect for the data from Figure 4-18 were (a) 4.3% with a standard deviation of 0.0193 and (b) 11.6% with standard deviation of 0.0285. This is expected as systems having higher magnetic energy than inertia tend to be tightly packed with little space in between compared to systems where inertia energy is higher than magnetic energy.

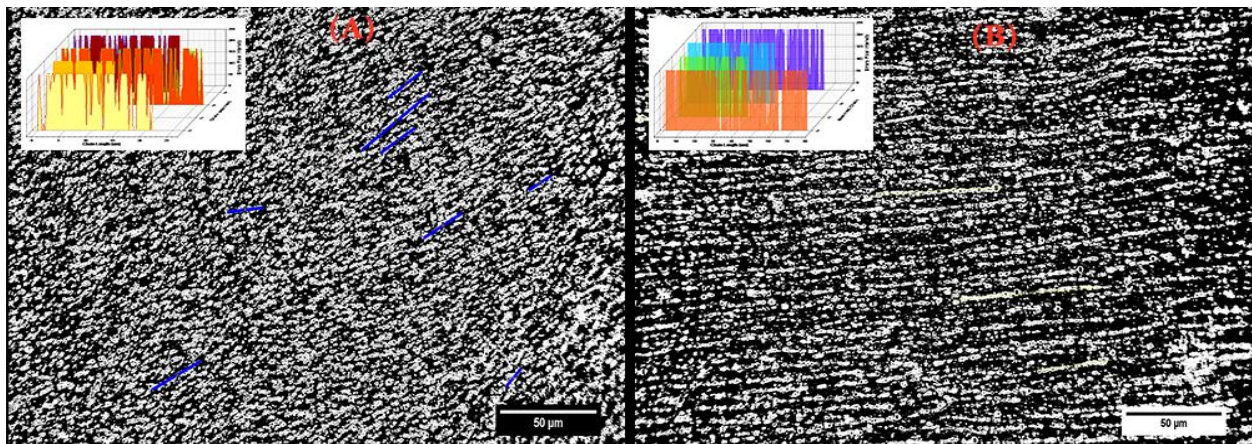


Figure 4-18 Defectivity trace detection for (a) $Q_{PI} = 75.4$ and (b) $Q_{PI} = 2.82$. The inserts are representative 3D plot profiles of 4 scan region of interest lines across varying chain length within each image. (a) tend to have shorter chains but thicker profile bars, while (b) have longer chains but less thicker bars. The defectivity for (a) is 4.3% with $SD = 0.0193$ and (b) is 11.6% with $SD = 0.0285$.

Although, this defectivity estimation is not complete without factoring in the respective chain lengths attained from differing energy ratio values. It can be noticed that within an array consisting of chain breaks, the gap existing is a defect to be accounted for and these were measured as well, taken to be (CM). This value is then added to the defectivity within the chains itself. If the chain doesn't have a defectivity, it is marked with a dashed (or null) point. **Table 4-6** shows calculated values of final defectivity estimate considering chain lengths.

Table 4-6 This is a result summary from image analysis of structured sample estimating its area defectivity from gap between consecutive tail and head of chains along an array and short gaps within individual chains (DEF_{CL}).

Q_{PI}	CL (μm)	Percent gap between head and tail of consecutive chain in an array (% of CM/CL)	Defectivity on individual chain (DEF _{CL})	Standard Deviation of DEF _{CL}	Area Defectivity DEF _A $DEF_{CL} + \frac{CM}{(CM + CL)}$	Standard Deviation
112.8	22.1	30.1	-	-	0.23	0.036
75.4	25.5	20.58	0.043	0.019	0.21	0.019
2.8	124	8	0.116	0.029	0.19	0.029

The summary of results shows that higher values of the ratio (Q_{PI}) generate more defectivity and thus instability within the structure. However, the overall defectivity across three energy ratios is not extremely far apart; which can then be averaged to give an overall defectivity value of 21.2%.

4.4.3.4 Ring Magnet Profile distribution

The introductory test of the type of setup shown in Figure 4-19, is inspired by conventional opposite pole (N-S) flux bridge. Two magnets with faces of opposite pole attract each other by creating a source (North pole) and sink (South pole) directional field lines which improves dipole interaction and organisation of magnetised particles along the imaginary flux lines as witnessed for two permanent magnets.

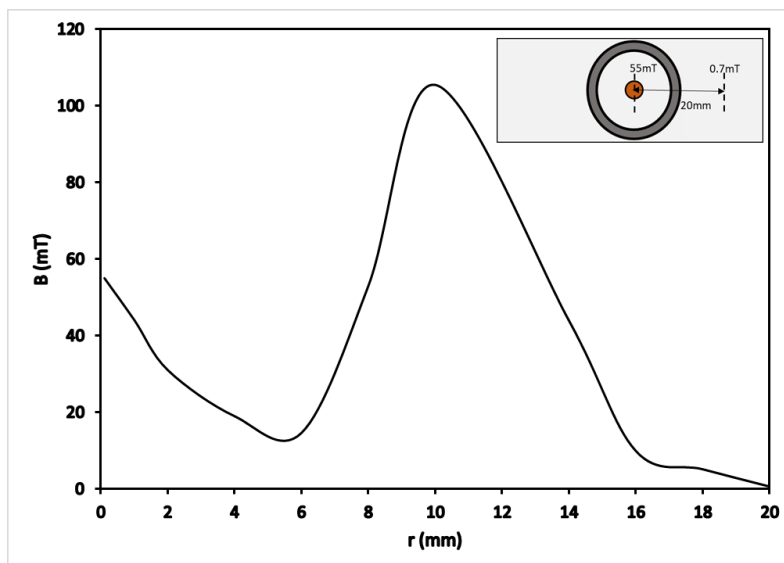


Figure 4-19 : measured and plotted magnetic field strength profile (B mT) along radial distance r (mm), with a small magnet of 1.5 mm in diameter, the ring is 8mm inner diameter and 12mm in outer diameter.

The thin film was prepared using PVA 3.3w% and spin speed of 3500 rpm. The samples possessed a birefringent ring of refracted light due to the cluster density/distribution of organised pickering droplets. Images of samples were taken with an Olympus digital camera (Figure 4-20a), a closer up look using an Olympus brightfield microscope with a 5X, N.A = 0.1 magnification lens (Figure 4-20 b), and a 20X, N.A = 0.4 magnification lens (Figure 4-20 c).

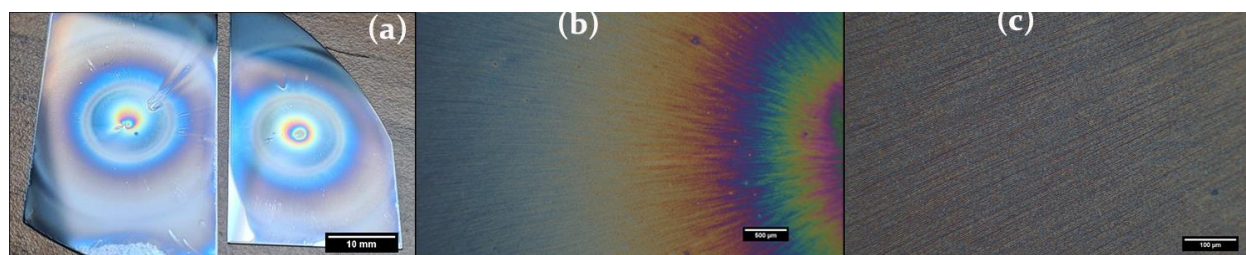


Figure 4-20 Nanopatterned thin film on silicon wafer prepared under 3500 rpm spin speed ~ (a) taken with Olympus digital camera, (b) taken with Olympus brightfield microscope under reflection mode with a 5X magnification lens, N.A. = 0.1, and (c) the same microscope but with a 20X magnification lens, N.A. = 0.4.

Images of a sample were taken using a 50X objective as conventionally carried out for previous setups and analysed the same way. The preparation process (Magnetic field and spin speed) was used to quantify the energy ratio (Q_{PI}) across the substrate as seen in *Appendix 8.10*. In terms of image analysis, the chain length is longer than

the length of the image frame making it challenging to quantify. If taken to the next magnification (20X), the resolution and distinction was hard to identify. However, the chain length about this region was assumed to be approximately 1500 μm . At radial distance between 2mm to 6mm the CL/CT are seen to soar beyond the mapped regions.

The images from different radial points of the samples were processed into binary and profile lines were drawn to obtain data on CT/CG using image J® and the simulation program in Appendix 8.6. Example of results are shown in Figure 4-21.

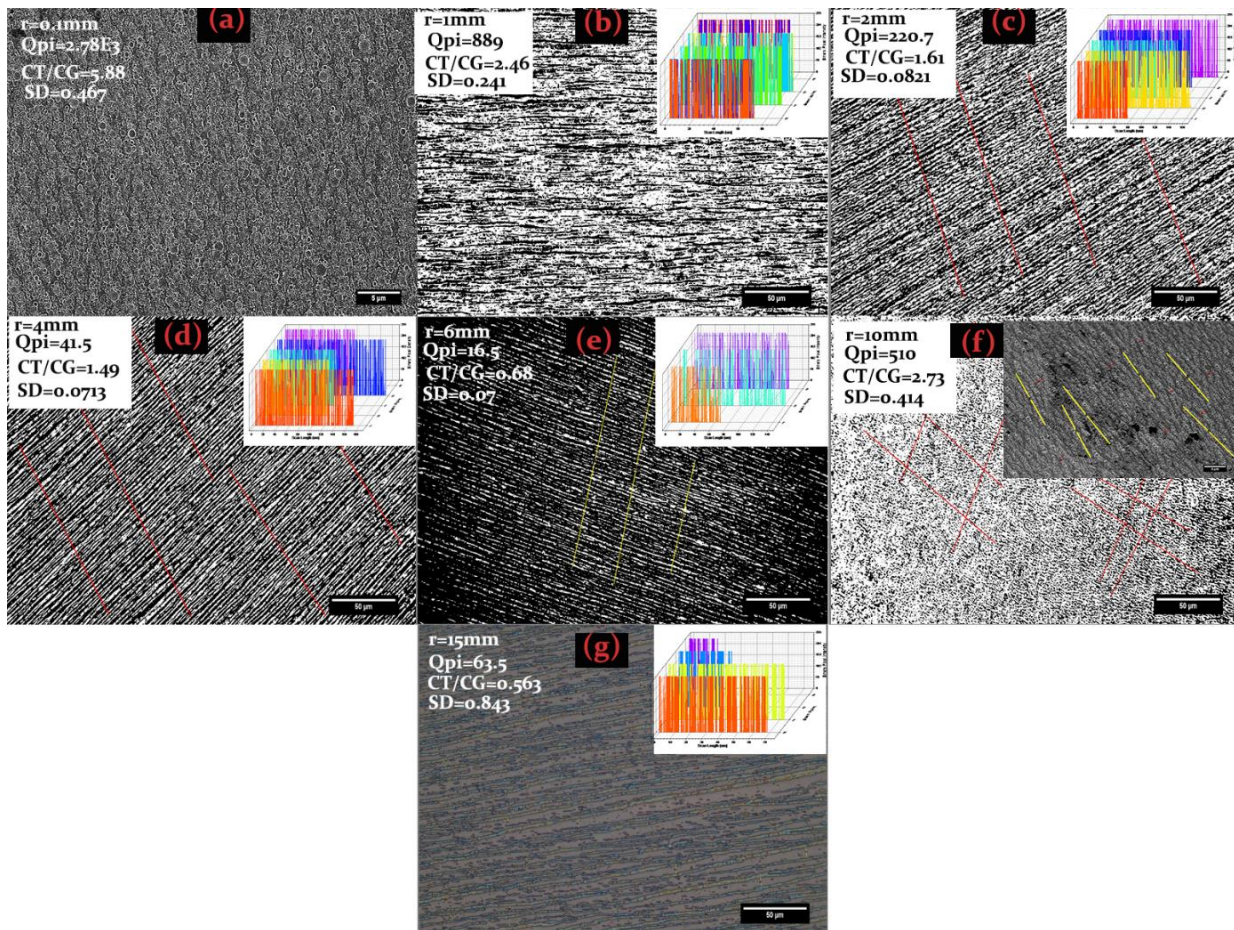


Figure 4-21 Thin film nanostructure profile on silicon wafer (a) SEM image 0.1mm close to the centre of the substrate, (b) Binary image 1mm from the centre of the substrate with binarized plot profile of resolution, (c) Binary image 2mm from centre of substrate with binarized plot profile of resolution, (d) Binary image, 4mm from middle of substrate with binarized plot profile of resolution, (e) Binary image, 6mm from middle of substrate with binarized plot profile of resolution, (f) Binary image, 10mm from centre of substrate with SEM image insert and measurements, (g) Binary image, 15mm from centre of substrate with binarized plot profile of resolution.

It can be seen that long chain and chain thickness and chain gap definition appear distinct and consistent for a long radial range, $\sim 10\text{mm}$, see Figure 4-21(a-e). This is evident when the CL/CT datapoints were plotted against Q_{PI} (Figure 4-22).

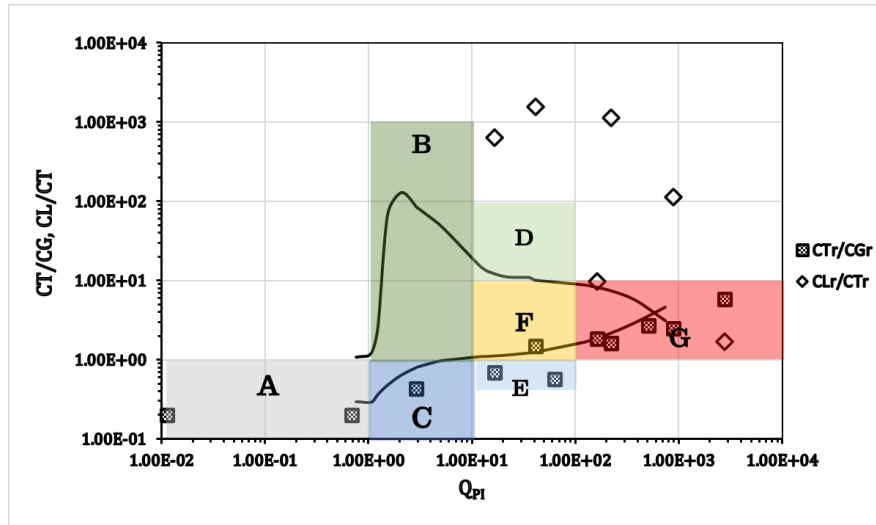


Figure 4-22 : Map showing ratio points of nanostructure. The CT/CG trend approximately followed the original CT/CG trend line further establishing the physical phenomenon of the shear and drag effect on column thickness. The CL/CT points between 2mm and 6mm are way higher (almost up to a thousand-fold) than the original CL/CT trend line..

This is because the flux lines between the inner and outer magnets acted as a form of continuum trapping mechanism which caused the droplets to act as tiny magnets with polarity and encouraging linear interaction. This led the chain lengths to be exceedingly longer than the length of captured image frame at radial section between 2mm to 6mm. Thus, when CL/CT was estimated by assuming the average chain length about this region to be approx. 1.5mm, the data points in the map were about a thousand-fold more than the original trend line running from D to G.

4.4.3.5 Defectivity

The chain length from the high-resolution CT/CG section of the sample was subjected under study to figure out if the defectivity (chain length consistency) has improved or not, compared to the other magnetic system setup. Profile lines were drawn upon each line of the binary image to obtain the pixel values. The pixel values higher than zero (0) were counted and pixel values that are zero (0) were counted separately (see Figure 4-23). The defectivity was calculated as the overall size of the gap

(number of 0's pixel counted X 0.167 $\mu\text{m}/\text{pixel}$) divided by the overall scan length. The outcome of results for selected profile scans are shown in *Appendix 8.11*.

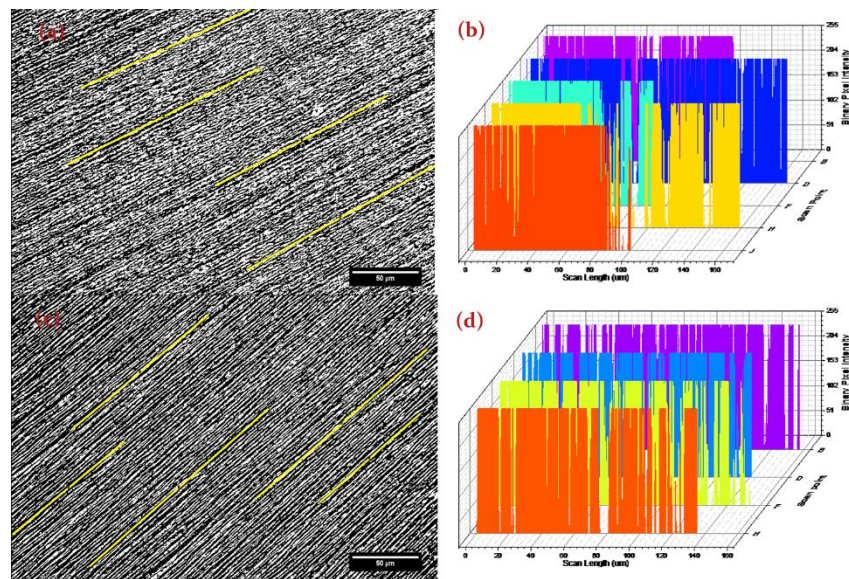


Figure 4-23 Defectivity profile measurements of random chains with (a) $Q_{pi} = 220.7$ and (b) representative binary plot profiles, (c) $Q_{pi} = 41.5$ and (d) representative binary plot profiles.

The final defectivity from the analysed profiles averaged $\sim 14.1\%$ as compared to 21% for the single magnet setup. Two magnetic setup seems to be an improved technique in achieving more improved structure resolution than for single magnet setup.

The defects could actually be lesser if it had not been for minor chain shift from one imaginary flux line to its neighbouring flux line. This specifically happens at dipole points where one droplet is exceedingly bigger than the rest which then causes branching of subsequently attached smaller droplets. The smaller side by side droplets would repel each other and then form a gap which when scanned using plot profile would be picked as a dis-continuum. Another contribution could be that images were taken using optical microscope reflection mode which has limited resolution due to the optical diffraction limit of light, and thus influence the observation of such anomalies. This is in contrast when using SEM, which can help picking on more visible droplets within the profile. Proof of such as shown in a SEM image (Figure 4-24) where the yellow straight line is an example of a scan profile for measuring

defectivity. Despite the chain being a continuum, it veers off the straight path (marked red oval circle 3), another gap detected due to branching at marked red oval 4. The effect of branching can be seen more evidently in yellow oval 1 as the bigger droplets having multiple polarities at its surface encourages multiple droplet attraction, which the branches at some point.

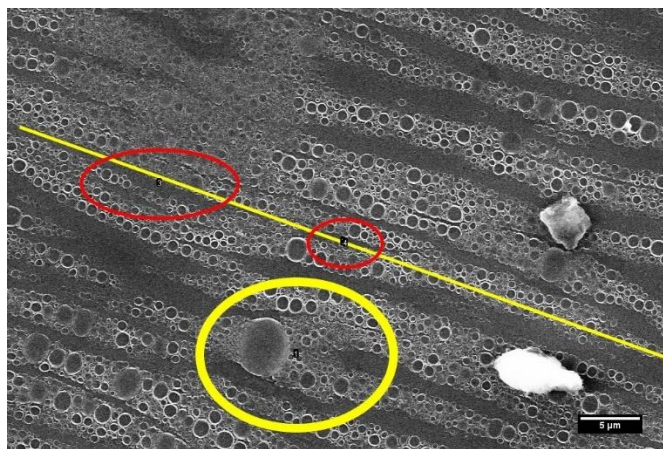


Figure 4-24 An SEM image of chain interactions upon a silicon wafer (referring to Fig. 4.21 (b)). The yellow oval 1 shows evidence of big droplet initiating branching of chains, The yellow straight line 2 is an example of profile line scan for detecting deflection which the highlights its deviation due to shifting of chain from straight path in the form of red oval 3 and 4.

4.5 Chapter Summary

This chapter presented an experimental study on a stimulated-directed self-assembly technique involving the design of magnetically tuned thin film nanostructure. A PEG-C-GM-pi-FF in aqueous PVA emulsion was subjected to magnetic field and spin coating action. This was in aim of investigating the effect of magnetic and inertia forces (by centrifugation) on the degree of cluster distribution and alignment of pickering droplets. Pickering droplets were dispersed in four separate concentrations of aqueous PVA with viscosities (43.2mPas, 15.2mPas, 3.2mPas, 1.9mPas), that were subjected to spin speeds of 700rpm, 1000rpm, 1500rpm, 2000rpm and 2500rpm, at an operating spin time of 60 seconds. This resulted in creating relationships amongst essential parameters such as magnetic strength, magnetic fluid susceptibility, continuous phase viscosity and spin coating speed. This study helped in achieving flexibility and tunability of manufacturing process for obtaining desired cluster distribution, as well as realising its limitations. Optical microscopy,

and scanning electron microscopy (SEM) were used to capture images of structure that were analysed to estimate pickering droplet density distribution and formed patterns resolutions. Therefore, from this study series of outputs were realised, such as;

- (i) The full width half measure (FWHM) of the distributions that represented the degree of spread of pickering droplets within the thin film was related to the spin speeds. It was realised that with higher viscosities (43.2mPas) and low spin speeds (700rpm), the FWHM was lowest ($\sim 13\text{mm}$) because of the low inertia due to viscous resistance. However, with low viscosities (1.9mPas) and high speeds (2500rpm), the FWHM was higher by $\sim 220\%$ because of the less viscous resistance and increased inertia force to overcome the magnetic force on pickering droplet. The FWHM for all PVA viscosities exponentially increased with increase in spin speed. Therefore, the rate of increase in FWHM across all spin speeds in relation to increase in viscosities exponentially declined at a rate of 63.4. The most prominent preparation combination under the terms of distinct chain order morphology and film stability was PVA viscosity at 15.2mPas and spin speed of 2500rpm.
- (ii) A patterning distribution map based on the r, θ coordinate system was created using the image analysis and profile measurements of chain thickness (CT), chain Length (CL) and chain gap (CG). Dimensionless ratios, CT/CG (for grating resolution) and CL/CT (for length of a particular chain thickness) were then plotted against the ratio (Q_{PI}) of magnetic packing energy (of pickering droplets) and fluid inertia (of polymer). Magnetic packing energy is quantified from dipole moment between droplets being multiplied by the magnetic field strength for a group of droplets within a chain or column (Suetsuna, et al., 2011). Where $Q_{PI} < 1$, individual droplets existed with huge relative gap in between. However, with increase in Q_{pi} to values as far as a hundred-fold, the CT/CG increased by a factor of 10, as CG reduces. In the case of CL/CT, the highest (by a factor of 100) was noticed in the region of $1 < Q_{pi} < 10$ for single magnet setup. Meanwhile, regions beyond this range experiences a decline in

- CL/CT. However, this was not the case for CL/CT in a concentric magnetic setup with two opposite poles that formed an imaginary flux line bridge for efficient dipole alignment of pickering droplets, experienced an increase as high as a 1000 fold from the Map trend line boundary was observed at $Q_{pi} = 100$, making CL dependent on magnetic setup/orientation.
- (iii) Defectivity test (i.e., a percentile quantification of irregularities, like chain breaks within the structure) was carried on pattern chains formed from the singular magnetic profiles which gave an estimated value of 21%. While for concentric magnetic setup, the defectivity values averaged $\sim 14.5\%$.
 - (iv) Lastly, the film thickness was measured using an SEM and the average thickness was 416 nm.

Chapter 5 Thin film Characterisation and Analysis

5.1 Chapter Objective

This chapter is focused on the optical characterisation of prepared thin film nanostructure. It is hypothesised that UV-VIS spectrophotometry would reveal the optical-charge dynamics between the gold and Fe_3O_4 dimer structure. The organisation of particles and degree of interaction at the nanoscale and the density of magnetically-ordered cluster chains would influence the degree of photo-absorption and electron diffusion across boundaries between Fe_3O_4 -gold, gold-gold, Fe_3O_4 - Fe_3O_4 dimer structures. The application effect of the gold- Fe_3O_4 dimer structure in array patterns can be tested using the specular reflectance mode for determining the surface enhanced infra-red absorption (SEIRA) of the coated polyvinyl alcohol (PVA). SEIRA using gold array strips for testing the molecular vibrational intensity enhancement of materials like MHDA (mercaptohexadecanoic acid) and Polymethyl methacrylate (PMMA) have been done before (Maß, et al., 2019) (Wang, et al., 2013). Therefore, taking cue from their observations would help in realizing the contributing effect of the gold- Fe_3O_4 assembly. On taking things further, the control of intensities by changing the direction of opto-generated charges offers a more advanced level in enhanced vibrational spectroscopy. In this case, magnetic controlled Surface Enhanced Raman Spectroscopy (SERS) is a method based on the well-known 'Kerr' magneto-optical effect. It is hypothesised that the presence of magnetically responsive iron oxide would create local magnetic field aligned in the direction of the external magnetic flux component, that would resultantly direct hot electrons generated by the nearby gold nanoparticles (Deng, et al., 2019). Such local control of dense charges would contribute further to the enhancement of vibrational signals of analyte molecules. In this study, Rhodamine 6G will be utilized because of the amount of existing literature on its use in SERS studies (Michaels, et al., 2000) (Chen & Ming, 2012).

5.2 Equipment and Procedures

5.2.1 UV-Vis

The spectra for the prepared (PVA viscosity of 15.3mPas, spin speed of 3000rpm) thin film samples on silicon wafer were obtained using a UV-Vis micro-

spectrophotometer connected to computer preinstalled with an Onyx forensic solutions software package. It consisted of an Olympus BX41 microscope that was connected via optical fibre to an SMCS Ltd, UK. spectrometer, with spectral resolution of 0.834nm. The light beam was directed through series of optical channels and then focused onto the sample through a 40X magnification, 0.65 NA objective lens. The microscopic system was set to reflection mode and the blank sample was scanned for background correction. The scan area from the objective field of view was 5 μm X 25.5 μm . The reflected beam from this area was collimated and transmitted through optical fibre into the spectrometer. Locations $r = 1 \text{ mm}, 2 \text{ mm}, 4 \text{ mm}, 6\text{mm},$ and 8 mm were scanned to obtain UV-Vis spectra in range from 350nm to 786nm.

5.2.2 FTIR-Transmission mode

The Thermo Scientific™ Nicolet™ iN™ 10 infra-red microscope (Thermo-Scientific, 2013) was used to obtain spectra in transmission mode for (PVA viscosities 43.2mPas, 15.2mPas, 3.2mPas and 1.94mPas, with spin speeds at 700rpm, 1000rpm, 1500rpm, 2000rpm, 2500rpm) thin film nanostructure deposited on glass slide. All samples' spectra were recorded in the mid-infrared range of 450 cm^{-1} to 4000 cm^{-1} using the 50 μm beam diameter. A background correction was performed by scanning a clean glass slide before taking measurements of spin coated glass slides. The number of scans was set to 16 per run and each set of data were analysed and plotted on Microsoft Excel.

5.2.3 FTIR-Specular reflectance

In this experiment, 45 and 82 degrees were tested for sample prepared (15.2mPas viscosity and spin speed of 2500rpm) using the Agilent® 4100 ExoScan FTIR analyzer, scanning spectral range between 5200-650 cm^{-1} , 64 background and sample scans with resolution of 8 cm^{-1} . The absorption of OH band at 3300 cm^{-1} was taken as reference point for analysis, and the peak ratios from normal incidence spectra were inverted to match consistency. It is also essential to note that the near normal incidence of beam interaction with surface of sample is a half angle - 20° from a 15X, 0.7 NA objective lens of the Thermo Scientific™ Nicolet™ iN™ 10 infra-red microscope (Thermo-Scientific, 2013), as it is common to have a slightly off normal incident beam for most commercial equipment (Kuroda, et al., 2021).

5.2.4 SQUID

A 5mm square area of coated silicon wafer hosting the middle of the thin film (PVA viscosity of 15.3mPas, spin speed of 3000rpm) with approximate density of 2421 Kg/m³ was tested using the SQUID magnetic property measurement system (MPMS, Quantum Design, Inc) at 300K. This was to estimate the coercivity of the iron oxide patterned nanoparticles within the structured.

5.2.5 Raman

Raman spectroscopy of thin film sample (PVA viscosity of 15.3mPas, spin speed of 3000rpm) on silicon wafer was tested using a Reinshaw inVia™ confocal Raman microscope, using a probing 2×10^3 W/cm² powered 633nm laser with spectral resolution of 0.3 cm⁻¹, 1024 pixel X 256 pixel Renishaw CCD Camera detector, and a 50X, NA 0.55 objective lens. Automatic settings made to mathematically pre-treat the data, such as; off-set and cosmic ray removal. Upon arrival of data, baseline correction via Origin ® was undertaken.

5.3 UV-Vis spectrophotometry

In this sub-section is presented the UV-vis optical study of designed structure, where the dimensionality of the pattern affects optical response when subjected to visible light. The two main constituents of the structure, gold and Fe₃O₄ nanoparticles, are optically responsive materials. The gold nanoparticle exhibits plasmon resonance absorption band within the visible region (~510 – 530nm) (Wu, et al., 2018), with high energy density of oscillating conducting electrons. This is a limit as it cannot resonate under UV region. The iron oxide on the other part exhibits low absorption quantum efficiency in response to the favourably high energy side of the visible spectrum (~400nm), in a way that the created hot electrons of iron oxide by the excitation beam are few and rapidly relaxes to the bottom of the conduction band as a result of electron-hole recombination, and low mobility of holes (Korobchevskaya, et al., 2011). This makes iron oxide a poor conductive material with poor photocurrent efficiencies (Anderman & Kennedy, 1988) (Alexandrov & Mott, 1996) (Iordanova, et al., 2005). A UV-Vis absorption spectra of pristine iron oxide

(Magnetite) is shown in Figure 5-1, with a distinct peak at ~ 400 nm, along with a long tail extending as far as ~ 1000 nm.

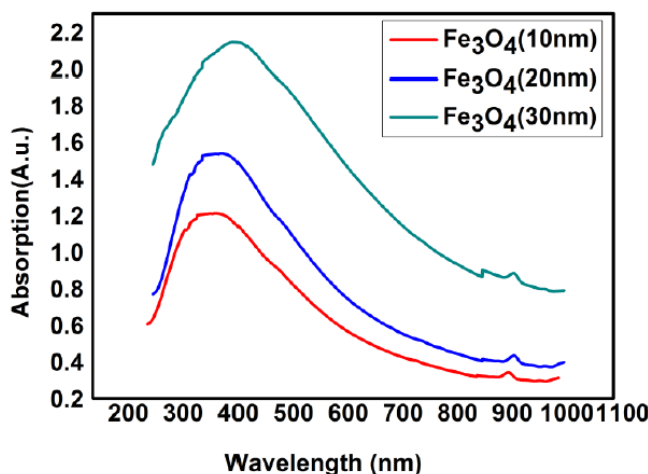


Figure 5-1 UV-Vis absorption spectra of magnetite at different sizes, the maximum peaks for 10 nm was 372nm, 20nm was 383nm and 30nm was 404nm. Courtesy (Horia, et al., 2020)

Despite gold nanoparticles also experiencing fast deactivation and limited electron mean free path through electron scattering (Ye, et al., 2018) (Kreibig & Frangstein, 1969), the high density of hot electrons enables it to be a high conducting material. This is why the excess electrons generated by gold may become mobile within the iron oxide lattice at room temperature when the metal oxide become thermally activated, yielding an electron hopping mechanism (Gilbert, et al., 2013) (Iordanova, et al., 2005).

The pairing of gold and iron oxide to form heterodimer structures is a technique that have been carried out for practices in areas like catalysis (Lee, et al., 2010) (Lin & Doong, 2011) (Wu, et al., 2009), Multimodal contrast imaging (Zhu, et al., 2014) (Cai, et al., 2012), hyperthermia treatment (Hedayatnasab, et al., 2020), drug delivery (Estelrich, et al., 2015), etc. The interfacial interaction between this pair is unique whereby excited electrons from gold nanoparticle tend to diffuse from the Fermi level of the material to the conduction band of the iron oxide causing charge accumulation at the interface. Thus, making the iron oxide material behave as an electron reservoir. This unique behaviour of this dimer nanostructures are often diagnosed with UV-vis spectroscopy in order to identify effective changes in spectra absorption of the heterostructures that can depend on their surface morphology,

sizes, concentration ratios and contact gap. Numerous works have been carried out regarding this pair using UV-vis spectroscopy and most spectra have similar outcomes. For example, the UV-vis spectra for iron core gold dumbbell nanostructure showed a red-shift, broadening and dampening of the plasmon peak of the gold (see Figure 5-2). Several authors claim this could be because of electron deficiency of gold due to the transfer of charged electrons across the interface (Daniel & Astruc, 2004) (Yu, et al., 2005). However, the transient absorption study (Korobchevskaya, et al., 2011) of the dimer structure showing the red-shifted plasmonic absorption peak did not observe any evidence of significant electron transfer between gold and iron oxide instead it concluded that the dielectric effect induced by iron oxide in the surrounding media was responsible for red-shift. Moreover, the estimation of number of free electrons around the gold nanoparticle within a prepared dimer heterostructure (Shi, et al., 2006) showed that it was unrealistic to observe the 10% red-shift of plasmon peak from 520nm to 570nm for a decrease of free electrons by 20%.

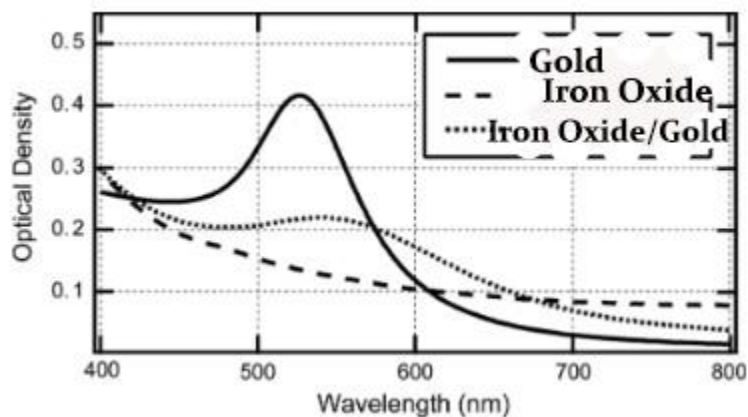


Figure 5-2 UV-Vis absorption spectra of Iron Oxide, Gold and dimer heterostructure of combined iron oxide and gold. Courtesy (Korobchevskaya, et al., 2011).

Conversely, the UV-Vis spectrum of the bimetallic nanoparticle alloy prepared using a thermal process (Dahal & Chikan, 2008) showed two peaks, one at ~670 nm and the other at 395 nm (see Figure 5-3). Observation of the two peaks was attributed to transfer of electron between gold and alloys particles resulted from the probable coupling of the plasmon oscillation of a thin gold layer with that of an alloy particle. Increasing the gold concentration in iron-gold bimetallic particle the plasmon peaks blue shift from the initial 670 nm of 1:1 ratio. This is a similar experience with iron

oxide-core-gold-shell dimer system, where the thinner the shell, the more red-shift of the plasmon peak, while with thicker gold shells, the reverse is the case (Wilcoxon & Abrams, 2006) (Wang, et al., 2005).

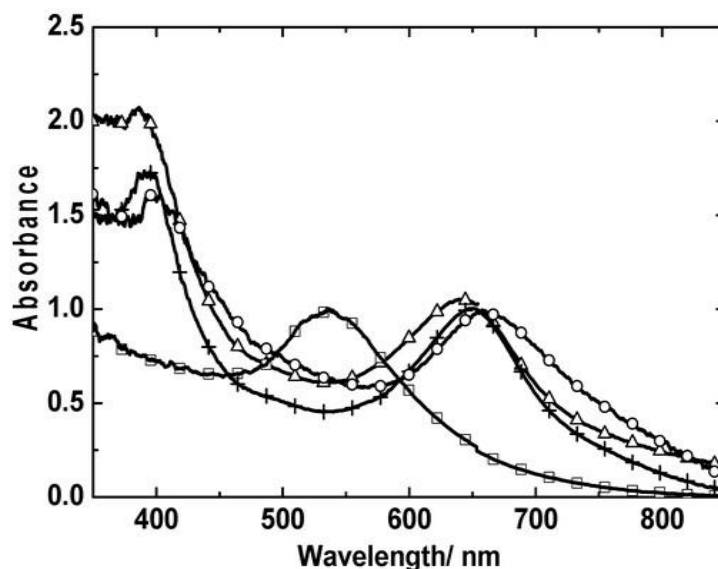


Figure 5-3 : UV-visible absorption spectra (in water) for pure gold and iron-gold alloy nanoparticles synthesized from FeO precursor with various molar ratios. The molar ratios of iron and gold are 1:1, 1:2, and 1:3, indicated by circle, cross, and triangle, respectively. Courtesy (Dahal & Chikan, 2008)

In summary the excited photoinduced metal on the metal oxide that leads to subsequent enhancement, shifts and broadening of absorption peaks through UV-Vis spectrometry diagnosis is dependent on the dimer preparation approach, concentration ratios and type of contact. This has been proven by a group of investigators who investigated the influence of gold nanoparticles on the photoactivity of iron oxide (Thimsen, et al., 2011). An embedded electrode configuration where Fe_3O_4 was deposited over gold nanoparticles that were distributed over a silicon oxide substrate. The output from this configuration was not only a red shift in plasmon resonance of gold particle, but also a rise in absorption intensity for the ~ 400 nm peak associated with the Fe_2O_3 . The surface configuration which involved gold directly and partly attached to the Fe_2O_3 electrode that was fused to the silicon oxide substrate (Figure 5-4 (a)), experienced no red shift of plasmon resonance. However, there was an increase in overall intensity of the spectrum (Figure 5-4(b)). The spectra outcome from the embedded configuration is similar to that of the thermally fused system described previously (Dahal & Chikan, 2008),

while that of surface configuration spectra is similar to results by (Yu, et al., 2005) (Shi, et al., 2006) involving dumbbell and core-shell configurations.

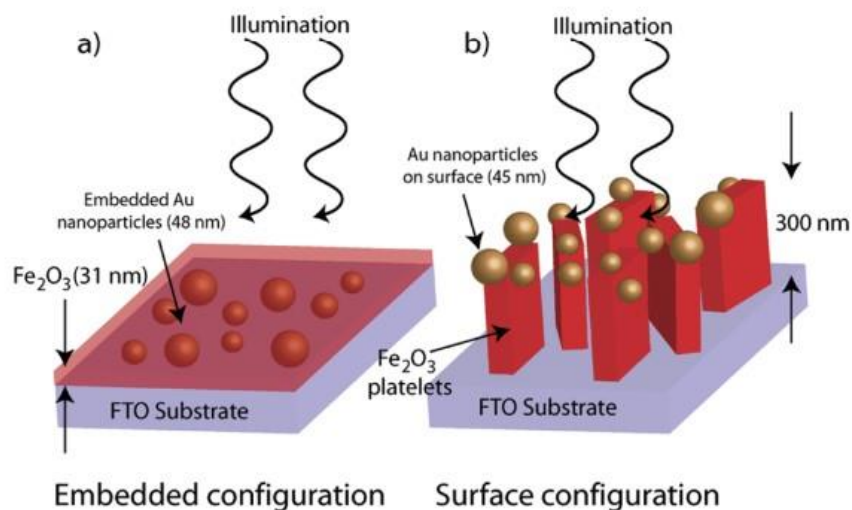


Figure 5-4 Illustration of system configuration of (a) gold deposited on substrate overlain by iron oxide, (b) iron oxide deposited on silicon oxide substrate with gold bounded to the iron oxide platelet surface. Courtesy (Thimsen, et al., 2011).

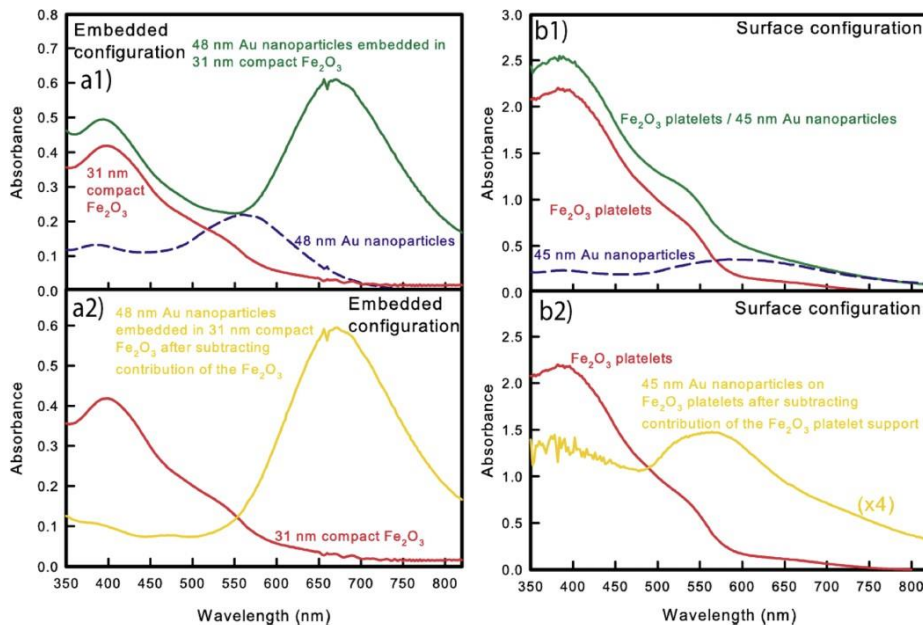


Figure 5-5 : Absorbance spectra for the different electrodes. (a1) As-measured absorbance data for the embedded configuration; (a2) comparison of the spectral overlap between Au nanoparticle plasmon resonance and compact Fe_2O_3 absorbance for the embedded configuration; (b1) as-measured absorbance data for the surface configuration; and (b2) comparison of the spectral overlap between the Au nanoparticle plasmon resonance and Fe_2O_3 platelet absorbance. Courtesy (Thimsen, et al., 2011)

5.3.1 Results and Analysis

The UV-Vis spectrum for each location ($r=1, 2, 4, 6$ and 8 mm from the centre) on the thin film are presented in

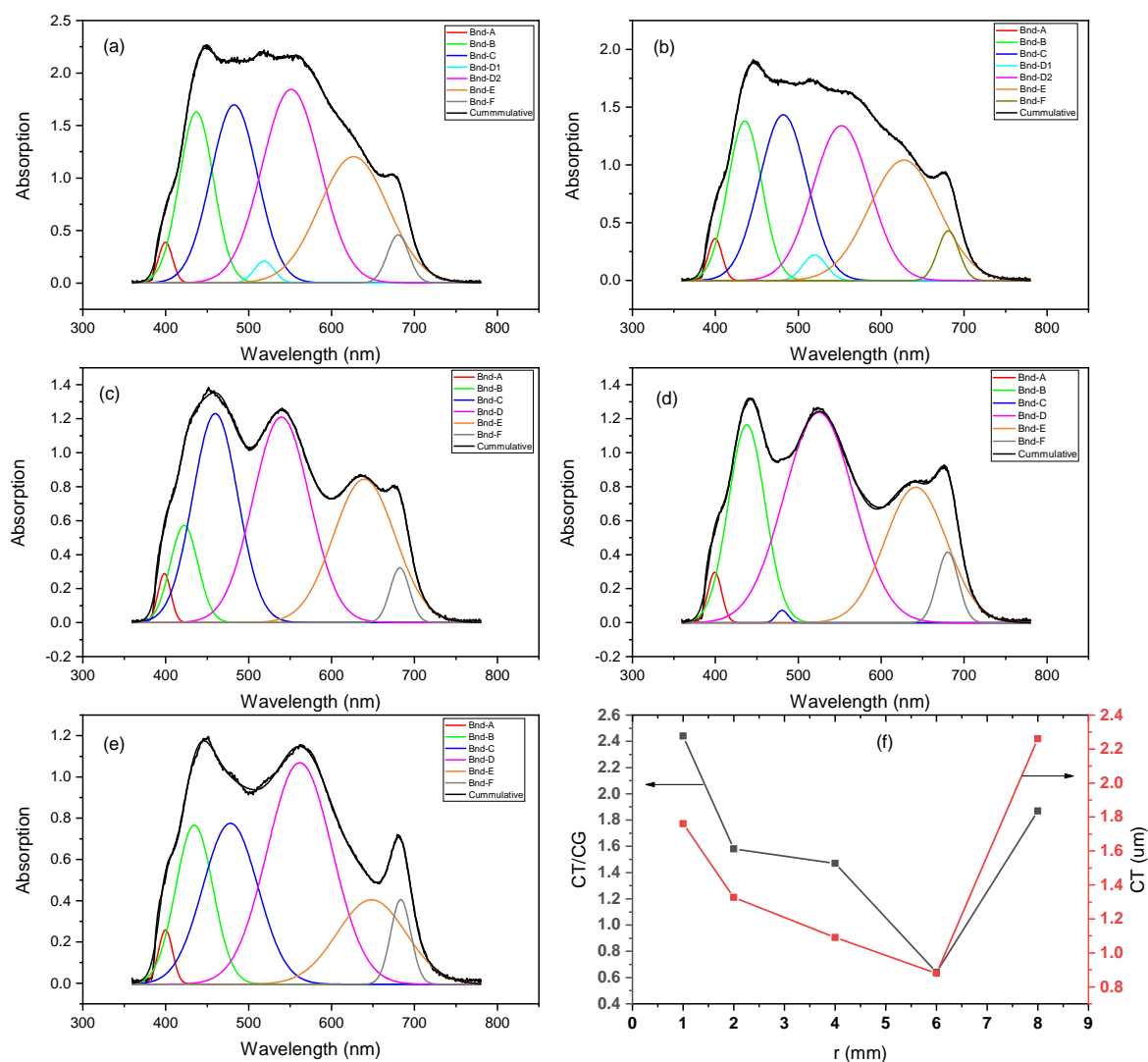


Figure 5-6(a to e). The CT/CG ratio and CT for each of the scanned locations plotted against the respective radial distance (where $r=1, 2, 4, 6$ and 8 mm from the centre) in Figure 5-6(f). Each spectrum appear as a broadband absorption spectrum with one or two distinct peaks at both ends of the spectrum (~ 400 nm and ~ 680 nm), along

with undulating peaks in-between. As seen in

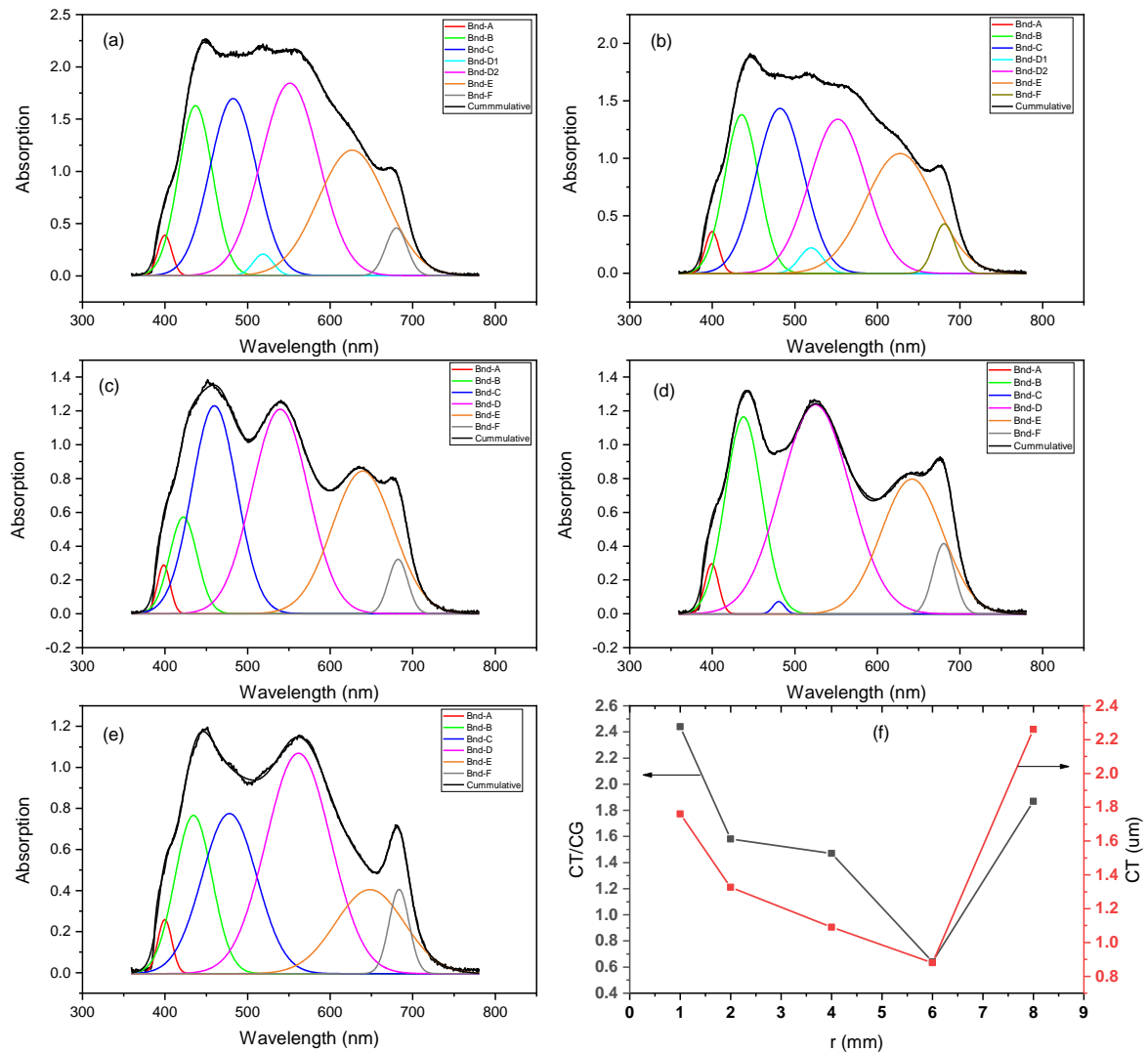


Figure 5-6 (a), the absorbance between the 440 nm and 560 nm was found to be twice as much as that of spectrum obtained from location, $r=8$ mm. However, the overall absorbance and the high absorbance band (440 nm – 560 nm) started reducing. At $r=4$ and 6 mm, the distinctive peaks are visible which can be attributed to a gritting structure and increased absorbance due to resonance. Each spectrum was deconvolved using gaussian model (Eqn. [5-1]) in Origin® software package. The resulting fitting details are presented in *Appendix 8.13*, while the summary of

the wavelength, peak intensity, Full width Half Measure (FWHM) for each deconvolved peak is presented in *Appendix 8.13*.

$$y = y_0 + \frac{A}{w\sqrt{\pi/(4 \ln 2)}} e^{-4 \ln 2 \frac{(x-x_c)^2}{w^2}} \quad [5-1]$$

Where; y_0 is the offset, x_c is the centre, w is the FWHM, A is the area of the curve.

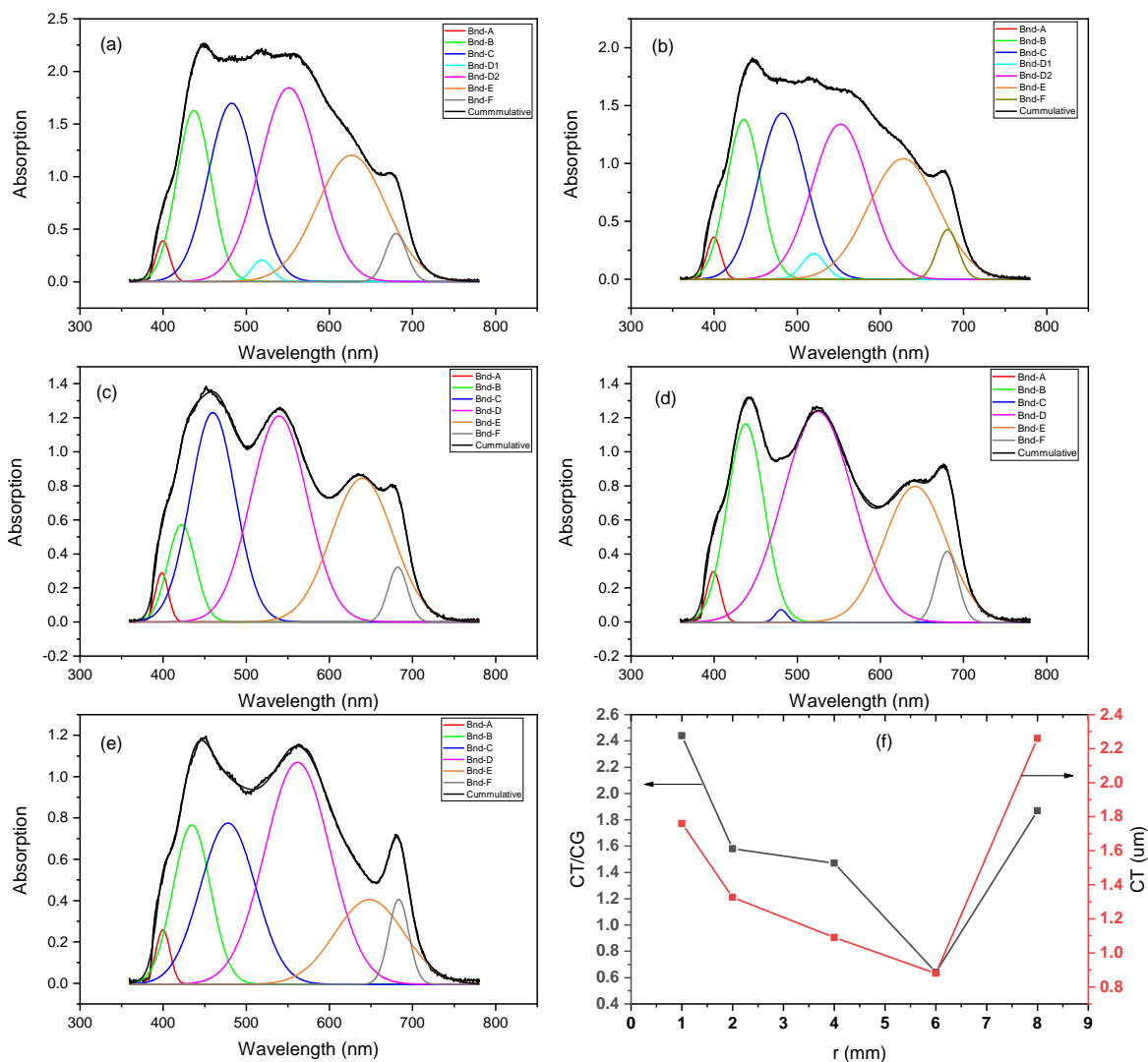


Figure 5-6 UV-Vis absorption spectra with internal deconvolved gaussian peaks at various radial locations (a) $r=1\text{mm}$, (b) $r = 2\text{mm}$, (c) $r=4\text{mm}$, (d) $r=6\text{mm}$ and (e) $r=8\text{mm}$. (f) is the plot showing relationship of CT/CG, CT against radial locations r (mm).

The values from the wavelength, peak intensity and FWHM were plotted against r (mm) as shown in

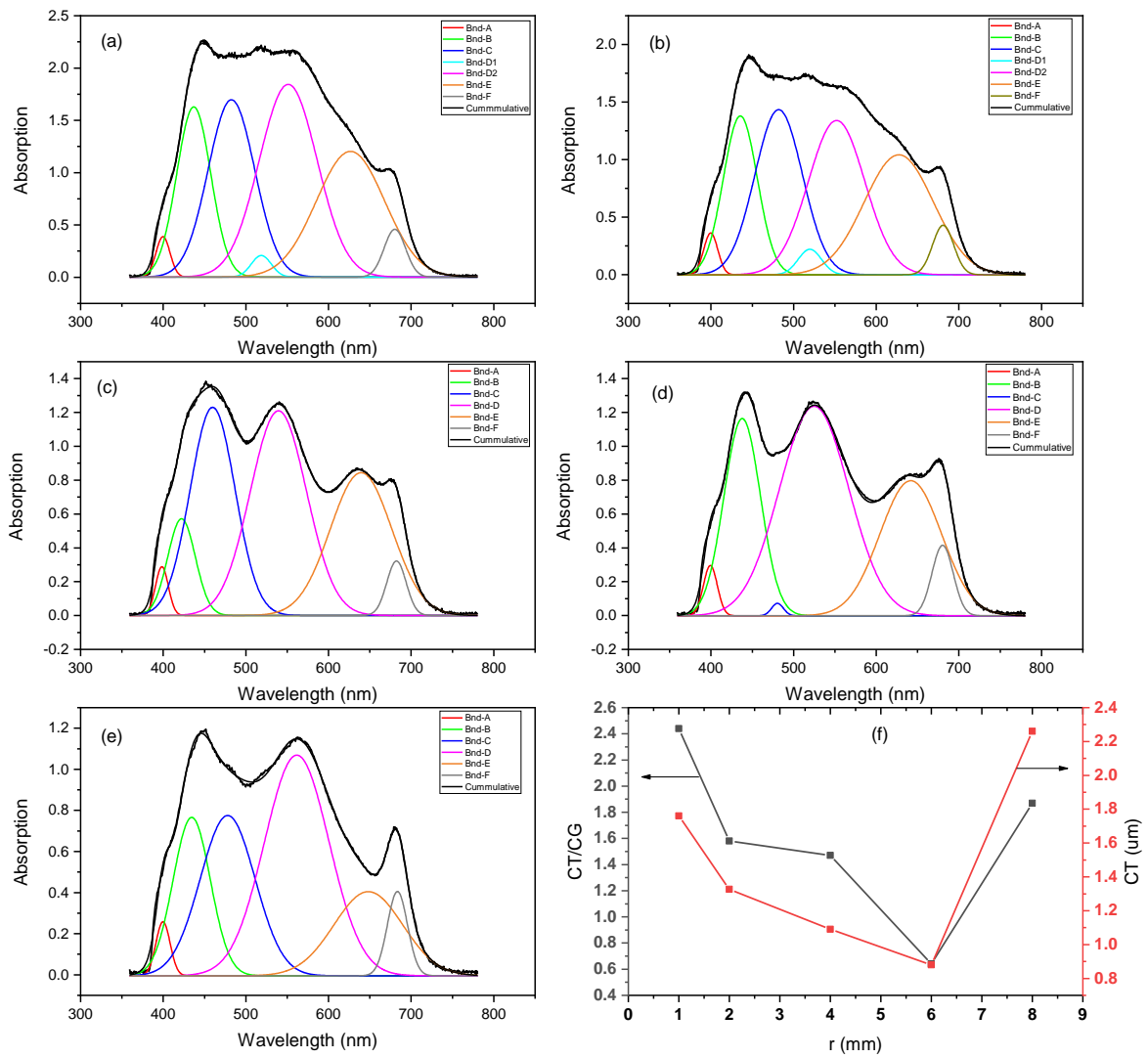


Figure 5-6(a, b and c) respectively. In order to quantify the quantity of species read from the collimated scanned area, CG was determined from CT/CG and CT , and CG was added to CT which gives the grating order of the pattern. Afterwards, the $5\ \mu\text{m}$ scan width perpendicular to the arrays was divided by the grating period to obtain the number of periods within the scanned area. Then, the obtained value was then multiplied by CT/CG to estimate the fraction of scanned material. This final solution was labelled as CT_w , which is a dimensionless variable.

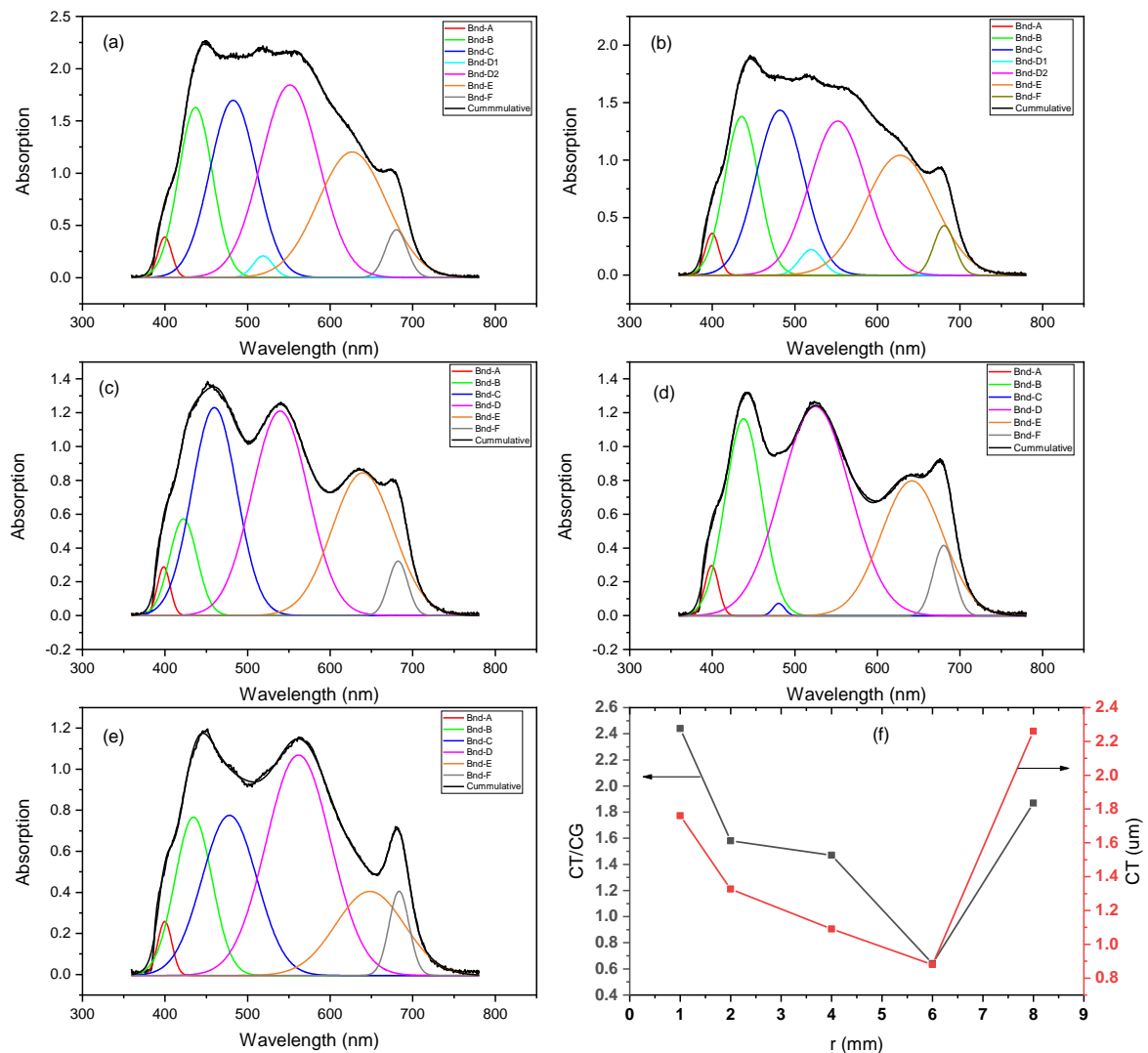


Figure 5-6(d) shows the plot of CT_w against r (mm).

$$CT_w = \frac{CT}{CG} \times \left[\left(CT + \frac{CT}{CT/CG} \right) / 5 \right] \quad [5-2]$$

5.3.1.1 Deconvolved Bands identification

The two distinct absorption bands across each resulting spectra at ~400nm (Bnd-A) and ~680nm (Bnd-F) are associated with Fe₃O₄ and redshifted plasmon resonance of gold nanoparticles. Since the dimer (iron oxide and gold) formed in the thin film nanostructure was not prepared by thermal process, they did not form into bimetallic nanoparticles as earlier highlighted (Dahal & Chikan, 2008) but resulted into structure

similar to gold particles embedded in the iron oxide layer. The peaks observed in

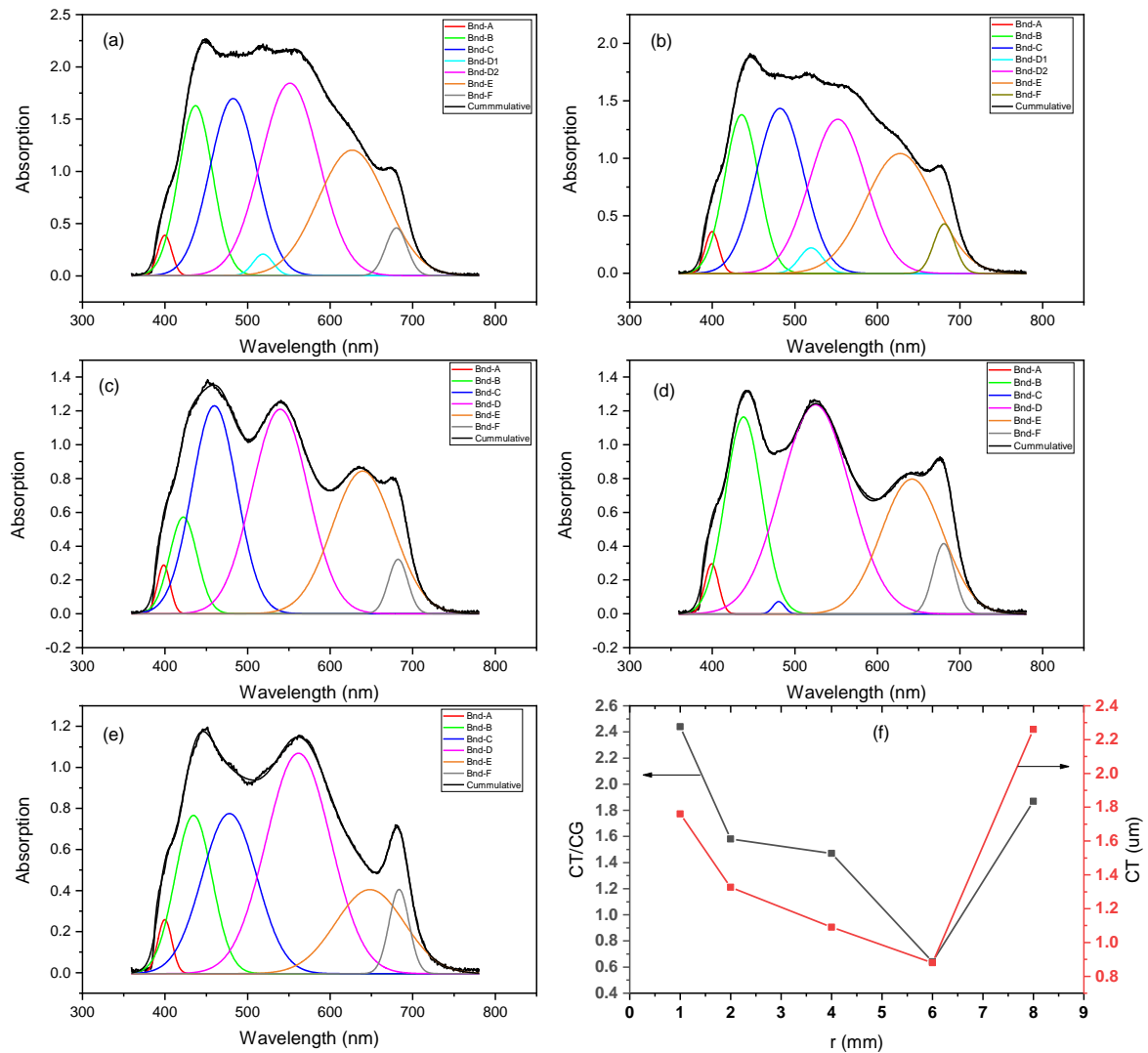


Figure 5-6 (a-d) were found to be similar to peaks observed in spectrum obtained from the structure where gold nanoparticles was embedded within iron oxide layer (Thimsen, et al., 2011).

The deconvoluted absorption bands between wavelengths 400nm and 500nm are associated with the iron oxide absorption. One of the peaks is close the established 444nm (Bnd-B) of pristine Fe_3O_4 (Bora, et al., 2012). The other band hovering around 480nm (Bnd-C) is associated with the spin flip Fe-Fe pair transition in the iron oxide structure (Sherman & Waite, 1985) (Velasco, et al., 2015), with its intensity and

absorption wavelength dependent on its size and/or shape (Mizuno & Yao, 2021). Within the 500nm to 650 nm band, the two absorption peaks at $\sim 548\text{nm}$ (Bnd-D) and $\sim 640\text{nm}$ (Bnd-E) were observed. The absorption band at 540nm could be attributed to interaction of the iron oxide and the gold nanoparticles on dielectric surface of silicon as a result of frequency oscillation coupling from small interfacial contact (Thimsen, et al., 2011) (Mizuno & Yao, 2021), (Ung, et al., 2002). This interaction causes a red shift in plasmon resonance of gold from its non-interacting plasmon mode ($\sim 520\text{nm}$) to $\sim 550\text{ nm}$ depending on the degree/density of interaction, as already seen in gold-silica nanostructures (Thomann, et al., 2011) (Ye, et al., 2018) (Bhattarai, et al., 2020) (Bossard-Giannesini, et al., 2016) (Engelbrekt, et al., 2021). Moreover, the shift can also be evident by the increased gold nanoparticles aggregation density and interparticle spacing. With every increase in volume fraction of gold nanoparticles per unit area and coupled with decrease in interspacing distance, a growing plasmon red-shift is realised away from a singlet particle (Liz-Marzán, 2006) (Ghosh & Pal, 2007). The absorption spectra at $r=1\text{mm}$

and

2mm

(

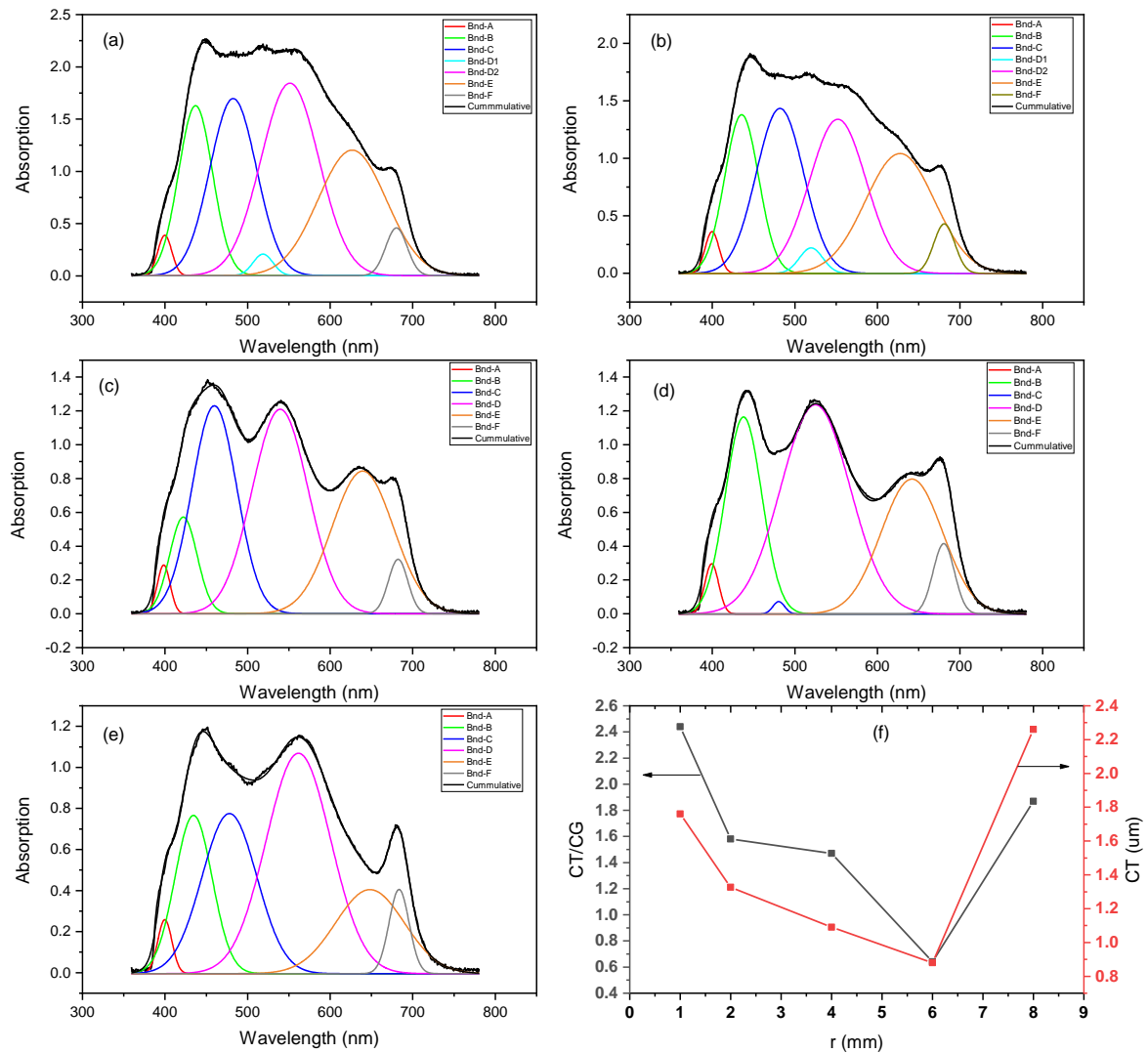


Figure 5-6 (a & b respectively) showed a short absorption peak at $\sim 515\text{nm}$, which could most likely be an uncoupled gold nanoparticle plasmonic resonance. The absorption bands between 630nm and 650nm inclusively is most likely associated with the plasmon resonance of gold/iron oxide nanostructure, which is a commonly observed when both iron oxide and gold are involved in making films or particles (Wang, et al., 2019).

5.3.1.2 Relationship with deconvolved bands (400nm, 444nm, 480nm, 550nm, 630nm and 680nm) and pattern morphology

Figure 5-7 shows the Wavelength, peak intensity and FWHM for each band was plotted against respective locations on the thin film, in accordance with the data from *Appendix 8.13*. Each band was then correlated to the CT_w as seen in *Figure 5-7* (a-d). CT_w relates to the gaps and length of pickering droplet chains covered within the scanned area.

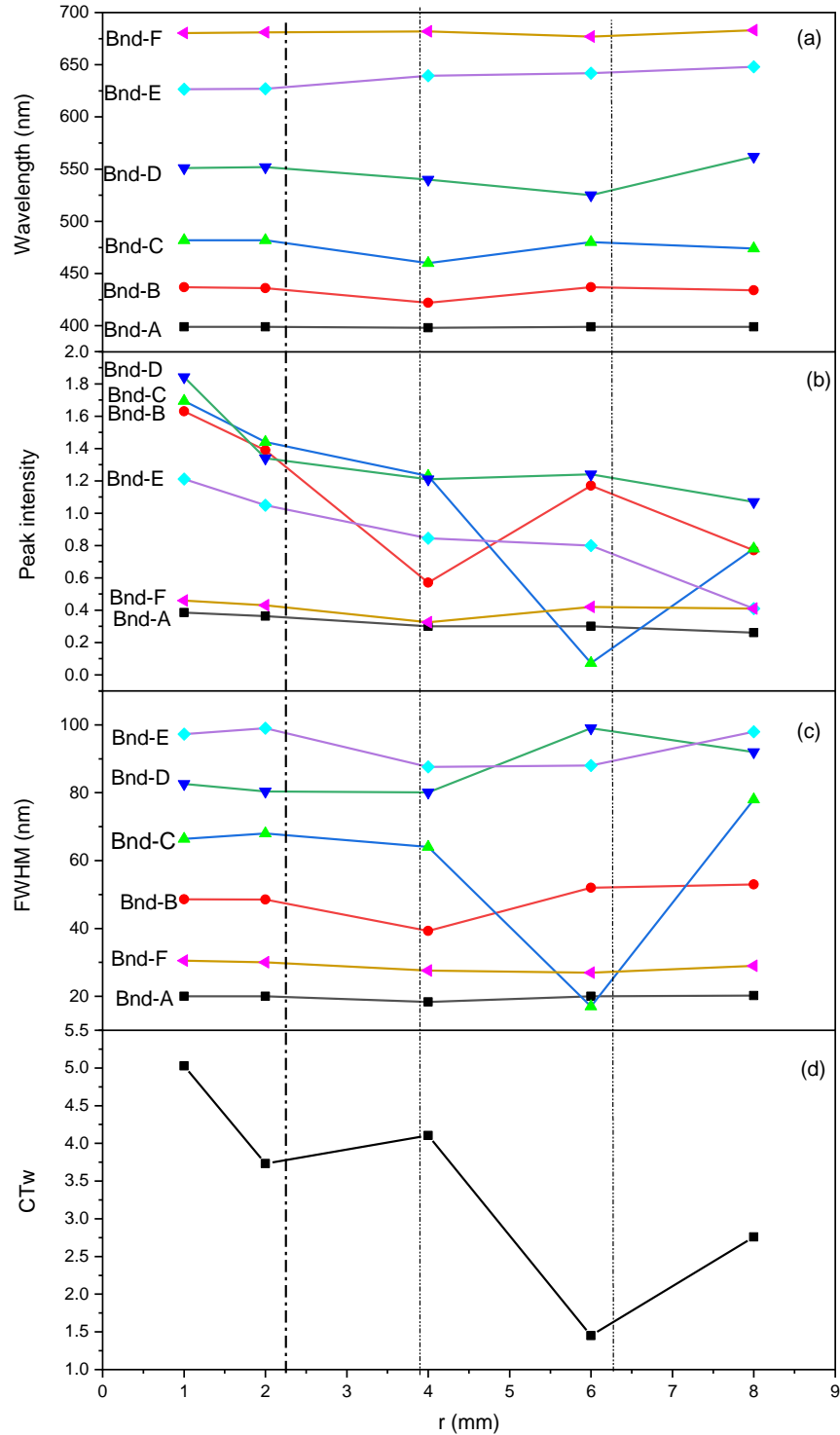


Figure 5-7 Relationship of deconvolved bands (Bnd-A, B, C, D, E & F) data points of their (a) wavelength (b) intensity and (c) FWHM with the radial distance, r (mm), while (d) shows the relation between calculated CT_w values from Eq. (5.2) against radial distance, r (mm). The trend of CT_w was relatively compared with the trends of wavelength, peak intensity and FWHM for all deconvolved bands.

At $r=1\text{mm}$, CT_w is at its highest point (~ 5) because of the thick chains and small gaps around this region. The general broadband spectrum has the highest intensity with the peak intensity for Bnd-D ($\sim 551\text{nm}$) at the highest (~ 1.84). As the observation point is moved toward the first trough, $CT_w \sim 2.25$ ($\sim 26\%$ from value at $r=1\text{mm}$), it is interesting to observe that the lesser the cluster density, the more redshifted the band Bnd-E becomes. Other band wavelengths were approximately the same at this scan region. At locations, $r=1\text{mm}$ to 2mm , 517nm band is observed due to excess gold nanoparticles that could be laying singly within the gaps of the clusters after being squeezed and drifted from pickering droplet due to cluster pressure (see Figure 5-8).

Along the way, where r is between 3.5mm to 4mm , there was a slight bump in CT_w ($\sim 16\%$ increase from the first trough at $r=2.25\text{mm}$), a significant blueshifts for Bnd-B and Bnd-C was seen. Bnd-B spectra has to do with the cumulative charged energy across interfaces between iron oxide and gold nanoparticles within a chain cluster. The blueshift of Bnd-B in this region of the substrate resulted from increase in iron oxide concentration in relation to the gold nanoparticles when compared to central regions of the structure. Bnd-C is a band that results from iron to iron interaction. This was initially hardly visible from a full UV-Vis iron oxide absorption spectra, but visible when gold nanoparticle was introduced. This makes it clear to presume that this spectrum comes from iron-iron oxides contact close to the proximity of gold-iron oxide contact (see Figure 5-8). Thus, the blue-shift in Bnd-C results from the increased aggregate concentration of iron oxide particles per scan area (CT_w) and low energy charge from the proximal gold-iron oxide contact (Mizuno & Yao, 2021).

The uniformity of wavelengths for band (Bnd-B) between $r=1\text{mm}$ and 2mm is as a result of ratio continuity between iron oxide concentration and gold. The reason could be that the thickness of the film at these locations were more and therefore accommodated more gold nanoparticles than the region at $r=3.7\text{mm}$. This could be as a result from a certain scenario where; during the spinning process, the channel (known as chain gap) created by fluid inertia is small and irregular at locations close to the centre (CT:CG, 71%:29%), while at locations $r=3.7\text{mm}$, the channels are well

defined with a higher resolution (CT:CG, 60%:40%). The inertia energy from spinning in this location is higher compared to the centre. This higher energy could possibly displace the gold nanoparticles that are barely attached to the surface of iron oxide clusters. This can be noticed from the slight blueshift in Bnd-D associated with degree of gold clusters attached to the surface of iron oxide (see Figure 5-8). This can be observed by the drastic reduction in peak intensity and FWHM for Bnd-B, as well as that of surface bound gold clusters (Bnd-D), which then supports the idea of more iron concentration than gold. A red shift and decrease in band intensity of Bnd-F supports this phenomenon as well, which according to literature, (Wilcoxon & Abrams, 2006) (Wang, et al., 2005), identified that a decrease in gold concentration leads to redshift of the 680nm band.

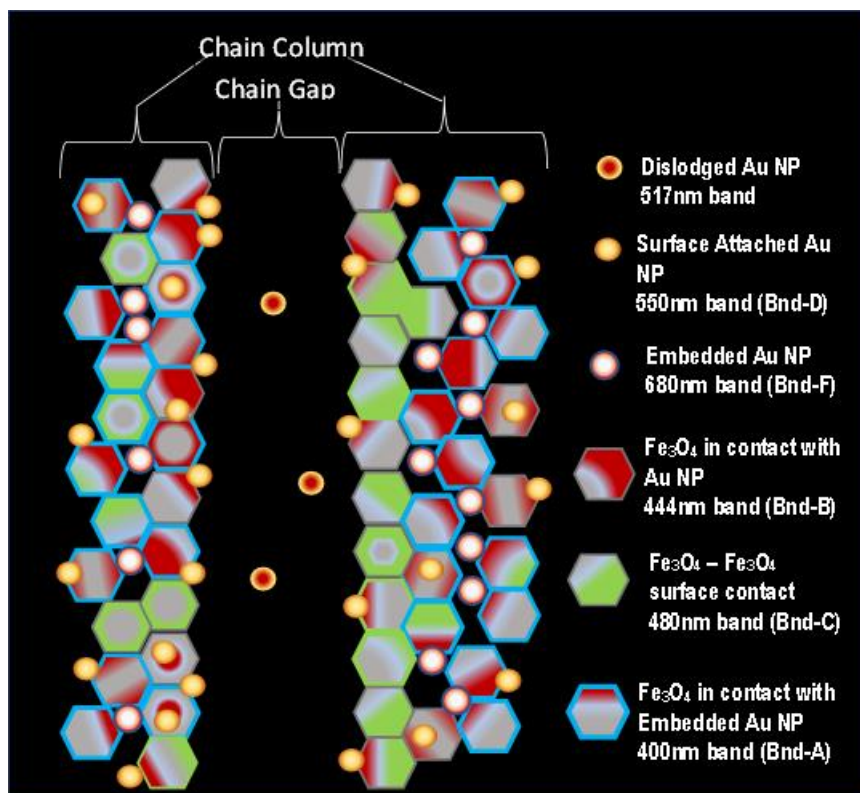


Figure 5-8 Schematic illustration of particle-particle interaction and charge transfer (red) within pattern. Added is the expected associated absorption band. Bnd-E has to do with overall density ratio between gold nanoparticles and iron oxide nanoparticles

At location $r=6.3\text{mm}$, CT_w is at its lowest, which is a 73% reduction from CT_w at $r=1\text{mm}$. Is at this region chain thickness size is at its smallest ($0.88\mu\text{m}$) and the magnetic pressure on droplets is less (magnetic field strength 14.7 mT). This lesser

pressure and lesser droplet aggregates minimizes the displacement of gold nanoparticles from their cluster. Despite high inertia energy at this location, coupled with the large chain gap, very few of gold nanoparticles could be displaced. This phenomenon has led to a return (red-shift) of Bnd-B, but a blue-shift for Bnd-D which indicates more surface bound gold-iron oxide particle contact. This is also supported by a slight blue-shift for Bnd-F which according to the same literatures (Wilcoxon & Abrams, 2006) (Wang, et al., 2005), is due to more gold particle concentration. The red shift in Bnd-C does not only result from the decrease in iron particle density per scanned area, but more iron-iron oxides contact that are influenced by sufficient charges from surrounding gold-iron oxide contact (see Figure 5-8). The sharp rise in band intensity and width of Bnd-B testifies on the impact of multiple gold nanoparticles interaction with iron oxide (Figure 5-7 b&c). This is not the case for Bnd-C, which experienced the opposite because of relatively lesser iron-iron contact density than central regions of the film.

As r approaches 8mm, CT_w experiences an increase of $\sim 100\%$ increase from $r \sim 6.3$ mm. At this location, the chain thickness increases about 153% from the lowest point at $r=6.3$ mm, however the gap in between the chains slightly reduced by 9.3%. This scanned section is approximately close to the region of the ring magnet's edge, therefore stronger magnetic field is experienced by the pickering droplets leading to increased cluster density and therefore pressure on droplets. Simultaneously, the fluid inertia is high at this region, which contests with the magnetic field energy, thereby creating increased amount of stress on structure. That is the reason why the chain gap is slightly higher ($\sim 124\%$) when compared to regions close to the centre of the sample. In terms of the spectra distribution, Bnd-B and Bnd-C bands experiences a slight blue shift from the previous point ($r=6.3$ mm). This is also coupled with a reduction in peak intensity for Bnd-B and increase for Bnd-C, as well as an increase in broadening for Bnd-C and slight decrease in band width for Bnd-B. This is an indication of reduced quantity of gold due to the pressure within cluster and dislodgement by fluid inertia within this region. This is further supported by the red shift of Bnd-F. The red shift in Bnd-D is as a result of lesser gold particle on partial surface contact with iron oxide as a result of dislodgement by high energy fluid

inertia. The reduction in peak intensity and slight decrease in broadness of Bnd-D indicates the few quantities of interacting gold nanoparticles per surface of iron oxide.

One absorption band that have not been discussed much about thus far is Bnd-E. The trend has appeared red-shifted with a decreasing peak intensity. This trend identifies with the average decrement of gold-iron oxide interaction ratio (see Figure 5-8), where more gold is located at the centre of the sample and decreasing as r increases. This can be confirmed from the FTIR spectra discussed in Section 5.4.2.3.

In summary regarding the optical response of this structure pattern, the overall spectrum consisted of overlap of oscillation bands of different configurations and degrees of specie interactions. Except for band Bnd-A and Bnd-F, which is an auto response for high concentration ratio of interaction of iron oxide per gold nanoparticle trapped within chain cluster. The other bands (Bnd-B and Bnd-C) respond by either frequency shifts, absorption intensity or band width in accordance with the concentration ratio of iron oxide and gold, and size of cluster chains. Thimsen and co. (Thimsen, et al., 2011) stated that in the embedded structural configuration, the spectral overlap, the peak plasmon resonance at a longer wavelength ($>630\text{nm}$) compared to the absorption of the semiconductor (between 400nm and 450nm), indicates the mismatch in frequencies between coupling of the oscillators in the metal nanoparticle and the semiconductor was low. While from their surface configuration, the small interfacial area of contact between iron oxide and gold led to the frequency oscillation matching of gold plasmon absorbance and iron oxide band gap absorbance at approximately 560nm . Interestingly it is favourable to identify our designed system as a multifaceted configuration of "embedded" and "surface". Just like embedded configurations, gold nanoparticles are trapped within the cluster chains and therefore have large surface area of interaction that led to the bimodal peaks. Meanwhile, just like surface configurations, the drifted gold nanoparticles toward to exposed surface of the chain cluster results in mid-visible absorption bands. Therefore, upon the combination of both configurations, their optical response would likely lead to a broadband spectrum that we obtained. To evidently demonstrate, Figure 5-9 shows an SEM image of a sample sintered at $\sim 600\text{ }^\circ\text{C}$, showing iron oxide nanoparticles (in dark oblate spheroid shape) and gold nanoparticles (bright spherical

beads). This is led to the generation of **Table 5-1** which shows a summary of the impact of variability of iron oxide-gold relationship and configuration on deconvolved bands behaviour.

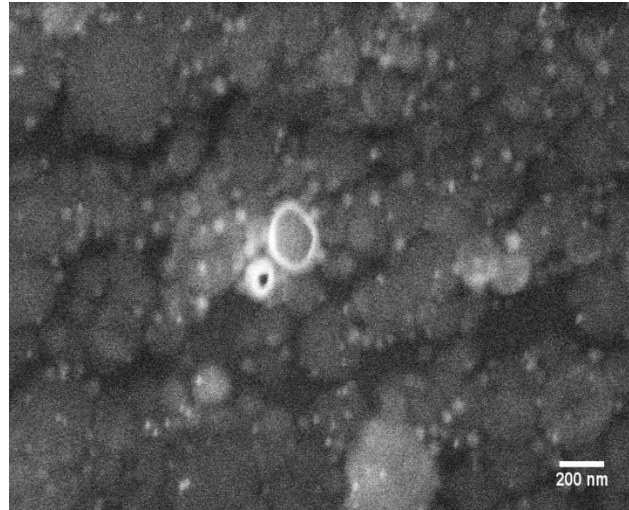
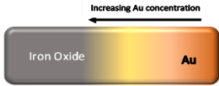
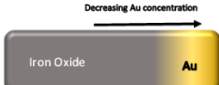
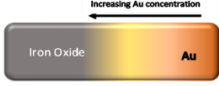
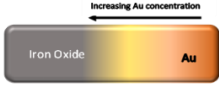
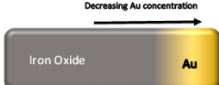
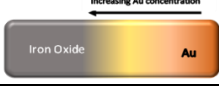
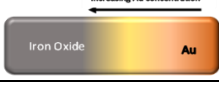


Figure 5-9 The SEM image of thin film sintered at 600° C sample showing iron oxide (dark oblate spheroid) and gold nanoparticles (bright spheres) for exemplary illustration on particle system configuration.

Table 5-1 Summary of band interpretation based on influence of specie ratios

Bands		Configuration	Assumed Gold-iron oxide concentration	Band behaviour (Red-shift= RS , Blue-shift= BS , Band broadening= BB , Band narrowing= BN . Peak intensity: decrease= ↓ , increase= ↑)	Reference
Bnd-A	400nm	Embedded		BS, ↑, BN	(Dahal & Chikan, 2008) (Thimsen, et al., 2011)
				RS, ↓, BB	
Bnd-B	440nm	Surface		RS, ↑, BB	(Bora, et al., 2012) (Korobchevskaya, et al., 2011)
				BS, ↓, BN	
Bnd-C	480nm	Fe-Fe quantity	Decrease in CT_w	RS, ↓, BN	(Velasco, et al., 2015) (Sherman & Waite, 1985)
			Increase in CT_w	BS, ↑, BB	
Bnd-D	540nm	Surface		BS, ↑, BB	(Velasco, et al., 2015) (Thimsen, et al., 2011) (Mizuno & Yao, 2021)
				RS, ↓, BN	
Bnd-E	630nm	Embedded/ Surface		BS, ↑, BB	(Wang, et al., 2019) (Dahal & Chikan, 2008) (Wilcoxon & Abrams, 2006)
				RS, ↓, BN	
Bnd-F	680nm	Embedded		BS, ↑, BN	(Dahal & Chikan, 2008) (Thimsen, et al., 2011)
				RS, ↓, BB	

This experience therefore confirms the hypothesis opposing the concept of electron diffusion from gold nanoparticles to iron oxide, instead the increase in electron density at their interface (Korobchevskaya, et al., 2011). This density of electrons at the interface bends the conduction band of the iron oxide, therefore improving its optical response in the form of increase in photo-absorption. Depending on the form

of configuration and degree of interaction, as well as the concentration ratio between gold and iron oxide strongly influences the characteristics of individual absorption bands within the convolved broadband spectrum.

5.4 Fourier Transform Infra-Red Spectroscopy

Fourier transform infra-red spectroscopy assists in the detection and label-free characterisation of matter in a non-destructive manner (Chalmers, 2002) (Ng & Simmons, 1999). The spectra signatures from molecular vibrations of species within a structure helps in qualitative estimation of a particular specie in relation to other groups (Russo, et al., 2014) (Hashim, et al., 2010). In a case involving tailored metallic structures in the form of periodic patterns, assist in surface lattice resonance and near field coupling to increase the absorption of molecules placed nearby (Adato, et al., 2009) (Mayerhöfer & Popp, 2018). Such structures have seen applications as antennas on substrate for surface enhanced infra-red absorption spectroscopy (Huck, et al., 2014) (Maß, et al., 2019). The inclusion of grazing incidence angle and thin film-based substrates enhances light absorption with uniform field enhancement on the detection of analytes (Gaillard, et al., 1999) (Griffiths & De Haseth, 2007). This procedure is comparably low but spatially extended. The tuning of thickness of arrays or array gaps to spectrally match the maximum local field enhancement with vibrational modes of interest within the diagnosed analyte. Thus, the FTIR test and analysis is utilized to understand the thin film pattern structure's behaviour on the role of combined lattice resonance and near field coupling for the enhancement of vibrational modes of spectrally responsive molecules of the PVA coated layer.

In this section, the FTIR analysis of the sample is split into two parts; (i) the scan by transmission mode and (ii) scan by different grazing angle of incidence.

5.4.1 Transmission mode FTIR data analysis

An example of spectra collected at various locations on the thin film nanostructure prepared using 43.2mPas PVA- PEG-C-GM-pi-FF at spin speed of 1000 rpm is shown in Figure 5-10. The spectra in relation to the spatial locations (r (m)) on the spin coated thin film were scanned from the centre of the film (0 m) to a farthest position ($r=0.0175\text{m}$).

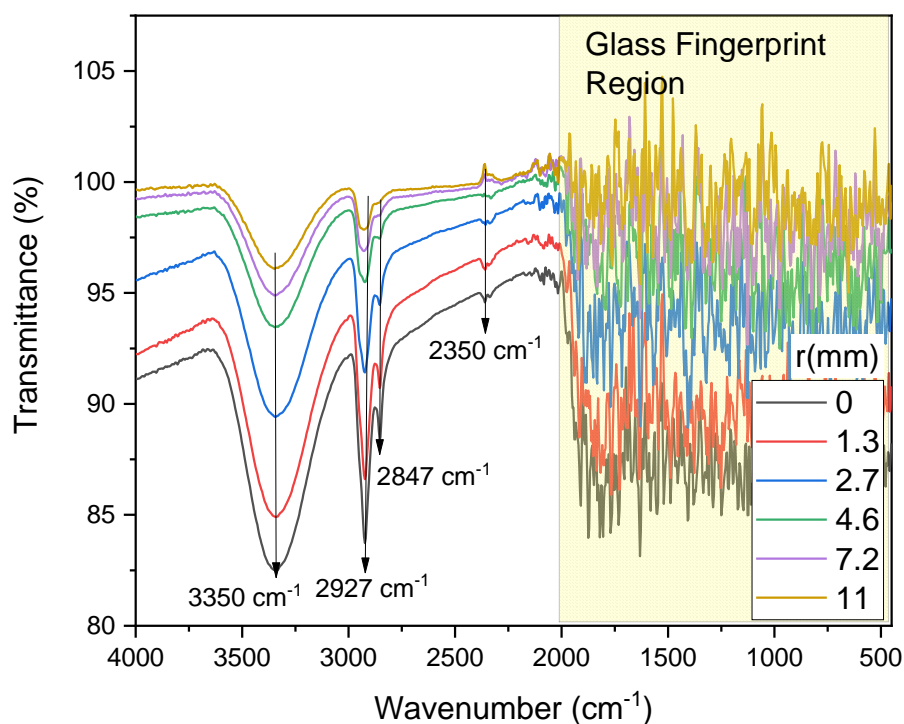


Figure 5-10 Spectra of thin film nanostructure (45.2mPas PVA- PEG-C-GM-pi-FF at spin speed of 1000 rpm) on glass substrate with different radial position r (mm)

The broad O-H peak around 3350 cm^{-1} is associated with gold ion interaction with methacrylic acid (MA) in PVA (Blout & Karplus, 1948). Peaks at 2927 cm^{-1} and 2847 cm^{-1} are believed to be the stretching vibrational transitions of methylene C-H bond of PVA molecules, exhibiting asymmetric $-\text{CH}_2$ stretch and symmetric $-\text{CH}_2$ stretch, respectively (Wexler, 1967). The peak at 2350 cm^{-1} is assigned to CO of carbon dioxide (Fogel & Rutherford, 1990). The regions from 1950 cm^{-1} and below appear scattered, which is due to the diffraction limit of infra-red light in glass within that range, clinically known to be the fingerprint region of glass (Finlayson, et al., 2019) (Pilling & Gardner, 2016). This is the zone where vibrational modes are excited by infra-red electromagnetic wave.

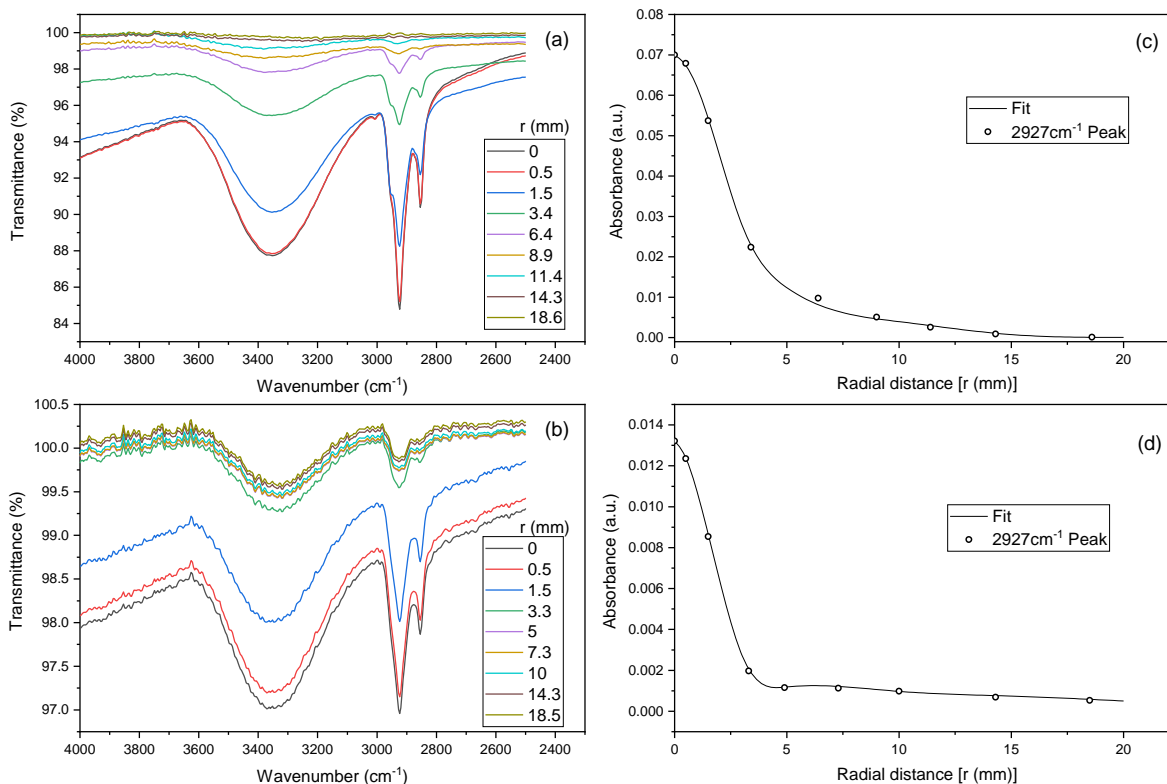


Figure 5-11 FTIR absorption spectra acquired at various radial points on the thin films prepared by spinning the PEG-C-GM-FF nanoemulsion dispersed in PVA solution having 1.9mPas viscosity (a) at 700 rpm (b) at 2500 rpm. The variation in values of the intensity of 2927 cm^{-1} peaks in relation to various radial locations extracted from the (c) spectra in (a) and (d) spectra in the (b). The fitted curve to the peak intensity data in (c) and (d) follow the half-normal distribution. Rest of the data and plots are in the supplementary information.

The absorbance intensity of band at 2927 cm^{-1} corresponding to C-H stretching vibration has been monitored at various radial distances. The transmittance was converted to absorbance using the formula, $(2-\text{Log}(\%T))$ (Larsen, 1971). The observed variation in intensity indicates the formation of pattern of droplet distribution (Figure 5-11). The curve fit of the data points appears to show a half-normal distribution. In order to have a full spatial (diametric) view of the distribution, the data was reflected on the opposite side of the x-axis scale, therefore turning into

a

Gaussian

distribution,

see

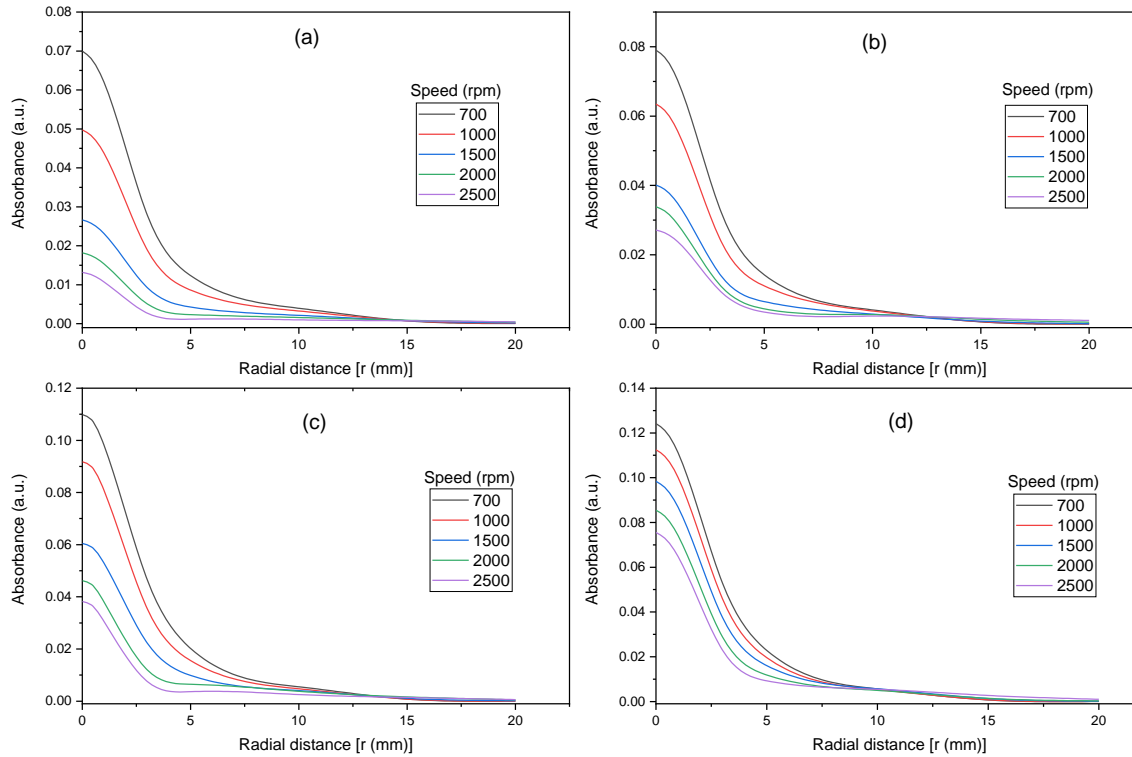


Figure 5-12(a to d). The variation in IR absorbance represents the pattern thickness of the pattern with the coating speed. This test was carried out on the same samples analysed with image processing in **Table 4-1**. A few of the data are presented in Figure 5-11, as the remainder are presented in *Appendix 8.10*.

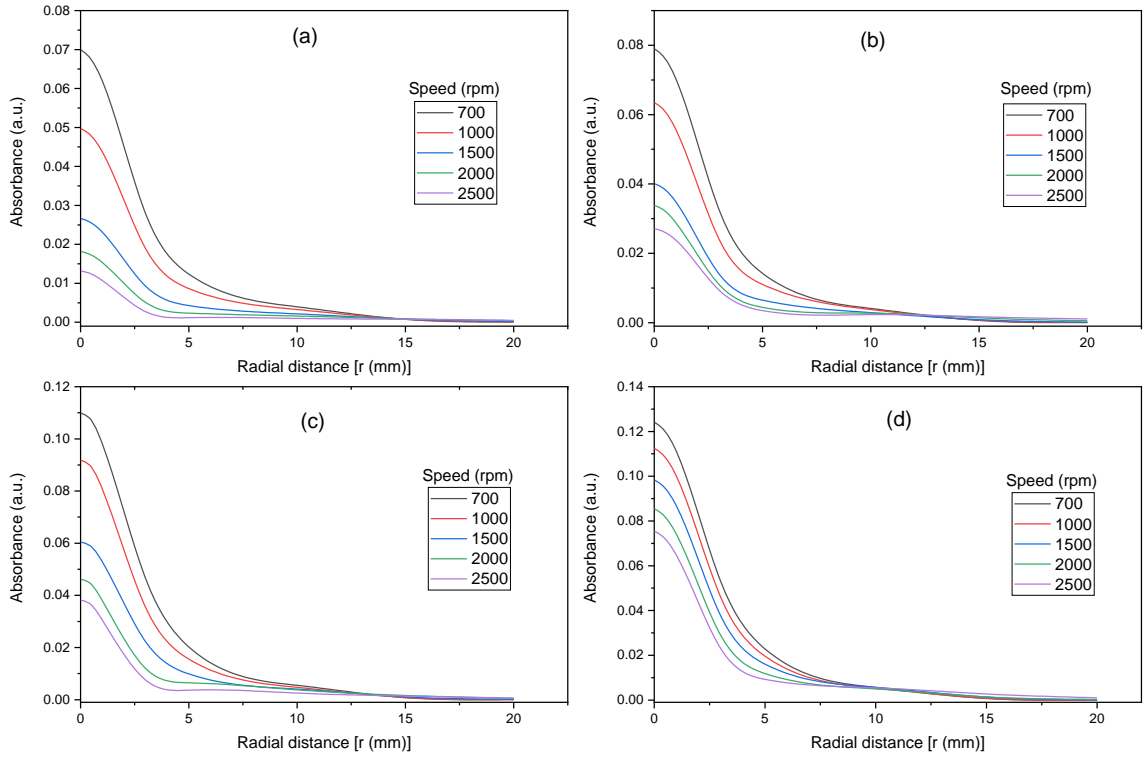


Figure 5-12 Spatial half-normal IR absorption intensity distribution obtained from the various radial location on the surface of the film prepared at different viscosities and coating speed.

Next, the Full width half measure (FWHM) of the FTIR transmission method (FTIR-Trans) absorption at 2927 cm^{-1} for all distributions in

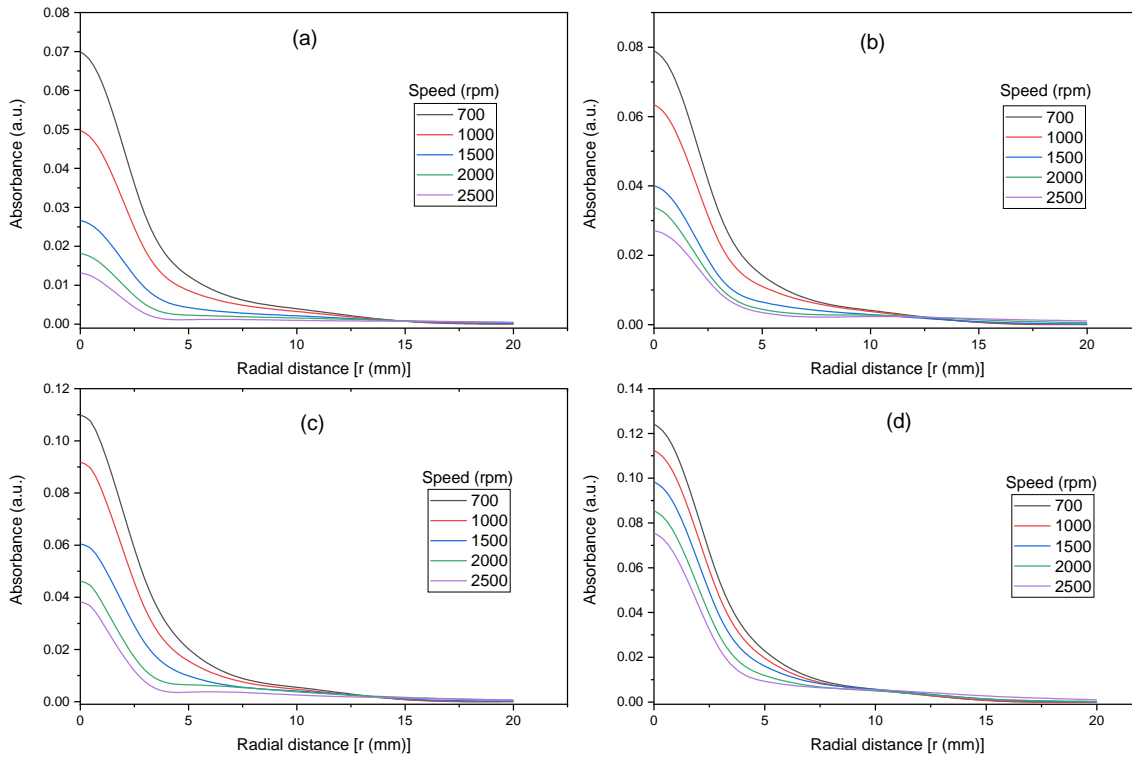


Figure 5-12 were related with the FWHM from ROI-image analysis (

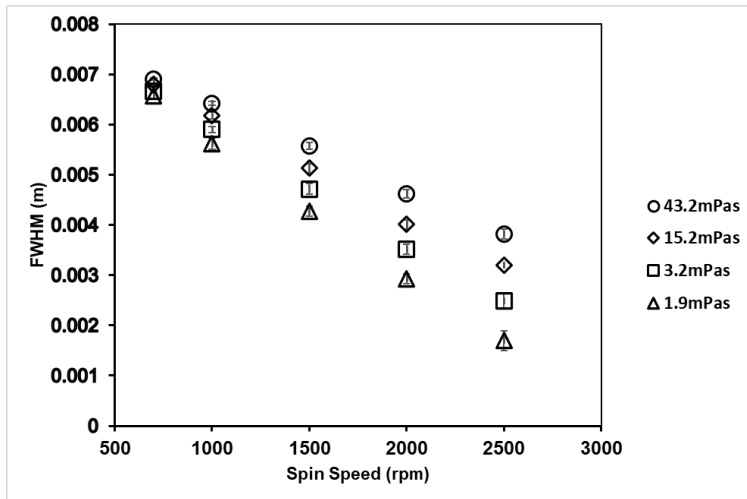
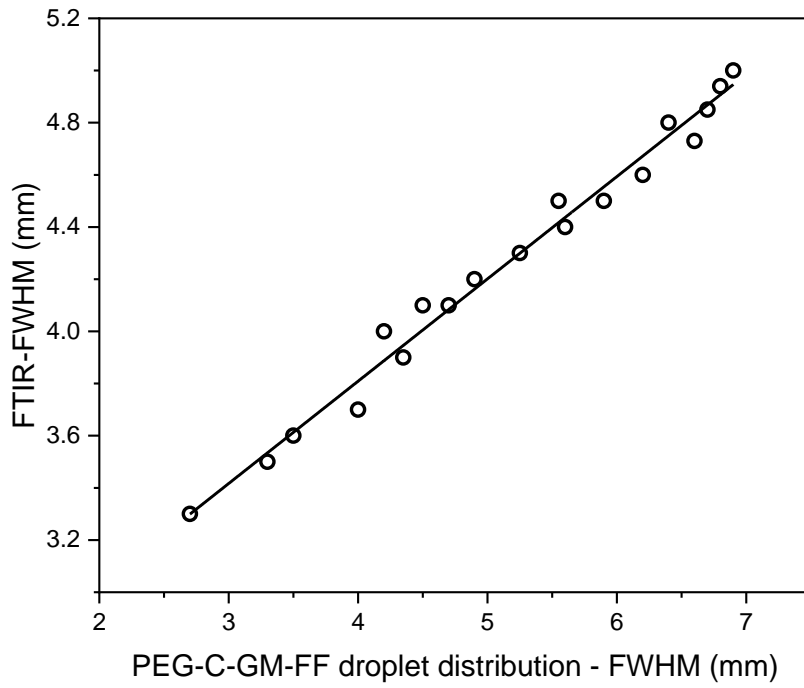


Figure 4-11). The plot of FWHM of FTIR-Trans versus FWHM of ROI-Image is shown



in

Figure 5-13. The relation between FWHM values was found to be linear with good fit and a slope of 0.39.

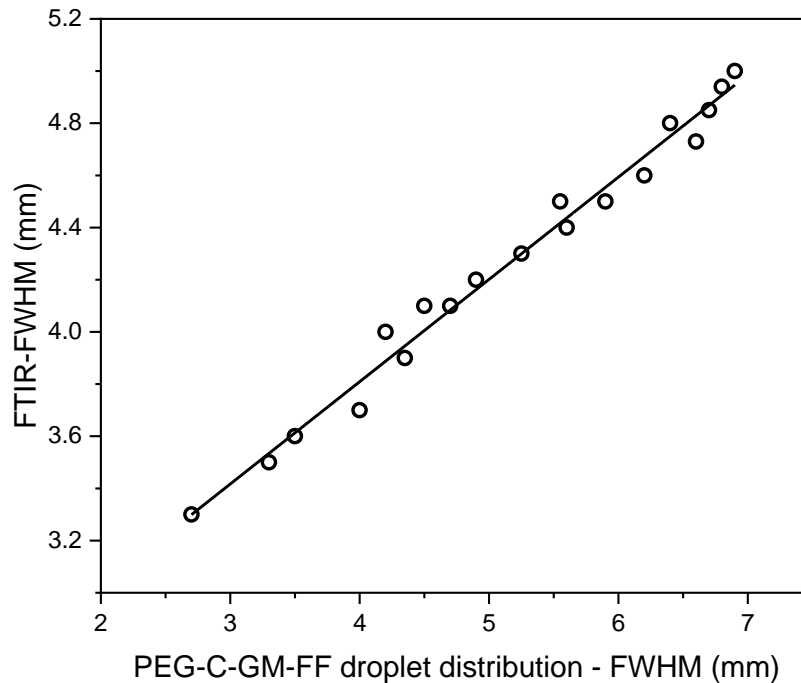


Figure 5-13 Linear fit of the FWHM-FTIR-Trans absorption at 2927 cm^{-1} versus FWHM of ROI-Image.

This trend reveals two aspects: The first, is with higher spin speeds which lead to thinner films and relatively well distributed particles (with lesser FWHM), the IR absorption is seen to be highly responsive to individual PEG-C-GM-pi-FF, and relatively less distinct cluster-wise across the substrate. The second, is with lesser spin speeds and thicker films, the densely layered clusters lead to high amount of IR internal reflection, therefore distinct degree of photo-absorption between middle of thin film and outer radial ranges. This is revealed by the lesser IR FWHM in comparison to increasing PEG-C-GM-pi-FF FWHM distribution.

5.4.2 FTIR Specular reflectance or grazing angle of incidence (FTIR-SR)

FTIR-SR is a technique employed to observe the local field enhancement created by the nanostructure under varying degree of incidence angle of infra-red beam (Maß, et al., 2019). A grating dimensions and order of gold strips deposited on the substrate is found to enhance the two CH_2 (asymmetric and symmetric) IR-absorption bands of the coated layer of MHDA (mercaptohexadecanoic acid). The intensity and shift of the $-\text{CH}_2$ peaks are also sensitive to the grating dimensions and order of gold strips

as sharpest resonance lineshape related to broadband local electric field is only evident for particular thickness of the strip. Similar observations also made for PMMA molecules adsorbed on regular gold grit (Wang, et al., 2013). The grating period of the gold strip closer to the vibrational excitation band of the molecules enhanced the absorbance (a factor of 6000 in their investigation). The presence of the gold was not only responsible for the local enhancement, but gold strip pattern dimensions also influenced a particular group of vibrational bands with frequencies close to the grating diffraction size. Therefore, a relationship between pattern dimension (chain length and gaps) of prepared thin film and enhancement in the vibrational bands were investigated. In addition to this, a qualitative estimation of the local concentration of molecules on thin film and pattern dimension were achieved. The thin film patterned structure investigated in this section was the prepared 15.2mPas PVA, spin coated at 2500rpm, because it gave a better grating profile than other selections as explained in section 4.5.2.3. The specular reflectance infra-red spectra taken at angles 20°, 45° and 80° for the prepared samples is shown in Fig. 5-14

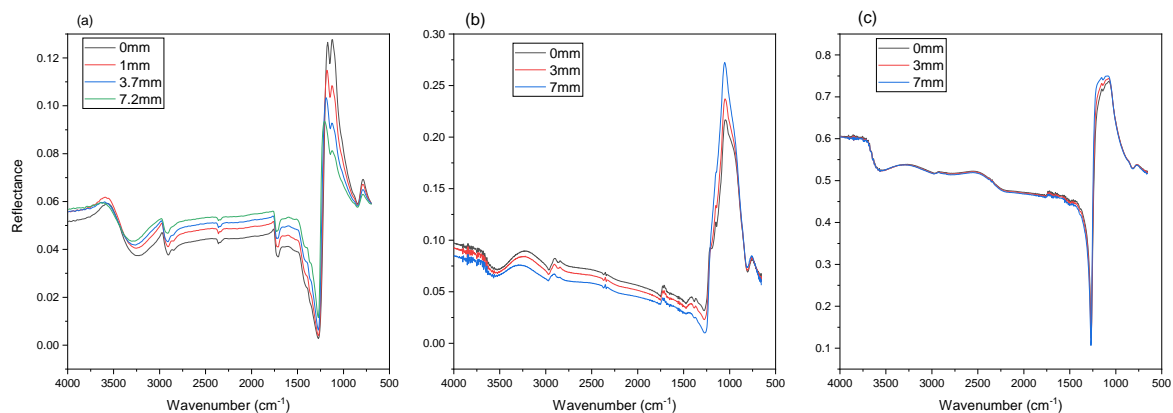


Figure 5-14 Full (4000 cm^{-1} to 650 cm^{-1}) reflectance spectra of thin film on optical glass substrate scanned at angle of incidence (a) 20°, (b) 45° and (c) 82°.

The Full FTIR spectra for all angles of incidence is split into 2 parts; with the first having a range 650 cm^{-1} to 2000 cm^{-1} , and the second having 2500 cm^{-1} to 4000 cm^{-1} . For the case of clarity, 20° is assumed as near normal incidence.

5.4.2.1 650cm^{-1} to 2000cm^{-1} (Figure 5-14 (a-c))

The peak identified between $756 - 762\text{ cm}^{-1}$ is associated with symmetric vibration mode of Si-O-Si (Binding oxygen) network (Geotti-Bianchini, et al., 1991), (Efimov, 1999) (Sidorov, 1967) in glass. The Shoulder peak seen at $\sim 936\text{ cm}^{-1}$ (specially for 45° incidence) is associated with corresponds to stretching vibration of the Si-O \cdot (Non-Binding Oxygen) group in the glass. Peaks between 1046 cm^{-1} and 1105 cm^{-1} are attributed to anti-symmetric vibration (Transverse) mode of Si-O-Si (Binding oxygen) network (Geotti-Bianchini, et al., 1991), (Efimov, 1999) (Sidorov, 1967) in glass. Peaks between 1180 cm^{-1} (ii) – 1210 cm^{-1} (i) are Si-O-Si anti-symmetric stretching (longitudinal) mode (Geotti-Bianchini, et al., 1991) (Geotti-Bianchini, et al., 2003) (Efimov, 1999) (Sidorov, 1967). The Reverse peak at 1272 cm^{-1} is the transmission peak where the glass is transparent related to the depth of wave propagation; where its reduction led to subsequent increase in material absorption and thus rise in LO mode (Tan & Arndt, 2000). Peaks 1367 cm^{-1} and 1409 cm^{-1} are associated with O-H bending for alcohol and carboxylic acid respectively. The peak $\sim 1707\text{ cm}^{-1}$ might be associated with C=O vibrational bond of carboxylic acid of methacrylic acid linked with the gold nanoparticle (Wexler, 1967) (Mahendia, et al., 2011), and $\sim 1729\text{ cm}^{-1}$ could potentially be C=O vibrational bond of residual acetate molecule within the PVA (recall, 88% hydrolysed) (Saini, et al., 2018). The band at 1707 cm^{-1} will be assigned CA-CO, and that of 1730 cm^{-1} will be assigned PVA-CO. It can be observed that at scan locations closest to the middle of the substrate, a relative increase in CA-CO absorption compared to PVAA-CO is observed while at farther scan points away from the centre the reverse is the case. The ratio between peaks is related to the chain thickness-chain gap ratio (CT/CG) and chain thickness (CT) for angles of incidence – 20° , 45° and 82° .

5.4.2.2 2500cm^{-1} to 4000cm^{-1} (Figure 5-14 (e-g))

The broad absorption peak between $\sim 3600\text{ cm}^{-1}$ and $\sim 3000\text{ cm}^{-1}$ is associated with the OH stretching vibrations of PVA and the sharp peak at between 2905 cm^{-1} and 2900 cm^{-1} is attributed to asymmetric stretching vibrations of methylene (C-H) group (Blout & Karplus, 1948) (Wexler, 1967). The 2846 cm^{-1} band is also associated with symmetric stretching vibrations of methylene group (Mahendia, et al., 2011), and it

tend to increase relatively to the $\sim 2918\text{ cm}^{-1}$ band at shorter radial distances. Regarding previous studies on FTIR analysis on PVA gold composite, the increase in both 2918 cm^{-1} and 2845 cm^{-1} bands was as a result of increase in gold nanoparticles concentration. This does not only increase the amount of C-H molecule of PVA that was attached to the gold (Moreno, et al., 2010), but the proximity of interface between gold nanoparticles potentially enhanced the local electromagnetic field (Ghosh & Burgi, 2017). Therefore, increase in these bands intensities reflects increase in gold concentration. Thus, from this observation the increase in the methylene bands leads to increase in methyl group of PVA and therefore increase in associated gold nanoparticles around the scanned location. Interestingly, since the PVA is the bulk (host) material, the $\sim 2918\text{ cm}^{-1}$ band is assigned PVA-CH-asm, and 2845 cm^{-1} band is assigned PVA-CH-sm. Their ratio (PVA-CH-sm/PVA-CH-asm) is fitted against CT/CG.

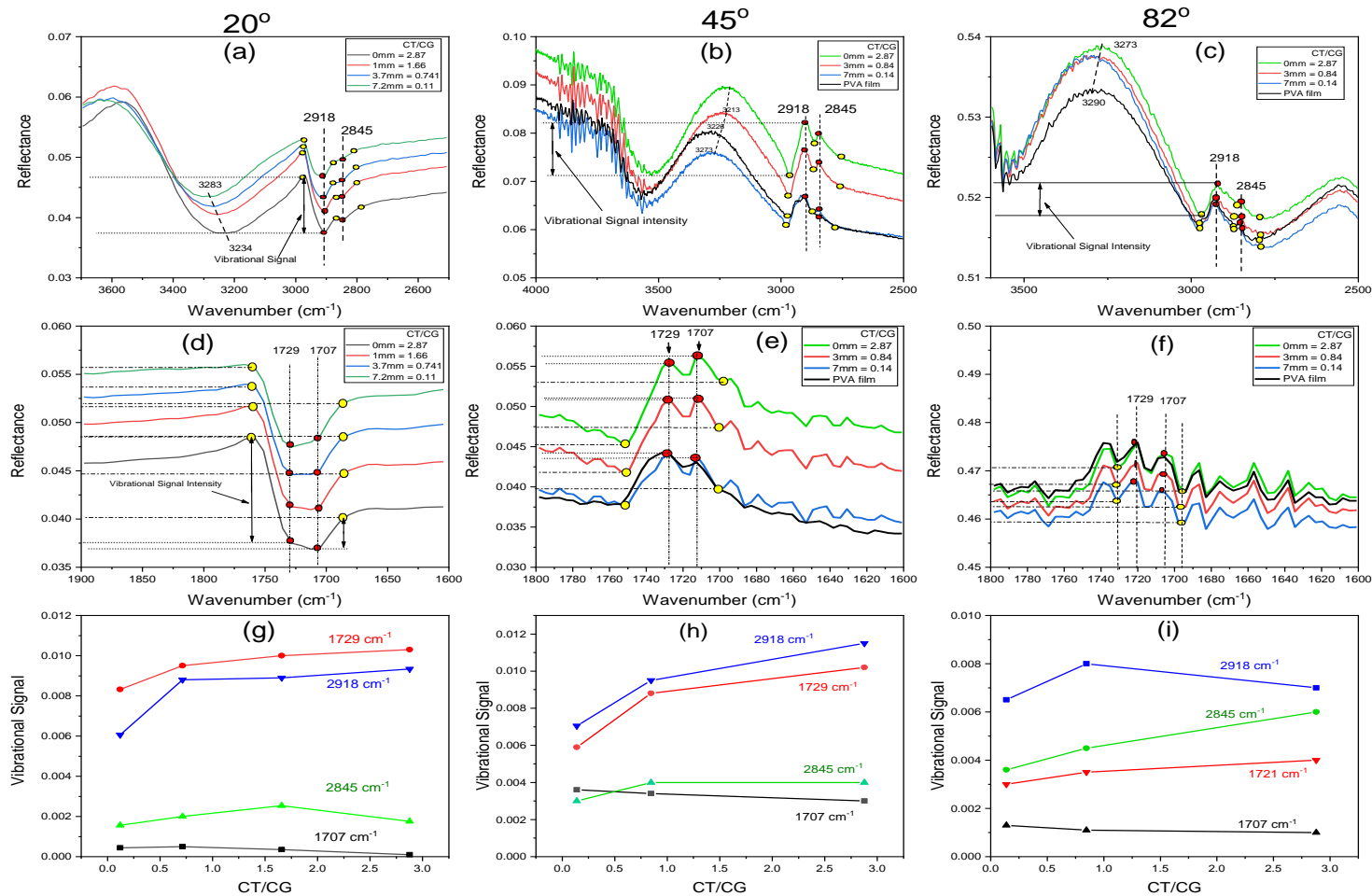


Figure 5-15 : Specular Reflectance spectra showing the vibration signal intensities of; PVA CH asymmetric (2918 cm⁻¹) and symmetric (2845 cm⁻¹) bonds (a) 20°, (b) 45° and (c) 82°, and PVA C=O (1729 cm⁻¹) and CA C=O (1707 cm⁻¹) for (d) 20°, (e) 45° and (f) 82°. The relationship plot between measured vibrational signal intensities for bands 1729 cm⁻¹, 2918 cm⁻¹, 2845 cm⁻¹ and 1707 cm⁻¹, against CT/CG, for (g) 20°, (h) 45° and (i) 82°.

5.4.2.3 Relationship between band Ratios and Pattern formation

From image analysis of the sample used for the FTIR study, the positions scanned were matched with the CT/CG values. These are presented in **Table 5-2**. The resolution of scan area was 50 μm . The peaks associated with each band (red circles) was subtracted by the absorption intensities of local minima points (yellow circles in *Figure 5-15*(insert – a, b, c) & d, e ,f) associated with the peaks to determine the change in vibrational intensity under each relative CT/CG ratio (*Figure 5-15 g, h & i*). It must be noted that corresponding the values of r(mm), CT (μm) and CT/CG are correlated and therefore, these terms are used interchangeably in discussion. Consult **Table 5-2** for clarity. The spectrum between 3200 cm^{-1} and 2600 cm^{-1} was baseline-corrected (BSL-C) using 2600 cm^{-1} as the reference point for each CT/CG spectra *Appendix 8.14*.

Table 5-2 CT and CT/CG from image analysis of 3.3wt% PVA under 3000 rpm spin speed

r (mm)	CT (μm)	CT/CG
0	2.82	2.88
1	2.68	1.30
3	2.24	0.85
3.7	2.01	0.72
7	1.087	0.014
7.2	1.01	0.012

The relation between CT/CG and the intensities of bands PVA-CH-sm and PVA-CH-asm are found to be nonlinear at most angles of incidence. The C-H asymmetric and symmetric vibration are seen in spectrum of the thin film to methylene group present in PVA is of the same intensity as $r \sim 7\text{mm}$, (*Figure 5-15 a, b & c*). At 20° incidence, the vibrational intensity of band - PVA-CH-asm is higher at values 2.88 of CT/CG than with CT/CG=0.12 (*Figure 5-15 g*). PVA-CH-asm increased by 35% along with increase in CT/CG by 185%, while the BSL-C version (*Appendix 8.14*), gave a signal increase of 39%. This also followed the trend of increment in chain thickness (**Table 5-2**). The change increment of PVA-CH-asm absorption was more pronounced at 45° incidence angle, with overall increase of 40% (*Figure 5-15 h*), while BSL-C version showed a 94% increase. The vibrational intensity of band - PVA-CH-sm observing from the BSL-C data (*Appendix 8.14*), showed that 20° incidence resulted in 350%

increase, while 40° yielded 667% increase in vibrational intensity (*Appendix 8.14*). This behaviour was not the same for 82° , where a PVA film read at values equivalent to the values at $CT/CG=2.88$ (or $r=0\text{mm}$) of the pattern. However, a noticeable decrement was observed from this point to $r=7\text{mm}$ with overall change of 25% (*Figure 5-15 i*). Thus, the thickness of the chain influenced multiple surface interaction with the C-H group of the PVA. Also, the small gaps between chains provide a large hot spot volume and a broadband local field enhancement (Wang, et al., 2013). This broadband field enhancement could play a role in enhancing absorption of spectrally distributed vibrational bands (Maß, et al., 2019). The gold nanoparticles spherical surface provides local electric field which can be enhanced when in close proximity with another, especially where the cluster is denser with little gaps in between particles (Ghosh & Burgi, 2017). Band PVA-CO also responds to the trend of chain thickness for all incident angles, where it has approximately the same absorption intensities at both 20° and 45° (*Figure 5-15 g & h*). At 20° incident angle, the change in PVA-CO intensity from $CT=1.01\mu\text{m}$ to $2.82\mu\text{m}$ was 19%. At 45° incident angle, this change was 42%. Meanwhile, for 82° , this was not the case, due to the absorption value at these bands for a single layer PVA film was the same as the value at $r=0\text{mm}$ (*Figure 5-15 b*), while there is noticeable decrement of peaks at lesser CT/CG values (*Figure 5-15 i*). This effect is explained in the next paragraph

The relative absorption tends to be higher at 45° incidence and 82° incidence the lowest signal response. Grazing angle method is a technique objected to improve the interaction of light with the material in order to enhance its detection. However, the drop in signal at 82° might probably be due to the decrement in intensity of light as it forms an oblique spheroid shape covering a relatively larger area on the surface of the material than at normal incidence. Adopting a practical concept of glancing angle deposition and the height of the chain from the substrate surface could likely form a shadow casting of one strip on the other might likely reduce the average interaction of light on the material (Hawkeye, 2007). Another possibility could be more back-scattering of incident wave (Gramotnev, et al., 2002). This indicates that with increase in incident angle, the waves are poorly interacting with the thin film pattern and just glancing though it.

On tracking the shift in absorption band for O-H bond (*Figure 5-15 d, e & f*), the band values for each radial position were converted from cm^{-1} to micrometres and the shift was calculated from $r = 7\text{mm}$. The corresponding change in CT/CG was also calculated and the relationship is presented in *Figure 5-16*. At 20° , 45° and 82° incidence, the relationship was generally linear as the thickness of the chain increases and the gap reduces. These red-shifts and increasing intensities potentially corresponds to the impact of local near field enhancement through the increase in chain thickness and decreasing gaps as established from simulations and experiments (Barho, et al., 2016) (Maß, et al., 2019). This linear relationship changed to higher values when $\text{CT/CG} > 1$, in the form of a drastic red-shift. This is as a result of smaller gaps relative to the chain thickness that established a grating order of $\sim 3.8\mu\text{m}$, which is close to the OH band wavelength ($3.1\mu\text{m}$); where the likelihood of a further drastic enhancement of intensity due to the coupling of lattice resonance and local near field resonance to establish an enhanced broadband local field.

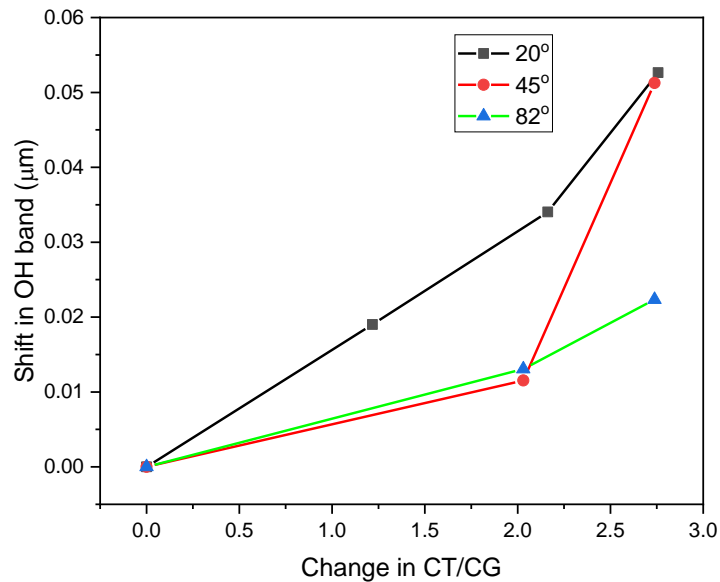


Figure 5-16: Shift of O-H band of PVA versus the change on CT/CG ratio

The spectra behaviour of bands between 1272 cm^{-1} and 1000 cm^{-1} at 20° incidence shown in *Fig. 5-16(a)* are known to be the phononic SiO_2 stretching vibration of SiO_2 coupled to the near field resonances from the patterned structure (in literature

context, it is identified as nano-antennas) (Neubrech, et al., 2017) (Mayerhöfer & Popp, 2018). The presence of a plasmonic material like gold can initiate excitation of surface phonon polariton where the enhanced phononic signal of SiO₂ is observed at the longitudinal optical (LO) vibrational frequency (Neubrech & Pucci, 2013). This behaviour is not possible at normal incidence without nanoantennas (Neubrech, et al., 2010), except at grazing angles > 60° (Amm, et al., 2015) (Wang, et al., 2003). An investigation on this LO peak behaviour from the hybridization of antenna/SiO₂ system have been investigated in the past (Neubrech & Pucci, 2013) (Neubrech, et al., 2017). Neubrech and co. investigated the effect of gold nanowire length on the optical behaviour of the Fano-type signals (LO and TO) of SiO₂ (Neubrech, et al., 2010) Fig. 5-17 (b). The increasing length of nanowire initiates more near field scattering that locally excite surface phonon polaritons yielding a resonance that is close to the vibrational frequency of the surface phonon polariton, which therefore leads to not only a shift in TO vibrational mode but an increase in LO mode vibrational intensity (Neubrech, et al., 2010) (Neubrech & Pucci, 2013) (Huck, et al., 2016).

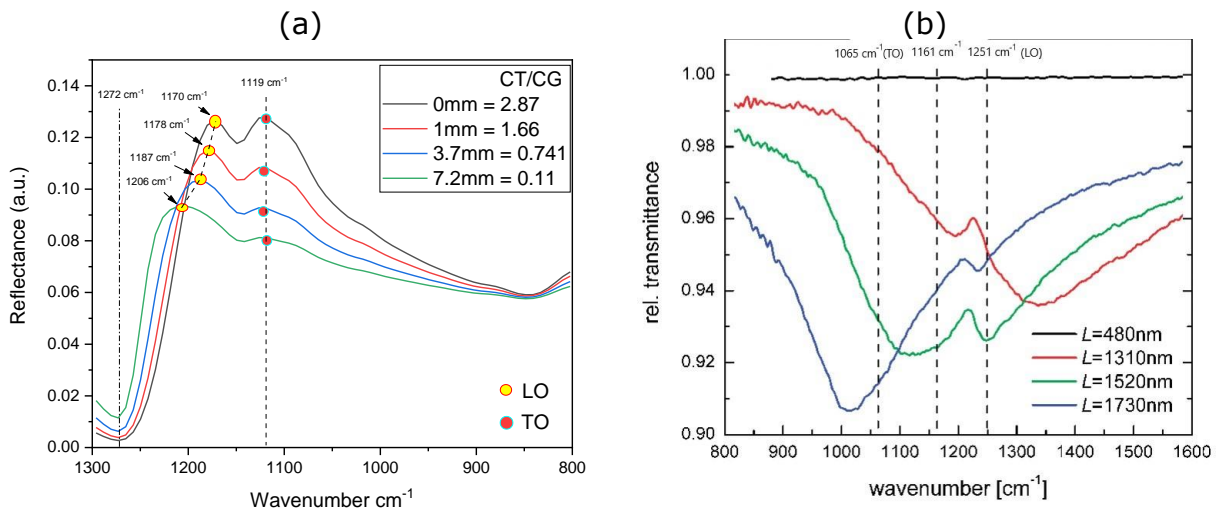


Figure 5-17: (a) Specular reflectance IR spectra at varying CT/CG ratios of gold-Fe₃O₄ heterostructures highlighting a change in vibrational intensities of longitudinal optical (LO) and Transverse optical (TO) bands of SiO₂. (b) Relative transmittance spectra of nano-antennas of different gold nanowire lengths prepared on silicon wafer with a natural SiO₂ Layer (thickness 3nm). Courtesy (Neubrech, et al., 2010).

Thus, this same situation likely occurred within the PEG-C-GM-pi-FF in thin film patterned designed structure where multiple near field scattering excited and

established phonon resonances at SiO₂ surface Fig. 5-16(a). This increases in intensity and redshift of the LO vibration band as CT/CG increases (having bigger chains and small gaps where scattering could resonate in high amplitude).

5.4.2.4 Multiple Layers

In the next part of the FTIR-SR analysis on thin film nanostructure, 3 layers, 6 layers and 9 layers of coating was laid over the substrate using the same conditions (15.2mPas and 2500 rpm spin speed). The spectra for 20°, 45° and 82° are all presented in Figure 5-18.

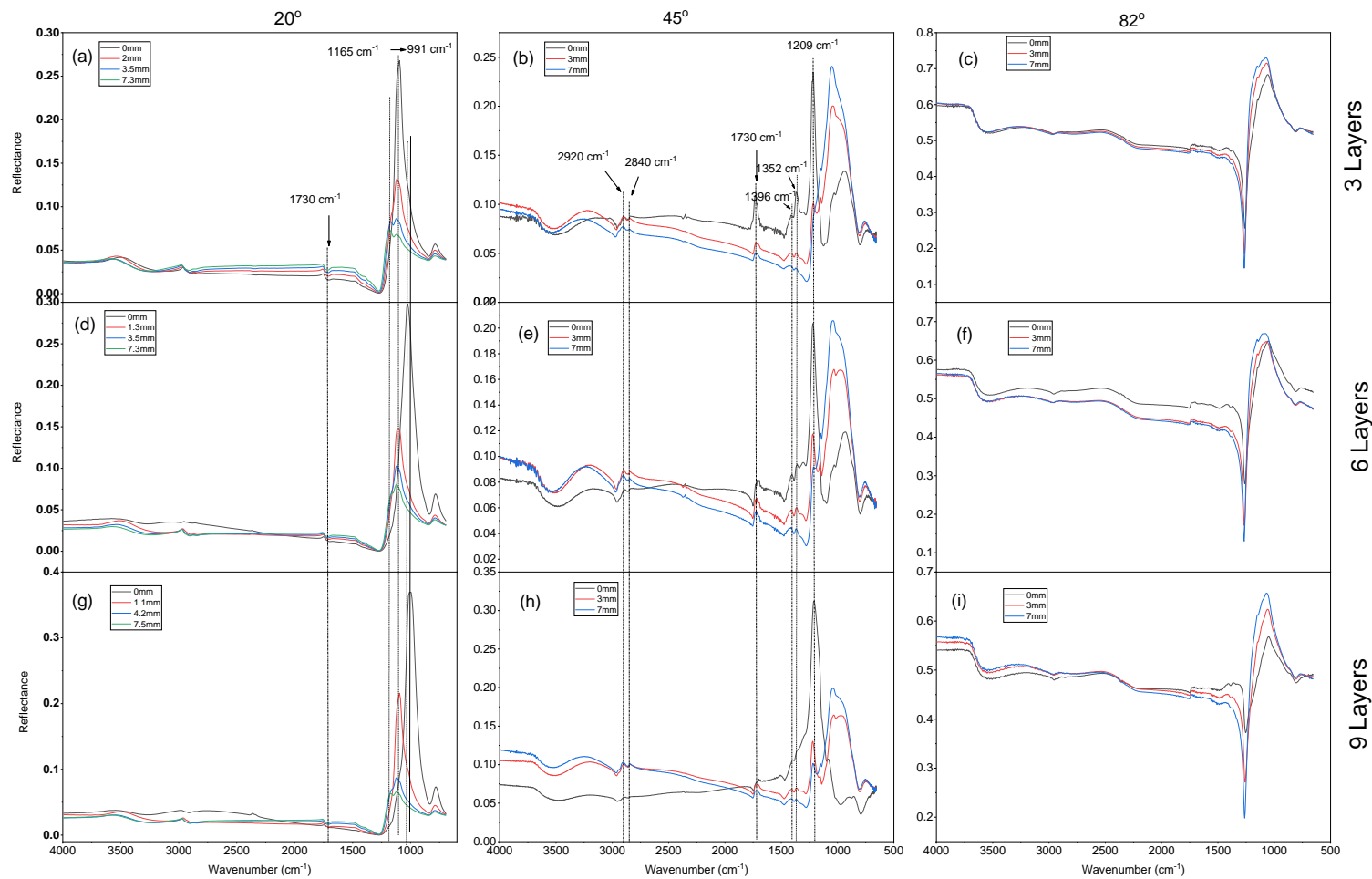


Figure 5-18: FTIR-SR of thin film patterned structure at (a) 20°, 3 layers (b) 45°, 3 Layers (c) 82°, 3 Layers (d) 20°, 6 layers (e) 45°, 6 Layers (f) 82°, 6 Layers (g) 20°, 9 layers (h) 45°, 9 Layers (i) 82°, 9 Layers.

Physically, the multiple layering increased the thickness of film. Also, the optical response changed. At incidence angle at 20° with 3 layers, C=O band at 1730 cm^{-1} increased by 6.4% from $r=7.2\text{mm}$ to 0mm , while with increasing layers (6 & 9) at $r=0\text{mm}$, the absorption intensity declined by 70%. At 45° incidence, where $r=7\text{mm}$ to 0mm , C=O bond increased by 700% for 3 Layers, 102% for 6 layers and 37.5% for 9 layers. However, the intensity of C=O band at $r=0\text{mm}$ between layers 3 and 9 decreased by 83%. As regards the OH band, significant redshift was observed as for $r=7\text{mm}$ to 0mm . In general, the spectra revealed that at thicker film sections, the incident wave is heavily diffracted and scattered within the thin film by the high density of PEG-C-GM-pi-FF. The scattering affects the degree of absorption detectable by the equipment. It also confirmed that the chain array for each layer did not align and therefore waves experience destructive interference within the thin film structure (see Figure 5-19). The density of PEG-C-GM-pi-FF within the thin film increases its refractive index beyond the glass slide and air, therefore, at some oblique incident angle (like 45° in this case), internal reflection between the surfaces of the film, glass and air might occur (Tien, 1971). This can be seen from the increase in LO band (responsible for SiO_2 surface vibrations) by 34%, increase in band 1272 cm^{-1} associated with transparency of glass slide by 62%.

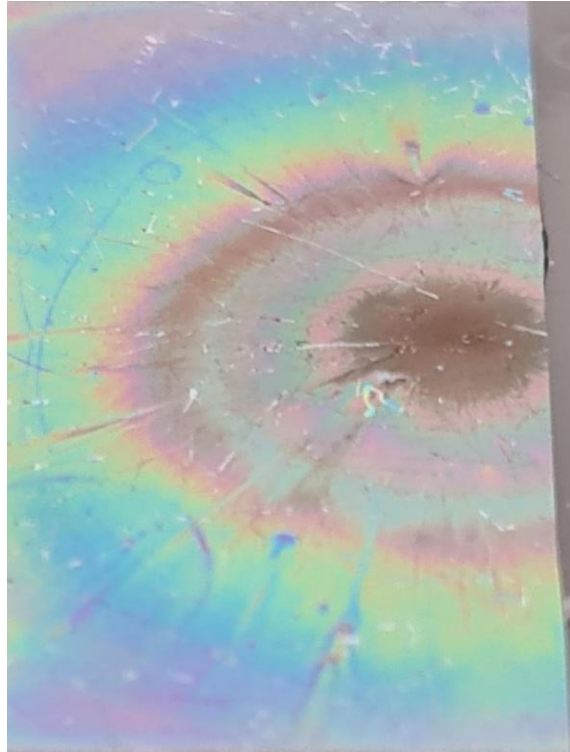


Figure 5-19: A 6 layered coating of (PVA 15.2mPas and spin speed of 2500) thin film nanostructure on glass slide, showing interference colour effect when tilted at oblique angles ($\sim 35^\circ$ from normal).

5.5 Magnetization curve

The hysteresis curve of thin film coated silicon wafer is shown in Figure 5-20. The insert in the figure showed a close look at the curve intersects at both sides of the axes. In order for the determination of necessary parameters, conversion of the units was applied. $A/m = \text{emu/g} \times \text{density of tested sample (Kg/m}^3\text{)}$, $1 \text{ Oe} = 79.56 \text{ A/m}$.

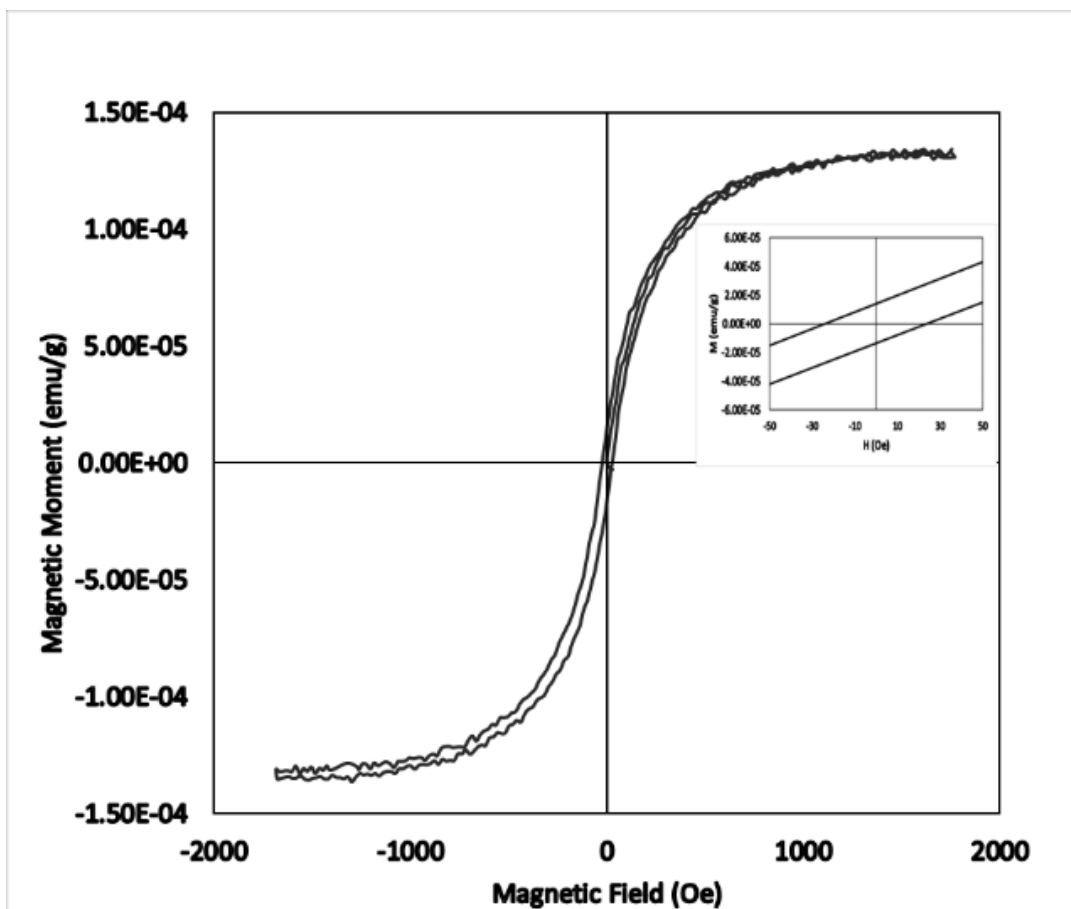


Figure 5-20 Magnetic Hysteresis curve of 5mm cut of coated sample on silicon wafer. Insert is the close look of magnetization curve close to the origin to identify the coercivity and magnetic susceptibility.

From the calculations, the saturation magnetization of this sample is 0.3254 A/m, The coercivity ($H=0$) is 0.0011 A/m, and magnetic susceptibility is 1.9×10^{-5} .

5.6 Raman Test and Analysis

This section discusses on experiment setup, results and analysis of obtained Raman spectral of nanostructure coated with an analyte substance.

5.6.1 Results

This sub-section presents Raman spectral response of Rhodamine 6G (R6G) molecules coated over the thin film nanostructure. Varying locations were probed to observe the change in intensity of molecular vibration of Rhodamine 6G molecules. It is expected to see the magneto-optical effect on vibrational signal intensity of the Rhodamine 6G molecules.

5.6.1.1 Rhodamine 6G coating and Raman spectra acquisition set up.

Approximately $4.6 \times 10^{-7} \text{M}$ of R6G in 95% acetone, 5% DI water was prepared and the thin film nanostructured coated wafer was immersed and left for 5 hours. The reason for the use of acetone was because it does not react with PVA and provides enough time to bind R6G to the nanostructured thin film (15.2mPas PVA, 3000rpm spin speed). The magnetic setup shown in Figure 5-21, consisted of two permanent magnets with field strength of 130 mT at their surface, were spread 15mm apart with opposite poles facing each other. The average magnetic field within the region of the supported silicon substrate was 43 mT as measured by the probe-type gaussmeter (mentioned in Section 3.3.2).

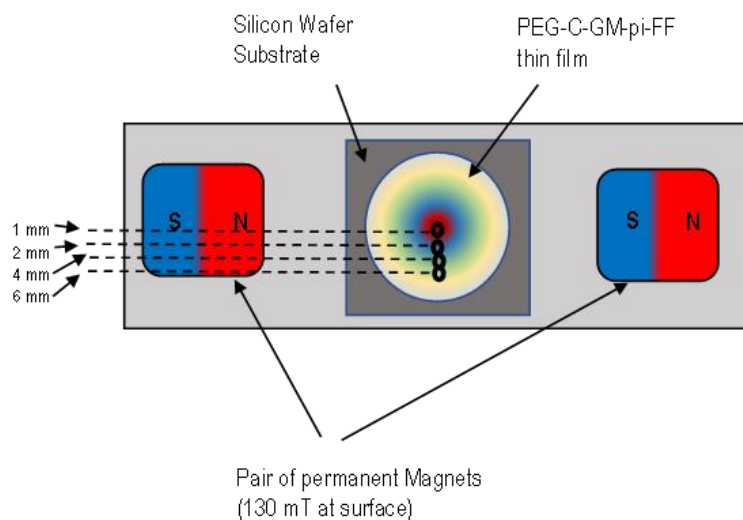


Figure 5-21: A schematic showing the setup to coat the pickerin gdroplet thin film structure deposited on silicon wafer with Rhodamine 6G. The wafer elevated 2mm from the supporting frame and in between two sets of 130 mT square magnets with opposite poles facing each other 15 mm apart. The measured average magnetic field above the substrate was 43mT. The Raman microscope beam was perpendicularly focused on the thin film at radial locations, $r = 1\text{mm}$, 2mm , 4mm and 6mm .

5.6.1.2 Magneto- Surface Enhanced Raman Scattering (SERS)

SERS (surface-enhanced Raman scattering) is widely used to increase the signal to noise ratio from biomolecules. Incident laser excites the surface of the precious metal nanoparticles such as gold to produce the surface plasmon resonance. However, the signal enhancement factor is directly proportion to four times the value of total electric field on surface. One way to boost the electric field is by increasing the laser

power, however, it can often burn the analyte molecule. To overcome, the increasing the magnetic field would be an appropriate technique, where weak magnetic field in iron oxide particle traverse through entire layer of gold nanoparticles and induce Lorentzian force on electron resulting into their polarisation. This polarisation field contributes to the total electric field on gold nanoparticles causing the increase in the Raman signal to noise ratio even at low concentration of analyte molecules.

5.6.1.3 Detection of Rhodamine 6G using Magneto-SERS.

The film produced from the gold pickering emulsion contain the gold nanoparticles embedded in the iron oxide particle layers as discussed in FTIR results section in this chapter. As seen in Figure 5-20, the M-H (magnetisation vs applied magnetic field) curve of pickering droplets in thin film on silicon substrate was used to estimate the degree of magnetization of iron oxide particles within the probed region. The M_{DR} (saturation magnetisation) was estimated to be 0.27 A/m. However, the iron oxide cluster density would be higher with increase in the chain thickness, it is therefore assumed that the local magnetic field would be strongest at regions with thicker chains than less thicker chains. This increased local magnetic field can be derived

from the CT/CG and CT distribution profile for this case as represented in

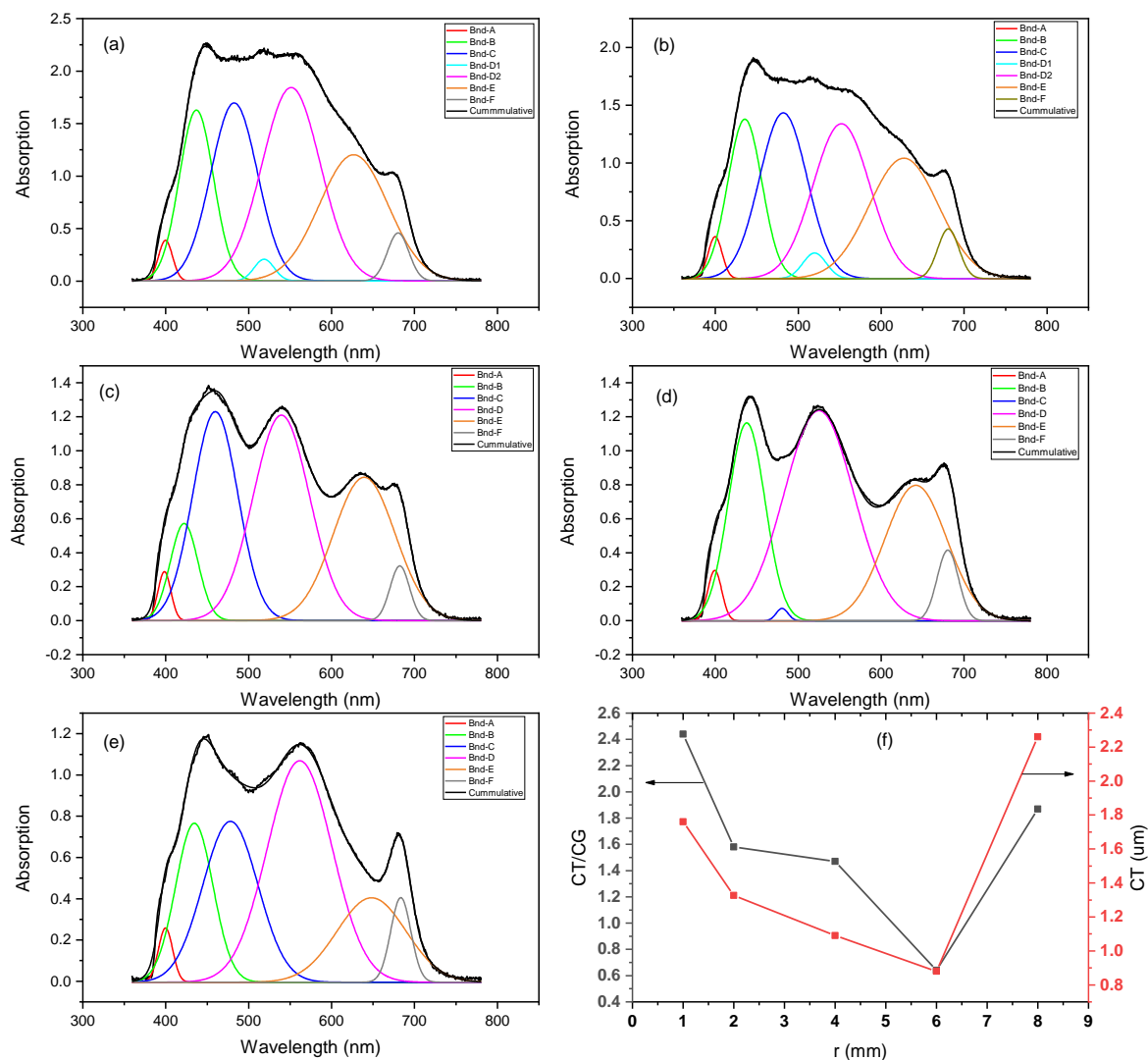


Figure 5-6.

To detect the low concentration Rhodamine 6G (R6G), the molecules of the R6G was adsorbed on the film. Applying the magnetic field parallel to the substrate it is hypothesised that the intensities of the peak attributed to various bond in R6G would be increased. As seen in FTIR results, the interaction between iron oxide and gold nanoparticles was established which contributed to -CH peak intensity increase. The structure achieved in the prepared thin film and the gap between them was satisfying the condition for interaction meaning the iron oxide particles and gold particles were

close enough to allow charge transfer at the interface. The resulting Raman spectra for scanned locations, 1mm, 2mm, 4mm and 6mm are shown in (Figure 5-22).

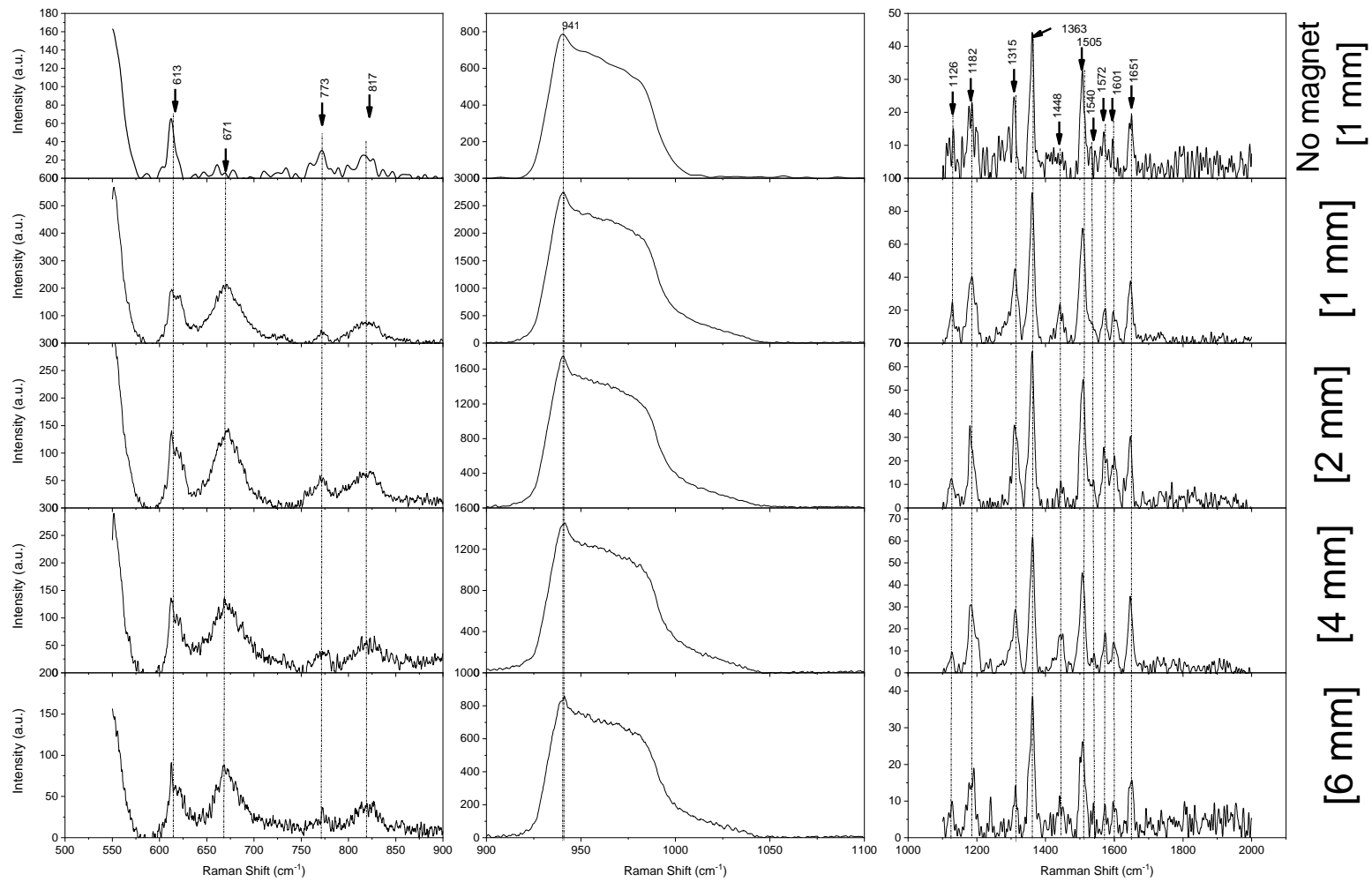


Figure 5-22: Raman Spectra of R6G on test sample (showing three separated Raman shift ranges) subjected to zero magnetic field (at $r=1\text{mm}$) and with magnetic field (at $r= 1\text{mm}, 2\text{mm}, 4\text{mm}$ and 6mm).

To observe the effect of magnetic field on the Raman peaks corresponding to R6G, the Raman spectra obtained at various radial locations on magnetised thin film as mentioned in previous section. All identified peaks for each scanned region, $r = 1\text{mm}$, 2mm , 4mm and 6mm (magnetized) and $r = 1\text{mm}$ for unmagnetized are hereby presented in **Table 5-3**. The effect of magnetic field across the selected scanned region was estimated by subtracting the intensities of each identified band from the unmagnetized intensities obtained at $r = 1\text{mm}$. Therefore, the percentage change was thereby quantified. The CT/CG values were highest at $r = 1$ location on thin film meaning high concentration of gold and iron oxide particles. Moreover, the gaps between chains were less providing an opportunity of R6G molecule adsorption as well as charge transfer across the gap.

Table 5-3: Identified Raman bands of Rhodamine 6G, the peak intensities at radial locations, $r = 1\text{mm}$, 2mm , 4mm , 6mm for magnetized and $r = 1\text{mm}$ for unmagnetized. The percentage change of magnetized regions from unmagnetized was estimated and placed at the side of respective peak intensities.

Raman Shift band cm^{-1}	Assignment	$r = 1\text{ mm}$ (zero Magnetic field) Peak intensity	$r = 1\text{ mm}$ Peak Intensity (% increase from zero magnetic field)	$r = 2\text{ mm}$ Peak Intensity (% increase from zero magnetic field)	$r = 4\text{ mm}$ Peak Intensity (% increase from zero magnetic field)	$r = 6\text{ mm}$ Peak Intensity (% increase from zero magnetic field)
1651	Aromatic C-C stretching in Xanthen ring	17.7	52(194%)	39(120%)	41(132%)	19(7%)
1601	Hybrid mode in phenyl ring with COOC_2H_5	11	35.2(220%)	22.4(104%)	18(64%)	15.2(38%)
1572	Aromatic C-C stretching phenyl ring	13.4	39(191%)	30.4(127%)	21(57%)	15.8(18%)
1540		10.4	26(150%)	18(74%)	13(25%)	11(6%)
1505	C-C stretching in Xanthen ring	33.6	77(129%)	61(82%)	59.4(77%)	26.4(-21%)
1448	C-N stretching in NHC_2H_5	8	25(213%)	10.5(32%)	30.5(281%)	13.1(64%)
1363	Aromatic C-C stretching in Xanthen ring	43	100(133%)	69(60%)	67.4(57%)	43.6(1.4%)
1315	Aromatic C-C stretching	24	63(163%)	41(71%)	44(83%)	24(0%)

Assignments were from papers; (Zhong, et al., 2018) and (He, et al., 2012).

Table 5-4 Contd.: Identified Raman bands of Rhodamine 6G, the peak intensities at radial locations, $r= 1\text{mm}$, 2mm , 4mm , 6mm for magnetized and $r= 1\text{mm}$ for unmagnetized. The percentage change of magnetized regions from unmagnetized was estimated and placed at the side of respective peak intensities.

1182	C-H in plane bending in Xanthen ring	22	49(123%)	47(114%)	33(50%)	29(32%)
1126	C-H in plane breathing in Xanthen/Phenyl rings	14	37(164%)	24(71%)	19.5(40%)	18(29%)
940	Ring Breathing	794	2753(247%)	1442(82%)	1735(119%)	854(8%)
817		4	71(1675%)	64(1500%)	66.3(1558%)	40.7(917%)
773	C-H out of phase bending	24	36(50%)	39(63%)	56(133%)	35(46%)
671	C-C-C ring in plane bending in Xanthen/Phenyl rings	1.8	217(11,956%)	130(7122%)	148(8122%)	84.4(4600%)
611 - 613	C-C-C ring in plane bending in Xanthen/Phenyl rings	66	192(191%)	139(111%)	137(108%)	84(27%)

Assignments were from papers; (Zhong, et al., 2018) and (He, et al., 2012).

As seen in **Table 5-3**, the peak intensities have increased significantly at the same location. Even with same thickness and gaps at the locations, the peak intensity for each R6G bond have increased 50 to almost 12000%. Upon irradiation with laser, the gold nanoparticles electrons get excited and migrate toward the interface between gold and iron oxide with strong $|E|$ -field localization between their defect states (Korobchevskaya, et al., 2011). These plasmonic electrons can induce a strong enhancement of the dipole moment of the nearby analyte molecules. The structure of 1D array chain sizes in terms of chain thickness and gap effectively diffract electromagnetic wave within the structure to counter the dampening of electron excitement and enhance the near field plasmonic resonance of nanoparticles (Gillibert, et al., 2016). The magnets were also placed at the bottom of the silicon wafer substrate; however, the magnetic field did not increase the intensity of the peaks as it was observed when the magnets were placed as shown in previous section. The alignment of the magnetic field with the electric field of SERS could have contributed to this observation. As both fields are vector fields, it is necessary to align the magnetic field to obtain the enhancement in signal to noise ratio.

The 14 nm iron oxide particles within the ferrofluid that possesses a single domain can easily switch in polarity along the direction of an applied magnetic field (Barhoum & Garcia-Betancourt, 2018). Therefore, with the electric field/charge being accumulated at the interface between gold nanoparticle and iron oxide nanoparticles, the magnetic field as an external force could effectively polarizes and aligns the electric charge in the direction of the magnetic field (Deng, et al., 2019). The directional manipulation of charges, analytes in close proximity would tend to vibrate more and therefore increase in absorption.

Next, five major bands of R6G were selected for comparative analysis because of their high sensitivity to Raman; $\sim 671\text{ cm}^{-1}$, 773 cm^{-1} , 1363 cm^{-1} , 1505 cm^{-1} and 1651 cm^{-1} , (Rigo, et al., 2011) were quantitatively related to the CT/CG for all radial points by estimating relatively to 1mm. A linear relationship for bands $\sim 671\text{ cm}^{-1}$ with CT/CG exists, where its absorption increased by 160% as CT/CG increased by 281%. Band 773 cm^{-1} remained fairly constant across all changes in CT/CG, which signifies that it is unresponsive to optical enhancement. Band 1363 cm^{-1} increased by 9400% with the same increase in CT/CG. Band 1505 cm^{-1} linearly but inversely related with CT, where it reduces by 700% as the CT increases by 100%, because of the increase in local magnetic field (Deng, et al., 2019). Band 1651 cm^{-1} increased in intensity by 2540% as CT increases by 100%.

5.7 General Discussion

The optical study offered a clear picture on the characteristics of the patterned structure and what significance it might hold going forward.

The UV-Vis measurement focused on the gold-iron oxide interaction within the structure. The deconvolved bands of each broadband spectra confirmed the relative concentration of iron oxide and gold at each radial location corresponding to the CT/CG value, as well as its interacting configuration (surface exposed or embedded) within the structure. In situations where gold nanoparticles are fewer and embedded within group of iron clusters, the multiple interfacial contact with rough edges of iron oxide nanoparticles causes the excited electrons from gold nanoparticle to diffuse from its Fermi level to the conduction band of the iron oxide causing charge

accumulation at the defect states of the interface (George, et al., 2011) (Comin, et al., 2012). This phenomenon leaves the gold nanoparticle deficient and therefore is represented as the redshifted band at 690 nm. This phenomenon causes the iron oxide in contact with an electron deficient gold to become more photo responsive with bands at ~ 400 nm. In surface configuration where gold is partially in contact with iron oxide, the same phenomenon occurs but not as deficient as the embedded configuration. These yield absorption bands at ~ 550 nm for gold and ~ 444 nm for iron oxide. If there would exist free gold nanoparticles within the chain gaps due to magnetic compression of droplets and shearing by fluid inertia. This generated a band of 512nm and iron-iron contact and energy transfer showed an absorption band at 480nm.

So far, the optical response from various degree of interactions makes this structure unique because of the volume of localized electrons within the structure. Therefore, more understanding and control on quantity of gold nanoparticles required for optimal performance of structure. Such could be useful in the interaction and enhancement of optical signals of analytes in contact with its surface.

The infra-red spectroscopy offered the opportunity in detecting sensitive vibrational fingerprints of the analyte under investigation. The Infra-red interacts with the dimensionality of the structure at microscale level because of its wavelength sizes. The chain thickness and gaps within the structure controls the degree of surface lattice resonance and near-field coupling, where C-H bond (2905 cm^{-1}) of surrounding PVA was enhanced by 35% from CT/CG=0.121 to CT/CG=2.878, at 20° incidence. The grazing angle detection at 45° enhanced the C-H band by $\sim 40\%$. The redshifts and peak intensities detected for O-H bands of PVA and LO vibrational bands of SiO_2 identifies with the structure dimensions, where thicker chains and smaller gaps increases the near field scattering and plasmon resonance coincides with and excites entities with same vibrational frequency.

Overall, the nanoscale dimensionality, concentration of gold and the variability of gold-iron oxide interaction at nanoscale sets its capacity to reach near UV region. The CT/CG varying micron-scale dimension offers easy tunability that a particular analyte can be efficiently diagnosed using the same manufactured patterned material.

5.8 Chapter Summary

To analyse the optical response of the thin film nanostructure, the UV-VIS spectrophotometry, Fourier transform infra-red spectroscopy were used. Furthermore, the magnetic field enhanced optical detection of the low concentration Rhodamine 6G on thin film nanostructure was investigated using Raman spectroscopy. The FTIR spectroscopy was performed in a Transmission mode setup and Specular reflectance mode to investigate the effect of grazing angle on the spectra. The absorption bands intensity for asymmetric and symmetric vibration of -CH_2 at 2927 cm^{-1} and 2847 cm^{-1} of PVA was found to be increasing with the distribution of pickering droplet density in the thin film prepared (PVA viscosities 43.2mPas, 15.2mPas, 3.2mPas and 1.9mPas, with spin speeds at 700rpm, 1000rpm, 1500rpm, 2000rpm, 2500rpm). The Full Width Half Measure (FWHM) of the IR-absorption peak (2927 cm^{-1}) of all the spectra obtained from various radial locations on each thin film samples were plotted against radial locations (r) values to show the distribution in relation to spatial locations on thin film. Such distribution was found to be correlated to pickering droplet density distribution obtained using the image analysis. The specular reflectance FTIR spectroscopy (SR-FTIR) was performed on thin film deposited on glass slides at a beam incidence angle of 20° , 45° and 80° . At 20° incident angle, the absorption bands 1730 cm^{-1} assigned to C=O group and 2910 cm^{-1} assigned to asymmetric vibrational mode C-H (methyl group) for PVA showed increased in intensity with the change in chain thickness and gap across the thin film. The increase in the absorbance was highest at glancing angle of 45° with 40% change in absorption, where CT increased by 106% from $1.01\mu\text{m}$, followed by 20° incidence with 32% increase, and the least 82° with 25% increase. The UV-Vis spectrophotometry results were helpful in explaining the interaction between iron oxide particles and gold nanoparticles as well as the correlation with values of CT/CG ratio. It was realised from the deconvolved bands of each broadband spectrum that there were contributions from different interacting systems along with their respective optical response that overlapped one another. This was broken down into contributing physical factors like; varying degree of particle concentrations (density), concentration ratios between iron oxide and gold nanoparticles, and orientation configurations. The overall contribution of gold through band 630 nm matches the

profile from SR-FTIR, while bands 444nm and 480nm qualitatively identifies the percentage of gold particles over the surface of the iron oxide clusters and those trapped within them respectively. Finally, the Raman spectroscopy was used in testing prepared (PVA viscosity of 15.2mPas, spin speed of 3000rpm) thin film pattern that was coated with 4.6×10^{-7} M of Rhodamine 6G. Introduction of ~ 43 mT of magnetic field within the scanned radial sections ($r=1$ mm, 2mm, 4mm, and 6mm) enhanced detection of selected peaks (~ 671 cm^{-1} , 1363 cm^{-1} , 1505 cm^{-1} and 1651 cm^{-1}). Where at 6mm with magnetic field, the least enhancement for 1651 cm^{-1} was 7% in comparison to unmagnetized at $r=1$ mm. A linear relationship for bands ~ 671 cm^{-1} increased by 160% as CT/CG increased by 281%. Band 1363 cm^{-1} increased by 9400% with the same increase in CT/CG. Band 1505 cm^{-1} linearly but inversely related with CT, where it reduces by 700% as the CT increases by 100%, Band 1651 cm^{-1} increased in intensity by 2540% as CT increases by 100%.

Chapter 6 Conclusion, Recommendation and Future Work

6.1 About Chapter

This chapter presents discussions on conclusive summary from each chapter of this thesis. It encompasses the manufacturing process and diagnostic test of the manufactured thin film nanostructure; from which the challenges, alternative solutions of some vital areas were identified for improvement. The manufacturing process has high potential of flexibility as few alternatives were demonstrated. The nanofabrication method was then ranked based on criteria in the form of cost, resolution, complexity and defectivity. The chapter was then finally concluded with recommendations and future work.

6.2 Conclusion

In this project, an alternative method for preparing an surface enhanced IR and magneto-optically sensitive nanostructure without using a complex, capital intensive and non-scalable nanofabrication technique. Firstly, the bottom-up process of the manufacturing of iron oxide (Fe_3O_4) and PEG capped gold methacrylate (PEG-C-GM) nanoparticles were prepared and confirmed through TEM, DLS, zeta potential and TGA measurements. Iron oxide nanoparticles were coated with oleic acid to prepare a ferrofluid in Cis-Cyclooctene, and was combined with PEG-C-GM nanoparticles to form gold pickering ferrofluid emulsion. The DLS, zeta potential and TEM confirmed the 240nm size of the emulsion droplet and adsorption of the gold colloids. The FTIR test revealed more than a 50% decrease in both C=H stretching ($\sim 3000\text{ cm}^{-1}$) and C-H (2845 cm^{-1}) bonds representing ferrofluid by the pickering PEG-C-GM nanoparticles, coupled with a 137% increase in OH bond ($\sim 3300\text{ cm}^{-1}$) from gold methacrylate. The contact angle measurement confirmed the, namely microscopic glass slide and silicon wafer at measurements of the PVA revealed 17° on glass slide and 49° on silicon wafer. The non-wetting nature of the PEG-C-GM-pi-FF emulsion droplets in water on both substrates was 175° .

The magnetic field and spin coating simultaneously applied to prepare the patterned thin film of gold pickering ferrofluid emulsion (PEG-C-GM-pi-FF). The PEG-C-GM-pi-FF droplets were dispersed in continuous phase of aqueous PVA to prepare the PEG-

C-GM-pi-FF-PVA. The PVA solution helped immobilising the PEG-C-GM-pi-FF droplets to form a pattern in the thin film after drying. The effect of three parameters such as viscosities of PVA solution continuous phase, spin speeds and spatial magnetic field distribution profile on the cluster density distribution and the droplet-droplet chain resolutions were studied. The image analysis of chain pattern formed in the thin film showed that with lower spin speeds and higher PVA viscosities, the degree of spread (in FWHM) of gold pickering droplet distribution will increase, due to the higher viscous resistance that creates more liquid film gaps between interacting dipole droplets. Meanwhile at higher spin speeds and lesser PVA viscosities, the FWHM decreases, due to lesser resistance to inertia and more displacement of pickering droplets and smaller gaps between interacting droplets. Regarding the pattern resolution, the image analysed and measured chain length (CL), chain thickness (CT) and chain gaps (CG) were related to the ratio between magnetic and fluid inertia energies (Q_{PI}); from which a map was successfully constructed. The map revealed that when $Q_{PI} > 100$, $CT/CG > 1$, revealing that with stronger magnetic field the density of magnetic flux are more and thus layering cluster of droplets. While with decreasing Q_{PI} , CT/CG declines gradually, until $Q_{PI} = < 1$ where CT/CG became constant, representing single droplets. CL/CT happened to be more responsive to the magnetic field configuration thus lacked consistency with Q_{PI} . The lowest deficiency of pattern achieved so far from this experiment was 15%.

UV-Vis spectra of the patterned thin film structure that was prepared from the concentric type of magnetic setup (Figure 4.19), spin speeds of 3000 rpm, viscosity of 15.2mPas revealed complimentary contribution of iron oxide interaction with gold nanoparticle to the overall spectra response. The presence of iron oxide initiated a redshift of gold nanoparticles plasmon resonance, while being optically active as a result of migrated electron density at the defect states of their interface, which yielded a two major absorption bands at 400nm and 680nm. The degree of agglomeration of nanoparticles and their interaction within the structure controlled other absorption bands within the mid visible spectrum such as; ~444nm (from Fe_3O_4 -Au surface interaction), ~480nm (Fe_3O_4 - Fe_3O_4 interaction), ~550nm (Au-Au interaction) and ~630nm (Au- Fe_3O_4 surface interaction), which overall average peak intensities decreased by 53% as CT/CG decreased by 74%. The entire absorption

bands convolved into a visible range broadband spectrum between 390nm to 700nm. This was successfully confirmed from a work by Thimsen and co.

The FTIR-specular reflectance of thin film patterned structure prepared using 15.2mPas viscosity under 2500rpm spin speed, was used to demonstrate the successful contribution of pattern resolution in the form of chain thickness and gap to the near field scattering, which results in broadband field enhancement and large hot spot volume for enhancing signal detection of analyte species. This phenomenon occurs for structures built with gold strips with varying dimensions. It was realised from the outcome that the CH₂ bonds for symmetric (2845 cm⁻¹) increased by 11% and asymmetric (2918 cm⁻¹) increased by 35% compared to intensities of empty PVA film, as the chain thickness increased from 1.01 μm by 179% at 20° grazing incidence. At 45° grazing incidence, CH₂ symmetric increased by 25% and asymmetric increased by 40%. Other detections were the excitation of SiO₂ phonons of the longitudinal optical vibrational bands of coated glass. The increase in LO intensities and redshift of the peaks towards other phonon bands (like the transverse optical – TO) revealed the impact of chain thickness on the near field scattering that locally excite the surface phonon polaritons. This revealed that with the increase in CT, there is subsequent red shift of LO mode. Which confirmed with similar outcome from Neubrech and co for increased gold nanowire length on SiO₂ film.

Going forward, multiplayer coating using the same preparation content and procedure was created. 3, 6 and 9 layers were formed on glass slides. Across the entire series of each spectrum at all incident angles (20°, 45° and 82°), revealed a decrement and disorderliness in CH₂ symmetric and asymmetric bands, OH bands and CO bands. The spectra revealed that at thicker film sections, the incident wave was heavily diffracted and scattered within the thin film by the high density of PEG-C-GM-pi-FF. The scattering affected the degree of absorption detectable by the equipment. It also confirmed that the chain array for each layer did not align and therefore the electromagnetic waves experienced destructive interference within the thin film structure both lattice-wise and local-wise.

Magneto-optical Raman test was carried out on the patterned thin film structure through the signal response of Rhodamine 6G (R6G). The (15.2mPas PVA, 3500 rpm)

thin film structure was placed between two magnets of opposite poles that generated an average magnetic field of 43mT within the scanned region of interest. Radial locations, 1mm, 2mm, 4mm, and 6mm from the centre of substrate were diagnosed. There was an overall enhancement for all Raman shift bands of R6G, except for band 773 cm^{-1} with no optical sensitivity. The scientific logic behind these enhancements had to do with the localized electric field/charge of the excited electrons from gold nanoparticles being accumulated at the interface between gold nanoparticle and iron oxide nanoparticles, that were then polarised by the magnetic field in the direction of the magnetic field. This gives the opportunity in tuning via the patterned structure at various regions the amplification of Raman signals.

So far with the manufacturing involving patterning and array designs, this technique process is fast in two parts; (i) the magnetic response and dipole—dipole alignment of ferromagnetic material is extremely fast (within fraction of a second) upon introduction of magnetic field, (ii) Spin coating process is quick in attaining thin film, where few seconds of spinning lead to carrier liquid height declining by almost 80%, while the remaining spinning process involves evaporation of solvent and shrinking of polymeric film. This level of speed can enable long range order organisation of pickering droplets. The range of organisation attained in this research was 40 mm in diameter with varying array resolutions, making the throughput rate as high as $0.1\text{ m}^2/\text{h}$. This setup can be scaled further into industrial spin coating set with more concentrically arranged magnets to build span into about hundreds of millimetres, and consequently increase the throughput rate to possibly as high as $50\text{ m}^2/\text{h}$, depending on the size of setup (assuming setup is up to 1m in diameter). Basically, magnetic field creates high resolution chain like arrays along an imaginary flux lines. Depending on size of pickering droplets or particles, the chain thickness and gap can range from hundreds of nanometres to tens of microns. In the designed structure, the range of chain gaps were between 600nm to $7.8\mu\text{m}$, while chain thickness was within the range of 250nm to $3\mu\text{m}$. Generally, most top-down process require lithographic templating of substrate prior to deposition of material of interest which takes a bit of time, like the electron beam lithography at $1.8 \times 10^{-6}\text{ m}^2/\text{h}$, Nanoimprint lithography at $0.1\text{ m}^2/\text{h}$, etc., See section 2.4 for summarised details.

An interesting addition involves flexibility of the system to offer multiple designs with multiple coatings such as; (i) the cross-coating pattern shown in Figure 6-1 (a), where one series of coating can be overlain over another by using a different magnetic configuration. (ii) A 5 μm iron-oxide-resin bulb that act as secondary mini-magnets by taking advantage of magnetic field strength too weak to organise assembly of smaller droplets in the form of establishing its secondary magnetic field for the assembly of droplets with an even higher resolution than that of the primary magnetic field (see Figure 6-1 b).

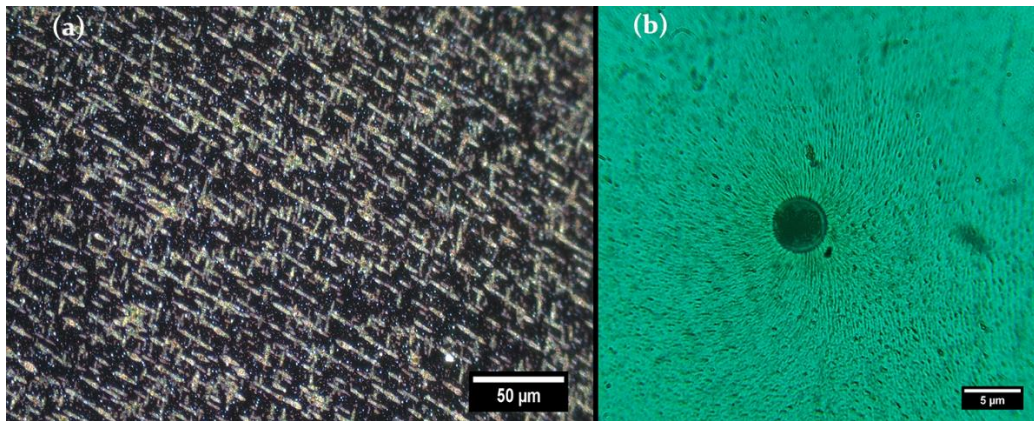


Figure 6-1 (a) sample of cross-coating pattern, (b) sample of iron oxide-resin pellets for generating secondary magnetic fields

This nanofabrication technique is advantageous in terms of cost. The subsidizing of gold with iron oxide reduces the required cost of base materials because iron oxide is an abundant material. Polyvinyl alcohol and permanent magnets are also very cheap. As for the appliances, probe-type ultrasonicator, centrifuge and spin coater are affordable appliances for the manufacturing, and finally the energy consumption required is minimal. The system does not require clean room nor excessive running cost for maintenance. Thus the cost of necessary equipment might be in the range of few thousands of pounds and entire processing would be in range of $\text{£}0.01/\text{m}^2$. Unlike ASML Extreme Ultraviolet (EUV) that can mark close to 5nm resolution cost about $\text{£}108$ million (Clark, 2021), electron beam lithography $\sim\text{£}2$ million and clean room maintenance of $\sim\text{£}10,000\text{s}$ per square meter depending on the application purpose (Bullimore, 2020).

Overall, this manufacturing technique was ranked in the bubble plot mentioned in Figure 2-1

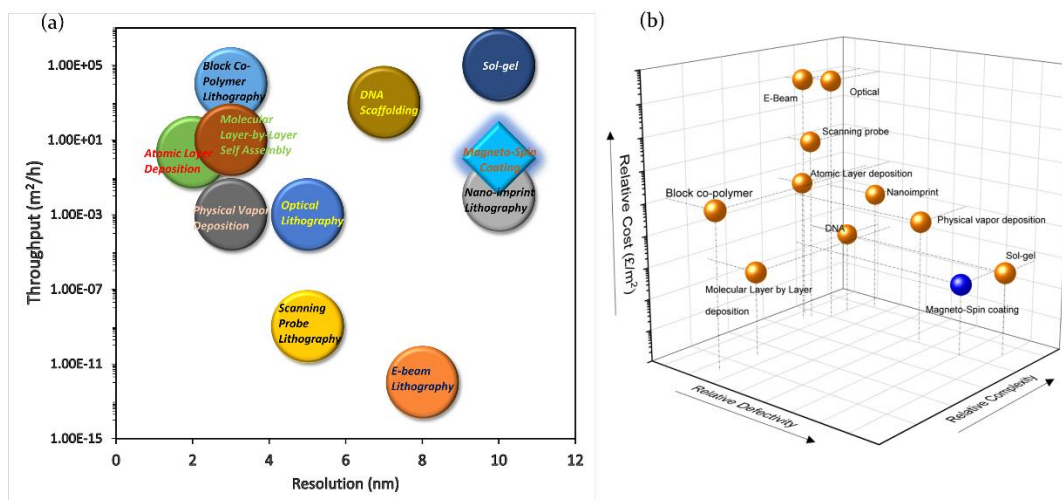


Figure 6-2 The ranking placement of magneto-spin coating nanofabrication technique based on criteria of resolution, throughput, defectivity, complexity and cost with reference from (Figure 2-1).

So far, from all optical studies, the iron-oxide – gold nanoparticle heterostructures revealed charge dynamics and plasmon enhancement of the iron oxide with increased local field intensity. The variability in chain thickness and gap contributed to the intensity tuneability of this material coupling, which was evident from the SEIRA measurements of molecular vibrations of PVA. These enhancements were further attained with grazing angle (maximum at 45°) where the incident infra-red wave interacted better with the thin film nanostructure, matching with the grating order (CT+CG) of the pattern. The application of magnetic field further enhanced the Raman vibrations of the attached molecule through electric field polarization, with different intensities across variable CT and CG sizes within the thin film. These sets of results have proved the potential of this design for nano-antenna based applications and as a microfluidics thin film for biomolecule detection.

6.3 Challenges and recommendations

The method of ultrasonication is chaotic, with energies needed for the breaking down of droplets randomly distributed within the vessel, which resulted into the production of uneven droplet sizes. The degree of polydispersity of droplets was drastically

reduced by using centrifugal sedimentation-segregation technique where bigger/heavier droplets were being driven to the bottom of the tube with smaller droplets floating within the carrier phase. Although, this inclusive process was not enough in reducing the polydispersity to almost unity as the size of $200\pm 30\text{nm}$ only accounted for 20% of the entire distribution (i.e., which ranged from 100nm – 400nm). In order to avoid these challenges, it was realised that iron oxide-gold nano-heterostructure one pot coupling synthesis could offer a better route in terms of size and reproducibility. A special example of such is the surface-functionalized gold-coated superparamagnetic iron oxide nanoparticles (Au-SPIONs) preparation technique, where the heterostructure is stabilized with citrate ions (Elbially, et al., 2014) (Stein, et al., 2020); which definitely seems a better recommendation for future manufacturing process.

Depending on the application required, the patterned structure in PVA thin film is sadly degradable when exposed to water-based environment. Therefore, a silica based polymeric material with inert characteristics to environmental conditions would be suitable as a coating layer for the structure. In the case of this project, the type of polymer used would be the one that wouldn't mix and is non-reactive to the chemical composition of the pickering droplets.

6.4 Future Work

- I. So far from the discussions presented, there are several aspects of this research that have potentials for improvement, but more series of test would be required to understand its characteristics. Such tests are; (a) Kerr effect experiment, (b) time-resolved UV-Vis absorption study, (c) ellipsometry, (d) Photoluminescence study, and (e) Near infra-red spectroscopy. These would assist in determining refractive index of the structure, its NIR response, its optical response under magnetic field, and rate of charge generation and distribution.
- II. The use of high-speed video capturing on particle dynamics under spin coating and magnetism effect; to better understand the controlling physics guiding the particle alignment to field lines while being spread by the carrier fluid.

III. As a follow up to II, the use of COMSOL Multiphysics, along with some user-defined equations of magnetism on droplets and spin coating mechanism would be helpful in studying the distribution of droplets under iterative time scale. This would establish a 4D computational process, improve the accuracy of the results, quality image representation of the physical process, and easy tweaking of the setup to suit variety of other designs and scenarios.

As seldom utilized in industrial scale, self-assembly remains a crux in research and development because of its dynamism. An investigation on one idea could “accidentally” branch out into more discoveries leading the way for multi-characteristic performance that can be utilized from a single product. This is the hopeful reason self-assembly form of nanofabrication would lead the way in technological advancement in the future.

References

- Acikgoz, C., Hempenius, M. A., Huskens, J. & Vancso, J. G., 2011. Polymers in conventional alternative lithography for fabrication of nanostructures. *European Polymer Journal*, 47(11), pp. 2033-2052.
- Adato, R. et al., 2009. Ultra-sensitive vibrational spectroscopy of protein monolayers with plasmonic nanoantenna arrays. *Proceedings of the National Academy of Sciences*, 106(46), pp. 19227-19232.
- AgarScientific, 2010. *Media - Light microscope accessories*. [Online]
Available at: https://www.agarscientific.com/media/import/06%E2%80%93Light_microscope_pgs_145-182_date_17_06_10_web.pdf
[Accessed 22 November 2021].
- Ahangaran, F., Hassanzadeh, A. & Nouri, S., 2013. Surface modification of Fe₃O₄@SiO₂ microsphere by silane coupling agent. *International Nano Letters*, 3(23).
- Akanny, E. et al., 2021. Surface enhanced Raman spectrscopy for bacteria: a review. *Applied Spectroscopy Reviews*, 56(5), pp. 380-442.
- Akella, M. & Juarez, J. J., 2018. High-throughput Acoustic Self-assembly of Colloidal Crytsals. *ACS Omega*, 3(2), pp. 1425-1436.
- Akella, M. & Juarez, J. J., 2018. High-Throughput Acoustofluidic Self-Assembly of Colloidal Crystals. *ACS Omega*, 3(2), pp. 1425-1436.
- Alaeian, H. & Dionne, J., 2012. Plasmon nanoparticle superlattices as optical-frequency magnetic metamaterials. *Optical Society of America*, 20(14), p. 166740.
- Aldrich, S., 2022. *Thiol terminated PEG*. [Online]
Available at: https://www.sigmaaldrich.com/GB/en/search/peg-thiol?focus=products&page=1&perpage=30&sort=relevance&term=peg%20thiol&type=product_name
[Accessed 20 March 2022].
- Alexandrov, A. & Mott, N., 1996. *Polarons and bipolarons*. s.l.:Worl Scientific.
- Amendola, V. et al., 2017. Surface plasmon resonance in gold nanoparticles: a review. *Journal of Physics: Condensed Matter*, 29(20), p. 203002.
- Amendola, V. et al., 2017. Surface plasmon resonance in gold nanoparticles: a review.. *Journal of Physics: Condensed Matter*, 29(20), p. 203002.
- Amma, S.-i., Luo, J., Pantano, C. G. & Kim, S. H., 2015. Specular reflectance (SR) and attnuated total reflectance (ATR) infrared (IR) spectroscopy of transparent flat glass surfaces: A case study of Soda Lime float glass. *Journal of Non-Crystalline Solids*, Volume 428, pp. 189-196.
- Andala, D., Shin, S., Lee, H. & Bishop, K., 2012. Templated synthesis of amphiphilic nanoparticles at the liquid–liquid interface.. *ACS nano*, 6(2), pp. 1044-1050.
- Anderman, M. & Kennedy, J., 1988. Semiconductor electrodes: IRON OXIDE (Fe₂O₃).. *Studies in Physical and Theoretical Chemistry*, Volume 55.

- Arcos, C. et al., 2008. Orientationally correlated colloidal polycrystals without long range positional order. *Phys. Rev. E*, 77(5), p. 050402.
- Argyres, P., 1955. Theory of the Faraday and Kerr effects in ferromagnetics. *Physical Review*, 97(2), p. 334.
- Aslam, R. & Gonzalez-Vinas, W., 2017. Spin coating of moderately concentrated superparamagnetic colloids in different magnetic field configuration. *Physicochemical and Engineering Aspects*, Volume 532, pp. 530-534.
- Aslam, R. & Gonzalez-Vinas, W., 2019. Pattern formation in spin-coating of hybrid colloids in different magnetic field configurations. *Journal of Physics D: Applied Physics*, Volume 52, p. 344001.
- Aslam, R., Shahrivar, K., de Vicente, J. & Gonzalez-Vinas, W., 2016. Magnetorheology of hybrid colloids obtained by spin coating and classical rheometry. *Smart Materials and Structures*, 25(7), p. 075036.
- Aubret, A., Youssef, M., Sacanna, S. & Palacci, J., 2018. Targeted assembly and synchronization of self-spinning microgears. *Nature Physics*, 14(11), pp. 1114-1118.
- Aubry, N., Singh, P., Janjua, M. & Nudurupati, S., 2008. Micro- and nanoparticles self-assembly for virtually defect-free, adjustable monolayers. *PNAS*, 105(10), pp. 3711-3714.
- Aveyard, R. & Binks, B. P. C. J. H., 2003. Emulsions stabilised solely by colloidal particles. *Adv. Colloid Interface Sci.*, Volume 100, pp. 503-546.
- Bailey, R. C., Stevenson, K. J. & Hupp, J. T., 2000. Assembly of Micropatterned Colloidal Gold Thin Films via MicroTransfer Molding and Electrophoretic Deposition. *Communication*, 12(24), pp. 1930-1934.
- Bajaj, M., Wangoo, N., Jain, D. V. S. & Sharma, R. K., 2020. Quantification of adsorbed and dangling citrate ions on gold nanoparticle surface using thermogravimetric analysis. *Scientific Report, Nature Publishing group.*, 10(1), pp. 1-7.
- Banik, M. & Mukherjee, R., 2018. Fabrication of Ordered 2D Colloidal Crystals on Flat Patterned Substrates by Spin Coating. *ACS Omega*, 3(10), pp. 13422-13432.
- Bapna, M. et al., 2013. Light induced diffusion driven self assembly of Ag nanoparticles in a-Se/Ag bilayer thin film with ultrafast optical response. *Applied Physics Letters*, 102(21), p. 213110.
- Barho, F. B. et al., 2016. All-semiconductor plasmonic gratings for biosensing applications in the mid-infrared spectral range. *Optics Express*, 24(14), pp. 16175-16190.
- Barhoum, A. & Garcia-Betancourt, 2018. Physicochemical characterization of nanomaterials: size, morphology, optical, magnetic, and electrical properties. In: A. Barhoum & H. A. S. Makhoul, eds. *Emerging Applications of Nanoparticles and Architecture Nanostructures: Current aspects and future trends Micro and Nano Technologies*. s.l.:Elsevier, pp. 279-304.
- Barnes, W. D. A. & E. T., 2003. Surface plasmon subwavelength optics. *nature*, 424(6950), pp. 824-830.
- Barrow, S. J. et al., 2011. Surface Plasmon Resonances in strongly coupled gold nanosphere chains from monomer to hexamer. *Nano Lett.*, 11(10), pp. 4180-4187.

- Bartlett, A. P. et al., 2012. Modified spin-coating technique to achieve directional colloidal crystallization. *Langmuir*, 28(6), pp. 307-3070.
- Bazin, D. & Faure, C., 2012. Electro-colloidal lithography: a versatile approach combining colloidal particles and electrical fields for the fabrication of patterned polymer and metal films. *Soft Matter*, 8(11), pp. 3053-3057.
- Beger, M., 2016. The Future is Flat—Two-Dimensional Nanomaterials. In: *Nanotechnology: the future is Tiny*. s.l.:Royal Society of Chemistry, pp. 85-114.
- Berger, T. et al., 2005. Light-induced charge separation in anatase TiO₂ particles. *The Journal of Physical Chemistry B*, 109(13), pp. 6061-6068.
- Beydoun, D., Amal, R., Low, G. & McEvoy, S., 1999. Role of nanoparticles in photocatalysis. *Journal of nanoparticle Research*, 1(4), pp. 439-458.
- Bharti, B., Fameau, A.-L., Rubinstein, M. & Velev, O. D., 2015. Nanocapillarity-mediated magnetic assembly of nanoparticles into ultraflexible filaments and reconfigurable networks. *Nature Materials*, Volume 14, pp. 1104-1109.
- Bhattarai, J. et al., 2020. Adhesion layer-free attachment of gold on silicon wafer and its application in localized surface plasmon resonance-based biosensing.. *Sensors and Actuators A: Physical*, Volume 312, pp. 112-155.
- Binker, C. J., Lu, Y., Sellinger, A. & Fan, H., 1999. Evaporation-Induced Self-Assembly: Nanostructures Made Easy. *Advanced Materials*, 11(7), pp. 579-585.
- Binker, J. C., 2013. Dip Coating. In: T. Schneller, R. Waser, M. Kosec & D. Payne, eds. *Chemical Solution Deposition of Functional Oxide Thin Films*. Vienna: Springer, pp. 233-261.
- Binks, B. & Lumsdon, S., 1999. Stability of oil-in-water emulsions stabilised by silica particles. *Physical Chemistry Chemical Physics*, 1(12), pp. 3007-3016.
- Binks, B., Murakami, R., Armes, S. & Fujii, S., 2006. Effects of pH and salt concentration on oil-in-water emulsions stabilized solely by nanocomposite microgel particles.. *Langmuir*, 22(5), pp. 2050-2057.
- Binks, B. P., 2002. Particles as surfactants - Similarities and differences. *Current opinion in colloid & interface science*, 7(1-2), pp. 21-41.
- Binks, B. P. & Clint, J. H., 2002. Solid Wettability from Surface Energy Components: Relevance to Pickering Emulsions. *Langmuir*, Volume 18, pp. 1270-1273.
- Binks, B. P. & Hozorov, T. S., 2006. *Colloidal Particles at Liquid Interfaces*. Cambridge: Cambridge University Press.
- Biswas, A. et al., 2012. Advances in top-down and bottom-up surface nanofabrication: Techniques, applications and future prospects. *Advances in Colloid and Interface science*, Volume 170, pp. 2-27.
- Blanco-Andujar, C., 2014. *Sodium Carbonate Mediated Synthesis of Iron Oxide NPs to Improve Magnetic Hyperthermia Efficiency and Induce Apoptosis*, London: PhD Thesis, University College London..

- Blatchford, G. C., Campbell, J. R. & Creighton, J. A., 1982. Plasma resonance-enhanced Raman scattering of absorbates on solid colloids: the effects of aggregation.. *J. A. Surf. Sci*, Volume 120, pp. 435-455.
- Blout, E. & Karplus, R., 1948. The infrared spectrum of polyvinyl alcohol. *Journal of the American Chemical Society*, 70(2), pp. 862-864.
- Boakye-Ansah, S., Khan, M. & Haase, M., 2020. Controlling surfactant adsorption on highly charged nanoparticles to stabilize bijels. *The Journal of Physical Chemistry C*, 124(23), pp. 12417-12423.
- Booth, S. & Dryfe, R., 2015. Assembly of nanoscale objects at the liquid/liquid interface.. *The Journal of Physical Chemistry C*, 119(41), pp. 23295-23309.
- Bora, D. et al., 2012. Functionalization of Nanostructured Hematite Thin-Film Electrodes with the Light-Harvesting Membrane Protein C-Phycocyanin Yields an Enhanced Photocurrent. *Advanced Functional Materials*, 22(3), pp. 490-502.
- Bornside, D., Macosko, C. & Scriven, L., 1987. Modelling of Spin Coating. *Journal of Imaging technology*, 4(13), pp. 122-130.
- Bossard-Giannesini, L., Cruguel, H., Lacaze, E. & Pluchery, O., 2016. Plasmonic properties of gold nanoparticles on silicon substrates: Understanding Fano-like spectra observed in reflection.. *Applied Physics Letters*, 109(11), p. 111901.
- Bowler, N., 2019. Ferromagnetic Materials. In: *Eddy-Current Nondestructive Evaluation*. s.l.:Springer Series, pp. 31-46.
- Bozorth, R. M., 1951. *Ferromagnetism*. New York: IEEE Press.
- Brisson, V. & Tilton, R. D., 2002. Self Assembly and two dimensional patterning of cell arrays by electrophoretic deposition. *Biotechnology and Bioengineering*, 77(3), pp. 290-295.
- Brongersma, M. L., Hartman, J. W. & Atwater, H. H., 2011. Plasmonics: Electromagnetic Energy Transfer and Switching in Nanoparticle Chain-Arrays Below the Diffraction Limit. *MRS online Proceedings Library*, Volume 582.
- Brown, R., Wang, J. & Milton, M., 2007. Electromagnetic modelling of Raman enhancement from nanoscale structures as a means to predict the efficacy of SERS substrates. *Journal of Nanomaterials*, p. 10pp.
- Brugnara, M., 2006. *Contact_Angle Image J NIH.GOV*. [Online] Available at: <https://imagej.nih.gov/ij/plugins/contact-angle.html> [Accessed 27 October 2020].
- Bryche, J. G. R. et al., 2016. Plasmonic enhancement by a continuous gold underlayer: Application to SERS sensing.. *Plasmonics*, 11(2), pp. 601-608.
- Bullimore, S., 2020. *Cleanroom Technology*. [Online] Available at: https://cleanroomtechnology.com/news/article_page/2019_Cleanroom_Construction_Round-up/161269 [Accessed 28 July 2021].

- Bunn, C., 1948. Crystal structure of polyvinyl alcohol. *Nature*, 161(4102), pp. 929-930.
- Byron, P. & Dalby, R., 1987. Effects of heat treatment on the permeability of polyvinyl alcohol films to a hydrophilic solute.. *Journal of pharmaceutical sciences*, 76(1), pp. 65-67.
- Cai, H. et al., 2012. Facile assembly of Fe₃O₄@ Au nanocomposite particles for dual mode magnetic resonance and computed tomography imaging applications. *Journal of Materials Chemistry*, 22(30), pp. 15110-15120.
- Cai, J., Xiao, J., Chen, X. & Liu, H., 2020. Essential oil loaded edible films prepared by continuous casting method: Effects of Casting cycle and loading position on the release properties. *Food packaging and Shelf-life*, Volume 26, p. 100555.
- Campion, A. & Kambhampati, P., 1998. Surface-enhanced Raman scattering. *Chemical society reviews*, 27(4), pp. 241-250.
- Carter, B. C. & Norton, G. M., 2007. Sols, Gels, and Organic Chemistry. In: *Ceramic Materials: Science and Engineering*. New York: Springer, pp. 400-411.
- Celik, N. et al., 2020. Fabrication of robust superhydrophobic surfaces by one-step spray coating: Evaporation driven self-assembly of wax and nanoparticles into hierarchical structures. *Chem. Eng. J.*, Volume 396, p. 125230.
- Celio, H., Barton, E. & Stevenson, K. J., 2006. Patterned Assembly of Colloidal Particles by Confined Dewetting Lithography. *Langmuir*, 22(26), pp. 11426-11435.
- Chalmers, J., 2002. *Handbook of vibrational spectroscopy*. 2nd ed. s.l.:Wiley & Sons.
- Chang, K.-H., 2015. Chapter 10 - Reliability Analysis. In: K. Chang, ed. *e-Design: Computer Aided Engineering Design*. ISBN 9780123820389: Academic Press, pp. 523-595.
- Chantrell, R., Popplewell, J. & Charles, S., 1978. Measurements of particle size distribution parameters in ferrofluids. *IEEE Transactions on Magnetics*, 14(5), pp. 975-977.
- Cheng, Y. et al., 2016. Luminescence quantum yields of gold nanoparticles varying with excitation wavelengths. *Nanoscale*, 8(4), pp. 2188-2194.
- Chen, J. et al., 2013. Controllable fabrication of 2D colloidal-crystal films with polystyrene nanospheres of various diameters by spin-coating. *Applied Surface Science*, Volume 270, pp. 6-15.
- Chen, J. et al., 2018. Dielectric waveguide-enhanced localized surface plasmon refractive index sensing. *Optical Materials express*, 8(2), p. 31336.
- Chen, L. B. et al., 1992. Structural changes and orientational order in a sheared colloidal suspension. *Phys. Rev. Lett.*, Volume 69, pp. 688-691.
- Chen, L. et al., 1997. Method to measure spectra of both the magneto-optical Kerr and the Faraday effect. *Optical Engineering*, 36(11), pp. 3188-3192.
- Chen, S. Y. H. & Kimura, K., 2001. Reversible transference of Au nanoparticles across the water and toluene interface: A Langmuir type adsorption mechanism.. *Langmuir*, 17(3), pp. 733-739.

- Chen, T. et al., 2013. Tailoring Plasmon coupling in self-assembled one-dimensional Au Nanoparticle chains through simultaneous control of size and gap separation.. *J. Phys. Chem. Lett.*, 4(13), pp. 2147-2152.
- Chen, X. et al., 2007. Langmuir–Blodgett Patterning: A Bottom–Up Way To Build Mesostructures over Large Areas. *Acc. Chem. Res.*, 40(6), pp. 393-401.
- Chen, Y., Ai, B. & Wong, Z., 2020. Soft optical metamaterials. *Nano Convergence*, 7(1), pp. 1-17.
- Chen, Y. et al., 2011. Free-standing polymer–nanoparticle superlattice sheets self-assembled at the air–liquid interface.. *Crystal growth & design*, 11(11), pp. 4742-4746.
- Chen, Y. & Ming, H., 2012. Review of surface plasmon resonance and localized surface plasmon resonance sensor. *Photonic Sensors*, 2(1), pp. 37-49.
- Chen, Z. et al., 2008. Protein microarrays with carbon nanotubes as multicolor Raman labels. *Nature biotechnology*, 26(11), pp. 1285-1292.
- Choi, M. et al., 2011. A terahertz metamaterial with unnaturally high refractive index.. *Nature*, 470(7334), pp. 369-373.
- Chuntonov, L. & Haran, G., 2013. Optical activity in single-molecule surface-enhanced Raman scattering: Role of symmetry. *MRS bulletin*, 38(8), pp. 642-647.
- Čižmár, T., Romero, L., Dholakia, K. & Andrews, D., 2010. Multiple optical trapping and binding: new routes to self-assembly.. *Journal of Physics B: Atomic, Molecular and Optical Physics*, 43(10), p. 102001.
- Claire, A. et al., 2019. Pickering emulsions: Preparation processes, key parameters governing their properties and potential for pharmaceutical applications. *Journal of Controlled Release, Elsevier*, Volume 309, pp. 302-332.
- Clark, D., 2021. *The New York Times*. [Online]
Available at: <https://www.nytimes.com/2021/07/04/technology/tech-cold-war-chips.html>
[Accessed 20 July 2021].
- Comin, A. et al., 2012. Plasmon bleaching dynamics in colloidal gold–iron oxide nanocrystal heterodimers. *Nano letters*, 12(2), pp. 921-926.
- Costanzo, P. & Beyer, F., 2007. Thermally driven assembly of nanoparticles in polymer matrices. *Macromolecules*, 40(11), pp. 3996-4001.
- Crassous, J. J. & Demirors, A. F., 2017. Multiscale directed self-assembly of composite microgels in complex electric fields. *Soft Matter*, 13(1), pp. 88-100.
- Crassous, J. et al., 2014. Field-induced assembly of colloidal ellipsoids into well-defined microtubules. *Nature communications*, 5(1), pp. 1-7.
- Crow, E. & Shimizu, K., 1987. *Lognormal distributions*. New York: Marcel Dekker.
- Cui, L. et al., 2009. Fabrication of large-area patterned photonic crystals by ink-jet printing. *Journals of Materials Chemistry*, 19(31), pp. 5499-5502.

- Dahal, N. & Chikan, V., 2008. Synthesis of Water-Soluble Iron-Gold Alloy Nanoparticles. *Chem. Mater.*, 20(20), pp. 6389-6395.
- Danielle C., B. & Alfred, R., 1985. Characterisation of ploy(vinyl alcohol). *Applied Polymer Science*, 30(10), pp. 4137-4147.
- Daniel, M. & Astruc, D., 2004. Gold nanoparticles: assembly, supramolecular chemistry, quantum-size-related properties, and applications toward biology, catalysis, and nanotechnology. *Chemical reviews*, 104(1), pp. 293-346.
- Danks, A. E., Hall, S. R. & Schnepf, Z., 2016. The Evolution of 'Sol-gel' chemistry as a technique for material synthesis. *Materials Horizons*, 3(2), pp. 91-112.
- Das, A., Das, S. & Raychaudhuri, A., 2008. Growth of two-dimensional arrays of uncapped gold nanoparticles on silicon substrates. *Bulletin of Materials Science*, 31(3), pp. 277-282.
- Daughton, W. & Givens, F., 1982. An Investigation of the Thickness Variation of Spun-on Thin Films Commonly Associated with the Semiconductor Industry. *Journal of The Electrochemical Society*, 129(1), p. 173.
- de Gennes, P. & Pincus, P., 1970. Pair correlations in ferromagnetic colloid. *Kondensierten Materie*, Volume 11, pp. 189-198.
- Delekta, S. S., Laurila, M.-M., Mantysalo, M. & Li, J., 2020. Drying-Mediated Self-Assembly of Graphene for Inkjet Printing of High-Rate Micro-supercapacitors. *Nano-Micro Letters*, 12(40).
- Demirors, A. F., Pillai, P., Kowalczyk, M. & Gryzbowski, B. A., 2013. Colloidal assembly directed by virtual magnetic moulds. *Nature*, Volume 503, pp. 99-103.
- Demirors, F. A. & Alison, L., 2018. Electric field assembly of colloidal superstructures. *J Phys Chem Lett*, Volume 9, pp. 4437-4443.
- Deng, M., Tu, N., Bai, F. & Wang, L., 2012. Surface Functionalization of Hydrophobic Nanocrystals with One Particle per Micelle for Bioapplications. *Chem. Mater.*, 24(13), pp. 2592-2597.
- Deng, S. et al., 2020. Ultranarrow plasmon resonances from annealed nanoparticle lattices. *Proc. Natl. Acad. Sci. USA*, 117(38), pp. 23380-23384.
- Deng, Z.-Y., Chen, K.-L. & Wu, C.-H., 2019. Improving the SERS signals of biomolecules using a stacked biochip containing Fe₂O₃/Au nanoparticles and a DC magnetic field. *Scientific Reports*, Volume 9, p. 9566.
- Dickerson, J. H. & Boccaccini, A. R., 2012. *Electrophoretic Deposition of Nanomaterials*. 1st ed. New York: Springer.
- Dolez, P. I., 2015. Nanomaterials Definitions, Classifications, and Applications. In: *Nanoengineering: Global Approaches to Health and Safety Issues*. s.l.:Elsevier, pp. 33-40.
- Domínguez-García, P., Pancorbo, M., Ortega, F. & Rubio, M., 2018. JColloids: Image analysis for video-microscopy studies of colloidal suspensions. *Computer Physics Communications*, Volume 231, pp. 243-244.

- Dommersnes, P. & Fossum, J. O., 2016. Surface structuring of particle laden drops using electric fields. *Eur Phys J Spec Top*, Volume 225, pp. 715-728.
- Dotan, H. et al., 2013. Resonant light trapping in ultrathin films for water splitting. *Nature materials*, 12(2), pp. 158-164.
- Dowling, A. et al., 2004. *Nanoscience and nanotechnologies: opportunities and uncertainties*. London, UK.: The Royal Society & The Royal Academy of Engineering.
- Dreyfus, R., Lacoste, D., Bibette, J. & Baudry, J., 2009. Measuring colloidal forces with the magnetic chaining technique. *Eur. Phys J. E*, Volume 28, pp. 113-123.
- Duan, T. et al., 2020. A novel fabrication technique for high-aspect-ratio nanopillar arrays for SERS application. *RSC Advances*, 10(73), pp. 45037-45041.
- Dubi, Y. & Sivan, Y., 2019. "Hot" electrons in metallic nanostructures—non-thermal carriers or heating?. *Light: Science & Applications*, 8(1), pp. 1-8.
- Durand-Gasselino, C., Capelot, M., Sanson, N. & Lequeux, N., 2010. Irreversible and Reversible Aggregation of Poly (ethylene oxide-st-propylene oxide) Grafted Gold Nanoparticles. *Langmuir*, 26(14), pp. 1231-12329.
- Efimov, A., 1999. Vibrational spectra, related properties, and structure of inorganic glasses. *Journal of Non-Crystalline Solids*, 253(1-3), pp. 95-118.
- Elbially, N., Fathy, M. & Khalil, W., 2014. Preparation and characterization of magnetic gold nanoparticles to be used as doxorubicin nanocarriers. *Physica Medica*, 30(7), pp. 843-848.
- Emslie, A., Bonner, F. & Peck, L., 1958. Flow of a viscous liquid on a rotating disk. *J. Appl. Phys.*, Volume 29, p. 858-862.
- Engelbrekt, C., Gargasya, Y. & Law, M., 2021. Silica shell growth on Vitreophobic Gold Nanoparticles Probed by Plasmon Resonance Dynamics. *J. Phys. Chem.*, 125(45), pp. 25119-25125.
- Erb, R. M. et al., 2009. Magnetic assembly of colloidal superstructures with multipole symmetry. *Nature*, Volume 457, pp. 999-2009.
- Escudero, A. et al., 2017. Rare earth based nanostructured materials: synthesis functionalization, properties and bioimaging and biosensing applications. *Nanophotonics*, 6(5), pp. 881-921.
- Estelrich, J., Escribano, E., Queralt, J. & Busquets, M. A., 2015. Iron Oxide Nanoparticles for Magnetically-Guided and Magnetically-Responsive Drug Delivery. *Int. J. Mol. Sci*, Volume 16, pp. 8070-8101.
- Fallah, M., Maleki, I., Zamani-Meymian, M. & Abdi, Y., 2019. Enhancing the efficiency of dye-sensitized solar cell by increasing the light trapping and decreasing the electron-hole recombination rate due to Ag@ TiO₂ core-shell photoanode structure.. *Materials Research Express*, 7(1), p. 016409.
- Fannin, P., Scaife, B. & Charles, S., 1993. Relaxation and resonance in ferrofluids. *Journal of magnetism and magnetic materials*, 122(1-3), pp. 159-163.
- Fan, P. & Luo, X., 2018. *Scanning Probe Lithography (SPL) Nanofabrication Approach*. Newcastle upon Tyne, UK, Proceedings of the 24th International Conference on Automation & Computing. IEEE.

- Fazio, E. et al., 2019. Light-matter interaction under intense field conditions: Nonlinear optical properties of metallic-dielectric nanostructures. *Current Nanomaterials*, 4(1), pp. 51-62.
- Ferrari, J. C., Castiños, F., Araujo, P. H. & Sayer, C., 2016. Modelling Particle Size Distribution in Heterogeneous Polymerization Systems Using Multimodal Lognormal Function. *Braz. J. Chem. Eng.*, 33(3).
- Fiebig, M. et al., 2008. Ultrafast magnetization dynamics of antiferromagnetic compounds. *Journal of Physics D: applied physics*, Volume 41, p. 164005.
- Finlayson, D., Rinaldi, C. & Baker, M., 2019. Is Infrared Spectroscopy Ready for the Clinic?. *Anal. Chem.*, 91(19), pp. 12117-12128.
- Fisslthaler, E. et al., 2008. Printing functional nanostructures: a novel route towards nanostructuring of organic electronic devices via soft embossing, inkjet printing and colloidal self assembly of semiconducting polymer nanospheres. *Soft Matter*, 4(12), pp. 2448-2453.
- Flatté, M., Kornyshev, A. & Urbakh, M., 2008. Understanding voltage-induced localization of nanoparticles at a liquid-liquid interface.. *Journal of Physics: Condensed Matter*, 20(7), p. 073102.
- Fogel, R. & Rutherford, M. J., 1990. The solubility of carbon dioxide in rhyolitic melts; quantitative FTIR study. *American Mineralogist*, 75(11-12), pp. 1311-1326.
- Fraden, S., Hurd, A. J. & Meyer, R. B., 1989. Electric field induced Association of colloidal particles. *Phys. Rev. Lett.*, Volume 63, p. 273.
- Franklin, T., 2003. *Ferrofluid flow phenomena (Doctoral dissertation)*, Massachusetts: Massachusetts Institute of Technology.
- Frens, G., 1973. Controlled Nucleation for the Regulation of the Particle Size in Monodisperse Gold Suspensions. *Nature*, Volume 241, pp. 20-22.
- Fritzsche, H., 1971. Optical and electrical energy gaps in amorphous semiconductors. *Journal of Non-Crystalline Solids*, 6(1), pp. 49-71.
- Fu, Y., Li, J. & Li, J., 2019. Metal/semiconductor nanocomposites for photocatalysis: fundamentals, structures, applications and properties. *Nanomaterials*, 9(3), p. 359.
- Gaillard, F. et al., 1999. Grazing-angle micro-FTIR spectroscopy (GAM-FTIR): applications to adhesion studies. *Surface and Interface Analysis: An International Journal devoted to the development and application of techniques for the analysis of surfaces, interfaces and thin films*, 27(9), pp. 865-870.
- Ganguly, R. & Puri, I. K., 2010. Microfluidic transport in magnetic mems and biomems. *Wiley Interdiscip. Rev. Nanomed Nanobiotechnol*, 2(4), pp. 382-399.
- Garcia, R., Knoll, A. W. & Riedo, E., 2014. Advanced scanning probe lithography. *Nature Nanotechnology*, 9(8), pp. 577-587.
- Garcia, R., Knoll, A. W. & Riedo, E., 2014. Advanced Scanning Probe Lithography. *Nature Nanotechnology*, Volume 9, pp. 577-587.

- Ge, J., He, L., Hu, Y. & Yin, Y., 2011. Magnetically induced colloidal assembly into field-responsive photonic structures. *Nanoscale*, Issue 1.
- George, C. et al., 2011. Optical and electrical properties of colloidal (spherical Au)-(spinel ferrite nanorod) heterostructures. *Nanoscale*, 3(11), pp. 4647-4654.
- Geotti-Bianchini, F. et al., 1991. New Interpretation of the IR Reflectance spectra of SiO₂ rich films on soda lime glass. *Galstech Ber.*, Volume 64, pp. 205-217.
- Geotti-Bianchini, F., Preo, M., Gugliemi, M. & Pantano, C. G., 2003. Infrared reflectance spectra of semi-transparent SiO₂ rich films on silicate glasses: influence of the substrate and film thickness. *J. Non-Cryst. Solids*, Volume 321, pp. 110-119.
- Ghosh, H. & Burgi, T., 2017. Mapping Infrared Enhancement around Gold Nanoparticles Using Polyelectrolytes. *The Journal of Physical Chemistry*, Volume 121, pp. 2355-2363.
- Ghosh, S. K. & Boker, A., 2019. Self-Assembly for nanoparticles in 2D and 3D: Recent Advances and Future trends. *Macro-molecular Chemistry and Physics*, 220(17), pp. 1900196-1900225.
- Ghosh, S. K. & Pal, T., 2007. Interparticle Coupling Effect on the Surface Plasmon Resonance of Gold Nanoparticles: From Theory to Applications. *Chem. Rev.*, 107(11), pp. 4797-4862.
- Gilbert, B., Frandsen, C., Maxey, E. & Sherman, D., 2009. Band-gap measurements of bulk and nanoscale hematite by soft x-ray spectroscopy. *Physical Review B*, 79(3), p. 035108.
- Gilbert, B. et al., 2013. Ultrafast electron and energy transfer in dye-sensitized iron oxide and oxyhydroxide nanoparticles. *Physical Chemistry Chemical Physics*, 15(40), pp. 17303-17313.
- Gillibert, R., Sarkar, M., Bryche, J.-F. & Yasukuni, R., 2016. Directional surface enhanced Raman scattering on gold nano-gratings. *Nanotechnology*, 27(11), p. 211502.
- Giuliani, M., Gonzalez-Vinas, W., Poduska, K. M. & Yethira, A., 2010. Dynamics of crystals structure formation in spin coated colloidal films. *J. Phys. Chem. Lett.*, 1(9), pp. 1481-1486.
- Globus, A. & Duplex, P., 1969. Initial Susceptibility of Ferrimagnetic Materials and Topography of Domain. *Physica status Solidi (B)*, 31(2), pp. 765-774.
- Gonzalez, A. E., 2016. Colloidal Aggregation Coupled with Sedimentation: A Comprehensive Overview. In: M. M. Rahman & A. M. Asiri, eds. *Advances in Colloid Science*. s.l.:IntechOpen.
- Gramotnev, D. K., Goodman, S. J. & Pile, D. F. P., 2002. Grazing angle scattering of electromagnetic waves in gratings with varying mean parameters. *Journal of Modern Optics*, 51(1), pp. 13-29.
- Grandidier, J., Callahan, D., Munday, J. & Atwater, H., 2011. Light absorption enhancement in thin-film solar cells using whispering gallery modes in dielectric nanospheres. *Advanced materials*, 23(10), pp. 1272-1276.
- Green, W. L. A., 2014. *Synthesis and Characterization of FePt Magnetic NPs*, London: PhD Thesis, University College London..

- Griffiths, P. & De Haseth, J., 2007. *Fourier transform infrared spectrometry*. 2nd ed. s.l.:John Wiley & Sons.
- Grillo, V. et al., 2017. Observation of nanoscale magnetic fields using twisted electron beams. *Nature communications*, 8(1), pp. 1-6.
- Grosso, D. et al., 2004. Fundamentals of Mesostructuring through evaporation-induced self-assembly. *Advanced Functional Materials*, 14(4), pp. 309-322.
- Grzelczak, M., Liz-Marzan, L. M. & Klajn, R., 2019. Stimuli-responsive self-assembly of nanoparticles. *Chem. Soc. Rev.*, Volume 48, pp. 1342-1361.
- Grzelczak, M., Vermant, J., Furst, E. M. & Liz-Marzan, L. M., 2010. Directed Self-Assembly of Nanoparticles: Review. *ACS Nano*, 4(7), pp. 3591-3605.
- Guédon, C. et al., 2012. Observation of quantum interference in molecular charge transport. *Nature nanotechnology*, 7(5), pp. 305-309.
- Guo, X. et al., 2017. Quick design of high efficiency light trapping nanostructures for thin film silicon solar cells. *Optics Communications*, Volume 395, pp. 122-126.
- Gupta, A., Pardasani, R. T. & Pardasani, P., 2017. *Magnetic properties of Paramagnetic Compounds*. 1 ed. Berlin: Springer.
- Gurudayal, Bassi, P., Sritharan, T. & Wong, L., 2018. Recent progress in iron oxide based photoanodes for solar water splitting. *Journal of Physics D: Applied Physics*, 51(47), p. 473002.
- Guttula, S. M., 2007. *Self-assembly of Colloidal Lattices at Pickering emulsion interface*, Texas: Thesis in Applied Physics, Texas Tech University.
- Haiss, W., Thanh, N. T. K., Aveyard, J. & Fernig, D. G., 2007. Determination of Size and Concentration of Gold Nanoparticles from UV-Vis Spectra. *Anal. Chem.*, Volume 79, pp. 4215-4221.
- Hall, D., Underhill, P. & Torkelson, J., 1998. Spin coating of thin and ultrathin polymer films. *Polymer Engineering & Science*, 38(12), pp. 2039-2045.
- Han, S. G. et al., 2019. Spin-Coating Process for 10 cm × 10 cm Perovskite Solar Modules Enabled by Self-Assembly of SnO₂ Nanocolloids. *ACS Energy Lett.*, 4(9), pp. 1845-1851.
- Han, W. & Lin, Z., 2012. Learning from "Coffee Rings": Ordered Structures Enabled by Controlled Evaporative Self-Assembly. *Angewandte Chemie Review*, 51(7), pp. 1534-1546.
- Harraq, A., Choudhury, B. & Bharti, B., 2022. Field-induced assembly and propulsion of colloids. *Langmuir*, 38(10), pp. 3001-3016.
- Harris, N., Arnold, M. D., Blaber, M. G. & Ford, M. J., 2009. Plasmonic Resonances of Closely Coupled Gold Nanosphere Chains. *J. Phys. Chem. C.*, 113(7), pp. 2784-2791.
- Hartmann, U. & Mende, H., 1984. Experimental investigation of Néel relaxation effects on magnetostatic properties of a ferrofluid. *Journal of Magnetism and Magnetic Materials*, 45(2-3), pp. 409-414.

- Hashim, D. et al., 2010. Potential use of Fourier transform infrared spectroscopy for differentiation of bovine and porcine gelatins. *food Chemistry*, 118(3), pp. 856-860.
- Hasley, T. C. & Toor, W., 1990. Structure of Electrorheological fluids. *Phys. Rev. Lett*, Volume 65, p. 2820.
- Haug, H. & Schmitt-Rink, S., 1984. Electron theory of the optical properties of laser-excited semiconductors. *Progress in Quantum Electronics*, 9(1), pp. 3-100.
- Hawkeye, M., 2007. Glancing angle deposition: Fabrication, properties, and applications of micro-and nanostructured thin films. *Journal of vacuum Science & Technology A*, 25(5).
- Hazle, M., Mehicic, M., Gardiner, D. & Graves, P., 1990. *Practical Raman Spectroscopy*. ISBN 3-540-50254-8 ed. Berlin: Springer Verlag.
- Hedayatnasab, Z., Dabbagh, A., Abnisa, F. & Daud, W., 2020. Polycaprolactone-coated superparamagnetic iron oxide nanoparticles for in vitro agnetic hypertheria therapy of cancer. *Eur. Polym. J.*, Volume 133, p. 109789.
- He, L., Mingsheng, W., Jiangping, G. & Yadong, Y., 2012. Magnetic Assembly route to colloidal responsive photonic nanostructures. *Accounts of Chemical Research*, pp. 1431-1440.
- He, L. et al., 2013. Magnetic assembly and patterning of general nanoscale materials through nonmagnetic templates. *Nano letters*, pp. 264-271.
- Helseth, L., 2009. Optical sensor for detecting colloidal phase transitions induced by magnetic fields. *Journal of Physics D: Applied Physics*, 42(10), p. p105005.
- Herman S., M., Carolina M., S., Adriana N., S. & Alexandra A. P., M., 2008. FTIR Spectroscopy characterisation of polyvinyl alcohol hydrogel with different hydrolysis degree and chemical crosslinked with glutaraldehyde. *Materials Science and Engineering: C*, 28(4), pp. 539-548.
- He, X. et al., 2012. Surface-enhanced Raman spectroscopy using gold-coated horizontally aligned caron nanotubes. *Nanotechnology*, Volume 23, p. 9pp.
- Homola, J., Yee, S. & Gauglitz, G., 1999. Surface plasmon resonance sensors. *Sensors and actuators B: Chemical*, 54(1-2), pp. 3-15.
- Horia, F. et al., 2020. Optical and Thermophysical Characterization of Fe₃O₄ nanoparticle. *IOP Conference Series: Materials Science and Engineering* , 956(1), p. 012016.
- Howell, S. T., Grushina, A., Holzner, F. & Brugger, J., 2020. Thermal Scanning probe lithography. *Microsystems & Nanoengineering*, 6(21), pp. 1-24.
- Huang, M. C. Y., Zhou, Y. & Chang-Hasnain, C. J., 2007. A Surface-Emitting Laser Incorporating a High-Index-Contrast Subwavelength Grating. *Nat. Photonics*, Volume 1, pp. 119-122.
- Huang, X. & El-Sayed, M., 2010. Gold nanoparticles: Optical properties and implementations in cancer diagnosis and photothermal therapy. *Journal of Advanced Research*, 1(1), pp. 13-28.
- Huck, C. et al., 2014. Surface-enhanced infrared spectroscopy using nanometer-sized gaps. *ACS nano*, 8(5), pp. 4908-4914.

- Huck, C. et al., 2016. Strong coupling between phonon-polaritons and plasmonic nanorods. *Optics express*, 24(22), pp. 25528-25539.
- Humayun, M., Raziq, F., Khan, A. & Luo, W., 2018. Modification strategies of TiO₂ for potential applications in photocatalysis: A critical review. *Green Chemistry Letters and Reviews*, 11(2), pp. 86-102.
- Hussain, I., Brust, M., Papworth, A. J. & Cooper, A. I., 2003. Preparation of Acrylate-Stabilized Gold and Silver Hydrosols and Gold-Polymer Composite Films. *Langmuir*, 19(11), pp. 4831-4835.
- Hwang, I. et al., 2007. Ultrafast electron transfer and decay dynamics in a small band gap bulk heterojunction material. *Advanced Materials*, 19(17), pp. 2307-2312.
- Imtiaz, F., Rashid, J. & Xu, M., 2019. Semiconductor nanocomposites for visible light photocatalysis of water pollutants. In: M. Rahman, A. Khan, A. Asiri & Inamuddin, eds. *Concepts of semiconductor photocatalysis*. London: IntechOpen.
- Iordanova, N., Dupuis, M. & Rosso, K., 2005. Charge transport in metal oxides: a theoretical study of hematite α -Fe₂O₃. *The Journal of chemical physics*, 122(14), p. 144305.
- Ivanov, A. et al., 2007. Magnetic measurements as a key to the particle size distribution in ferrofluids: experiment, theory and computer simulations. *Magneto hydrodynamics*, 43(4), pp. 393-399.
- Ivanov, A. O. & Zubarev, A., 2020. Chain Formation and Phase separation in Ferrofluids: The influence on Viscous Properties. *Materials Review*, Volume 13, pp. 3956-3981.
- Jaime, I. et al., 2015. Synthesis and characterization of magnetite/PGLA/Chitosan nanoparticles. *Materials Research Express*, Volume 2, p. 095010.
- Janjua, M. et al., 2009. Electric field induced alignment and self-assembly of rods on fluid-fluid interfaces. *Mechanics Research Communications*, 36(1), pp. 55-64.
- Jia, Y. et al., 2020. Controllable formation of periodic wrinkles in Marangoni-driven self-assembled graphene film for sensitive strain detection.. *Science China Materials*, 63(10), pp. 1983-1992.
- Ji, J. et al., 2016. Giant magneto-optical Raman effect in a layered transition metal compound. *Proceedings of the National Academy of Sciences*, 113(9), pp. 2349-2353.
- Jordan, K., Long, L., McGwin, G. & Childers, N., 2019. Average are under the curve: An alternative method quantifying the dental caries experience in longitudinal studies. *Community Dentistry and Oral Epidemiology*, 47(5), pp. 441-447.
- Jose, b. M., 2015. *Dynamic Wetting, Self-assembly, and Coalescence of Droplets in Microchannels*, Stony Brook University: PhD Dissertation.
- Kamat, P., 1993. Photochemistry on nonreactive and reactive (semiconductor) surfaces. *Chemical Reviews*, 93(1), pp. 267-300.
- Kang, T., Hulsen, M. & den Toonder, J., 2004. Dynamics of magnetic chains in a shear flow under the influence of a uniform magnetic field. *Physics of Fluids*, 24(4), pp. 2001-2018.
- Kao, K. C., 2004. Introduction. In: *Dielectric Phenomena in Solids*. s.l.:Elsevier, pp. 1-39.

- Kasani, S., Curtin, K. & Wu, N., 2019. A review of 2D and 3D plasmonic nanostructure array patterns: fabrication, light management and sensing applications.. *Nanophotonics, De Gruyter*, 8(12), pp. 2065-2089.
- Kato, H., 2012. Size Determination of NPs by Dynamic Light Scattering. In: S. C. Singh, Z. H., C. Guo & W. Cai, eds. *Nanomaterials: Processing and Characterization with Lasers*. s.l.:Wily-VCH, p. Chapter 8.
- Kazmaier, P. & Chopra, N., 2000. Bridging size scales with self-assembling supramolecular materials. *MRS Bull*, Volume 25, pp. 30-35.
- Kearns, P., 2010. Nanomaterials: getting the measure. *OECD*, Volume 279, pp. 34-35.
- Kelly, K., Coronado, E., Zhao, L. & Schatz, G., 2003. The optical properties of metal nanoparticles: the influence of size, shape, and dielectric environment.. *The Journal of Physical Chemistry B*, 107(3), pp. 668-677.
- Khan, I., Saeed, K. & Khan, I., 2019. Nanoparticles: Propewrties, applications and toxicities. *Arabian Journal of Chemistry, Elsevier*, 12(7), pp. 908-931.
- Kim, H., Lee, H.-B.-R. & Maeng, .. J., 2009. Applications of atomic layer deposition to nanofabrication and emerging nanodevices. *Thin Solid Films*, 517(8), pp. 2563-2580.
- Kim, H. et al., 2014. Plasmon-enhanced photoelectrochemical water splitting with size-controllable gold nanodot arrays. *ACS nano*, 8(10), pp. 10756-10765.
- Kim, J. et al., 2019. Assembly of gold nanoparticles into chiral superstructures driven by circularly polarized light.. *Journal of the American Chemical Society*, 141(30), pp. 11739-11744.
- Kim, M. H., Im, S. H. & Park, O. O., 2005. Rapid Fabrication of Two and Three Dimensional Colloidal Crystal Films via Confined Convective Assembly. *Advanced Functional Materials*, 15(8), pp. 1329-1335.
- Kimmins, S. & Cameron, N., 2011. Functional porous polymers by emulsion templating: recent advances. *Advanced Functional Materials*, 21(2), pp. 211-225.
- Koenderink, F. A., 2009. Plasmon Nanoparticle Array Waveguides for Single Photon and Single Plasmon Sources. *Nano Letters*, 9(12), pp. 4228-4233.
- Kohoutek, T., Parchine, M., Bardosova, M. & Pemble, M. E., 2020. Controlled self-assembly of Langmuir-Blodgett colloidal crystal films of monodispersed silica particles on non-planar substrates. *Colloids and Surfaces A: Physiochemichal and Engineering Aspects*, Volume 593, p. 124625.
- Ko, H.-Y., Park, J., Shin, H. & Moon, J., 2004. Rapid Self-Assembly of Monodisperse Colloidal Spheres in an Ink-Jet Printed Droplet. *Chem. Mater.*, 16(22), pp. 4212-4215.
- Kole, M. & Khandekar, S., 2021. Engineering applicatins of ferrofluids: A review. *Journal of Magnetism and Magnetic materials*, Volume 537, p. 168222.
- Kong, L. Y. et al., 2015. Deposition of Quantum Dots in Capillary Tube. *Langmuir*, 31(45), pp. 12560-12566.

- Korobchevskaya, K. et al., 2011. Ultrafast carrier dynamics in gold/iron-oxide nanocrystal heterodimers. *Applied Physics Letters*, 99(1), p. 011907.
- Kozlov, M., 2004. *Ultra-Thin Films of Polyvinyl Alcohol on Hydrophobic Surfaces: Preparation, Properties, Chemistry, and Applications*, Massachusetts: PhD Dissertation, University of Massachusetts Amherst..
- Krafcik, A., Babinec, P., Strbak, O. & Frollo, I., 2021. A Theoretical Analysis of Magnetic Particle Alignment in External Magnetic Fields Affected by Viscosity and Brownian Motion. *Applied Sciences*, 11(20), p. 9651.
- Kralchevsky, P. & Nagayama, 2001. *Particles at Fluid Interfaces and Membranes: Attachment of Colloid Particles and Proteins to Interfaces and Formation of Two-Dimensional Arrays*. s.l.:ScienceDirect.
- Kravetz, V. G., Kabashin, A. V., Barnes, W. L. & Grigorenko, A. N., 2018. Plasmonic Surface Lattice Resonances: A Review of Properties and Applications. *Chem. Rev.*, 118(12), pp. 5912-5951.
- Kreibig, U. & Frangstein, C., 1969. The limitation of electron mean free path in small silver particles. *Zeitschrift für Physik*, 224(4), pp. 307-323.
- Krishnan, S., 1978. *On the manufacture of very thin elastomeric films by spin coating*, Massachusetts: Dept. of Mechanical Engineering, Massachusetts Institute of Technology.
- Kumar, A., Kumar, A., C. H. & Krishnan, V., 2022. Upconversion nanomaterials for photocatalytic applications. In: T. Sabu, U. Kanchan, K. T. Raunak & K. Nandakumar, eds. *Upconversion Nanophosphors*. s.l.:Elsevier, pp. 391-406.
- Kumar, N. & Kumbhat, S., 2016. Unique Properties. In: *Essentials in Nanoscience and Nanotechnology*. s.l.:Wiley & Sons, Inc, pp. 326-360.
- Kuroda, T. et al., 2021. Apparatus for high-precision angle-resolved reflection spectroscopy in the mid-infrared region. *Applied Spectroscopy*, 75(3), pp. 259-264.
- Kuzyk, A. et al., 2016. A light-driven three-dimensional plasmonic nanosystem that translates molecular motion into reversible chiroptical function.. *Nature communications*, 7(1), pp. 1-6.
- Lai, C., Low, F., Tai, M. & Abdul-Hamid, S., 2017. Iron oxide nanoparticles decorated Oleic acid for high colloidal stability. *Adv. Polym. Technol.*, 37(6), pp. 1712-1721.
- Lai, J., 1979. An investigation of spin coating of electron resists. *Polymer Engineering & Science*, 19(15), pp. 1117-1121.
- Lakshminarasimhan, N., Choi, W. & Kim, W., 2008. Effect of the Agglomerated state on the Photocatalytic Hydrogen Production with in Situ Agglomeration of Colloidal TiO₂ Nanoparticles. *The Journal of Physical Chemistry C*, 112(51), pp. 20451-20457.
- Lamour, G. et al., 2010. Contact Angle Measurement using a Simplified Experimental Setup. *J. Chem. Educ.*, 87(12), pp. 1403-1407.
- Landers, J. et al., 2016. Simultaneous study of brownian and neel relaxation phenomena in ferrofluids by mossbauer spectroscopy. *Nano letters*, 16(2), pp. 1150-1155.

Landfester, K., 2006. Synthesis of colloidal particles in miniemulsions. *Annu. Rev. Mater. Res*, Volume 36, pp. 231-279.

Larsen, I. L., 1971. Slide rule conversion of percent transmittance to absorbance. *Journal of Chemical Education*, 48(6), p. 388.

Larson-smith, K. & Pozzo, D. c., 2011. Scalable synthesis of self-assembling nanoparticle clusters based on controlled steric interactions. *Soft Matter*, Volume 7, pp. 5339-5347.

Larson-Smith, K. & Pozzo, D. C., 2012. Pickering Emulsion Stabilized by Nanoparticle surfactants.. *Langmuir*, 28(32), pp. 11725-11732.

Lässer, R., Smith, N. & Benbow, R. L., 1981. Empirical band calculations of the optical properties of d-band metals. I. Cu, Ag, and Au.. *Physical Review B*, 24(4), p. 1895.

Lawes, R. A., 2007. Manufacturing costs for microsystems/MEMS using high aspect ratio microfabrication techniques. *Microsyst. Technol., Springer*, Volume 13, pp. 85-95.

Lawrence, C., 1988. The mechanics of spin coating of polymer films. *The Physics of Fluids*, 10(13), pp. 2786-2795.

Lawrence, C. J., 1988. The Mechanism of Spin coating of Polymer Films. *The Physics of Fluids*, 31(10), pp. 2786-2795.

Lawrence, C. J. & Zhou, W., 1991. Spin coating of non-Newtonian fluids. *Journal of Non-Newtonian Fluid Mechanics*, Volume 39, pp. 137-187.

Lawrence, C. & Zhou, W., 1991. Spin coating of non-Newtonian fluids. *Journal of non-newtonian fluid mechanics*, 39(2), pp. 137-187.

Lawrence, E. M. et al., 1994. Field-Induced Structure of Confined Ferrofluid Emulsion. *International Journal of Mordern Physics B*, 8(20), pp. 2765-2777.

Leal-Calderon, F. et al., 1994. Direct measurement of colloidal forces. *Physical Review Letters* 72(18), pp. 2959-2964.

Lee, S., 2015. Colloidal superlattices for unnaturally high-index metamaterials at broadband optical frequencies. *Optics Express*, 23(22), p. 246741.

Lee, W. et al., 2004. Nanoparticle-Mediated Epitaxial Assembly of Colloidal Crystals on Patterned Substrate. *Langmuir*, 20(13), pp. 5262-5270.

Lee, Y., Garcia, M. A., Frey Huls, N. A. & Sun, S., 2010. Synthetic Tuning of the Catalytic Properties of Au-Fe₃O₄ Nanoparticles. *ngewandte Chemie, International Edition*, Volume 49, pp. 1271-1274.

Lehman, G. & Ziesche, P., 1990. *Electronic Properties of Metals*. s.l.:Elsevier Science Publishers.

Lewis, W., 1937. The electric charge at an oil-water interface. *Transactions of the Faraday Society*, Volume 33, pp. 708-713.

Libaers, W. et al., 2009. Engineering colloidal photonic crystals with magnetic functionalities. *Colloids and Surfaces A: Physicochemical and Engineering Aspects*, 339(1-3), pp. 13-19.

Liddle, A. & Gallatin, G. M., 2016. Nanomanufacturing: A perspective. *ACS, Nano*, 10(3), pp. 2995-3014.

Li, H., Carter, J. D. & LaBan, T. H., 2009. Nanofabrication by DNA self-assembly. *materials today*, 12(5), pp. 24-32.

Li, H. & Cullum, B. M., 2005. Dual Layer and Multilayer Enhancements from Silver Film over Nanostructured Surface-Enhanced Raman Substrates. *Applied Spectroscopy*, 59(4), pp. 410-417.

Li, H. & Rothberg, L., 2004. Colorimetric detection of DNA sequences based on electrostatic interactions with unmodified gold nanoparticles. *Proceedings of the National Academy of Sciences*, 101(39), pp. 14036-14039.

Li, J. et al., 2008. Coordinated chain motion resulting in intensity variation of light transmitted through ferrofluid film. *Physics Letters A*, 372(46), pp. 6952-6955.

Liljestrom, V. et al., 2019. Active structuring of colloids through field-driven self-assembly. *Colloidal & Interface Science*, Volume 40, pp. 25-41.

Lin, F. & Doong, R., 2011. Bifunctional Au-Fe₃O₄ Heterostructures for Magnetically Recyclable Catalysis of Nitrophenol Reduction. *J. Phys. Chem. C*, Volume 115, pp. 6591-6598.

Ling, Z., Rong, H. & Hong-Chen, G., 2006. Oleic acid coating on the monodisperse magnetite nanoparticles. *Applied Surface Science*, 253(5), pp. 2611-2617.

Linic, S., Christopher, P. & Ingram, D., 2011. Plasmonic-metal nanostructures for efficient conversion of solar to chemical energy. *Nature materials*, Volume 10, pp. 911-921.

Lin, Z., 2012. *Evaporative Self-assembly of Ordered Complex Structures*. s.l.:World Scientific.

Li, Q. et al., 2017. Correlation between particle size/domain structure and magnetic properties of highly crystalline Fe₃O₄ nanoparticles. *Sci Rep*, Volume 7, pp. 9894-9900.

Li, R. et al., 2020. Study on the assembly structure variation of cetyltrimethylammonium bromide on the surface of gold nanoparticles. *ACS omega*, 5(10), pp. 4943-4952.

Liu, B., Z. H. & Ding, Y., 2018. Au-Fe₃O₄ heterostructures for catalytic, analytical, and biomedical applications. *Chinese Chemical Letters*, 29(12), pp. 1725-1730.

Liu, D. et al., 2019. Air-Liquid Interfacial Self-Assembly of Two-Dimensional Periodic Nanostructured Arrays. *Chemnanomat*, 5(11), pp. 1338-1360.

Liu, H. L. et al., 2010. The synthesis and characterization of polymer-coated FeAu multifunctional nanoparticles. *Nanotechnology*, Volume 21, p. 335602.

Liu, J. et al., 2018. Recent advances of plasmonic nanoparticles and their applications. *Materials*, 11(10), p. 1833.

Liu, M. et al., 2014. Dark-field microscopy in imaging of plasmon resonant nanoparticles. *Colloids and Surfaces B: Biointerfaces*, Volume 124, pp. 111-117.

Liu, Y. et al., 2021. pH-Driven Reversible Assembly and Disassembly of Colloidal Gold Nanoparticles. *Frontiers in chemistry*, Volume 9.

- Liu, Y. et al., 2022. Coupling red-to-blue upconversion organic microcrystals with Cd_{0.5}Zn_{0.5}S for efficient and durable photocatalytic H₂ production. *Chemistry—An Asian Journal*.
- Liu, Z. et al., 2009. Magneto-optical Kerr effect in perpendicularly magnetized Co/Pt films on two-dimensional colloidal crystals. *Applied Physics Letters*, 95(3), p. 032502.
- Liu, Z., Tian, L., Liu, S. & Waller, L., 2014. Real-time brightfield, darkfield, and phase contrast imaging in a light-emitting diode array microscope. *Journal of biomedical optics*, 19(10), p. 106002.
- Li, X. et al., 2020. Thermally induced, tension-gradient-driven self-assembly of nanoparticle films for superhydrophobicity and oil-water separation. *Cell Reports Physical Science*, 1(10), p. 100220.
- Li, X., Niltsoo, O. & Couzis, A., 2013. Electrostatically driven adsorption of silica nanoparticles on functionalized surfaces. *Journal of Colloid Interface Science*, Volume 394, pp. 26-35.
- Li, X. & Wang, J., 2020. One-dimensional and two-dimensional synergized nanostructures for high-performing energy storage and conversion. *InfoMat*, 2(1), pp. 3-32.
- Liz-Marzán, L., 2006. Tailoring surface plasmons through the morphology and assembly of metal nanoparticles. *Langmuir*, 22(1), pp. 32-41.
- López-Ortega, A. et al., 2020. Enhanced magnetic modulation of light polarization exploiting hybridization with multipolar dark plasmons in magnetoplasmonic nanocavities. *Light: Science & Applications*, 9(1), pp. 1-14.
- Lotito, V. & Zambelli, T., 2016. Self-Assembly of Single-Sized and Binary Colloidal Particles at Air/Water Interface by Surface Confinement and Water Discharge. *Langmuir*, 32(37), pp. 9582-9590.
- Lo, Y., Chiu, Y., Tseng, H. & Chen, J., 2017. Thermal-Annealing-Induced Self-Stretching: Fabrication of Anisotropic Polymer Particles on Polymer Films. *Langmuir*, 33(43), pp. 12300-12305.
- Lu, C. et al., 2015. An actively ultrafast tunable giant slow-light effect in ultrathin nonlinear metasurfaces. *Light: Science & Applications*, 4(6), p. 302.
- Maccaferri, N. et al., 2014. Effects of a non-absorbing substrate on the magneto-optical Kerr response of plasmonic ferromagnetic nanodisks. *physica status solidi*, 211(5), pp. 1067-1075.
- Mahendia, S. et al., 2011. Optical and Structural properties of poly(vinyl alcohol) films embedded with citrate-stabilized gold nanoparticles. *Journal of Physics D*, Volume 44, p. 8pp.
- Majee, B. P. & Mishra, A. K., 2021. Fundamentals and Applications of Surface Enhanced Raman Spectroscopy. In: D. K. Pradhan & A. Materny, eds. *Modern Techniques of Spectroscopy*. Singapore: Springer, pp. 185-208.
- Majhi, S. et al., 2018. Au@ NiO core-shell nanoparticles as a p-type gas sensor: Novel synthesis, characterization, and their gas sensing properties with sensing mechanism. *Sensors and Actuators B: Chemical*, Volume 268, pp. 223-231.
- Manstrangeli, M., Ruythooren, W., Van Hoof, C. & Celis, J.-P., 2009. Conformal dip-coating of patterned surfaces for capillary die-to-substrate self-assembly. *Journal of Micromechanics and Microengineering*, Volume 19, p. 045015.

- Maria, M. O., 2017. Study of static magnetic properties of transformer oil based magnetic fluids for various technical applications using demagnetizing field correction. *Journal of Nanomaterials*.
- Martinez-Chapa, S. O., Salazar, A. & Madou, M. J., 2020. Two-Photon Polymerization as a Component of Desktop-Integrated Manufacturing Platforms. In: S. Holt, ed. *Three-Dimensional Microfabrication Using Two-Photon Polymerization*. Oxford: Matthew Deans, pp. 577-623.
- Martin-Garcia, B. & Velazquez, M. M., 2014. Nanoparticle Self-Assembly Assisted by Polymers: The Role of Shear Stress in the Nanoparticle Arrangement of Langmuir and Langmuir–Blodgett Films. *Langmuir*, 30(2), pp. 509-516.
- Maß, T., Nguyen, V., Schnakenberg, U. & Taubner, T., 2019. Tailoring grating strip widths for optimizing infrared absorption signals of an adsorbed molecular monolayer.. *Optics Express*, 27(8), pp. 10524-10532.
- Maula, J. & Oy, B., 2010. *Atomic layer deposition (ALD) for optical nanofabrication*. San Francisco, California, United States, Proceedings Volume 7591, Adv. Fabrication Technologies for Micro/Nano Optics and Photonics. SPIE.
- Mayerhöfer, T. & Popp, J., 2018. Periodic array-based substrates for surface-enhanced infrared spectroscopy. *Nanophotonics*, 7(1), pp. 39-79.
- Mayer, M. et al., 2016. Template-assisted colloidal self-assembly of macroscopic magnetic metasurfaces. *Faraday discussions*, Volume 191, pp. 159-176.
- McConnell, G. A., Lin, M. Y. & Gast, A. P., 1995. Long range order polymeric Miscelles under steady shear. *Macromolecules*, Volume 28, pp. 6754-6764.
- Megiel, E., 2017. Surface modification using TEMPO and its derivatives. *Advances in Colloid and Interface Science*, Volume 250, pp. 158-184.
- Mehdihasan I., S. et al., 2018. Methacrylate copolymers and their composites with nano-CdS: Synthesis, characterization, thermal behavior, and antimicrobial properties. *Int. J. Indust. Chem., Springer*, Volume 9, pp. 153-166.
- Merck, 2020. *IR Spectrum Table and Chart*. [Online]
Available at: <https://www.sigmaaldrich.com/GB/en/technical-documents/technical-article/analytical-chemistry/photometry-and-reflectometry/ir-spectrum-table>
[Accessed 13 June 2020].
- Meyerhofer, D., 1978. Characteristics of resist films produced by spinning. *Journal of Applied Physics*, 49(7), pp. 3993-3997.
- Michaels, A., Jiang, J. & Brus, L., 2000. Ag nanocrystal junctions as the site for surface-enhanced Raman scattering of single rhodamine 6G molecules. *he Journal of Physical Chemistry B*, 104(50), pp. 11965-11971.
- Minati, L. et al., 2015. Fabrication and optical properties of assembled gold nanoparticles film on elastomeric substrate. *Colloids and Surfaces A: Physicochemical and Engineering Aspects*, Volume 482, pp. 431-437.

- Minelli, C. et al., 2018. Measuring the size and density of nanoparticles by centrifugal sedimentation and flotation. *Analytical Methods*, 10(15), pp. 1725-1732.
- Mingos, D., 2014. *Gold clusters, colloids and nanoparticles I*. 1st ed. Switzerland: Springer.
- Mingsheng, W., Le, H. & Yadong, Y., 2013. Magnetic field guided colloidal assembly. *Materials Today, Elsevier*, pp. 110-116.
- Mittal, M., Lele, P. P., Kaler, E. W. & Furst, E. M., 2008. Polarization and interactions of colloidal particles in AC Electric fields. *J. Chem. Phys*, Volume 129, p. 064513.
- Mizuno, S. & Yao, H., 2021. On the electronic transitions of α -Fe₂O₃ hematite nanoparticles with different size and morphology: Analysis by simultaneous deconvolution of UV-vis absorption and MCD spectra. *Journal of Magnetism and Magnetic Materials*, Volume 517, p. 167389.
- Mohsen-Nia, M. & Modarress, H., 2006. Viscometric study of aqueous poly(vinyl alcohol) PVA solutions as a binder in adhesive formulations. *J. Adhesion Sci. Technol.*, 20(12), pp. 1273-1280.
- Molet, P. et al., 2021. Engineering Plasmonic Colloidal Meta-Molecules for Tunable Photonic Supercrystals. *Advanced Optical Materials*, 9(20), p. 2100761.
- Moreno, M., Hernandez, R. & Lopez, D., 2010. Crosslinking of poly(vinyl alcohol) using functionalized gold nanoparticles. *European Polymer Journal*, Volume 46, pp. 2099-2104.
- Moss, T., 1967. Photoelectricity in solids. *Physics Education*, 2(3), p. 121.
- Mouhamad, Y. et al., 2014. Dynamics of Polymer Film Formation During Spin Coating. *J. App. Phys.*, Volume 116, p. 123513.
- Mourdikoudis, S., Pallares, R. & Thanh, N. T. K., 2018. Characterization techniques for nanoparticles: comparison and complementarity upon studying nanoparticle properties. *Nanoscale*, Volume 10, p. 12871.
- Mourkas, A., Zarlaha, A., Kourkoumelis, N. & Panagiotopoulos, I., 2021. Self-Assembly Magnetic Micro- and Nanospheres and the Effect of Applied Magnetic Fields. *Nanomaterials*, 11(4), p. 1030.
- Mou, T. et al., 1994. The evolution of Field INduced Structure of Confined Ferrofluid Emulsion. *International Journal of Mordern Physics B*, 8(20), pp. 2779-2787.
- Nair, A. et al., 2018. Optical characterization of nanomaterials. In: *Characterization of Nanomaterials*. s.l.:Woodhead Publishing, pp. 269-299.
- Nasseri, B. et al., 2016. Antenna-type radiofrequency generator in nanoparticle-mediated hyperthermia. *RSC Adv.*, 6(54), pp. 48427-48343.
- Neubrech, F. et al., 2017. Surface-Enhanced Infra-red Spectroscopy using Resonant Nanoantennas. *Chemical Reviews*, Volume 117, pp. 5110-5145.
- Neubrech, F. & Pucci, A., 2013. Plasmonic enhancement of vibrational excitations in the infrared. *IEEE J. Sel. Topics Quantum Electron*, 19(3), p. 4600809.

- Neubrech, F. et al., 2010. Antenna sensing of surface phonon polaritons. *J. Phys. Chem C.*, 114(16), pp. 7299-7301.
- Ng, L. & Simmons, R., 1999. Infrared spectroscopy. *Analytical chemistry*, 71(12), pp. 343-350.
- Nguyen, N.-T., 2012. Micro-magnetofluidics: interactions between magnetism and fluid flow on the microscale. *Microfluid Nanofluid*, 12(1), pp. 1-16.
- Nguyen, T., Mammeri, F. & Ammar, S., 2018. Iron Oxide and Gold Mased Magneto-Plasmonic nanostructures for Medical Applications: A Review. *nanomaterials*, 8(149), pp. 1-29.
- Nie, Z. et al., 2008. An "inside-out" microfluidic approach to monodisperse emulsions stabilized by solid particles. *Journal of the American Chemical Society*, 130(49), pp. 16508-16509.
- Ni, I. et al., 2012. Formation mechanism, patterning, and physical properties of gold-nanoparticle films assembled by an interaction-controlled centrifugal method.. *The Journal of Physical Chemistry C*, 116(14), pp. 8095-8101.
- Noorsaiyyidah Darman, S., Nurul Akmal, C. L., Mohd Rafie, J. & Ahmad, R., 2012. FTIR Studies on Silver-Poly(Methylmethacrylate) Nanocomposites via In-Situ Polymerization Technique. *Int. J. Electrochem.Sci.*, pp. 5596-5603.
- Oberdick, S. D. & Majetich, S. A., 2013. Electrophoretic Deposition of Iron Oxide Nanoparticles on Templates. *J. Phys. Chem. C.*, 117(36), pp. 18709-18718.
- O'grady, K., El-Hilo, M. & Chantrell, R., 1993. The characterisation of interaction effects in fine particle systems. *IEEE transactions on magnetics*, 29(6), pp. 2608-2613.
- Ohring, M., 1995. Magnetic Properties of Materials. In: *Engineering Materials Science*. s.l.:Elsevier, pp. 711-746.
- Okazaki, S., 2015. High resolution optical lithography or high throughput electron beam lithography: The technical struggle from the micro to the nano-fabrication evolution. *Microelectronic Engineering*, Volume 133, pp. 23-35.
- Ozin, G. A. & Yang, S. M., 2001. The Race for the Photonic Chip: Colloidal Crystal Assembly in Silicon Wafers. *Advanced Functional Materials*, 11(2), pp. 95-104.
- P., B. et al., 2013. Magnetization and Specific Absorption Rate Studies of BALL-milled Iron Oxide Nanoparticles for Biomedicine. *Journal of Nanoparticles*, p. 181820.
- Pancholi, K. et al., 2018. Observation of stimulated emission from Rhodamine 6G-polymer aggregate adsorbed at foam interfaces. *Journal of Physics: Energy*, 1(1), p. 015007.
- Panine, P., Narayanan, T., Vermant, J. & Mewis, J., 2002. Structure and and Rheology During Shear-Induced Crystallization of a Latex Suspension. *Phy Rev. E*, Volume 66, pp. 022401-022405.
- Pan, K. et al., 2014. pH-driven encapsulation of curcumin in self-assembled casein nanoparticles for enhanced dispersibility and bioactivity. *Soft Matter*, 10(35), pp. 6820-6830.

- Park, Y. & Park, S., 2008. Directing close-packing of midnanosized gold nanoparticles at a water/hexane interface.. *Chemistry of Materials*, 20(6), pp. 2388-2393.
- Patra, J. & Baek, K., 2014. Green nanobiotechnology: factors affecting synthesis and characterization techniques.. *Journal of Nanomaterials*.
- Patricia, B. et al., 1999. Preparation and properties of an aqueous ferrofluid. *Journal of Chemical Education*, 76(7), pp. 943-948.
- Pellegrino, F., Pellutic, L., Sordello, F. & Minero, C., 2017. Influence of agglomeration and aggregation on photocatalytic activity of TiO₂ nanoparticles. *Applied Catalysis B Environmental*, Volume 216, pp. 80-87.
- Peng, Y. et al., 2015. Recent advances in optical imaging with anisotropic plasmonic nanoparticles. *Analytical Chemistry*, 87(1), pp. 200-215.
- Pepper, S. V., 1995. Characterization and Application of a Grazing Angle Objective for Quantitative Infrared Reflection Microspectroscopy. *Applied Spectroscopy*, 49(3), pp. 354-360.
- Perez-Murano, F., Martin, J. I. & De Teresa, J. M., 2020. Optical Lithography. In: *Nanofabrication: Nanolithography techniques and their applications*. s.l.:IOP Publishing limited, pp. 2-40.
- Pham, K., Temerov, F. & Saarinen, J., 2020. Multicomponent inverse opal structures with gold nanoparticles for visible light photocatalytic activity. *Materials & Design*, Volume 194, p. 108886.
- Pichumani, M. & Gonzalez-Vinas, W., 2011. Spin -Coating of Dilute Magnetic Colloids in a Magnetic field. *Magneto hydrodynamics*, 47(2), pp. 191-199.
- Pichumani, M. & Gonzalez-Vinas, W., 2013. Magnetoheology from surface coverage of spin-coated colloidal films. *Soft Matter*, Volume 9, pp. 2506-2511.
- Pi-Kem, 2019. *Electronics and Photonics Research Catalogue*. [Online]
Available at: <https://www.pi-kem.co.uk/images/cms/Electronics%20&%20Photonics%20Research%20-%20For%20web.pdf>
[Accessed 17 Novembr 2021].
- Pilapil, B., Jahandideh, H., Bryant, S. & Trifkovic, M., 2016. Stabilization of oil-in-water emulsions with noninterfacially adsorbed particles. *Langmuir*, 32(28), pp. 7109-7116.
- Pilling, M. & Gardner, P., 2016. Fundamental developments in infrared spectroscopic imaging for biomedical applications.. *Chemical Society reviews*, 45(7), pp. 1935-1957.
- Pluchery, O., 2012. Optical properties of gold nanoparticles. In: *Gold Nanoparticles for Physics, Chemistry and Biology*. London: Imperial College Press, pp. 43-73.
- Poirier, G. E. & D., P. E., 1996. The Self-Assembly Mechanism of Alkanethiols on Au(111). *Report*, 272(5265), pp. 1145-1148.
- Poulin, P., Cabul, V. & Weitz, D. A., 1997. Direct measurement of colloidal forces in anisotropic solvent. *Physical Review Letters*, pp. 4862-4865.

- Powell, R., 1976. Photoconductive processes in Al₂O₃ films. *Journal of Applied Physics*, 47(10), pp. 4598-4604.
- Promislow, J. H. E. & Gast, A. P., 1996. Magnetorheological fluid structure in a pulsed magnetic field. *Langmuir*, Volume 12, pp. 4095-4102.
- Pu, S., Yao, L., Guan, F. & Liu, M., 2009. Threshold-tunable optical limiters based on nonlinear refraction in ferrosols. *Optics communications*, 282(5), pp. 908-913.
- Pylarinou, M. et al., 2021. Visible Light Trapping against Charge Recombination in FeO_x-TiO₂ Photonic Crystal Photocatalysts. *Materials*, 14(23), p. 7117.
- Qi, D., Cao, Z. & Ziener, U., 2014. Recent advances in the preparation of hybrid nanoparticles in miniemulsions. *Advances in colloid and interface science*, Volume 211, pp. 47-62.
- Qin, D., Xia, Y. & Whitesides, G. M., 2010. Soft lithography for micro- and nanoscale patterning. *Nature Protocols*, 5(3), pp. 491-502.
- Qiu, Z. & Bader, S., 1995. Surface magnetism and Kerr spectroscopy. *MRS Bulletin*, 20(10), pp. 34-37.
- Rabani, E., Reichman, D. R., Geissler, P. L. & Brus, L. E., 2003. Drying-mediated self-assembly of nanoparticles. *Nature*, Volume 426, pp. 271-274.
- Radha, B. & Kulkarni, G. U., 2014. Direct write nanolithography. In: *SPR-Nanoscience: Volume 2*. s.l.:s.n., p. Chapter 3.
- Radoń, A., Drygała, A., Hawełek, Ł. & Łukowiec, D., 2017. Structure and optical properties of Fe₃O₄ nanoparticles synthesized by co-precipitation method with different organic modifiers. *Materials Characterization*, Volume 131, pp. 148-156.
- Reguera, J. et al., 2016. Synthesis of Janus plasmonic-magnetic, star-sphere nanoparticles, and their application in SERS detection. *Faraday Discussions*, Volume 191, pp. 47-59.
- Reich, T., Ortlepp, T. & Uhlmann, F., 2006. September. Development of a digital SQUID device for high sensitive measurement of widely varying magnetic fields. *Information technology and electrical engineering-devices and systems, materials and technologies for the future*, Volume 51.
- Reimer, L. & Kohl, H., 2009. Transmission Electron Microscopy Physics of Image Formation. *Springer*, Volume 51, pp. 1-15.
- Reincke, F., Hickey, S., Kegel, W. & Vanmaekelbergh, D., 2004. Spontaneous assembly of a monolayer of charged gold nanocrystals at the water/oil interface. *Angewandte Chemie*, 116(4), pp. 464-468.
- Richards, B., Ivaturi, A., MacDougall, S. & Marques-Hueso, J., 2012. *Up-and down-conversion materials for photovoltaic devices*. s.l., Conference: SPIE European Photonics Symposium Volume: 1, p. 843802.
- Rigo, M. V., Seo, J., Kim, W.-J. & Jung, S., 2011. Plasmon coupling of R6G-linked gold nanoparticle assemblies for surface-enhanced Raman spectroscopy. *Vibrational Spectroscopy*, 57(2), pp. 315-318.
- Ritala, M. & Leskela, M., 1999. Atomic layer epitaxy - a valuable tool for nanotechnology?. *Nanotechnology*, Volume 10, pp. 19-24.

- Rius, G., Baldi, A., Ziaie, B. & Atashbar, M. Z., 2017. Introduction to Micro-/Nanofabrication. In: B. Bhushan, ed. *Handbbook of Nanotechnology*. Berlin, Heidelberg: Springer, pp. 51-86.
- Roe, E. T., Scanlan, J. T. & Swern, D., 1949. Fatty Acid Amides. I. Preparation of Amides of Oleic and the 9, 10-Dihydroxystearic Acids. *J. Am. Chem. Soc.*, 71(6), pp. 2215-2218.
- Roger, K., Sparr, E. & Wennerstrom, H., 2018. Evaporation, diffusion and self-assembly at drying interfaces. *Phys. Chem. Chem. Phys.*, Volume 20, pp. 10430-10438.
- Rogers, J. A. & Nuzzo, R., 2005. Recent Progress in soft Lithography. *materials today*, 8(2), pp. 50-56.
- Rosensweig, R. E., 1985. *Ferrohydrodynamics*. New York: Dover Publications, Inc..
- Russier-Antoine, I. B. F. et al., 2014. Non-linear optical properties of gold quantum clusters. The smaller the better. *Nanoscale*, 6(22), pp. 13572-13578.
- Russo, C., Stanzone, F., Tregrossi, A. & Ciajolo, A., 2014. Infrared spectroscopy of some carbon-based materials relevant in combustion: qualitative and quantitative analysis of hydrogen. *Carbon*, Volume 74, pp. 127-138.
- Rycenga, M., Camargo, P. & Xia, Y., 2009. Template-assisted self-assembly: a versatile approach to complex micro-and nanostructures.. *Soft Matter*, 5(6), pp. 1129-1136.
- Sachdev, S. et al., 2017. Synthesis and assembly of gold and iron oxide particles within an emulsion droplet; Facile production of core@ shell particles. *Colloid and Interface Science Communications*, Volume 16, pp. 14-18.
- Saini, A. et al., 2021. Magnetic Particle Self-Assembbly at functionalized interfaces. *Langmuir*, 37(14), pp. 4064-4071.
- Saini, I. et al., 2018. Ag nanoparticles induced modification in microhardness of polyvinyl alcohol. *Advanced Material Proceedings*, 3(8), pp. 508-511.
- Saunders, B. & Turner, M., 2008. Nanoparticle–polymer photovoltaic cells. *Advances in colloid and interface science*, 138(1), pp. 1-23.
- Sawadh, P. & Kulkarni, D., 2000. *Magnetic and electrical behaviour of CaNi₂Fe₁₆O₂₇*, s.l.: s.n.
- Scanlon, M. D., Smirnov, E., Stockmann, T. J. & Peljo, P., 2018. Gold Nanofilms at Liquid-Liquid Interfaces: An Emerging Platform for redox Electrocatalysis, Nanoplasmonics Sensors, and Electrovariable Optics. *Chem Rev.*, 118(7), pp. 3722-3751.
- Scarabelli, L., 2018. Recent advances in the rational synthesis and self-assembly of anisotropic plasmonic nanoparticles. *Pure and Applied Chemistry*, 90(9), pp. 1393-1407.
- Scarabelli, L., Vila-Liarte, D., Mihi, A. & Liz-Marzan, L. M., 2021. Templated Colloidal Self-Assembly for Lattice Plasmon Engineering. *Acc. Mater. Res.*, 2(9), pp. 816-827.
- Schulz, F. et al., 2020. Structural order in plasmonic superlattices. *nature communications*, 11(3821), pp. 1-9.

- Shabaniverki, A., Thorud, S. & Juarez, J. J., 2018. Vibrationally directed assembly of micro- and nanoparticle-polymer composite. *Chemical Engineering Science*, Volume 192, pp. 1209-1217.
- Shabaniverki, S. & Juarez, J. J., 2021. Directed Assembly of Particles for Additive Manufacturing of Particle-Polymer Composites. *Micromachines*, MDPI, 12(8), p. 935.
- Sharma, Y. & Dhawan, A., 2019. Nanoline-gap controlled self-assembly of plasmonic nanoparticles inside plasmonic nanolines. *Journal of Physics Communications*, Volume 3, p. 115013.
- Sherman, D. & Waite, T., 1985. Electronic spectra of Fe³⁺ oxides and oxide hydroxides in the near IR to near UV. *American Mineralogist*, 70(11-12), pp. 1262-1269.
- Shin, J. I. et al., 2019. Three-dimensional micropatterning of semiconducting polymers via capillary force assisted evaporative self-assembly. *Soft Matter*, 15(19), pp. 3854-3863.
- Shi, W. et al., 2006. A general approach to binary and ternary hybrid nanocrystals. *Nano Letters*, 6(4), pp. 875-881.
- Shi, Y., Zhou, X. & Yu, G., 2017. Material and structural design of novel binder systems for high-energy, high-power lithium-ion batteries. *Accounts of chemical research*, 50(11), pp. 2642-2652.
- Sidorov, T., 1967. Vibration spectra of three-component silicate glasses and the role of chemical elements in the structure of glass. *Journal of Applied Spectroscopy*, 7(3), pp. 258-261.
- Silenko, A., Zhang, P. & Zou, L., 2017. Manipulating twisted electron beams. *Physical Review Letters*, 119(24), p. 243903.
- Singamaneni, S., Bliznyuk, V. N., Binek, C. & Tsymbal, E. Y., 2011. Magnetic nanoparticles: recent advances, synthesis, self-assembly and applications. *J. Mater. Chem.*, Volume 21, pp. 16819-16845.
- Singh, S. & Nalwa, H. S., 2007. Nanotechnology and health safety—toxicity and risk assessments of nanostructured materials on human health. *Journal of nanoscience and nanotechnology*, 9(7), pp. 3048-3070.
- Soni, U. & Desai, R. P., 2022. Analyzing magnetic nanofluid structure. *Phys. Fluids*, Volume 34, pp. 012009(1-8).
- Sowade, E., Blaudeck, T. & Baumann, R. R., 2016. Self-Assembly of Spherical Colloidal Photonic Crystals inside Inkjet-Printed Droplets. *Cryst. Growth Des.*, 16(2), pp. 1017-1026.
- Stalder, A. et al., 2010. Low-bond axisymmetric drop shape analysis for surface tension and contact angle measurements of sessile drops. *Colloids and Surfaces A: Physicochemical and Engineering Aspects*, 364(1-3), pp. 72-81.
- Stein, R. et al., 2020. Synthesis and characterization of citrate-stabilized gold-coated superparamagnetic iron oxide nanoparticles for biomedical applications. *Molecules*, 25(19), p. 4425.
- Strehlow, W. H. & Cook, E. L., 1973. Compilation of Energy Band Gaps in Elemental and Binary Compound Semiconductors. *Journal of Physical and Chemical Reference Data*, 2(1), pp. 163-199.

- Sudha, P. N., Sangeetha, K., Vijayalakshmi, K. & Barhoum, A., 2018. Nanomaterials history, classification, unique properties, production and market. In: *Emerging Applications of Nanoparticles and Architectural Nanostructures*. s.l.:Elsevier, pp. 341-344.
- Suetsuna, T. et al., 2011. Effects of Crystalline grain size and packing ratio of self-forming core/shell nanoparticles on magnetic properties at up to GHz bands. *Journal of magnetism and magnetic materials*, 323(13), pp. 1792-1798.
- Surek, T., 2005. Crystal growth and materials research in photovoltaics: progress and challenges. *ournal of Crystal Growth*, 275(1-2), pp. 292-304.
- Surwade, S. P., Zhao, S. & Liu, H., 2011. Molecular lithography through DNA-mediated etching and masking of SiO₂. *Journal of the American Chemical Society*, 133(31), pp. 11868-11871.
- Tan, C. Z. & Arndt, J., 2000. Interaction of longitudinal and transverse optic modes in silica glass. *Journal of Chemical Physics*, 112(13), pp. 5970-5974.
- Tang, M. et al., 2014. Factors that affect the stability, type and morphology of pickering emulsion stabilized by silver nanoparticles/graphene oxide nanocomposites. *Mater. Res. Bull.*, Volume 60, pp. 118-129.
- Tarkistani, M., Komalla, V. & Kayser, V., 2021. Recent Advances in the Use of Iron–Gold Hybrid Nanoparticles for Biomedical Applications. *Nanomaterials*, 11(5), p. 1227.
- Thermo-Scientific, 2013. *ThermoFisher Scientific*. [Online]
Available at: <https://www.thermofisher.com/document-connect/document-connect.html?url=https://assets.thermofisher.com/TFS-Assets%2FCAD%2FSpecification-Sheets%2FNicolet%20iN10-PS51510.pdf>
[Accessed 13 01 2022].
- Thimsen, E., Le Formal, F., Grätzel, M. & Warren, S. C., 2011. Influence of Plasmonic Au Nanoparticles on the Photoactivity of Fe₂O₃ Electrodes for Water Splitting. *Nano Letters*, 11(1), pp. 35-43.
- Thomann, I. et al., 2011. Plasmon enhanced solar-to-fuel energy conversion. *Nano Letters*, 11(8), pp. 3440-3446.
- Tien, P. K., 1971. Light waves in Thin Films and Integrated Optics. *Applied Optics*, 10(11), pp. 2395-2413.
- Tiginyanu, I., Ursaki, V. & Popa, V., 2011. Nanoimprint Lithography (NIL) and related techniques for electronics applications. In: *Nanocoatings and ultra-thin films*. s.l.:Woodhead Publishing Limited, 2011, pp. 280-329.
- Tisdale, W. et al., 2010. Hot-electron transfer from semiconductor nanocrystals. *Science*, 328(5985), pp. 1543-1547.
- Tracy, J. & Crawford, T., 2013. Magnetic field-directed self-assembly of magnetic nanoparticles.. *MRS Bulletin*, Volume 38, pp. 915-920.
- Tronc, E., 1996. Nanoparticles. *Il Nuovo Cimento D*, 18(2), pp. 163-180.

Tsendzughul, N. & Ogwu, A., 2020. Visible light activated antimicrobial silver oxide thin films. In: *Advances in Medical and Surgical Engineering*. s.l.:Academic Press, pp. 179-239.

Tseng, A. A., Notargiacomo, A. & Chen, T. P., 2005. Nanofabrication by scanning probe microscope lithography: A review. *Journal of Vacuum Science & Technology B: Microelectronics and Nanometer Structures Processing, Measurement, and Phenomena*, 23(3), pp. 877-894.

Tsurko, E. S. et al., 2017. Large Scale Self-Assembly of Smectic Nanocomposite Films by Doctor Blading versus Spray Coating: Impact of Crystal Quality on Barrier Properties. *Macromolecules*, 50(11), pp. 4344-4350.

Tyona, M., 2013. A theoretical study on spin coating technique.. *Advances in materials Research*, 2(4), p. 195.

Uemura, Y. I. A. P. S. et al., 2022. Hole Dynamics in Photoexcited Hematite Studied with Femtosecond Oxygen K-edge X-ray Absorption Spectroscopy. *Journal of Physical Chemistry Letters*, Volume 13, pp. 4207-4214.

Ulman, A., 1991. *An introduction to Ultrathin Organic Film from Langmuir-Blodgett to Self-Assembly*. San Diego, California: Academic Press. Inc..

Ung, T., Liz-Marzan, L. M. & Mulvaney, P., 2002. Gold nanoparticle thin films. *Colloids and Surfaces A*, Volume 202, pp. 119-126.

Urbach, A. R., Love, C., Prentiss, M. G. & Whitesides, G. M., 2003. Sub-100nm Confinement of Magnetic Nanoparticles using localized Magnetic field Gradients. *Journal of American Chemical Society*, 125(42), pp. 12704-12705.

Valenti, M. et al., 2016. Plasmonic nanoparticle-semiconductor composites for efficient solar water splitting. *Journal of Materials Chemistry A*, 4(46), pp. 17891-17912.

Vallabani, N. & Singh, S., 2018. Recent advances and future prospects of iron oxide nanoparticles in biomedicine and diagnostics. *3 Biotech*, 8(6), pp. 1-23.

van Dommelen, R., Fanzio, P. & Sasso, L., 2018. Surface self-assembly of colloidal crystals for micro- and nano-patterning. *Adv. Colloid and Interf. Sci.*, Volume 251, pp. 97-144.

Velasco, V. et al., 2015. Chemically Synthesised Au-Fe₃O₄ nanostructures with controlled optical and magnetic properties. *J. Phys. D: Applied Physics*, Volume 48, p. 11pp.

Višňovský, Š., Postava, K. & Yamaguchi, T., 2001. Magneto-optic polar Kerr and Faraday effects in magnetic superlattices. *Czechoslovak Journal of Physics*, 51(9), pp. 917-949.

Wang, D., Duan, H. & Möhwald, H., 2005. The water/oil interface: the emerging horizon for self-assembly of nanoparticles.. *Soft Matter*, 1(6), pp. 412-416.

Wang, L., Nakajima, T. & Zhang, Y., 2019. Simultaneous reduction of surface, bulk, and interface recombination for Au nanoparticle-embedded hematite nanorod photoanodes toward efficient water splitting. *Journal of Materials Chemistry A*, Volume 7, pp. 5258-5265.

- Wang, M., He, L. & Yin, Y., 2013. Magnetic Field guided Colloidal Assembly. *Materials today*, 16(4), pp. 110-116.
- Wang, T. B., Liu, Z. G. & Tan, C. Z., 2003. Relationship between the frequency of the main LO mode of silica glass and angle of incidence. *Journal of Chemical Physics*, 119(1), pp. 505-509.
- Wang, T. et al., 2013. Surface enhanced infrared spectroscopy with gold strip gratings. *Optics Express*, 21(7), pp. 9005-9010.
- Wang, W. et al., 2005. Monodispersed core-shell Fe₃O₄@ Au nanoparticles. *The Journal of Physical Chemistry B*, 109(46), pp. 21593-21601.
- Wang, W. & Qi, L., 2019. Light management with patterned micro-and nanostructure arrays for photocatalysis, photovoltaics, and optoelectronic and optical devices. *Advanced Functional Materials*, 29(25), p. 1807275.
- Wang, Y., Dostalek, J. & Knoll, W., 2011. Magnetic nanoparticle-enhanced biosensor based on grating-coupled surface plasmon resonance. *Analytical chemistry*, 83(16), pp. 6202-6207.
- Wang, Y. et al., 2020. Enhanced dispersion stability of gold nanoparticles by the physisorption of cyclic poly (ethylene glycol). *Nature communications*, 11(1), pp. 1-12.
- Wang, Z., Liu, Y. & Zhang, Z., 2003. *Dynamic Properties of Nanoparticles*. Academic ed. Boston: Springer.
- Wan, Y., Yashuai, A. & Luogen, D., 2017. Plasmonic enhanced low-threshold random lasing from dye doped nematic liquid crystals with TiN nanoparticles in capillary tubes. *Scientific reports, Nature.*, Volume 7.
- Watt, F. et al., 2005. Ion beam lithography and nanofabrication: A review. *International Journal of Nanoscience*, 4(3), pp. 269-286.
- Weidner, D. E., 2018. Analysis of the flow of a thin liquid film on the surface of a rotating, curved, axisymmetric substrate. *Physics of Fluids*, Volume 30, p. 082110.
- Wei, Q. H. S. K. H., Durant, S. & Zhang, X., 2004. Plasmon Resonance of Finite One-Dimensional Au Nanoparticle Chains. *Nano Lett*, 4(6), pp. 1067-1071.
- Wexler, A., 1967. Integrated Intensities of Absorption Bands in Infrared Spectroscopy. *Applied Spectroscopy Reviews*, 1(1), pp. 29-98.
- Wheeler, D. A. et al., 2012. Magnetic Fe₃O₄-Au core-shell nanostructures for surface enhanced Raman scattering. *Ann. Phys.*, 524(11), pp. 670-679.
- Whitesides, G., Kriebel, J. & Mayers, B., 2005. Self-assembly and nanostructured materials.. In: *In Nanoscale assembly*. Boston, MA.: Springer, pp. 217-239.
- Wilcoxon, J. & Abrams, B., 2006. Synthesis, structure and properties of metal nanoclusters. *Chemical Society Reviews*, 35(11), pp. 1162-1194.
- Wiley, B. J., Qin, D. & Xia, Y., 2010. Nanofabrication at High throughput an low cost. *ACS Nano*, 4(7), pp. 3554-3559.

Williams, P., Carpino, F. & Zborowski, M., 2010. Characterization of magnetic nanoparticles using a programmed quadruple magnetic field-flow fractionating. *Philosophica transactions Royal Society of America*, Volume 368, pp. 4419-4437.

Winkleman, A., Gates, B. D., McCarty, L. S. & Whitesides, G. M., 2005. Directed Self-Assembly of Spherical Particles on Patterned Electrodes by an Applied Electric Field.. *Adv. Mater.*, Volume 17, pp. 1507-1511.

Wong, S. et al., 2021. Physical stability and rheological behavior of Pickering emulsions stabilized by protein-polysaccharide hybrid nanoconjugates. *Nanotechnology Reviews*, 10(1), pp. 1293-1305.

Wu, B. et al., 2009. Interfacial activation of catalytically inert Au (6.7 nm)-Fe₃O₄ dumbbell nanoparticles for CO oxidation. *Nano Research*, 2(12), pp. 975-983.

Wu, J. et al., 2012. Unidirectional water-penetration composite fibrous film via electrospinning. *Soft Matter*, 8(22), pp. 5996-5999.

Wu, S.-K., Tang, T.-P. & Tseng, W. J., 2008. Self-assembly of polystyrene microspheres within spatially confined rectangular microgrooves. *Journal of Material Science*, Volume 43, pp. 6453-6458.

Wu, W.-T., Chen, C.-H., Chiang, C.-Y. & Chau, L.-K., 2018. Effect of Surface Coverage of Gold Nanoparticles on the Refractive Index Sensitivity in Fibre-Optic Nanoplasmonic Sensing. *Optical Chemical Nanosensors*, 18(6).

Xia, D., Biswas, A., Li, D. & Brueck, S. R. J., 2004. Direct Self-Assembly of Silica Nanoparticles into Nanometer-Scale Patterned Surface Using Spin-Coating. *Advanced Materials Communication*, 16(16), pp. 1427-1432.

Xia, D., Biswas, A., Li, D. & Brueck, S. R. J., 2004. Directed Self-Assembly of Silica Nanoparticles into Nanometer-Scale Patterned Surfaces Using Spin-Coating. *Advanced Materials Communication*, 16(16), pp. 1427-1432.

Xia, D. & Brueck, S. R. J., 2004. A facile Approach to Directed Assembly of Patterns of Nanoparticles Using Interference Lithography and Spin Coating. *Nano Letters*, 4(7), pp. 1295-1299.

Xiao, L. & Yeung, E., 2014. Optical imaging of individual plasmonic nanoparticles in biological samples.. *Annual Review of Analytical Chemistry*, Volume 7, pp. 89-111.

Xia, Y., Yin, Y., Lu, Y. & McLellan, J., 2003. Template-assisted self-assembly of spherical colloids into complex and controllable structures. *Advanced Functional Materials*, 13(12), pp. 907-918.

Xing, C. et al., 2020. Convective Self-Assembly of 2D Nonclose-Packed Binary Au Nanoparticle Arrays with Tunable Optical Properties. *Chem. Mater.*, 33(1), pp. 310-319.

Xue, X. & Furlani, P. E., 2014. Template-assisted nano-patterning of magnetic core-shell particles in gradient fields. *Physical Chemistry Chemical Physics*, 16(26), pp. 13306-13317.

Xu, H., Aizpurua, J., Kall, M. & Apell, P., 2000. Electromagnetic contributions to single-molecule sensitivity in surface-enhanced Raman scattering. *Phys. Rev. E*, Volume 62, pp. 4318-4324.

- Xu, K. & Chen, J., 2020. High-resolution scanning probe lithography. *Applied Nanoscience*, Volume 10, pp. 1013-1022.
- Yang, L., 2003. *Life Cycle Costing for Cleanroom Construction*. Master of Science Thesis ed. Singapore: Department of Building, National University, Singapore.
- Ye, M. et al., 2015. Fast assembling microarrays of superparamagnetic Fe₃O₄@ Au nanoparticle clusters as reproducible substrates for surface-enhanced Raman scattering.. *Nanoscale*, 7(32), pp. 13427-13437.
- Ye, Y., Chen, T. P., Liu, Z. & Yuan, X., 2018. Effect of Surface Scattering of Electrons on Ratios of Optical Absorption and Scattering to Extinction of Gold Nanoshell. *Nanoscale Research Letters*, 13(229), pp. 1-11.
- Yin, Y., Lu, Y., Gates, B. & Xia, Y., 2001. Template-assisted self-assembly: a practical route to complex aggregates of monodispersed colloids with well-defined sizes, shapes, and structures.. *Journal of the American Chemical Society*, 123(36), pp. 8718-8729.
- Younan, N., Hojeij, M., Ribeaucourt, L. & Girault, H., 2010. Electrochemical properties of gold nanoparticles assembly at polarised liquid| liquid interfaces.. *Electrochemistry communications*, 12(7), pp. 912-915.
- Yuan, C. Y. & Dornfeld, D. A., 2010. Integrated Sustainability Analysis of Atomic Layer Deposition for Microelectronics Manufacturing. *J. Manuf. Sci. Eng.*, 132(3), p. 030918(7).
- Yu, D. et al., 2022. Recent Advances in Luminescent Downconversion: New Materials, Techniques, and Applications in Solar Cells. *Advanced Optical Materials*, p. 2200014.
- Yu, H. et al., 2005. Dumbbell-like bifunctional Au- Fe₃O₄ nanoparticles. *Nano letters*, 5(2), pp. 379-382.
- Zare, Y., 2016. Study of nanoparticles aggregation/agglomeration in polymer particulate nanocomposites by mechanical properties. *Compos A: Appl Sci Manuf.*, Volume 84, pp. 158-164.
- Zare, Y., 2016. The roles of nanoparticles accumulation and interphase properties in properties of polymer particulate nanocomposites by a multi-step methodology. *Compos A: Appl Sci Manuf.*, Volume 91, pp. 127-132.
- Zhang, C., Geng, Z. & Ma, J., 2013. Self-assembly synthesis of ordered mesoporous carbon thin film by a dip coating technique. *Microporous and Mesoporous Materials*, Volume 170, pp. 287-292.
- Zhang, C. et al., 2014. Closely Packed nanoparticle monolayer as a strain gauge fabricated by convective assembly at a confined angle. *Nano Research*, 7(6), pp. 824-834.
- Zhang, G., Surwade, S. P., Zhou, F. & Liu, H., 2013. DNA nanostructure meets nanofabrication.. *Chemical Society Reviews*, 42(7), pp. 2488-2496.
- Zhang, Q., Uchaker, E., Candelaria, S. & Cao, G., 2013. Nanomaterials for energy conversion and storage. *Chemical Society Reviews*, 42(7), pp. 3127-3171.
- Zhang, X. & John, S., 2020. Enhanced photocatalysis by light-trapping optimization in inverse opals. *Journal of Materials Chemistry A*, 8(36), pp. 18974-18986.

- Zhang, X. & John, S., 2021. Photonic crystal light trapping for photocatalysis. *Optics Express*, 29(14), pp. 22376-22402.
- Zhang, Y. et al., 2011. Magnetic manipulation and optical imaging of an active plasmonic single-particle Fe–Au nanorod. *Langmuir*, 27(24), pp. 15292-15298.
- Zhao, X.-M., Xia, Y. & Whitesides, G. M., 1997. Soft lithographic methods for nano-fabrication. *J. Mater. Chem.*, 7(7), pp. 1069-1074.
- Zhong, F., Wu, Z., Guo, J. & Jia, D., 2018. Porous Silicon Photonic Crystals Coated with Ag Nanoparticles as Efficient Substrates for Detecting Trace Explosives Using SERS. *Nanomaterials*, 8(8), pp. 1-12.
- Zhou, Q., Dong, P., Liu, L. & Bingying, C., 2005. Study on the sedimentation self-assembly of colloidal SiO₂ particles under gravitational field. *Colloids and Surfaces A: Physicochemical and Engineering Aspects*, 253(1-3), pp. 169-174.
- Zhu, J. et al., 2014. Synthesis of Au–Fe₃O₄ heterostructured nanoparticles for in vivo computed tomography and magnetic resonance dual model imaging. *Nanoscale*, 6(1), pp. 199-202.
- Zhu, X., 1994. Surface photochemistry. *Annual Review of Physical Chemistry*, 45(1), pp. 113-144.
- Zhu, Z., Wu, S., Zhang, C. & Zhou, J., 2021. Length Measurement of Chain-Like Structure of Micron Magnetic Particles Dispersing in Carrier Fluid Effected by Magnetic Field. *Journal of Superconductivity and Novel Magnetism*, Volume 34, pp. 805-816.
- Zong, X. & Wang, L., 2014. Ion-exchangeable semiconductor materials for visible light-induced photocatalysis. *Journal of Photochemistry and Photobiology C: Photochemistry Reviews*, Volume 18, pp. 32-49.

Appendices

8.1 Estimation of gold methacrylate molecules calculation steps

Gold methacrylate

The mass of gold remaining (G_{res}): $0.935855 \times 17.515mg = 16.39151mg$

Volume of gold (G_{vol}) using standard density of gold ($\rho = 19.3$ g/ml):

$$\frac{0.01639151}{19.3} = 8.493 \times 10^{-4}ml \text{ or } 8.493 \times 10^{-10}m^3$$

Volume of gold nanoparticle ($G_{NP(vol)}$) with particle diameter ($d = 17.43nm$):

$$\frac{\pi}{6} \times (17.43 \times 10^{-9})^3 = 2.7726 \times 10^{-24}m^3$$

Number of gold nanoparticles ($G_{NP(i)}$) in residue is:

$$\frac{8.493 \times 10^{-10}}{2.7726 \times 10^{-24}} = 3.0632 \times 10^{14}particles$$

The mass of Methacrylate molecules burnt off from gold nanoparticle (MC_m) is:

$$17.515mg - 16.39151mg = 1.12349mg$$

Number of moles in Methacrylate (MC_n) where molecular mass of Methacrylic acid ($MM=86.06$ g/mol) is:

$$\frac{1.12349 \times 10^{-3}}{86.06} = 1.3055 \times 10^{-5} moles$$

Number of molecules of burnt Methacrylic acid (MC_i) using Avogadro's number ($Av = 6.02214 \times 10^{23} \text{ mol}^{-1}$):

$$1.3055 \times 10^{-5} \times 6.02214 \times 10^{23} = 7.8619 \times 10^{18}molecules$$

Number of Methacrylic molecules per gold nanoparticle ($MC_i/ G_{NP(i)}$) is

$$\frac{7.8619 \times 10^{18}}{3.0632 \times 10^{14}} = 25665 \text{ molecules/nanoparticle}$$

OR

Number of methacrylic molecules per surface area of gold nanoparticle is:

$$\frac{25665}{\pi d^2} = \frac{25665}{9.5443 \times 10^{-16}} = 2.689 \times 10^{19} \text{ molecules/m}^3$$

8.2 Code for droplet size distribution following centrifugation

```

Sub PDF_Centrifugated_Droplets()
Dim M1, M2, F1, F2, SD1, SD2, x, PDF, Pi, nM1, nM2, nVar1, nVar2, SPdf As Double
'M1=Mean1, M2=Mean2, F1=Fraction1, F2=Fraction2, SD1=Standard Deviation1, SD2=Standard Deviation2,
nM1=Lognormal mean of modal1, nM2=Lognormal mean of modal2, nVar1=Lognormal variance of modal1,
nVar2=lognormal variance of modal2, SPdf=Sum of PDF values.
Dim row, i, j, v, w, m, q, p As Integer
Pi = 3.142
For i = 15 To 28
x = Sheet1.Cells(1, i).Value
For j = 2 To 31
M1 = Sheet1.Cells(j, 3).Value
M2 = Sheet1.Cells(j, 4).Value
F1 = Sheet1.Cells(j, 5).Value
F2 = Sheet1.Cells(j, 6).Value
SD1 = Sheet1.Cells(j, 7).Value
SD2 = Sheet1.Cells(j, 8).Value

'Calculate the Probability Density values for all values of SizeA
If Sheet1.Cells(j, 4) = Empty Then
'Apply formula to calculate mean and variance 1
nVar1 = Sqr(Log(1 + (SD1 / M1) ^ 2))
nM1 = Log(M1) - 0.5 * (nVar1) ^ 2
Sheet1.Cells(j, 9) = nM1
Sheet1.Cells(j, 13) = nVar1
PDF = ((F1 / (Sqr(2 * Pi) * nVar1 * Log(x))) * Exp(-((Log(x) - nM1) ^ 2 / (4 * (nVar1) ^ 2))))
GoTo 35
Else
'Apply formula to calculate mean and variance 1 & 2
nVar1 = Sqr(Log(1 + (SD1 / M1) ^ 2))
nM1 = Log(M1) - 0.5 * (nVar1) ^ 2
nVar2 = Sqr(Log(1 + (SD2 / M2) ^ 2))
nM2 = Log(M2) - 0.5 * (nVar2) ^ 2
Sheet1.Cells(j, 9) = nM1
Sheet1.Cells(j, 13) = nVar1
Sheet1.Cells(j, 10) = nM2
Sheet1.Cells(j, 14) = nVar2
PDF = ((F1 / (Sqr(2 * Pi) * nVar1 * Log(x))) * Exp(-0.5 * ((Log(x) - nM1) / (nVar1)) ^ 2)) + ((F2 / (Sqr(2
* Pi) * nVar2 * Log(x))) * Exp(-0.5 * ((Log(x) - nM2) / (nVar2)) ^ 2))
End If
35:
If PDF < 0.001 Then
PDF = 0
End If
If IsError(PDF) Then
PDF = 0
End If
Sheet1.Cells(j, i).Value = PDF
Next j

```

Next i

'OBTAIN RELATIVE VALUES AND RELATIVE PDF'S

For v = 15 To 28

For w = 2 To 31

p = v - 14

SPdf = Sheet1.Cells(w, 30)

Sheet2.Cells(w, p) = Sheet1.Cells(w, v).Value / SPdf

Next w

Next v

End Sub

8.3 Centrifugal size sorting fit trend equation

$$Size (nm) = 580460 \times Revs^{(-0.63539)} \quad [0-1]$$

With R squared fitting of 0.8497

8.4 Region of interest measurements for 3.5mPas at 700rpm and 2000rpm

Region of interest pixel intensity density Measurements for 0.035kg/ms at 700rpm sample

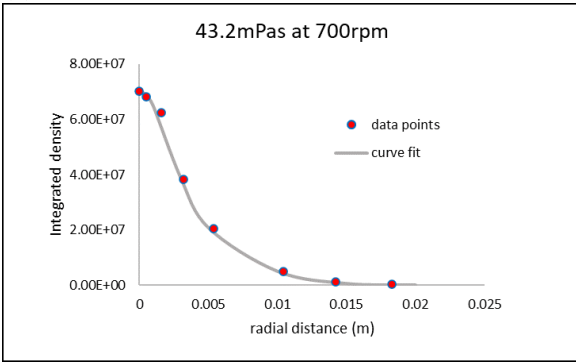
Label	Radius (um)	Area	Mean	StdDev	Min	Max	IntDen	Int/Area
ROI_1	1.64E+01	8.48E+02	1.25E+02	3.30E+01	1.00E+01	2.30E+02	3.46E+06	4.08E+03
ROI_2	4.05E+01	5.15E+03	1.05E+02	1.40E+01	1.20E+01	2.65E+02	2.10E+07	4.08E+03
ROI_3	7.10E+01	1.58E+04	1.04E+02	1.43E+01	1.50E+01	3.18E+02	6.45E+07	4.08E+03
ROI_4	1.11E+02	3.84E+04	1.03E+02	1.44E+01	2.00E+01	3.33E+02	1.55E+08	4.04E+03
ROI_5	1.50E+02	7.03E+04	1.02E+02	1.45E+01	2.00E+01	3.53E+02	2.80E+08	3.99E+03
ROI_6	2.10E+02	1.38E+05	9.95E+01	1.46E+01	1.90E+01	3.78E+02	5.37E+08	3.89E+03

Region of interest pixel intensity density Measurements for 0.035kg/ms at 2000rpm sample

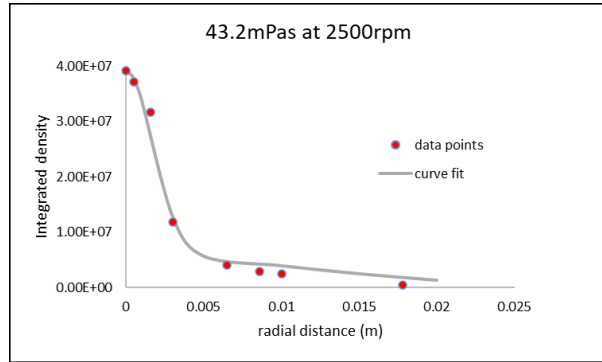
Label	Radius (um)	Area	Mean	StdDev	Min	Max	IntDen	Int/Area
ROI_1	1.64E+01	8.48E+02	1.25E+02	3.30E+01	1.00E+00	2.30E+02	1.32E+06	1.56E+03
ROI_2	4.05E+01	5.15E+03	1.29E+02	2.71E+01	1.00E+00	2.30E+02	8.04E+06	1.56E+03
ROI_3	7.10E+01	1.58E+04	1.26E+02	2.54E+01	1.00E+00	2.47E+02	2.47E+07	1.56E+03
ROI_4	1.11E+02	3.84E+04	1.16E+02	2.58E+01	1.00E+00	2.55E+02	5.49E+07	1.43E+03
ROI_5	1.50E+02	7.03E+04	1.06E+02	2.64E+01	1.00E+00	2.55E+02	9.16E+07	1.30E+03
ROI_6	2.10E+02	1.38E+05	9.46E+01	2.57E+01	1.00E+00	2.55E+02	1.61E+08	1.17E+03

8.5 Image density fitting

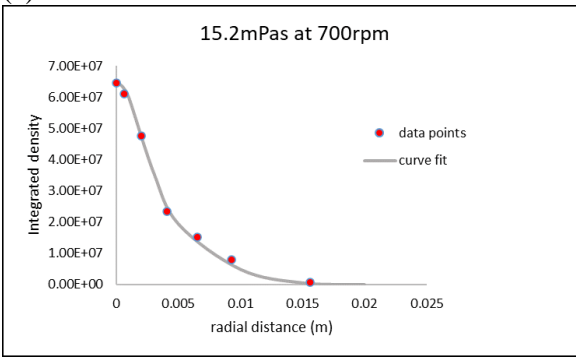
(a)



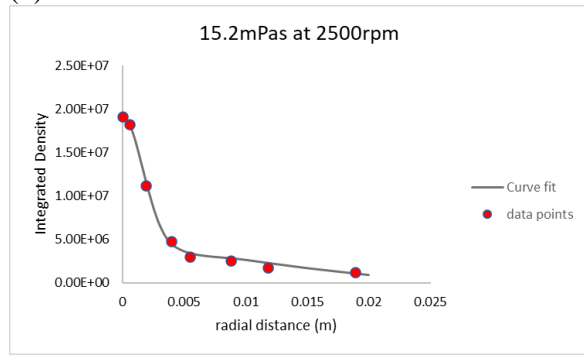
(b)



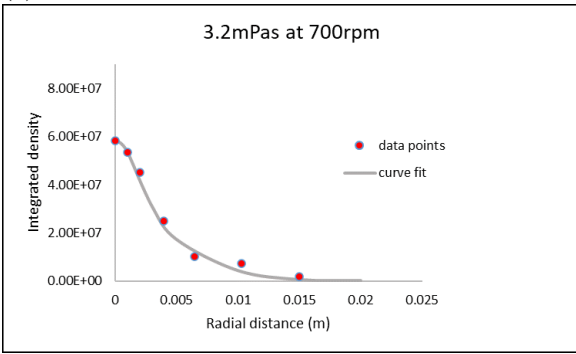
(c)



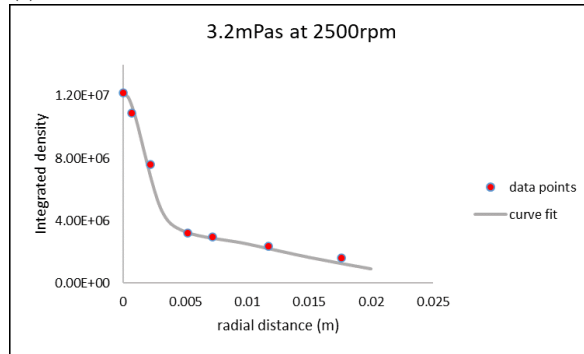
(d)



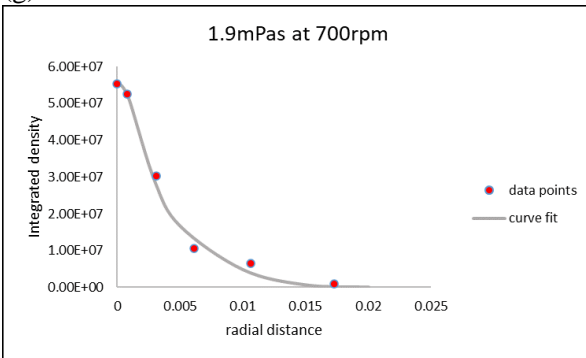
(e)



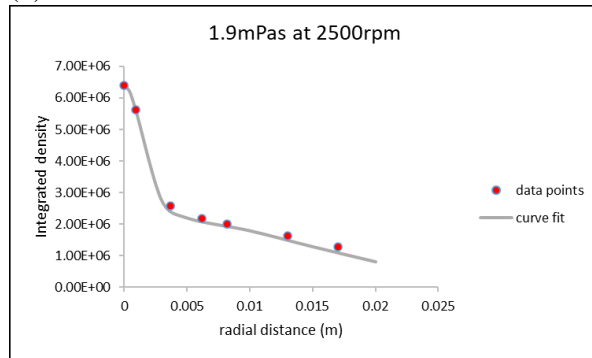
(f)



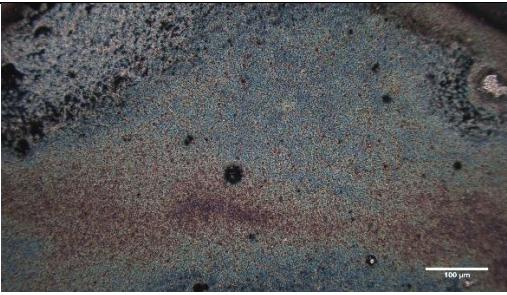
(g)

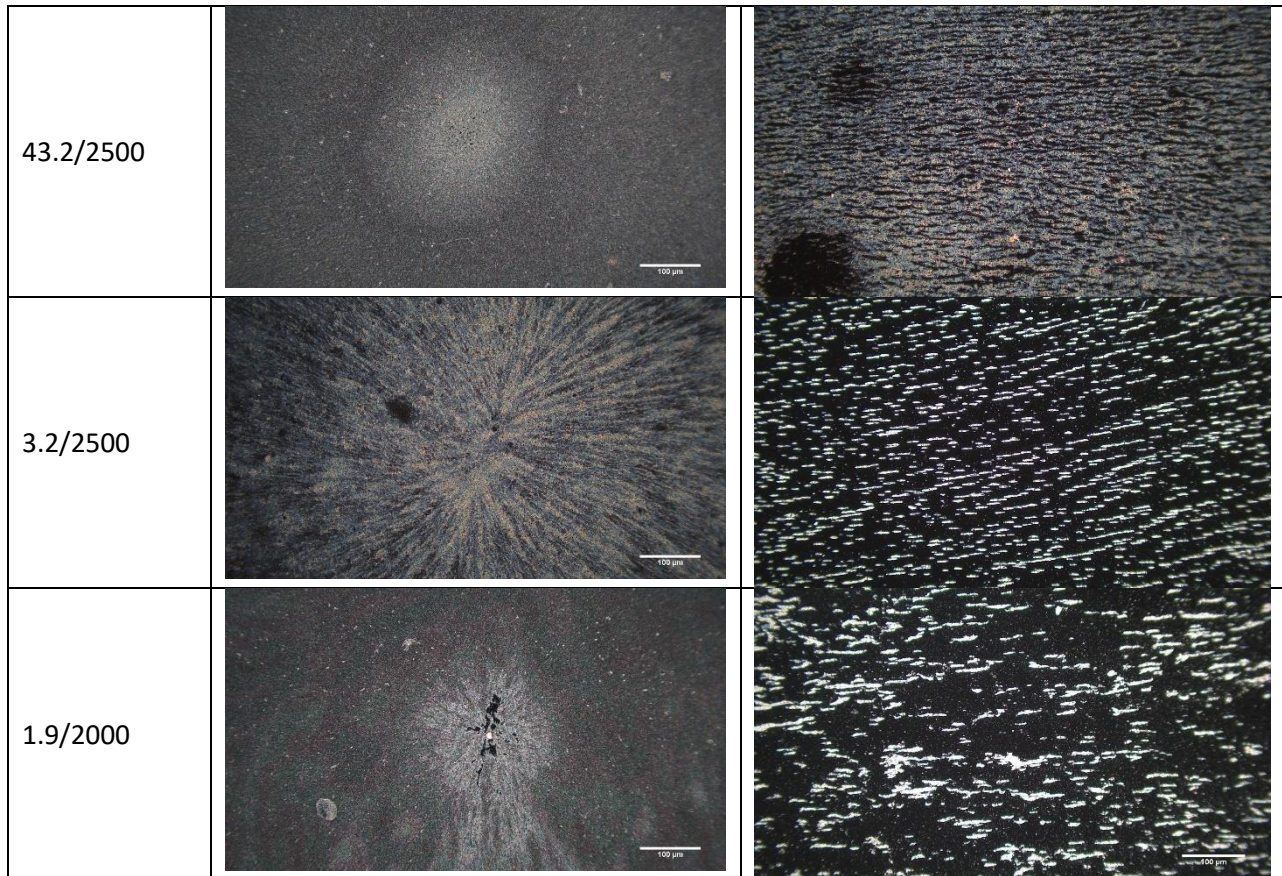


(h)



8.6 Sample images of spin coated thin films

Viscosity(mPa s)/speed(rpm)	R= 0mm	R=7mm
1.9/1500		
3.2/2000		
15.2/1000		
15.2/2500		
3.2/2500		



8.7 Simple Code for Chain thickness and gap Profile scan

```

Sub CL-CT_Scan()
Dim i, M, rw, CntCh, CntGap, K, L, CL1, CL2, d, W As Integer
'This is for estimating the chain thickness and gap from image scan
'i is counter for number of column/lines to be scanned, M = Number of 'scanned 'lines,
CntCH = Chain thickness pixel counts, CntGap = Chain 'gap pixel 'counts, K, CL2 =
variable associated with CntCH, L, CL1 = 'variable 'associated with CntGap, d = pixel
count (rows - W).
M = Sheet3.Cells(30, 25).Value      'number of columns to be scanned
For i = 1 To M
CntCh = 0
CntGap = 0
K = 1
L = 1
W = Sheet3.Cells(30, i * 2 + 24).Value  'number of rows per column
For d = 2 To W Step 1
If Sheet3.Cells(d, 2 * i).Value > 0 Then
If CntCh = 0 Then
K = K + 1
CL2 = K
Else
K = CL2
End If
CntCh = CntCh + 1
Sheet3.Cells(K + 31, i * 2 + 24) = CntCh
CntGap = 0

```

```

Else
If CntGap = 0 Then
L = L + 1
CL1 = L
Else
L = CL1
End If
CntGap = CntGap + 1
Sheet3.Cells(L + 31, i * 2 + 25) = CntGap
CntCh = 0
End If
Next d
Next i
End Sub

```

8.8 Example of scan plot profile for one of the red lines from Figure 4-12(b) with X as pixel divisions (168nm/pixel) and Y as the binary pixel intensity.

Red Line (B)		Red Line (D)		Red Line (F)		Red Line (H)	
X (divisions-nm/pixel)	Y (pixel intensity)						
0	255	0	0	0	255	0	255
168	255	168	0	168	238	168	255
337	0	337	0	337	247	337	0
505	0	505	0	505	255	505	0
673	0	673	0	673	255	673	0

8.9 Summary of pattern morphology image analysis for PVA 15.2mPas

2000	RPM								
x	CG	CT	CL	SD-CG	SD-CT	SD-CL	CL/CT	CT/CG	Qpi
0.0001	7.26E-01	3.59E+00	11.6	0.113	0.445	2.34	7.26E+03	4.95E+00	741.6753
0.0006	1.17E+00	3.35E+00	2.50E+01	0.197634	0.331624	8.39374	1.95E+03	2.87E+00	121.9136
0.0028	1.77E+00	1.89E+00	2.49E+01	0.281709	0.120368	4.298348	6.32E+02	1.07E+00	21.41232
0.0055	2.85E+00	1.70E+00	6.41E+01	0.721376	0.134699	5.718723	5.19E+02	5.96E-01	6.282408
0.0061	3.41E+00	1.40E+00	5.82E+00	0.532055	0.887868	1.382119	5.59E+02	4.12E-01	4.787218
0.0096	4.08E+00	1.215	1.21	0.742	0.0142	0.113	4.25E+02	2.98E-01	0.821803
2500	RPM								
x	CG	CT	CL	SD-CG	SD-CT	SD-CL	CL/CT	CT/CG	Qpi
0.0001	1.02E+00	3.04E+00	15.3	0.125	0.743	1.84	1.02E+04	2.97E+00	379.7368
0.0009	1.45E+00	2.75E+00	2.55E+01	0.240141	0.134112	2.36005	1.61E+03	1.90E+00	41.03946
0.0023	2.36E+00	2.41E+00	2.76E+01	0.397652	0.190433	3.732972	1.03E+03	1.02E+00	14.24194
0.0042	2.74E+00	1.72E+00	6.90E+01	0.455631	0.09421	3.03916	6.53E+02	6.28E-01	5.728691
0.0057	3.34E+00	1.51E+00	1.54E+01	0.772788	0.052178	4.219714	5.85E+02	4.53E-01	2.939852
0.0085	4.14E+00	1.215	1.21	0.025	0.321	0.254	4.87E+02	2.94E-01	0.760879
3000	RPM								
x	CG	CT	CL	SD-CG	SD-CT	SD-CL	CL/CT	CT/CG	Qpi
0.0001	1.31E+00	2.82E+00	22.1	0.035	0.176	1.2	1.31E+04	2.14E+00	219.7548
0.0006	1.91E+00	2.77E+00	3.03E+01	0.700762	0.362586	0.700762	3.18E+03	1.45E+00	36.12242
0.0017	2.56E+00	2.62E+00	4.09E+01	0.446337	0.07389	0.446337	1.50E+03	1.03E+00	11.87122
0.0031	2.66E+00	2.27E+00	8.66E+01	0.64685	0.147469	0.64685	8.59E+02	8.51E-01	5.480763
0.0044	3.02E+00	1.68E+00	1.24E+02	0.538161	0.210776	0.538161	6.85E+02	5.56E-01	3.033705
0.0064	4.63E+00	1.215	1.21	0.453	0.075	0.325	7.23E+02	2.63E-01	1.235146
3500	RPM								
R (m)	CG (μm)	CT (μm)	CL (μm)	SD-CG	SD-CT	SD-CL	CL/CT	CT/CG	Qpi
0.0001	1.70E+00	2.80E+00	28.3	0.351	0.183	0.642	1.70E+04	1.65E+00	138.3877
0.001	2.32E+00	2.66E+00	4.27E+01	1.40E-01	2.30E-01	5.32E+00	2.32E+03	1.15E+00	13.38585
0.0025	2.65E+00	2.46E+00	9.30E+01	0.217497	0.18849	1.721369	1.06E+03	9.29E-01	4.659019
0.0042	2.82E+00	2.15E+00	2.09E+02	0.522639	0.073206	19.06515	6.72E+02	7.63E-01	2.087711
0.0049	3.05E+00	1.94E+00	9.83E+01	0.577078	0.139186	13.47646	6.22E+02	6.36E-01	1.531205
0.0057	5.03E+00	1.215	1.21	0.321	0.076	0.342	8.83E+02	2.41E-01	1.071372

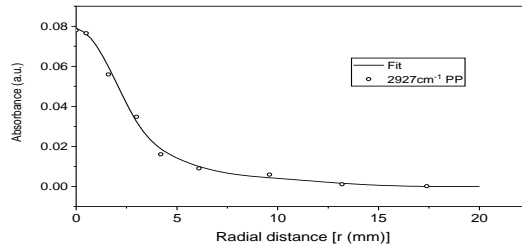
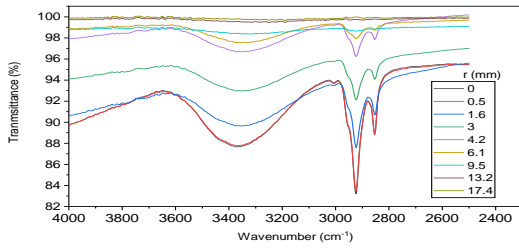
8.10 Energy ratio (QPI) determined from magnetic profile shown in Fig. 4.21 and emulsion property from Table 4.1 and preparation angular speed 3500 rpm

r(mm)	B (mT)	Q _{PI}
0.1	55	2.78E+03
1	44	889.2264
2	31	220.699
4	19	41.45283
6	14.7	16.54209
8	53	161.2756
10	105.4	5.10E+02
14	44	6.35E+01
16	10	2.87E+00
18	5.2	6.90E-01
20	0.7	1.13E-02

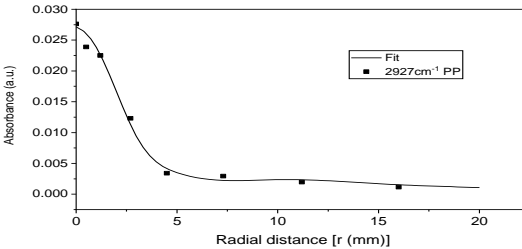
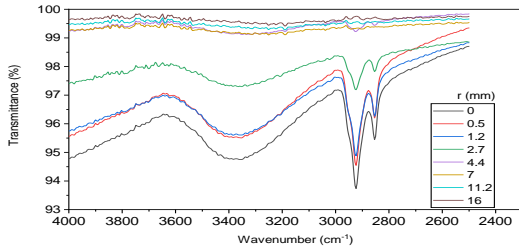
8.11 Defectivity determination from Profile scan results from Figure 4-23

Qpi	Pixel Count	Droplets pixel counts	Gap pixel counts	CL (um) 0.1677 um/pixel	Defect on Individual profiles	Mean Defectivity	SD
220.7	744	702	42	124.7688	0.056452	0.13	0.0566
	994	895	99	166.6938	0.099598		
	555	471	84	93.0735	0.151351		
	949	752	197	159.1473	0.207587		
	605	524	81	101.4585	0.133884		
41.5	938	830	108	157.3026	0.115139	0.153	0.0315
	843	726	117	141.3711	0.13879		
	924	759	165	154.9548	0.178571		
	804	660	144	134.8308	0.179104		

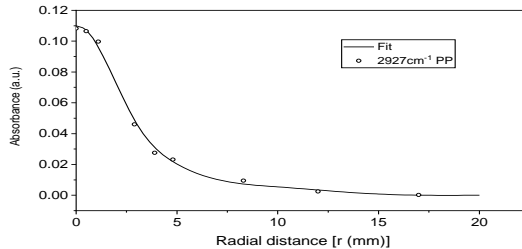
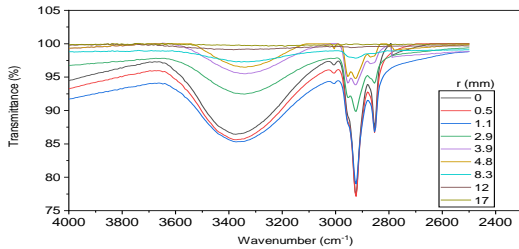
8.12 FTIR Transmission mode absorption data for thin film pattern on optical glass



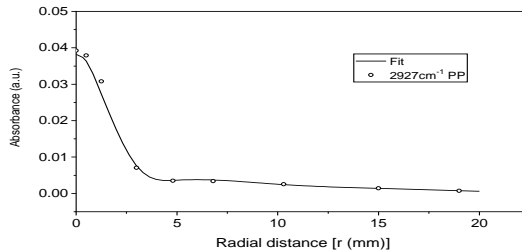
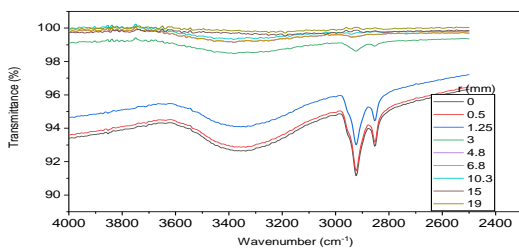
3.2mPas @ 700rpm



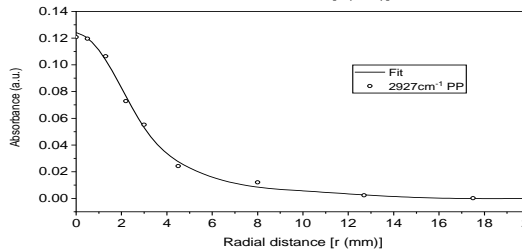
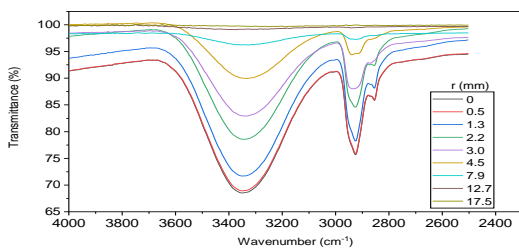
3.2mPas @ 2500rpm



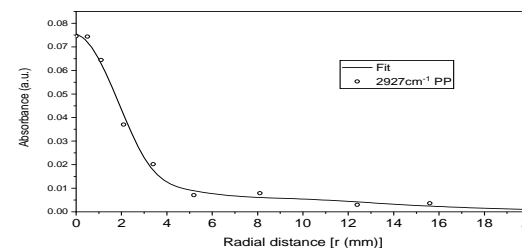
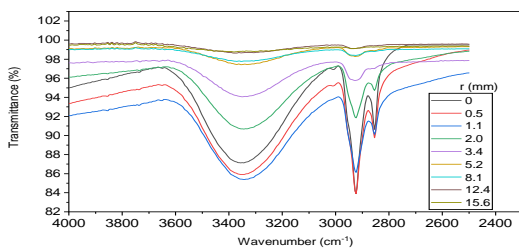
15.2mPas @ 700rpm



15.2mPas @ 2500rpm



43.2mPas @ 700rpm



43.2mPas @ 2500rpm

8.13 Deconvolved band of UV-Vis Spectra of Samples

1mm	y0	y0	xc	xc	A	A	w	w	Statistics	Statistics
	Value	Standard Error	Value	Standard Error	Value	Standard Error	Value	Standard Error	Reduced Chi-Sqr	Adj. R-Square
Bnd-A	0.00186	0.00228	399.7132	0.18385	8.19983	0.60117	19.9426	0.64671	2.79E-04	0.99961
Bnd-B	0.00186	0.00228	436.9593	2.37128	84.18413	26.30917	48.62346	2.77105		
Bnd-C	0.00186	0.00228	482.5653	1.46447	119.7757	55.33897	66.39669	18.42418		
Au-Plasmon	0.00186	0.00228	518.6418	0.87931	6.25058	4.23525	28.45128	4.64816		
Bnd-D	0.00186	0.00228	551.2614	3.97162	161.9763	37.89718	82.61143	9.56529		
Bnd-E	0.00186	0.00228	626.638	4.19911	124.3371	12.55267	97.24893	3.21195		
Bnd-F	0.00186	0.00228	680.2538	0.18612	14.83764	0.59798	30.50193	0.61449		
2mm	y0	y0	xc	xc	A	A	w	w	Statistics	Statistics
	Value	Standard Error	Value	Standard Error	Value	Standard Error	Value	Standard Error	Reduced Chi-Sqr	Adj. R-Square
Bnd-A	-0.00135	0.00213	399.7149	0.18268	7.72436	0.65961	19.96809	0.70135	2.31E-04	0.99948
Bnd-B	-0.00135	0.00213	435.5272	3.20759	71.29655	33.02917	48.52605	3.98133		
Bnd-C	-0.00135	0.00213	481.9525	1.80108	103.5608	66.72176	67.78104	29.17143		
Au-Plasmon	-0.00135	0.00213	519.6286	1.79984	7.86066	8.98066	33.27981	7.42798		
Bnd-D	-0.00135	0.00213	552.031	6.06634	114.8371	34.7952	80.43278	11.012		
Bnd-E	-0.00135	0.00213	627.3301	3.82717	109.4589	9.58847	98.6192	3.08121		
Bnd-F	-0.00135	0.00213	680.9405	0.17432	13.75147	0.50845	30.01278	0.57056		
4mm	y0	y0	xc	xc	A	A	w	w	Statistics	Statistics
	Value	Standard Error	Value	Standard Error	Value	Standard Error	Value	Standard Error	Reduced Chi-Sqr	Adj. R-Square
Bnd-A	3.20E-04	0.0019	398.4045	0.224	5.62246	0.74674	18.34109	0.89707	1.97E-04	0.99904
Bnd-B	3.20E-04	0.0019	422.1689	0.52131	23.92705	4.93328	39.32663	2.77959		
Bnd-C	3.20E-04	0.0019	459.8012	1.22226	83.83328	5.86519	64.03908	2.79122		
Bnd-D	3.20E-04	0.0019	539.4439	0.44697	103.1296	2.17473	80.10591	1.33655		
Bnd-E	3.20E-04	0.0019	639.4037	0.43941	78.72753	1.05329	87.65236	0.9051		
Bnd-F	3.20E-04	0.0019	682.2525	0.1755	9.4556	0.32524	27.57419	0.56856		
6mm	y0	y0	xc	xc	A	A	w	w	Statistics	Statistics
	Value	Standard Error	Value	Standard Error	Value	Standard Error	Value	Standard Error	Reduced Chi-Sqr	Adj. R-Square
Bnd-A	-0.0015	0.00201	399.2408	0.18487	6.27727	0.29249	19.83895	0.55351	2.36E-04	0.99869
Bnd-B	-0.0015	0.00201	437.8185	0.13412	64.60604	0.80416	52.06999	0.50952		
Bnd-C	-0.0015	0.00201	480.4685	0.66123	1.32356	0.22444	16.88234	1.92302		
Bnd-D	-0.0015	0.00201	524.8594	0.19439	130.2947	1.1794	98.85733	0.95763		
Bnd-E	-0.0015	0.00201	641.7571	0.44448	74.58941	0.92169	87.77785	0.79916		
Bnd-F	-0.0015	0.00201	680.27389	0.16023	13.39711	0.41218	30.21214	0.5303		

Deconvolved band of UV-Vis spectra of samples continued.

8mm	y0	y0	xc	xc	A	A	w	w	Statistics	Statistics
	Value	Standard Error	Reduced Chi-Sqr	Adj. R-Square						
Bnd-A	-0.00474	0.00342	399.7204	0.23727	5.65469	0.49535	20.21296	0.82104	2.31E-04	0.99861
Bnd-B	-0.00474	0.00342	434.4863	1.61621	43.53983	17.82246	53.06523	4.27585		
Bnd-C	-0.00474	0.00342	477.9885	5.41885	64.83962	28.75254	78.10634	18.45879		
Bnd-D	-0.00474	0.00342	561.6438	1.76448	105.3384	21.16599	92.16334	10.88206		
Bnd-E	-0.00474	0.00342	648.2168	10.04688	42.63346	10.26937	97.85916	9.87544		
Bnd-F	-0.00474	0.00342	683.4437	0.16142	12.49712	0.57394	28.64209	0.63033		

Summary of data of deconvolved bands

r (mm)	CT/CG	CT (um)	Bnd-A			Bnd-B			Bnd-C		
			Wavelength (nm)	FWHM (nm)	Peak Intensity	Wavelength (nm)	FWHM (nm)	Peak Intensity	Wavelength (nm)	FWHM (nm)	Peak Intensity
1	2.44	1.761	399	20	0.3842	437	48.6	1.63	482	66.4	1.6954
2	1.58	1.326	399	20	0.363	436	48.5	1.39	482	68	1.44
4	1.47	1.09	398	18.34	0.3	422	39.3	0.57	460	64	1.23
6	0.64	0.88	399	20	0.3	437	52	1.17	480	17	0.073
8	1.87	2.26	399	20.21	0.26	434	53	0.77	474	78	0.78
r (mm)	CT/CG	CT (um)	Bnd-D			Bnd-E			Bnd-F		
			Wavelength (nm)	FWHM (nm)	Peak Intensity	Wavelength (nm)	FWHM (nm)	Peak Intensity	Wavelength (nm)	FWHM (nm)	Peak Intensity
1	2.44	1.761	551	82.6	1.843	626.6	97.25	1.212	680.25	30.5	0.46
2	1.58	1.326	552	80.4	1.34	627	99	1.05	681	30	0.43
4	1.47	1.09	540	80.1	1.21	639.4	87.6	0.845	682	27.6	0.325
6	0.64	0.88	525	99	1.24	642	88	0.8	677	27	0.42
8	1.87	2.26	562	92	1.07	648	98	0.41	683	29	0.41
r (mm)	CT/CG	CT (um)	Gold Plasmon band								
			Wavelength (nm)	FWHM (nm)	Peak Intensity						
1	2.44	1.761	518.6	28.5	0.215						
2	1.58	1.326	520	33.3	0.22						

8.14 Deconvolved band of UV-Vis Spectra of Samples

